Studies on calcineurin and calcium ATPase PMR-1 roles in azole drug susceptibility in *Neurospora crassa*, and their interactions with azoles and phytochemical compounds

A Thesis

Submitted in Partial Fulfilment of the
Requirements for the Degree of

DOCTOR OF PHILOSOPHY

by

SANGEETA DEKA

Centre for The Environment
Indian Institute of Technology Guwahati
Guwahati-781039, Assam, India

August 2025

Dedicated to my parents

Mr. Ratneswar Deka (Deuta)

and

Mrs. Girija Deka (Maa)

and my Family

INDIAN INSTITUTE OF TECHNOLOGY GUWAHATI

CENTRE FOR THE ENVIRONMENT

STATEMENT

I do hereby declare that the research findings of this thesis are the result of research work carried out by me at the Centre for The Environment, Indian Institute of Technology Guwahati, Assam, India, under the supervision of **Prof. Ranjan Tamuli**.

As per the general norms of reporting research findings, due acknowledgments have been made, wherever the research findings of other researchers have been cited in this thesis.

Sangeeta Deka

IIT Guwahati
August 2025

Sangeeta Deka

Enrolment No.: 196152007
Centre for The Environment
Indian Institute of Technology Guwahati,
Guwahati-781039, Assam, India

INDIAN INSTITUTE OF TECHNOLOGY GUWAHATI

CENTRE FOR THE ENVIRONMENT

CERTIFICATE

It is certified that the work described in this thesis entitled “ **Studies on calcineurin and calcium ATPase PMR-1 roles in azole drugs susceptibility in *Neurospora crassa*, and their interactions with azoles and phytochemical compounds**” by **Sangeeta Deka (**196152007) for the award of the degree of **Doctor of Philosophy** is an authentic record of the results obtained from the research work carried out under my supervision in the **Centre for The Environment, Indian Institute of Technology Guwahati, Assam, India,** and this work has not been submitted elsewhere for the award of any other degree.

Ranjan Tamuli

IIT Guwahati

August 2025

Dr. Ranjan Tamuli

Professor

Centre for The Environment

Indian Institute of Technology Guwahati,
Guwahati-781039, Assam, India

ACKNOWLEDGEMENT

I feel privileged to pen down my wholehearted gratitude towards all the wonderful people who have directly or indirectly extended their valuable support and contributed imperatively to the completion of this thesis work. I am fortunate to acknowledge each one of them below for their consistent support during my years of scientific journey.

First and foremost, I am profoundly grateful to my thesis supervisor and mentor, **Prof. Ranjan Tamuli**, Sir, for his invaluable guidance and deep engagement in every aspect of my research. His insightful discussions and feedback have tremendously enriched my work, and his extensive knowledge has been a guiding light throughout this journey. More than a mentor, Prof. Tamuli has been a constant source of encouragement and wisdom, teaching me not just about science but also the art of staying calm and resilient under any circumstances. These lessons, learned by his side, will stay with me always. Thank you, Sir, for believing in me and supporting me in every step of the way.

I would also extend my gratitude to my Doctoral committee members, Prof. Utpal Bora and Prof. Ajaikumar B Kunnumakkara of the Department of BSBE, and Dr. Lal Mohan Kundu of the Department of Chemistry for their valuable, constructive suggestions throughout my PhD journey.

I would like to thank the present and former heads of the Center for the Environment, Prof. Mihir Kumar Purkait, Prof. Utpal Bora, and Prof. Animes Kr. Golder and head of the Department of BSBE, Prof. Rakhi Chaturvedi, and all the faculty members for their support and teachings. I would like to acknowledge the Center for the Environment and the Department of BSBE, IITG, for providing the infrastructural facility for my research work. I would also like to recognize the Central Instrumentation Facility (CIF), the supercomputing facility of IIT Guwahati, for providing high-end instruments to execute some of the research experiments.

It is my pleasure to thank all members of the Calcium signaling RT lab group who have given me a friendly and happy environment in the lab. I want to acknowledge the help I got from all the lab members for their constant cooperation when I started my work. This gratitude extends to Dr. Ajay Kumar Chandra, Dr. Himadree Das, Dr. Rahul Kumar Thaosen, Dr. Surabhi, Krishna, Megha, Rebecca, Shomina, Priyanuj, Ambika, Bijita as well as the alumni members of this group – Dr. Rekha Deka, Dr. Ravi Kumar, Dr. Vijaya Laxmi, Dr. Ananya Barman, Dr. Dibakar Gohain, Dr. Ajeet Kumar, Dr. Avishek Roy, Dr. Anand Tiwari, Dr. Tarinee Phukan, Dr. Christy K Marak, Dr. Darshana Baruah, Dr. Serena Ngiimei D, Shalini, Nayan Mani Bania, Divya, Smriti Sudha, Mohit, Aravind, Abhilash and Yogendra.

The very beginning of my Ph.D. journey would not have been so smooth without your help. My heartfelt thanks to Umesh, lab members, and co-authors from the lab group for sharing their knowledge and helping me with critical experiments. I will always cherish the memories I made with all of you, who have played varied roles of colleagues, life coaches, and teachers. My heartfelt gratitude to Dr. Rekha Deka Ma'am for celebrating with us in all the lab events, and to Trishani and Tanesh for filling this journey with memorable moments. I am grateful to all of you for your constant support, encouragement, and suggestions for this work.

I am also thankful to my alma mater, IIT Guwahati, and my friends Himadri, Aswani, Rajendra, Priyanka, Aniket, Gariyoshi, Pulak, Banhisikha, Shivani, Pinky, Krishna Kanta, Udangshree, Onkar, Rounak, Uzini; they made my stay at the IITG campus memorable. I have no words to explain their constant source of encouragement and joy during my ups and downs. Moreover, the greenery and serenity of the IITG campus made me self-motivated.

I fondly remember my late grandparents, Sishu Ram Deka Keot, Gunada Deka, Daibaki Saikia, and Dimbeswar Saikia, and seek their blessings. Special thanks to my beloved parents, Mrs. Girija Deka & Mr. Ratneswar Deka, and my beloved sisters, Rajashree Deka and Susmita Deka, for their unconditional love, belief, and encouragement in achieving my goals since childhood. I am deeply grateful to my family pillars, Mrs. Jaybala Gangrade and Mr. Gopaldas Gangrade, for their constant support and unconditional love. In this journey, my husband, Dr. Ankit Gangrade, has stood by my side as a pillar of support. His patience, unshakable faith in my goals, and profound understanding have provided me with strength during adversity. His positivity and encouragement are my wings of confidence, and he has stood beside me not only in victories but also during struggles, reminding me that every step forward brings me closer to my aspirations. And to my dearest Angad, whose gentle presence is already a quiet source of love and inspiration, thank you for being a beautiful part of my strength.

My brothers, Arup, Ankur, and Aditya, along with their wisdom, have enlightened my career and life goals. Furthermore, I extend my heartfelt love to my nephew Priyansh, Ekansh, and nieces Adhya, Aishvi, who have filled my life with boundless joy and great moments. My sisters from another mother, Shalini and Priya, have consistently shown me the significance of life's journey, keeping me focused on my goals.

Simple thanks are not enough to convey my deep respect and gratitude to all. I thank God, the Almighty, for showering blessings and grace at each and every step.

Sangeeta Deka

%	Percentage
.dpf	docking parameter files
.gpf	grid parameter files
$[Ca^{2+}]_c$	Cytosolic Ca^{2+} concentration
°C	Degree Celsius
µM	Micromolar
ADMET	Absorption-Distribution-Metabolism-Excretion Toxicity
ADT	AutoDock Tools
ANOVA	Analysis of Variance
BLAST	Basic Local Alignment Tool NCU Neurospora crassa unit
Bp	Base pair
Ca^{2+}	Calcium ion
CADD	Computer-Aided Drug Design
CaM	Calmodulin
cDNA	complementary Deoxyribonucleic Acid
ChIP	Chromatin Immunoprecipitation
cm	Centimetre
CNA-1	Calcineurin, consisting of a catalytic A subunit
CNB-1	Calcineurin, consisting of a catalytic B subunit
CRZ-1	calcineurin responsive zinc-finger-1
CSP-1	Transcription repressor conidial separation 1
CT	cycle threshold
CTAB	Cetyltrimethyl ammonium bromide
CTC	Chlortetracycline Hydrochloride
Co-IP	Co-immunoprecipitation
DCFH-DA	2',7'-dichlorodihydrofluorescein diacetate
DEPC	Diethyl pyrocarbonate
DMSO	Dimethyl sulfoxide
DNA	Deoxyribonucleic Acid
EMBL	European Molecular Biology Laboratory
EMSA	Electrophoretic Mobility Shift Assay
ER	Endoplasmic reticulum

EtBr	Ethidium bromide
ExPASy	Expert Protein Analysis System
FESEM	Field Emission Scanning Electron Microscope
FGSC	Fungal Genetics Stock Centre p Probability
FGSC	Fungal Genetic Stock Center
g	Gram
g	Relative Centrifugal Force
GFP	Green Fluorescent Protein
GUI	graphical user interface
h	Hour
I-TASSER	Iterative Threading ASSEmbly Refinement
kb	Kilo base pair
kcal	kilocalorie
kDa	Kilo Dalton
KV	Kilovolt
LG	Linkage Group
M	Metre
mA	Miliampere
MD	Molecular Dynamics
MIC	Minimum Inhibitory Concentrations
ml	Milliliter
mm	Millimeter
MSA	multiple sequence alignment
N	Normal
N. crassa	*Neurospora Crassa*
NCBI	National Centre for Biotechnology Information
NFAT	nuclear factor of activated T cells
ng	Nanogram
NIH	National Institute of Health
nM	Nanomolar
NMR	Nuclear Magnetic Resonance spectroscopy
ns	Non-significant

PCR	Polymerase Chain Reaction
PDB	Protein Data Bank
pm	Picometre
qRT-PCR	Quantitative Real-Time Polymerase Chain Reaction
Rg	radius of gyration
RIP	Repeat Induced Point Mutation
RMSD	Root Mean Square Deviation
RMSF	Root Mean Square Fluctuation
RNA	Ribonucleic Acid
ROS	Reactive Oxygen Species
rpm	Revolution per minute
RT-PCR	Reverse Transcription Polymerase Chain Reaction
s	Second
SASA	Solvent Accessible Surface Area
SD	standard deviation
SDS	Sodium dodecyl sulphate
SPRR	serine-proline-rich
UCR	University of California Riverside
USA	United States of America
UV	Ultraviolet
V	Volt
VGN	Vogel's Glucose Medium
VMD	Visual Molecular Dynamics
w/v	weight per volume
w/w	weight per weight
µL	Microlitre
µm	Micrometre

List of Tables

CHAPTER 1

CHAPTER 2

CHAPTER 3

CHAPTER 4

CHAPTER 5

CHAPTER 1

CHAPTER 3

CHAPTER 4

CHAPTER 5

Abstract

This thesis describes the effect of azoles in *Neurospora crassa*, and the molecular basis of interactions of the calcineurin and PMR-1 proteins with the fluconazole, itraconazole, and ketoconazole drugs. Azole treatments reduced ergosterol levels and increased reactive oxygen species (ROS) in the *N. crassa* calcineurin and *pmr-1* mutant strains. In addition, field emission scanning electron microscopy (FESEM) analysis revealed altered hyphal morphology in the calcineurin RIP and Δ*pmr-1* mutants treated with the azole drug fluconazole. Furthermore, expression of the *pmr-1* was upregulated under itraconazole treatment. Molecular docking and molecular dynamics (MD) simulations revealed the stable interactions of the azole drugs within the active site of the protein calcineurin and PMR-1 with efficient binding energies. Preliminary computational insights also show the critical amino acid residues for drug-target interactions. In addition, this study also delves into phytochemical compounds as potential inhibitors against Ca^{2+} signaling proteins pivotal in fungal pathogenicity, using computer-aided drug design (CADD). A total of 11 phytochemicals were assessed for their inhibitory potential, adhering to Lipinski's rule of drug-likeness, and *in silico* studies identified isorhamnetin as a promising phytochemical inhibitor for PMR-1 and CNA-1 proteins and dillenetin as a potential inhibitor of CNB-1 protein with the formation of the most stable complex. In conclusion, this thesis enhances our understanding of the molecular basis of azole susceptibility in *N. crassa.* The study also provides a promising future for the development of target-specific new antifungals targeting calcineurin and PMR-1.

Objectives of the Thesis

Objective 1: To determine the minimum inhibitory concentrations of azole drugs and to study the effects of azoles in the calcium signaling gene calcineurin and *pmr-1*, in *Neurospora crassa.*

Objective 2: To study the interaction of the CNA-1, CNB-1, and PMR-1 proteins with azole drugs using the molecular docking and molecular dynamics (MD) simulation approaches.

Objective 3: To study the phytochemical inhibitors targeting calcineurin and PMR-1 proteins using computer-aided drug design (CADD).

In line with the stated objectives, the thesis is organized into five chapters, outlined as follows:

Chapter 1: Introduction and Literature Review

Chapter 2: Materials and Methods

Chapter 3: To determine the minimum inhibitory concentrations of azole drugs and to study the effects of azoles in the calcium signaling gene calcineurin and *pmr-1*, in *Neurospora crassa*

Chapter 4: Studies on the interactions of the CNA-1, CNB-1, and PMR-1 proteins with azole drugs using molecular docking and molecular dynamics simulations

Chapter 5: Studies on phytochemical inhibitors of calcineurin and PMR-1 proteins using computer-aided drug design (CADD) approach

Chapter 1

Fungal pathogens pose a significant threat to both humans and plants. Fungi account for over 70% of plant diseases, affecting approximately one billion individuals and contribute to over 1.5 million deaths in humans annually (Bongomin, et al. 2017, Brown, et al. 2012, Cools, et al. 2013, Revie, et al. 2018). Therefore, understanding fungal pathogenesis and the development of antifungals are crucial for global agriculture and health. Azoles are the first line of defense against fungal pathogens (Celia-Sanchez, et al. 2023). Azoles, including triadimenol and propiconazole, are used against fungal infections in plants (Cools, et al. 2013). In human, fluconazole, ketoconazole, and itraconazole are the commonly used azoles for the treatment of fungal diseases (Partha, et al. 2022).

Azole medications act on the ergosterol synthesis pathway. Ergosterol is crucial for the fungal cell membrane's structure; blocking its production leads to the buildup of 14α-methyl sterols, which compromises the membrane's stability, permeability, and the functioning of enzymes attached to the membrane (Cowen, et al. 2015b). Azoles specifically inhibit an enzyme belonging to the cytochrome P450 family called lanosterol 14α-demethylase, which is known as ERG11 in yeast and CYP51A in molds that are necessary for removing the 14α-methyl group from lanosterol during ergosterol biosynthesis (Cowen, et al. 2015a). The binding of azoles to the heme-binding site, particularly the ferric iron component, prevents lanosterol from accessing the enzyme, thus interrupting the production pathway (Odds, et al. 2003). Certain drugs, such as doxycycline, can enhance azoles like fluconazole's effectiveness, likely through reducing heme-bound iron (Fiori and Van Dijck 2012). Resistance to azole drugs in candida often involves amino acid changes in the Erg11 enzyme that prevent the drug from binding to the target, and over 140 such mutations have been identified in the drug resistant strains (Morio, et al. 2010). The R467K and G464S mutations, close to the heme-binding site of the enzyme, are most frequent in *Candida albicans* (Casalinuovo, et al. 2004).

Calcineurin plays a role in regulating susceptibility to antifungals (Onyewu, et al. 2003). The study of calcineurin and crz1 mutants among various *Candida* species revealed variations in their roles. Mutants of *C. albicans* and *C. dubliniensis* deficient in calcineurin and the crz1 gene showed decreased resistance to azole and echinocandin classes of antifungal agents (Chen, et al. 2011). Conversely, calcineurin-deficient mutants of *C. lusitaniae* demonstrated increased sensitivity to azoles, whereas crz1-deficient mutants exhibited an elevated tolerance to these antifungal compounds. Additionally, resistance to azoles influenced by calcium and calcineurin has been widely reported (Edlind, et al. 2002). Research shows that elements of the calcium signaling pathway are crucial in fungal physiological functions, in managing stress response, and in enhancing virulence (Patenaude, et al. 2013). Calcineurin, a protein phosphatase, is essential for overcoming the stress on cell membranes caused by azoles (Juvvadi, et al. 2014).

The calcium signaling pathway plays a significant role in fungal physiology, facilitates reactions to stress, and enhances virulence (Patenaude, et al. 2013). In the presence of external factors like the drug FK506, calcium ions enter the fungal cell through the high-affinity calcium channels, Cch1 and Mid1. When calmodulin (CaM) binds to four calcium ions, it changes shape (Juvvadi, et al. 2017). Calcineurin, the human homolog of the nuclear factor of activated T cells (NFAT) in fungi, is the only serine-threonine phosphatase that requires both calcium (Ca^{2+}) and calmodulin (CaM) for its activity (Li, et al. 2011). Calcineurin is essential for virulence and drug resistance in pathogenic fungi, including *Aspergillus fumigatus*, *C. albicans*, and *Cryptococcus neoformans* (Karkowska-Kuleta, et al. 2009). In *C. albicans* and *A. fumigatus*, calcineurin regulates ergosterol biosynthesis and drug efflux, which are vital mechanisms for azole resistance (Park, et al. 2016). In *C. glabrata*, calcineurin-Crz1 signaling enhances CgYor1-dependent azole resistance, stress responses, and pathogenicity (Ceballos-Garzon, et al. 2022, Kumari, et al. 2022). Moreover, loss of the retrograde transport protein Pep8 increases calcineurin activity, causing azole resistance in *C. albicans* (Mount, et al. 2018). Blocking calcineurin pathway might improve the effectiveness of antifungals and reduce drug resistance (Chen, et al. 2011, Juvvadi, et al. 2017, Park, et al. 2016). Mutants of calcineurin exhibited decreased resistance to azoles in *C. lusitaniae* (Zhang, et al. 2012). Calcineurin is considered as a promising focus for antifungal treatment for diverse fungal species, including

A. fumigatus, *C. albicans*, and *C. neoformans* (Ahmad, et al. 2014, Ahmad, et al. 2013, Saeed, et al. 2013). Calcineurin, which contains a catalytic A (CNA-1) and a regulatory B (CNB-1) subunits, is also critical for growth, development, and fertility in *N. crassa* (Tamuli et al. 2016; Kumar et al. 2019). The CNA-1 catalytic subunit is characterized by an N-terminal phosphatase domain, a helix for regulatory subunit binding (CnBBH), and a domain that binds calmodulin (CaMBD). Interestingly, a unique serine-proline-rich (SPRR) linker domain, found exclusively in filamentous fungi like *A. fumigatus* within the calcineurin catalytic subunit, bridges the CnBBH and CaMBD (Juvvadi, et al. 2013). This domain undergoes phosphorylation at four serine clusters, and mutations here affect fungal growth and virulence, highlighting the critical role of calcineurin phosphorylation in its function. Analysis of calcineurin and crz1 mutants in various Candida species revealed variations in their functions related to antifungal activity. Therefore, calcineurin A subunit (cnaA) is a promising target for developing new antifungal treatments. However, the interaction between azole and calcineurin has not been demonstrated in molecular dynamics simulations, an area that remains crucial for understanding the mechanism of azole interaction with proteins.

This activated Ca^{2+}-calmodulin complex activates calcineurin, which dephosphorylates the Crz1 transcription factor, facilitating its move into the nucleus where it boosts the expression of genes involved in drug resistance, it regulates the stress response, cell wall integrity and growth (Juvvadi, et al. 2017). The expression of *pmr-1* gene is necessary for regulating the transport of Ca^{2+} and Mn^{2+} cations across the Golgi membrane and maintaining the structural integrity of the cell wall in various fungi, including *N. crassa* (Antebi and Fink 1992, Bowman, et al. 2012). The *pmr-1* gene also plays a critical role in Ca^{2+} homeostasis, cell wall integrity, and antifungal drug resistance in *A. fumigatus* and *C. albicans* (Bates, et al. 2005, Pinchai, et al. 2010). In *C. albicans PMR*1p, a P-type Ca^{2+}/Mn^{2+}-ATPase in the secretory pathway, is necessary for virulence (Bates, et al. 2005). The *PMR1* disruption in *Saccharomyces cerevisiae* causes several defects, including protein-sorting abnormalities such as increased secretion of heterologously produced proteins (Bates, et al. 2005, Kang, et al. 1998) and aberrant processing of the α factor (Sorin, et al. 1997). *PMR1* has a role in the tolerance and pathogenicity in fungi, including *C. neoformans*, *S. cerevisiae*, and *A. fumigatus* (De Castro, et al. 2014, Mielniczki-Pereira, et al. 2011, Pittman, et al. 2004).

The extensive use of antifungal therapy promotes the development of drug resistance which poses a serious challenge to the treatment of fungal infections (Gulshan and Moye-Rowley 2007, Maertens 2004, Revie, et al. 2018). The most common fungal infections caused by *Candida auris* and *Candida glabrata* are becoming resistant to azoles (Berkow and Lockhart

2017, Lee, et al. 2020). Furthermore, the agricultural use of azole triazoles has also led to the development of azole resistance in *A. fumigatus* (Arendrup and Patterson 2017, Arikan-Akdagli, et al. 2018, Meis, et al. 2016). In fungi, the acquisition of drug resistance is a step-wise adaptation from physiological alterations to genetic mutations during a process of adaptive evolution (Yona, et al. 2015).

The rising rates of occurrence and deaths from severe fungal infections, including aspergillosis, candidiasis, and cryptococcosis caused by Aspergillus, Candida, and Cryptococcus species, respectively, pose an increasing risk to immunocompromised patients. The current available antifungal medications such as pyrimidine analogs, polyenes, azoles, and echinocandins are limited and face significant challenges due to their toxicity, effectiveness, and the growing problem of drug resistance, which hinder the achievement of successful treatment outcomes (Vitiello, et al. 2023). Although these medications attack different fungal processes, there is a critical need for a deeper understanding of their mechanisms of resistance to aid in the creation of new antifungal drugs. Fungal species can use different strategies to counteract azole drugs, including upregulation of the genes for drug efflux pumps, which can reduce the concentration of the drug in the fungal cell, making it less effective (Sanglard 2016). Additionally, fungi can modify the drug target, typically the ergosterol biosynthesis pathway, which is targeted by azole drugs (Berman and Krysan 2020). Fungi also can modify the structure of the target enzyme, lanosterol 14α-demethylase (Cyp51), which reduces the binding affinity of the drug and thereby decreases its effectiveness (Perlin et al., 2019; Ma et al. 2019; (Zhang, et al. 2019).

The azole interaction with the calcineurin and Golgi calcium ATPase PMR-1 protein is still not well understood. Therefore, this remains an active research area to fully understand the molecular mechanisms of antifungal drug resistance in *N. crassa* to determine the potential involvement of the calcineurin and *pmr-1* gene for new antifungal therapy. *N. crassa* has been extensively studied as a model organism for investigating the molecular basis of azole drug resistance (Víglaš and Olejníková 2023). In *N. crassa,* ERG11, CYP51, MDR1, and ABC transporters have been comprehensively investigated for their role in azole drug resistance (Zhou, et al. 2022). The involvement of calcineurin and *pmr-1* gene in azole resistance in *N. crassa* is yet to be investigated in detail. Therefore, in this study, I performed both invitro and molecular dynamics (MD) simulations, a computational approach enabling a deep dive into molecular interactions between calcineurin subunit A (CNA-1) and PMR-1 protein in complex fluconazole, itraconazole, ketoconazole. I determined the minimum inhibitory concentrations (MIC) of three azole drugs fluconazole, itraconazole, and ketoconazole in *N. crassa*. I also determined the effect of these azoles in the *N. crassa* wild type, *Cna-1*^{RIP} mutants and Δ*pmr-1* knockout strain. The *Cna-1*^{RIP} mutants and Δ*pmr-1* strain exhibited increased susceptibility to the azole drugs. In addition, the *Cna-1*^{RIP} mutants and Δ*pmr-1* also showed a reduced membrane ergosterol content, and increased levels of the reactive oxygen species (ROS) and cytosolic free Ca^{2+} under the azole treatment. Furthermore, the FESEM studies revealed that the hyphal morphology was damaged in *Cna-1*^{RIP} mutants and Δ*pmr-1* strains under the azole treatment. The MD simulation was spanning 50 nanoseconds, to elucidate hydrogen-bonding interactions within the active site of the protein, ensuring the stability of the compounds within this crucial region. I identified detailed molecular interactions of fluconazole, itraconazole, and ketoconazole with the PMR-1 and CNA-1 proteins. This finding could be useful to overcome azole drug resistance in fungi. Despite the availability of potential antifungal drugs, the emergence of resistance among fungi poses significant challenges, particularly for immunocompromised patients.

I also explored phytochemical compounds from the PubChem database as potential inhibitors of the Ca^{2+} signaling proteins PMR-1, CNA-1, and CNB-1 in fungi. The aim was to identify the potent phytochemical compounds inhibiting target protein for both calcineurin subunit CNA-1, CNB-1 and calcium ATPase PMR-1, for target specific antifungal drug discovery. I selected 11 compounds from the *Dillenia indica* and studied using CADD tools to identify compounds with antifungal properties.

Chapter 2

Chapter 2 describes the materials and methods used in this thesis work. Growth and maintenance of *N. crassa* strains were grown essentially as described previously (Davis and de Serres 1970, Westergaard and Mitchell 1947). The *N. crassa* strains used in this study were either obtained from the Fungal Genetic Stock Centre (FGSC, Manhattan, KS) or generated in our laboratory. Standard chemicals and reagents, subjected to autoclaving or filter sterilization when necessary, were procured from standard suppliers. PCR, Real-time PCR, reactive oxygen species (ROS), CTC and other experiments were performed by using the standard protocols essentially as described by Sambrook and Russell (2001) or according to the manufacturer's instructions. I used Autodocktool-1.5.7 (ADT) and Raccoon for *in silico* studies. The molecular dynamics simulation studies have been performed using the supercomputing facility of IIT Guwahati to investigate the ligand-protein interactions using GROMACS 2018.1.

Chapter 3

Chapter 3 describes the cellular functions of calcineurin and Golgi calcium ATPase *pmr-1* in azole susceptibility. The mutants of the calcineurin catalytic subunit A (*Cna-1*$^{\mathrm{RIP}}$), generated using the repeat-induced point mutation (RIP), and the Δ*pmr-1* strains showed a growth defect in response to the azole drugs. Moreover, in the *Cna-1*$^{\mathrm{RIP}}$ (24 a and 122A) and Δ*pmr-1* mutant strains, total ergosterol content was reduced and ROS levels were increased upon azole treatment. The azole drug-induced altered hyphal morphology was revealed by light microscopy and FESEM studies, which indicated that calcineurin and *pmr-1* are pivotal for maintaining hyphal morphology in *N. crassa* mutant strains under fluconazole treatment. Furthermore, expression of the *pmr-1* was upregulated under itraconazole treatment. This indicates differential regulation of *pmr-1* under azole treatments, as evidenced by the significant upregulation of *pmr-1* under itraconazole stress ($p \leq 0.0001$). This differential regulation suggests that these genes respond distinctly to different azole stress conditions, highlighting their potential involvement in azole stress response pathways. The significant upregulation of *pmr-1* under itraconazole treatment suggests a role in managing ion homeostasis under ER or Golgi stress. These findings suggest differential regulation of the *pmr-1* gene under itraconazole stress. Therefore, the above study highlights that *pmr-1* and calcineurin might play important roles in azole susceptibility in *N. crassa*. Further investigation is required to elucidate the specific molecular mechanisms underlying their regulation and involvement in azole stress adaptation.

Chapter 4

Chapter 4 describes the *in silico* analysis of calcineurin and PMR-1 interactions with the azole drugs. The 3D protein structures of CNA-1, CNB-1, and PMR-1 were predicted using I-TASSER and validated by Ramachandran plot analysis. In addition, the structural accuracy of the modelled CNA-1, CNB-1, and PMR-1 proteins was assessed by superimposing the homologous structures using UCSF Chimera. Subsequently, molecular docking studies were conducted for CNA-1, CNB-1, and PMR-1 proteins with fluconazole, itraconazole, and ketoconazole. Moreover, molecular dynamics (MD) simulations were performed to calculate binding energies and assess the stability of the protein-drug complexes. The analysis of binding energies and interactions of azole drugs with predicted CNA-1, CNB-1, and PMR-1 proteins revealed specific amino acid residues involved in hydrogen bonding and hydrophobic interactions. MD simulations revealed stable interactions within the active sites of proteins with the ligands, indicating their potential as antifungal drug targets. Further analysis identified key amino acid residues crucial for drug binding. The binding energies and interactions of the azole drugs with CNA-1, CNB-1, and PMR-1 proteins were analyzed.

Computational insights suggest that the CNA-1 and ketoconazole complex had a binding energy of −6.67 kcal/mol, formed the hydrogen bond with Tyr353, His189. In this complex, the hydrophobic interactions occurred between Leu350, Tyr349, Ala321, Glu320, His319, Arg292, Leu194, Trp270, Phe198, Arg160. Moreover, the binding energy for CNA-1 protein and fluconazole was -4.56 kcal/mol, and the hydrogen bonds were formed with Tyr349, Ala321, Arg292 and the hydrophobic interactions are formed between His130, Glu320, His319, Asp156, Leu194, His189, Trp270, Asn188, Arg160, Tyr353, Leu350. MD simulations revealed stable interactions within the active site of both proteins, suggesting their potential as antifungal drug targets. MD analysis, including Root Mean Square Deviation (RMSD), root mean square fluctuation (RMSF), radius of gyration (Rg), and hydrogen bond formation, provided insights into binding processes. Moreover, the RMSD trajectories of the fluconazole and ketoconazole complexes with CNA-1 indicated that the ketoconazole-calcineurin complex possesses the highest backbone stability compared to the CNA-1 apoprotein and CNA-1 fluconazole complex. Notably, the amino acid residues ranging from 50 to 400 positions, both the CNA-1 apoprotein and the ketoconazole-CNA-1 complex, exhibited maximum RMSF values within the same range at ~0.5 nm. The assessment of the compactness of the CNA-1 complex with the ligands fluconazole and ketoconazole was calculated using radius of gyration (Rg). To assess structural compactness, the Rg was determined using GROMACS. Throughout the MD simulation period, both the CNA-1 apoprotein and its ketoconazole-CNA1 complex consistently exhibited a similar pattern in their calculated Rg values. Notably, the ketoconazole-CNA-1 complex mirrored the Rg pattern observed in the CNA-1 apoprotein, reaching a maximum Rg value of approximately 3.1 nm for both entities. Conversely, the Fluconazole-CNA-1 complex showed a maximum Rg value of ~4.2 nm; however, after 35 ns of MD simulation time, the Rg value decreased to ~3.1 nm.

The binding energies and interactions of the azole drugs with CNB-1 proteins with the azole drugs were also analyzed. The CNB-1-ketoconazole complex exhibited a binding energy of -5.07 kcal/mol, CNB-1-fluconazole exhibited binding energy of -4.2 kcal/mol. Moreover, the RMSD trajectories of the ketoconazole and fluconazole complexes with CNB-1 indicated that the CNB-1-ketoconazole complex possesses the highest backbone stability compared to the CNB-1 apoprotein and CNB-1 fluconazole complex. Notably, all the 156 amino acid residues of CNB-1 protein exhibited the maximum RMSF values of at the same range at ~0.3 nm, for both CNB-1 apoprotein and the CNB-1-ketoconazole complex. The CNB-1-fluconazole complex showed the highest RMSF value at the amino acid residue 40 to 60 positions and at 120 to 135 positions at 0.5 and 0.6 nm, respectively. The amino acid residues Phe153, Arg96, Tyr109, Glu154, Asp103, Lys100, Arg106, Gly108, Phe99 are common amino acid residues within the CNB-1 protein-ligand complexes throughout molecular docking study of CNB-1 protein with fluconazole and ketoconazole. Moreover, the CNB-1-ketoconazole complex formed the hydrogen bond with Arg96 and CNB-1-fluconazole formed the hydrogen bond with Phe153, Arg96, Tyr109.

PMR-1 ketoconazole forms the complex with the binding energy −7.68 kcal/mol, hydrogen bond is formed with Asn254 and the hydrophobic interactions are formed between Met426, Asp646, Lys417, Glu255, Ser645, Ser279, Val257, Ile259, Val282, Leu250, Asp277, Asp278, Ala247, Thr251, Glu253, Thr676, Asp672, Gly604, Ile680, Thr418. The PMR1-fluconazole complex exhibited a binding energy of -5.61 kcal/mol, with hydrogen bonds formation with the specific amino acid Asn254, Glu255, Asp646 and hydrophobic interactions with Pro506, Met426, His425, Asn424, Ser645, Glu253, Asp672, Gly604, Thr418, Lys417. The itraconazole and PMR-1 complex (−3.73 kcal/mol) showed only hydrophobic interaction with the amino acid residues Asn254, Met426, Asp646, His425, Glu255, Asn424, Ser645, Val257, Ile259, Val282, Thr287, Lys276, Asp277, Leu250, Tyr284, Asn278, Ala247, Thr251, Glu253, Thr676, Asp672, Gly604. The RMSD trajectories indicated stability within the azole and PMR-1 complexes, PMR-1 protein with the itraconazole exhibits the highest backbone stability with a maximum deviation of at ~0.6 nm. Analysis of RMSF values highlighted fluctuations in active site residues, with itraconazole showing the stable and lowest fluctuation among the fluconazole-PMR-1 and ketoconazole-PMR-1 complexes. The calculated Rg values for the Apo-protein of PMR-1 and all its azole complexes ranged approximately between 3.65 and 3.8 nm up to 30 ns. Beyond 30 ns of simulation time, all azole-PMR-1 complexes exhibited lower Rg values than the PMR-1 apoprotein, suggesting increased compaction upon binding of protein-ligand complexes compared to the unbound Apo-protein state. In the PMR-1- fluconazole complexes, the H-bond formed between the Asn254, Glu255 and Asp646 exclusively and hydrophobic interactions with Pro506, Met426, His425, Asn424, Ser645, Glu253, Asp672, Gly604, Thr418, Lys417. However, for the PMR-1 protein complexes with fluconazole, itraconazole, and ketoconazole, the Asp646, Glu255, Asn254, Met426, Ser645, Glu253, Asp672, Gly604 were common amino acid residues involved in H-bond formation and hydrophobic interactions. Hydrogen bond formation and hydrophobic interactions are crucial for drug binding and in stabilizing protein-ligand interactions.

These findings are useful for understanding the interactions of the antifungal drugs with the target protein and might contribute for the development of novel antifungal strategies.

Chapter 5

Chapter 5 describes the potent phytochemical compounds that could inhibit calcineurin and PMR-1. Computational insights suggest that certain phytochemicals from *D. indica* may serve as potential inhibitors of fungal calcium signaling proteins. I explored antifungal compounds from *D. indica* using CADD tools, including MGLTools-1.5.6, Raccoon, and MD simulation. I studied 11 phytochemicals for the molecular docking studies with three protein targets CNA-1, CNB-1, and PMR-1. Based on the molecular docking studies, the top four phytochemicals, namely isorhamnetin, dillenetin, kaemperol, and myricetin, were further selected for the MD simulations. I found isorhamnetin as a promising phytochemical inhibitor for CNA-1 and PMR-1 protein and dillenetin as a potential inhibitor of CNB-1 protein with the formation of the most stable complex. The ADMET (absorption, distribution, metabolism, excretion, and toxicity) profiles confirmed that the phytochemicals isorhamnetin and dillenetin possess the required characteristics as per the Lipinski's 'Rule of Five' and Veber's criteria. Specifically, Lipinski's rule suggests optimal absorption and permeation characteristics for compounds with no more than five hydrogen bond donors, ten hydrogen bond acceptors, a molecular weight under 500 Daltons, and a calculated Log P (octanol-water partition coefficient) not exceeding 5. In addition, Veber's rule emphasizes the importance of a topological polar surface area (TPSA) of 140 $Å^2$ or less for oral bioavailability. The CNA-1isorhamnetin complex forms the hydrogen bond with the amino acid His189, Asp156, Asp128 and hydrophobic interactions with the amino acid residues Arg160, Tyr349, Phe344, His319, His130, Arg292, Asn188, Phe198, Leu350. The dillenetin compound acts as the most potent inhibitors targeting CNB-1 proteins forms the stable complex with the formation of hydrogen bond with the key amino acid residue Arg106, Arg96 and the hydrophobic interaction with amino acids Asp107, Asp103, Lys100, Phe99, Ser152, Tyr109, Glu154, Gly108, Phe153. PMR-1-isorhamnetin complex forms the H bond with the amino acid Asp646, Asn424, Asn254, Asp672 and hydrophobic interaction with the amino acids Pro506, Met426, Pro256, Ser645, Lys417, Glu253, Glu255, His425. These results suggested that isorhamnetin and dillenetin could serve as potent antifungal candidates targeting calcineurin and PMR-1, offering a novel approach to inhibiting key proteins involved in fungal pathogenicity. These findings could contribute to the development of target specific antifungal drugs, with the potential to overcome resistance mechanisms in fungal pathogens. However, further validation through in vitro and in vivo experiments is necessary for comprehensive investigation into their mechanism of action and therapeutic potential.

Conclusions and future perspectives

This chapter describes the conclusions and future prospects of my thesis work. In this study, I showed that the *N. crassa* strain lacking calcineurin and *pmr-1* genes are more susceptible to azole drugs, namely fluconazole, itraconazole, and ketoconazole. I found that the ergosterol level decreases and ROS level increases under azole drug treatment in the *N. crassa* calcineurin and Δ*pmr-1* mutant strains. Furthermore, the FESEM analysis revealed hyphal morphology alterations in the calcineurin-RIP and Δ*pmr-1* mutants under azole drug treatment, which suggested that calcineurin and *pmr*-1 play a role in the cell membrane integrity in response to the azole drug fluconazole. The expression levels were analysed with and without the fluconazole, itraconazole, and ketoconazole treatments. The relative expression levels, normalized to the untreated control, were used to measure the fold changes. In response to the itraconazole treatment, the *pmr-1* gene expression was increased by ~5-fold. MD simulation analysis determined the binding energies for CNA-1 with ketoconazole and fluconazole as −6.67 kcal/mol and −4.56 kcal/mol, respectively. The binding energy for the PMR-1 complex with fluconazole, Itraconazole, and ketoconazole was determined as −5.61 kcal/mol, −3.73 kcal/mol −7.68 kcal/mol, respectively. MD simulations also revealed stable interactions of the azole drugs within the active sites of the calcineurin and PMR-1 proteins, indicating these proteins as promising antifungal drug targets. The amino acid Tyr349, Ala321, Arg292, Tyr353, Trp270, Leu194, Arg160, Leu350, His189, Glu320, His319 are common residues for the interaction of CNA-1 with fluconazole and ketoconazole. Additionally, amino acid residues Phe153, Arg96, Tyr109, Glu154, Asp103, Lys100, Gly108, Phe99 are common residues for CNB-1 protein complex with fluconazole and ketoconazole. Moreover, the amino acid residues Asp646, Glu255, Asn254, Met426, Ser645, Glu253, Asp672, Gly604 were identified as the common residues for the formation of complexes of PMR-1 with fluconazole, itraconazole, and ketoconazole. Therefore, these common amino acid residues might be considered as the critical amino acids for the development of novel drugs targeting calcineurin protein CNA-1, CNB-1, and PMR-1 in the future. Despite the availability of potential antifungal drugs, the emergence of resistance among fungi poses significant challenges, particularly for immunocompromised patients. In response to this growing concern, I also explored phytochemical compounds from the PubChem database as potential inhibitors of the Ca^{2+} signaling proteins CNA-1, CNB-1, and PMR-1. I performed docking analysis of 11 compounds with calcineurin and PMR-1 proteins using the CADD. The phytochemicals isorhamnetin, kaempferol, naringenin, dillenetin, quercetin, adhered to Lipinski's rule for drug-likeness with zero violation. However, six phytocompounds, namely myricetin, betulinaldehyde, betulin, betulinic acid, stigmasterol, and lupeol showed 1 violation for drug-likeness; and 1 violation of the lipinski rule is acceptable (Hudson, et al. 2017, Roskoski Jr 2023). Despite natural products often deviate from Lipinski's and other ADMET rules due to distinct physiochemical characteristics, a previous study reported that over 50% of natural products displayed favorable drug-like properties with their predicted pharmacokinetic traits and drug-likeness (Veber, et al. 2002). Based on the RMSD, RMSF, hydrogen bonds and Rg parameters, I found isorhamnetin as the best inhibitor for the CNA-1 and PMR-1, and dillenetin as the best inhibitor for CNB-1 protein with formation of more stable complex. Hence, the computational insights strongly suggested that the isorhamnetin and dillenetin phytochemical compounds can be potent antifungal candidates by inhibiting the function of calcineurin and PMR-1. Thus, identification of phytochemical compounds with inhibitory effects on the CNA-1, CNB-1, and PMR-1 proteins, essential for fungal physiology and pathogenicity, might contribute to the advancement of target specific antifungal drug discovery in the future and also to combat drug resistance in fungi.

Chapter 1

Introduction and Literature Review

1.1. An introduction to the model filamentous fungus *Neurospora crassa*

Neurospora crassa, a member of the phylum Ascomycota, was first identified as the organism responsible for causing orange bread mold in French bakeries and was initially documented under the different names *Oidium aurantiacum* by Payen (1843) and *Penicillium sitophilum* by Montagne (1843) (Perkins 1992; Roche et al. 2014). *N. crassa* was later classified by Shear and Dodge in the mid-1920s as a heterothallic fungus with two mating types (*A* and *a*), capable of forming asci containing eight ascospores, a common characteristic feature in many ascomycetes (Shear and Dodge 1927; Perkins 1992). In the mid-1930s, Carl Lindegren and Bernard Lodge demonstrated Mendelian inheritance in the individual asci of *N. crassa* (Perkins 1992). *N. crassa* is also known as "nerve spores" due to the nerve-like striations on its sexual spores, called ascospores. *N. crassa* significantly contributed to our understanding of biology and, therefore, is called "the organism behind the molecular revolution" (Perkins 1992; Davis and Perkins 2002; Riquelme et al. 2011; Baker et al. 2012). *N. crassa* is commonly found in substrates rich in carbohydrates and residues generated during sugarcane processing (Davis and Perkins 2002). Beadle and Tatum used *N. crassa* as a model system to isolate the first biochemical mutants, demonstrating that a specific gene controls the production of a particular enzyme. This groundbreaking discovery led to the formulation of the "one gene – one enzyme" hypothesis (Beadle and Tatum 1941). In recognition of their pioneering work with *N. crassa*, which significantly advanced the fields of genetics and molecular biology, Beadle and Tatum were jointly awarded the Nobel Prize in Physiology or Medicine in 1958 (Hausmann and Hausmann 2002).

N. crassa has a relatively simple genetic structure, making it suitable for various genetic, biochemical, developmental, and subcellular studies (Borkovich et al. 2004). In addition, *N. crassa* is preferred as a model organism due to several other advantages, including rapid growth, ease of propagation on minimal media, and a short life cycle. Furthermore, *N. crassa*, a heterotroph, utilizes various carbon and nitrogen sources, simple salts, trace elements, and biotin (Davis and de Serres 1970). Moreover, being primarily haploid during the life cycle, *N. crassa* facilitates genetic manipulations such as mutagenesis, complementation tests, and genetic mapping. *N. crassa* is also a model organism for studying circadian rhythms, population biology, morphogenesis, mitochondrial import, DNA repair and recombination, DNA methylation, and other epigenetic processes (Borkovich et al. 2004), epigenetic regulation through DNA methylation (Davis and Perkins 2002; Aramayo and Selker 2013), and RNA interference (RNAi) based post-transcriptional gene silencing (Cogoni and Macino 1999). Additionally, *N. crassa* is used in biotechnological research, including ethanol production from lignocellulosic sources (Dogaris et al. 2013) and host-virus interactions (Honda et al. 2020).

In addition, establishing the Fungal Genetic Stock Center (FGSC) in 1960 was a milestone in fungal research, ensuring the accessibility of strains generated in earlier studies for future researchers (McCluskey 2003; McCluskey et al. 2010). The sequencing of the *N. crassa* genome revealed a genome size of ~43 Mb with 10,082 protein-coding genes in seven chromosomal linkage groups (LG I-VII) (Galagan et al. 2003). The *N. crassa* genome sequence project also paved the way for a high-throughput knockout project to generate deletion mutants for all the genes (Colot et al. 2006).

1.1.1 Life cycle of the *N. crassa*

The multicellular fungus *N. crassa* exhibits a complex life cycle that includes both asexual and sexual phases, depending on the environmental conditions (Figure 1.1) (Raju 1992; Springer 1993). *N. crassa* is a heterothallic filamentous fungus with two non-switching mating types, *mat A* and *mat a*, determined by alternate DNA sequences known as idiomorphs at a single mating type locus in the linkage group I (Ferreira et al. 1998). *N. crassa* undergoes an asexual cycle, forming branched, multinucleate vegetative hyphae that grow parallel to the surface of a solid medium under nutrient-rich conditions (Springer 1993). The vegetative hyphae contain incomplete cross walls called septa, which allow the movement of organelles between compartments (Schmit and Brody 1976; Springer 1993), and repeated fusion of hyphal filaments results in a complex network known as mycelium (Springer and Yanofsky 1989; Springer 1993). Furthermore, when nutrients are scarce or the mycelium is exposed to an air-water interface, specialized aerial hyphae develop and form conidiophores that produce uninucleate asexual spores called microconidia or multinucleate macroconidia (Springer 1993).

The sexual phase is triggered by nitrogen starvation, light exposure, and cold temperatures, leading to the development of female reproductive structures called protoperithecia (Raju 1992). The protoperithecium, the female sexual structure, consists of coiled multicellular hyphae called ascogonium, enveloped by surrounding hyphae (Nelson and Metzenberg 1992; Bistis et al. 2003). A specialized hypha known as the trichogyne extends from the protoperithecium and chemotropically grows towards male cells of the opposite mating type, which can be either microconidia, macroconidia, or hyphal fragments (Bistis 1981). The fusion (plasmogamy) between the trichogyne and the male cell is followed by the entry of the male nucleus through the trichogyne into the protoperithecium, which initiates the development of a multicellular sexual structure called the perithecium, which is a mature protoperithecium (Aramayo and Selker 2013). In the protoperithecium, the male and female nuclei coexist as a dikaryon within a specialized structure called the ascogenous hypha without immediate fusion (Bistis 1981; Springer 1993). In the ascogenous hypha, the paired nuclei undergo synchronous mitotic divisions at the tip of a hook-shaped structure called the crozier. The central cell in the crozier is known as the ascus mother cell, which undergoes karyogamy followed by two sequential meiotic divisions and a post-meiotic mitosis, resulting in the formation of eight spindle-shaped sexual spores known as ascospores, arranged linearly within the narrow ascus (Raju 1992; Bistis et al. 2003; Aramayo and Selker 2013). Once matured, the ascospores are ejected through an ostiole opening at the tip of the perithecium (Springer 1993; Bistis et al. 2003; Kim et al. 2012). These released ascospores eventually germinate upon heat activation, giving rise to new vegetative hyphae and thus initiating the vegetative life cycle (Raju 1992).

N. crassa also possesses one of the most extensive genome defense mechanisms known in the eukaryotic organism. The *N. crassa* genome defense system includes the reversible post-transcriptional gene silencing mechanism known as "quelling" in the vegetative phase (Romano and Macino 1992), a fungal-specific transcriptional gene silencing mechanism called "repeat-induced point mutation" (RIP) that occurs after fertilization, but before karyogamy (Cambareri et al. 1989), and "meiotic silencing" during meiosis in the sexual phase (Shiu et al. 2001). These genome defense mechanisms limited DNA repeats, inactivated transposable elements, and trimmed the *N. crassa* genome (Galagan et al. 2003).

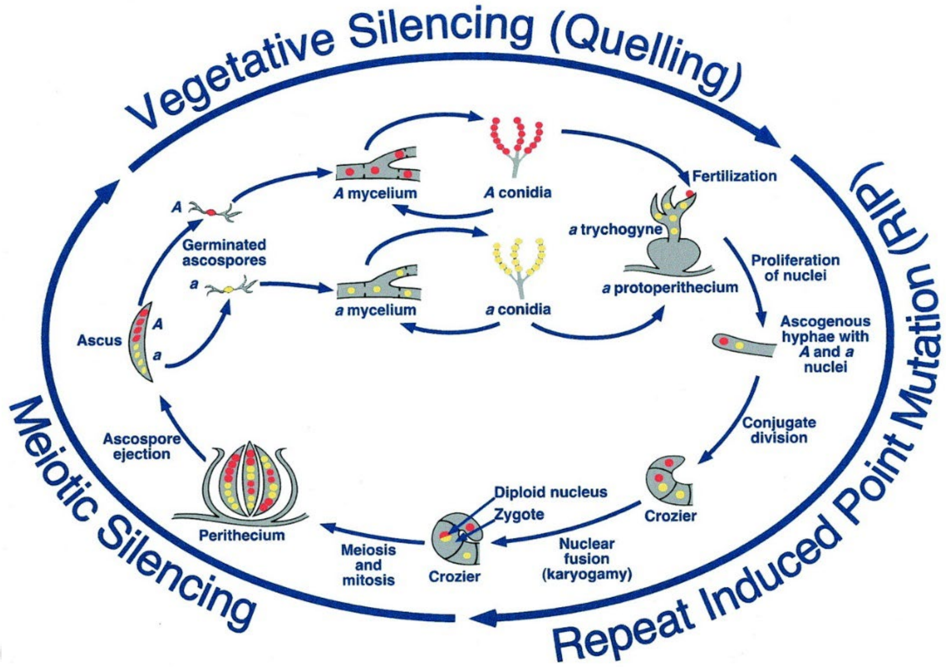

Figure 1.1. Life cycle of *N. crassa*. *N. crassa* undergoes an asexual cycle in a nutrient-rich medium, where multinucleate, branching vegetative mycelium develops aerial hyphae that produce asexual spores of either multinucleate macroconidia or uninucleate microconidia. These spores disperse and germinate upon landing on suitable substrates, repeating the asexual cycle. The sexual cycle is triggered by nitrogen starvation and low temperatures. The *Neurospora* colonies of either *mat A* or *mat a* mating types generate a female sexual structure called protoperithecium, which is fertilized by conidia of the opposite mating type. This fertilized structure develops into a perithecium, where both the nuclei undergo a series of premeiotic divisions, and then nuclear fusion or karyogamy occurs, yielding a diploid zygote. The resulting zygote undergoes one round of meiosis followed by a mitotic division, producing eight linearly arranged ascospores within an ascus sac. The mature ascospores are multinucleate, pigmented with melanin. The ascospores germinate upon heat activation and develop into new hyphae during an asexual cycle. The figure is reproduced with permission from the author (Borkovich et al. 2004; attached in the appendix).

1.1.2: Calcium signaling in *N. crassa*

Calcium ions (Ca^{2+}) are universal signaling molecules indispensable for life. The mechanisms of Ca^{2+} signaling are evolutionarily conserved across all domains of life, from prokaryotes to eukaryotes (Chin and Means 2000). Due to the cytotoxic effects of elevated intracellular Ca^{2+} concentrations, cells maintain a tightly regulated low resting level of free $[Ca^{2+}]c$ (Bagur and Hajnóczky 2017). Transient increases in $[Ca^{2+}]c$ serve as pivotal signals that activate downstream signaling cascades. In fungi, Ca^{2+} signaling regulates various physiological processes, including growth, development, reproduction, stress tolerance, and virulence (Roy et al. 2021). The extracellular Ca^{2+} concentration is approximately 10^{-3} M (Chin and Means 2000), whereas the resting free $[Ca^{2+}]c$ concentration is maintained at ~100 nM. This establishes a more than 10,000-fold concentration gradient across the plasma membrane (Berridge et al. 2003). To prevent toxic Ca^{2+} overload, cells store excess Ca^{2+} in intracellular reservoirs such as the endoplasmic reticulum (ER), mitochondria, and vacuoles (Cornelius and Nakashima 1987). Within the ER, the Ca^{2+} concentration ($[Ca^{2+}]_{ER}$) is maintained in the range of several hundred µM. Additionally, intracellular Ca^{2+} homeostasis is critical to preventing severe Ca^{2+} fluctuations and deleterious effects (Berridge et al. 2003). The entry of Ca^{2+} into the cytosol across the plasma membrane is mediated by specific receptors and channels that respond to various stimuli, such as membrane depolarization, mechanical stretch, and external agonists (Al-Ewaidat et al. 2024). The release of Ca^{2+} from intracellular stores is primarily facilitated by the inositol 1,4,5-triphosphate receptors (IP3Rs) and ryanodine receptors (RyRs) (Mikoshiba and Hattori 2000; Zeng et al. 2003; Hamilton 2005). Several transporter proteins play key roles in restoring cytosolic Ca^{2+} to resting levels. These include the plasma membrane Ca^{2+}-ATPase (PMCA), the sarcoplasmic/endoplasmic reticulum Ca^{2+}-ATPase (SERCA), the Na^+/Ca^{2+} exchanger, and the mitochondrial uniporter, which collectively transport excess Ca^{2+} either to the extracellular space or into intracellular compartments (Berridge et al. 2003). Thus, Ca^{2+} signaling pathways are activated in response to various stimuli, ultimately leading to the expression of specific target genes in the nucleus.

The filamentous fungus *N. crassa* possesses a complex Ca^{2+} signaling system that consists of 48 distinct Ca^{2+}-signaling proteins (Zelter et al. 2004). Calcium in *N. crassa* is stored in various intracellular compartments, such as vacuoles, plasma membrane vesicles, microsomes, and mitochondria. However, second messenger systems responsible for releasing Ca^{2+} from these internal stores have yet to be identified in *N. crassa* or other filamentous fungi. The $[Ca^{2+}]c$ in living *N. crassa* can be measured using Ca^{2+}-sensitive tools such as microelectrodes, fluorescent probes, or aequorin, a photoprotein derived from the jellyfish *Aequorea Victoria* (Granatiero et al. 2014). In *N. crassa*, Ca^{2+} signaling plays a critical role in regulating various physiological and developmental processes, including calcium stress tolerance, circadian rhythm regulation, growth, ion transport, sexual development, and ultraviolet (UV) stress survival (Deka et al. 2011). The Ca^{2+}-signaling genes and proteins in *N. crassa* exhibit unique sequence features. Advances in mutant analysis and the availability of the *N. crassa* genome sequence have significantly enhanced our understanding of the functions of specific Ca^{2+}-signaling genes in this organism.

1.1.3. A brief overview of pathogenic fungi

Fungal pathogens pose a significant threat to both plants and animals. Fungi contribute to approximately 1.5 million annual deaths in humans, particularly among immunocompromised individuals (Thambugala et al. 2024). Fungi account for over 70% of plant diseases (Cools et al. 2013; Revie et al. 2018). The filamentous ascomycete *Magnaporthe oryzae* , causes rice blast disease, one of the most destructive diseases affecting rice globally (Ou 1980; Dean et al. 2012). The grey mould *Botrytis cinerea* can remain dormant for a considerable time in the host plant, affects a wide range of dicotyledonous hosts, which causes rotting of tissues when host physiology changes under favorable environmental conditions (Williamson et al. 2007). *Fusarium graminearum* is a major pathogen in cereals, particularly damaging crops during the flowering stage (Leonard and Bushnell 2003). *Fusarium oxysporum* causes vascular wilt on numerous crops, including tomatoes and bananas (Michielse and Rep 2009). *Blumeria graminis* affects cereals such as wheat and barley , and results in powdery mildew (Wyand and Brown 2003). *Mycosphaerella graminicola* causes septoria tritici blotch on wheat, significantly impacting productivity (Orton et al. 2011). Furthermore, *Puccinia spp*. encompasses various rust diseases, posing a significant threat to wheat crops (Zadoks 1985). *Ustilago maydis* causes corn smut, and used as a model organism for studying plant-pathogen interactions (Holliday 2004). In addition, *Colletotrichum spp.* affects many crops and is notable for its postharvest infections (Prusky 1996). Azoles, including triadimenol and propiconazole, are used against plant fungal infections (Cools et al. 2013).

Several fungal species also cause hazardous diseases in animals and humans, resulting in significant morbidity and mortality (Gnat et al. 2021). The most common animal fungal infections include candidiasis caused by *Candida* species, ranging from superficial mucosal infections to life-threatening systemic infections (Mayer et al. 2013). Furthermore, the rising rates of occurrence and deaths from severe fungal infections, including aspergillosis, candidiasis, and cryptococcosis caused by *Aspergillus*, *Candida*, and *Cryptococcus* species, pose an increasing risk to immunocompromised patients

(Table 1.1). Aspergillosis, primarily caused by *Aspergillus fumigatus*, frequently occurs in immunocompromised patients, leading to severe respiratory and systemic infections (Arastehfar et al. 2021). Cryptococcosis, caused by *Cryptococcus neoformans* and *Cryptococcus. gattii*, often results in meningoencephalitis, particularly in the individuals with acquired immunodeficiency syndrome (AIDS) (Chayakulkeeree and Perfect 2008; Franco-Paredes et al. 2015). Histoplasmosis and blastomycosis, caused by *Histoplasma capsulatum* and *Blastomyces dermatitidis*, respectively, can cause respiratory and disseminated infections (Linder and Kauffman 2021). Therefore, understanding fungal pathogenesis and the development of antifungals are crucial for global health and agriculture.

Table 1.1. Some common fungal diseases

S. No.	Disease	Causative fungus	References
1	Asthma	*Aspergillus fumigatus*	(Agarwal et al. 2022)
2	Mycosis in a diabetic patient	*Talaromyces stipitatus*	(Sharma and Nonzom 2022)
3	Skin disease (small, painful lumps to form under the skin)	*Saccharomyces cerevisiae*	(Berthelot et al. 2021)
4	Brainstem phaeohyphomycosis	*Curvularia lunata*	(Liatis et al. 2021)
7	Canine onychomycosis	*Malassezia pachydermatis*	(Bajwa 2017)
11	Coccidioidomycosis	*Coccidioides immitis* and *C. posadasii*	(Seyedmousavi et al. 2018)
12	Histoplasmosis	*Histoplasma capsulatum*	(Seyedmousavi et al. 2018)

			(Pincelli et al. 2019)
13	Paracoccidioidomycosis	*Paracoccidioides brasiliensis* and *P. lutzii*	(Seyedmousavi et al. 2018)
14	Blastomycosis	*Blastomyces dermatitidis*	(McKinnell and Pappas 2009; Liew et al. 2017; Seyedmousavi et al. 2018)
16	Salamandrines (*Salamandra salamandra*)	*B. salamandrivorans* (*Bsal*)	(Seyedmousavi et al. 2018)
17	Bat white-nose syndrome	*Pseudogymnoascus destructans* (*Pd*)	(Campbell et al. 2022)
18	Sporotrichosis	*Sporothrix schenckii*	(Chakrabarti et al. 2015) (Seyedmousavi et al. 2018)

1.1.4. Azoles: The first line of defense against pathogenic fungi

Azole, which targets the ergosterol biosynthesis pathway, is the first line of defense against fungal pathogens (Celia-Sanchez et al. 2023). Ergosterol is crucial for the membrane structure, and blocking the ergosterol biosynthesis using azoles yields accumulation of 14α-methyl sterols, compromising membrane stability, permeability, and the functioning of membrane-associated enzymes (Cowen et al. 2015a). Azoles specifically inhibit an enzyme belonging to the cytochrome P450 family called lanosterol 14α-demethylase, which is known as ERG11 in yeast and CYP51A in molds that are necessary for removing the 14α-methyl group from lanosterol during ergosterol biosynthesis (Trösken et al. 2006; Keniya et al. 2018). The binding of azoles to the heme-binding site of the ferric iron component in the enzyme, prevents lanosterol binding and thus disrupts the ergosterol biosynthesis pathway (Odds et al. 2003; Cowen et al. 2015b).

Fluconazole, ketoconazole, and itraconazole are widely used azole antifungal agents for treating fungal infections in humans (Partha et al. 2022). The fungi responsible for human diseases can also cause severe infections in various animal species, often leading to significant morbidity and mortality, and azole drugs are used for treating these diseases (Table 1.2); (Seyedmousavi et al. 2018). However, the widespread use of antifungal therapy has led to the development of drug resistance, making the treatment of fungal infections more difficult (Maertens 2004; Gulshan and Moye-Rowley 2007; Shapiro et al. 2011; Revie et al. 2018). Drug resistance in fungi has emerged due to the process of adaptive evolution under the selection pressure of the antifungal drugs, which starts with physiological changes and corresponding genetic mutations (Yona et al. 2015). *Candida auris* and *C. glabrata*, causative organisms for most common fungal infections, also developed resistance to azoles (Berkow and Lockhart 2017; Lee et al. 2020). Azole resistance has also been developed in *A. fumigatus* contributed by the agricultural use of triazoles (Meis et al. 2016; Arendrup and Patterson 2017; Arikan-Akdagli et al. 2018).

Table 1.2: Azole drugs used for the treatment of fungal infections in birds and animals

S. No.	Azole	Disease	Species	References
1	Fluconazole	Candidiasis	Birds	(Talazadeh et al. 2022)
		Aspergillosis (nasal), Cryptococcosis, Blastomycosis	Dogs	(Seyedmousavi et al. 2018)
		Aspergillosis (CNS infection), Blastomycosis, Cryptococcosis, Coccidioidomycosis	Cats	(Seyedmousavi et al. 2018; Wang et al. 2023)
2	Itraconazole	Aspergillosis, Candidiasis	Birds	(Carrasco et al. 1993; Arné et al. 2021)

		Aspergillosis, Histoplasmosis Blastomycosis, Sporotrichosis, Dermatophytosis Cryptococcosis, Coccidioidomycosis	Dogs	(Seyedmousavi et al. 2018)
		Dermatophytosis	Rodents, rabbits	(Fehr 2015)
		Aspergillosis, Sporotrichosis, Cryptococcosis, Blastomycosis, Histoplasmosis, Phaeohyphomycosis	Cats	(Seyedmousavi et al. 2018)
		Aspergillosis, Coccidioidomycosis, Mycotic keratitis, Dermatophytosis	Horses	(Seyedmousavi et al. 2018)
3	Ketoconazole	Blastomycosis, *Malassezia dermatitis*, Histoplasmosis, Cryptococcosis, Coccidioidomycosis, Dermatophytosis and Sporotrichosis	Dogs	(Seyedmousavi et al. 2018)
		Candidiasis, Aspergillosis	Birds	(ABD EL MOTELIB and AMEN 2019; Talazadeh et al. 2022)

		Blastomycosis, Cryptococcosis, Histoplasmosis, Dermatophytosis, Coccidioidomycosis, Sporotrichosis	Cats	(Roberson et al. 2011; Seyedmousavi et al. 2018)
4	Voriconazole	Aspergillosis	Cats	(Smith and Hoffman 2010)
		Scedosporiosis, Aspergillosis	Dogs	(Taylor et al. 2014; Bray et al. 2020)
		Aspergillosis	Birds	(Di Somma et al. 2007; Beernaert et al. 2009)
		Aspergillus keratitis, Aspergillosis (systemic)	Horses	(Davis et al. 2006; Chan 2008; Tamura et al. 2020)
5	Miconazole	Dermatophytosis, *Malassezia* dermatitis	Cats	(Moriello et al. 2017; Moriello 2019; Hobi et al. 2024)
		Malassezia dermatitis	Dogs	(Hobi et al. 2024)
		Dermatophytosis	Rodents, rabbits and fur animals	(Fehr 2015; Debnath et al. 2016; Mishra et al. 2022)

6	Posaconazole	Mucormycosis, Aspergillosis	Cats	(McLellan et al. 2006; Wray et al. 2008)
		Aspergillosis	Dogs	(Corrigan et al. 2016)
7	Parconazole	Candidiasis (thrush)	Guinea fowl (Birds)	(Seyedmousavi et al. 2018)
8	Enilconazole	*Malassezia* dermatitis	Cats	(Hobi et al. 2024)
		Malassezia dermatitis	Dogs	*(Hobi et al. 2024)*
		Aspergillosis Disinfection (*Aspergillus*)	Birds	(Redmann and Schildger 1989)
		Dermatophytosis	Rodents, rabbits	(Sharma et al. 2011; Chang et al. 2022)
		Dermatophytosis Disinfection (dermatophytes)	Ruminants	(Chermette et al. 2008)
9	Clotrimazole	Aspergillosis, Dermatophytosis	cats	(Moriello 2014; Fawsitt et al. 2023)
		Aspergillosis, Dermatophytosis, *Malassezia* dermatitis	Dogs	(Negre et al. 2009; Moriello 2019; Belton and Lobb 2023)

		Aspergillosis	Birds	(IT)
		Dermatophytosis	Rodents, rabbits	(Moriello et al. 2017; Jackson 2022)
10	Thiabendazole	Disinfection	Birds	(Akand et al. 2020)
		Dermatophytosis	Horses	(Drudge et al. 1962)
		Dermatophytosis	Rodents, rabbits	(Scott et al. 2001; Seyedmousavi et al. 2018)

1.1.5. Azole resistance in fungi

Invasive fungal infections have increased in frequency over the past few years (Figures 1.2, 1.3; (Pfaller and Diekema 2010; Burks et al. 2021). Most antifungal medications used in humans and animals are azoles, which are widely prescribed to treat fungal infections (Natarajan et al. 2010; Kaur et al. 2021). The extensive use of antifungal therapy promotes the development of drug resistance, which poses a serious challenge for treating fungal infections (Maertens 2004; Gulshan and Moye-Rowley 2007; Revie et al. 2018). *C. auris* and *C. glabrata*, the causative agents of the most common fungal infections, are becoming resistant to azoles (Berkow and Lockhart 2017; Lee et al. 2020). Furthermore, the agricultural use of triazoles has also led to developing azole resistance in *A. fumigatus* (Meis et al. 2016; Arendrup and Patterson 2017; Arikan-Akdagli et al. 2018).

In addition, due to insufficient removal of pollutants in wastewater treatment plants, commonly used azole antifungal drugs are also frequently found in surface water and sediment (Cai et al. 2021). The antifungal-resistant microorganisms pose a more significant threat to aquatic creatures (Garvey et al. 2022). *A. fumigatus*, widely distributed and thrives as a saprotroph on decaying plant matter, is an opportunistic pathogen causing aspergillosis, a range of respiratory illnesses acquired from the environment (Burks et al. 2021). Azole resistance has been observed in fungal isolates from various animals, and several studies have found unexpectedly high resistance levels in yeast species (Berman and Krysan 2020). In a previous study, 59% of *Candida. tropicalis* isolates from healthy animals were found resistant to fluconazole (Seyedmousavi et al. 2018) In addition, 40% of the *C. tropicalis* isolates from the nasolacrimal duct of healthy horses were resistant to fluconazole and itraconazole (Brilhante et al. 2015; Seyedmousavi et al. 2018). Itraconazole and fluconazole resistance rates were reported as 19% and 2%, respectively, for fungal strains isolated from horse uteri collected between 1999 and 2011 (Beltaire et al. 2012; Seyedmousavi et al. 2018). *Candida* isolates from rheas and cockatiels were reported to have significant fluconazole and itraconazole resistance rates with efflux pumps being a primary resistance mechanism (Seyedmousavi et al. 2018). Due to limited therapeutic choices Azole-resistant *A. fumigatus* infections are challenging to treat (Bosetti and Neofytos 2023).

Azoles, targeting Cyp51A in the ergosterol synthesis pathway, are the primary drugs used to treat aspergillosis and plant fungal diseases. Remarkably, *A. fumigatus* has become azole-resistant worldwide, predominantly found in hospitals, gardens, and agricultural soils due to agricultural use of triazoles (Astvad et al. 2014; Burks et al. 2021). The most common fungal infections, such as invasive mycoses caused by *C. albicans*, are becoming resistant to azoles (Whaley et al. 2017).

Figure 1.2. The map shows the global distribution of azole-resistant *A. fumigatus* isolates worldwide: (A) the world and (B) Europe; the figure is reproduced with permission from Burks et al, 2021, and the permission approval is included in the appendix.

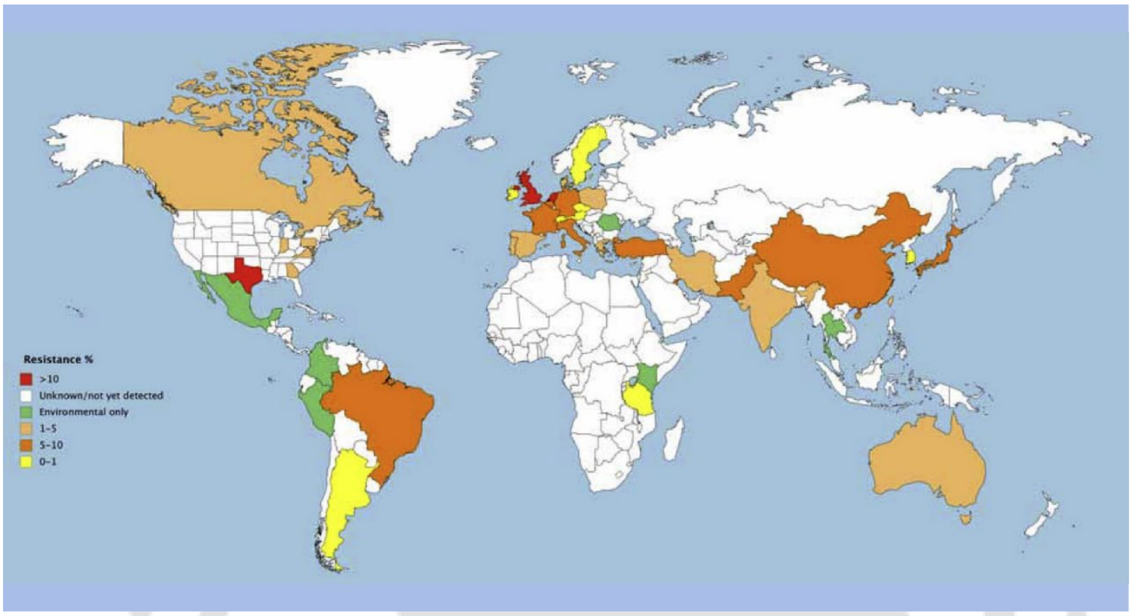

Figure 1.3. The figure shows the percentage of azole-resistant *A. fumigatus*; the figure is reproduced with permission from Burks et al, 2021, and the permission approval is included in the appendix.

1.1.6. Mechanism of azole resistance in fungi

Antifungal treatments also promote the development of drug resistance, causing a serious challenge in treating fungal infections (Maertens 2004; Gulshan and Moye-Rowley 2007; Revie et al. 2018). Fungi adapt various strategies, including the upregulation of genes for drug efflux pumps to reduce the intracellular concentration of the drug for making the drug less effective (Sanglard and Coste 2016). Alternatively, stress pathways essential for survival might indirectly influence efflux activity, allowing cells to survive and grow in the presence of the drug (Berman and Krysan 2020). Azole antifungal drugs disrupt ergosterol biosynthesis by inhibiting CYP51 (Parker et al. 2014). By inhibiting CYP51, azole antifungal drugs disrupt ergosterol biosynthesis, thereby exerting their antifungal effects. However, mutations in the CYP51 gene can lead to azole resistance in *A. fumigatus* (Parker et al. 2014; Gonzalez-Jimenez et al. 2020). Azole resistance in *A. fumigatus* is also caused by point mutations in the CYP51A gene, which encodes (Howard et al. 2009; Vermeulen et al. 2013; Seyedmousavi et al. 2014). Tandem repeats in the promoter region and point mutations such as TR34/L98H and TR46/Y121F/T289A cause increased protein levels have been discovered in *A. fumigatus* strains exposed to azoles in the environment (Hsu et al. 2022). Recently, pan-azole-resistant *A. fumigatus* strains were found infecting azole-unexposed patients, which could be due to the TR34/L98H and TR46/Y121F/T289A mutations in the *cyp51A* gene (Burks et al. 2021). The TR34/L98H resistance allele is commonly found allele globally, except in South America, where TR46/Y121F/T289A allele is prevalent in *A. fumigatus* (Burks et al. 2021).

Azole antifungal drugs are commonly used to treat fungal infections by inhibiting lanosterol 14α-demethylase enzyme encoded by the *ERG11* gene, which is essential for ergosterol biosynthesis (Shapiro et al. 2011). In *C. albicans*, upregulation of drug transporter and drug target *ERG11* genes are associated with drug resistance (Urbanek et al. 2022). Additionally, mutations in the *ERG11* gene in *C. albicans* contributes to azole resistance (Flowers et al. 2015). Resistance to azole drugs in Candida often involves amino acid changes in the Erg11 enzyme that prevent the drug from binding to its target, and over 140 such mutations have been identified in the drug-resistant strains (Morio et al. 2010). The R467K and G464S mutations, close to the heme-binding site of the enzyme, are most frequent in *C. albicans* (Casalinuovo et al. 2004). *C. albicans* can also utilize efflux systems to transport drugs extracellularly, reducing intracellular drug concentrations (Prasad and Rawal 2014). The overexpression of efflux pumps targeting azole is a key mechanism for azole resistance in *C. albicans*. The multidrug resistance gene (*MDR1*), which encodes a multidrug efflux pump belonging to the major facilitator superfamily (MFS) of transporters, plays a significant role in mediating resistance to fluconazole and voriconazole in *C. albicans* (Xiao et al. 2004; Cheng et al. 2007; Sanglard and Coste 2016; Nishimoto et al. 2020). Several candida species have shown resistance to azole drugs (Seyedmousavi et al. 2018). Several point mutations in the *ERG11* gene alters its protein lanosterol 14-demethylase resulting in reduced susceptibilities to the azoles (Brun et al. 2004; Sanguinetti et al. 2005).

The oropharyngeal candidiasis, isolated from HIV-infected individuals, was the first to be linked to clinical azole resistance (Nishimoto et al. 2020). The ATP-binding cassette (ABC) transporters *CDR1* and *CDR2* are well-documented regulators of azole resistance (Sanglard et al. 1999). In previous studies, isolates from HIV-infected individuals showed an increased mRNA level of CDR1, conferring resistance to azole antifungals (Sanglard et al. 1995; White 1997; Niimi et al. 2004; Nishimoto et al. 2020).

Azole resistance is also caused by the overexpression of the efflux pump genes CDR-1 and CDR2in *C. albicans* (Rad et al. 2016). The *MDR1* gene encodes for an ABC transporter protein that plays a role in drug efflux and overexpression of this gene confers resistance to azoles in *C. albicans* (Prasad and Kapoor 2005). In *C. albicans*, the *UPC2* gene homologue of the *S. cerevisiae ScUPC2* gene, upregulates the ergosterol biosynthesis genes *ERG2* and *ERG11* in response to fluconazole (Silver et al. 2004). A Zn(II)-Cys(6) transcription factor, Upc2 is also involved in sterol biosynthesis and azole resistance in fungi (Yin et al. 2021a). Overexpression of *ERG11* upregulates the azole target 14α-lanosterol demethylase, resulting in reduced azole susceptibility in *C. albicans* (Nishimoto 2019). Alterations in ergosterol biosynthetic enzymes are common among azole-resistant clinical isolates of *C. albicans* and other *Candida* species such as *C. glabrata*, *C. parapsilosis*, *C. tropicalis*, and *C. krusei* (Whaley et al. 2017).

Mechanisms underlying azole resistance include the upregulation or downregulation of mRNA expression levels of *ERG11*, *PDR1*, and *CDR1* genes upon exposure to azoles (Henry et al. 2000). Mutations in *ERG11* and *PDR1* genes also play a pivotal role in acquired resistance to azole agents. In *C. glabrata,* 27 mutated genes associated with fluconazole susceptibility, those involved in the retrograde signaling pathway (RTG2), calcium homeostasis, transcription activation, mitochondrial function, ribosomal biogenesis, cell wall biosynthesis (Kaur et al. 2004). The reduction of intracellular azole concentrations through the activation of drug efflux systems is another critical mechanism of azole resistance. In *C. glabrata*, ABC transporters, such as Pdh1p, Cdr1p, and Snq2p, facilitate the efflux of toxic compounds and prevent the intracellular accumulation of azoles. Like *PDR1*, *STB5* regulates ABC transporter genes involved in azole resistance in *C. glabrata* (Ferrari et al. 2011; Paul et al. 2011). Interestingly, while *PDR1* disruption reduces resistance, disruption of *STB5* leads to increased azole resistance in mutant fungal cells. Conversely, overexpression of *STB5* mRNA levels may enhance the susceptibility of *C. glabrata* strains to azoles (Paul et al. 2011; Vale-Silva et al. 2013). The aldo-keto reductase (AKR) gene superfamily, which is involved in protecting fungal cells from various stresses, also contributes to azole resistance. Overexpression of AKR genes has been correlated with increased azole resistance in *C. glabrata* strains (Castaño et al. 2005; Farahyar et al. 2013). Additionally, *C. glabrata* Drug:H^+ Antiporter (DHA) transporters are implicated in imidazole resistance. Overexpression of *CgQDR2* in *C. glabrata* confers resistance to miconazole, tioconazole, clotrimazole, and ketoconazole. The CgQdr2 protein, localized to the plasma membrane, reduces intracellular clotrimazole accumulation and facilitates antifungal efflux in drug treated cells (Costa et al. 2013). Furthermore, the DHA transporter CgTpo1 is overexpressed in response to clotrimazole and is involved in reducing its intracellular concentration (Pais et al. 2016). Proteins such as CgQdr2 are plasma membrane-localized and linked to clotrimazole efflux. The upregulation of these genes is likely regulated by the *CgPdr1* transcription factor, which is a major regulator of multidrug resistance in *C. glabrata* strains (Costa et al. 2013; Pais et al. 2016).

1.1.7. Azole resistance and mechanism in *N. crassa*

The model filamentous fungus *N. crassa* has also been used to investigate the molecular mechanisms underlying azole drug resistance (Zhang et al. 2012a; Víglaš and Olejníková 2023). In *N. crassa*, ergosterol biosynthesis genes, *erg11* as well as ABC transporter CDR4 have been identified and extensively studied as key contributors to azole drug resistance (Zhou et al. 2022).The transcription repressor conidial separation-1 (CSP-1) is downregulated under azole stress, facilitating the activation of genes necessary for azole resistance (Chen et al. 2016). In addition, the sterol C-22 desaturase *erg-5* (NCU05278), and azole pump encoding *cdr-4* (NCU05591) gene show significant transcriptional upregulation in *N. crassa* upon ketoconazole treatment (Sun et al. 2013; Yin et al. 2021a). Sterol C-22 desaturase ERG-5 regulates the azole antifungal sensitivity in *N. crassa* and *Fusarium verticillioides* (Sun et al. 2013). The deletion of erg5 enhances azole sensitivity in both *N. crassa* and *F. verticillioides* (Sun et al. 2013) Moreover, CDR-4, an ortholog of *C. albicans* Cdr1p and *S. cerevisiae* Pdr5p, functions as the primary azole efflux pump in *N. crassa* (Zhang et al. 2012c). Additionally, the novel kinase STK-17 is upregulated in the presence of azoles, and essential for azole resistance (Hu et al. 2022). Deletion of STK-17 affects sterol biosynthesis and modulates ergosterol biosynthesis genes such as *erg-11*, *erg-2*, *erg-6*, and *erg-24* in *N. crassa* (Hu et al. 2022). The ADS-1, CCG-8, and CSP-1 transcription factors also contribute to azole sensitivity in *N. crassa* (Sun et al. 2014; Wang et al. 2015; Xue et al. 2019; Yin et al. 2021a). The transcription factor ADS-1, which positively regulates the transcriptional responses of azole efflux pumps, was first discovered and characterized in *N. crassa* (Yin et al. 2021b). Mutations in *ERG11* gene result in reduced binding affinity of azole drugs to the lanosterol 14-alpha demethylase enzyme that contributes to azole resistance in *C. albicans* (Xiang et al. 2013). Homologs of ADS-1 are broadly conserved among filamentous fungi within the phylum Ascomycota. The deletion of the gene encoding an

ADS-1 homolog in *Aspergillus flavus* results in increased susceptibility to ketoconazole and itraconazole (Yin et al. 2021b).

1.1.8. Involvement of the calcineurin and *pmr-1* genes in azole drug resistance

Calcineurin, consisting of a catalytic A (CNA-1) subunit and a regulatory subunit B (CNB-1), is vital for growth, development, and fertility in *N. crassa* (Tamuli et al. 2016; Kumar et al. 2020). Calcineurin is the only serine-threonine phosphatase requiring both calcium (Ca^{2+}) and calmodulin (CaM) for activation (Li et al. 2011). Calcineurin is essential for overcoming the azole-induced cell membrane stress (Juvvadi et al. 2014). The CaM protein binds to four Ca^{2+} ions and undergoes a conformational change (Kumar et al. 2020). This activated Ca^{2+}-CaM complex activates calcineurin, which dephosphorylates the Crz1 transcription factor to facilitate its localization in the nucleus for the expression of targets, including the genes involved in growth, stress response, cell wall integrity, and drug resistance (Figure 1.4; (Chen et al. 2010; Juvvadi et al. 2017; Roy et al. 2021). In mammals, the Crz1 homolog is called the nuclear factor of activated T cells (NFAT), which is also activated by calcineurin and involved in multiple cellular functions, including development and diseases (Thewes 2014). Calcineurin plays a role in regulating susceptibility to antifungals (Onyewu et al. 2003). Mutants of *C. albicans* and *C. dubliniensis* deficient in calcineurin and the crz1 genes showed decreased resistance to azole and echinocandin classes of antifungal agents (Chen et al. 2011). The *C. lusitaniae* calcineurin-deficient mutants showed increased sensitivity to azoles, whereas crz1-deficient mutants exhibited enhanced tolerance to these antifungal compounds (Zhang et al. 2012b). Additionally, resistance to azoles mediated by Ca^{2+} and calcineurin are widely reported (Edlind et al. 2002).The calcineurin catalytic subunit includes an N-terminal phosphatase domain, a regulatory subunit binding helix (CnBBH), and a CaM-binding domain (CaMBD) (Dunlap 2013; Juvvadi et al. 2017). In the filamentous fungi, including *A.fumigatus*, the calcineurin catalytic subunit contains a unique serine-proline-rich (SPRR) linker domain that connects the CnBBH and CaMBD domains, and its phosphorylation at four serine clusters affects fungal growth and virulence (Rusnak and Mertz 2000; Juvvadi et al. 2013). In Candida species, calcineurin and Crz1 mutants exhibit antifungal activity variations, highlighting the critical role of calcineurin in fungal pathogenicity (Miyazaki et al. 2010; Park et al. 2019).

In several pathogenic fungi, including *A. fumigatus*, *C. albicans*, and *Cryptococcus neoformans*, calcineurin is crucial for virulence and drug resistance

(Karkowska-Kuleta et al. 2009). In *C. albicans* and *A. fumigatus*, calcineurin regulates ergosterol biosynthesis and drug efflux, which are key mechanisms in azole resistance (Cowen et al. 2015b; Park et al. 2016) . In *C. glabrata,* calcineurin signaling activates Crz1, enhancing CgYor1-mediated azole resistance, stress responses, and pathogenicity (Ceballos-Garzon et al. 2022; Kumari et al. 2022). Additionally, the retrograde transport protein Pep8 deletion increases calcineurin activity, contributing to azole resistance in *C. albicans* (Mount et al. 2018). Inhibiting the calcineurin pathway may improve antifungal efficacy and reduce drug resistance in fungi (Park et al. 2016). Calcineurin mutants in *C. lusitaniae* showed decreased azole resistance (Juvvadi et al. 2017). Calcineurin is a promising antifungal target for species such as *C. neoformans, C. albicans, and A. fumigatus* (Juvvadi et al. 2017). The calcineurin inhibitor FK506 induces Ca^{2+} entry into fungal cells via high-affinity channels Cch1 and Mid1 (Muller et al. 2003). The involvement of calcineurin in fungal virulence suggests it may be a promising target for antifungal therapy. Blocking calcineurin signaling might improve antifungal treatment effectiveness and reduce drug resistance (Chen et al. 2011; Park et al. 2016; Juvvadi et al. 2017).

The *pmr-1* gene encodes a Ca^{2+} ATPase, which affects azole sensitivity. The expression of the *pmr-1* gene is necessary for regulating the transport of Ca^{2+} and Mn^{2+} cations across the Golgi membrane and maintaining the structural integrity of the cell wall in various fungi, including *N. crassa* (Antebi and Fink 1992; Bowman et al. 2012). The *pmr-1* gene also plays a crucial role in regulating Ca^{2+} homeostasis, cell wall integrity, and antifungal drug resistance in *A. fumigatus* and *C. albicans* (Bates et al. 2005; Pinchai et al. 2010). The *C. albicans PMR*1p, a P-type Ca^{2+}/Mn^{2+}-ATPase in the secretory pathway, is necessary for virulence (Bates et al. 2005). The disruption of *PMR1* in *Saccharomyces cerevisiae* causes several defects, including protein-sorting abnormalities, such as increased secretion of heterologous proteins (Antebi and Fink 1992; Bates et al. 2005). Additionally, PMR1 disruption causes the aberrant processing of the α factor in *S. cerevisiae* (Sorin et al. 1997; Kang et al. 1998). *PMR1* has a role in pathogenicity in *S. cerevisiae*, *C. neoformans*, and *A. fumigatus* (Pittman et al. 2004; Mielniczki-Pereira et al. 2011; De Castro et al. 2014). The antifungal drug itraconazole induces a transient up-regulation of calcineurin (cnaA), a transcription factor (crzA), and two Ca^{2+} transporters (*pmr*A/pmcA) in Aspergilli, suggesting their involvement in the azole stress-response reaction (Liu et al. 2015). In addition, the interaction of the *pmr-1* gene with the calcineurin pathway is crucial for regulating Ca^{2+} homeostasis, cell wall integrity, and antifungal drug resistance in *A. fumigatus* and *C. albicans* (Bates et al. 2005; Pinchai et al. 2010). Specifically, *C. albicans Pmr*1p, a P-type Ca^{2+}/Mn^{2+}-ATPase in the secretory pathway, is necessary for virulence (Bates et al. 2005). *PMR1* has a role in pathogenicity and drug tolerance in *C. neoformans*, *S. cerevisiae*, and *A. fumigatus* (Pittman et al. 2004; Mielniczki-Pereira et al. 2011; De Castro et al. 2014). The *PMR1* gene regulates Ca^{2+} homeostasis, cell wall integrity, and antifungal resistance in *C. albicans* and *A. fumigatus* (Bates et al. 2005; Pinchai et al. 2010). The *pmr-1* gene is essential for transporting Ca^{2+} and Mn^{2+} across the Golgi membrane and maintaining cell wall structure in fungi like *N. crassa* (Antebi and Fink 1992; Bowman et al. 2011).

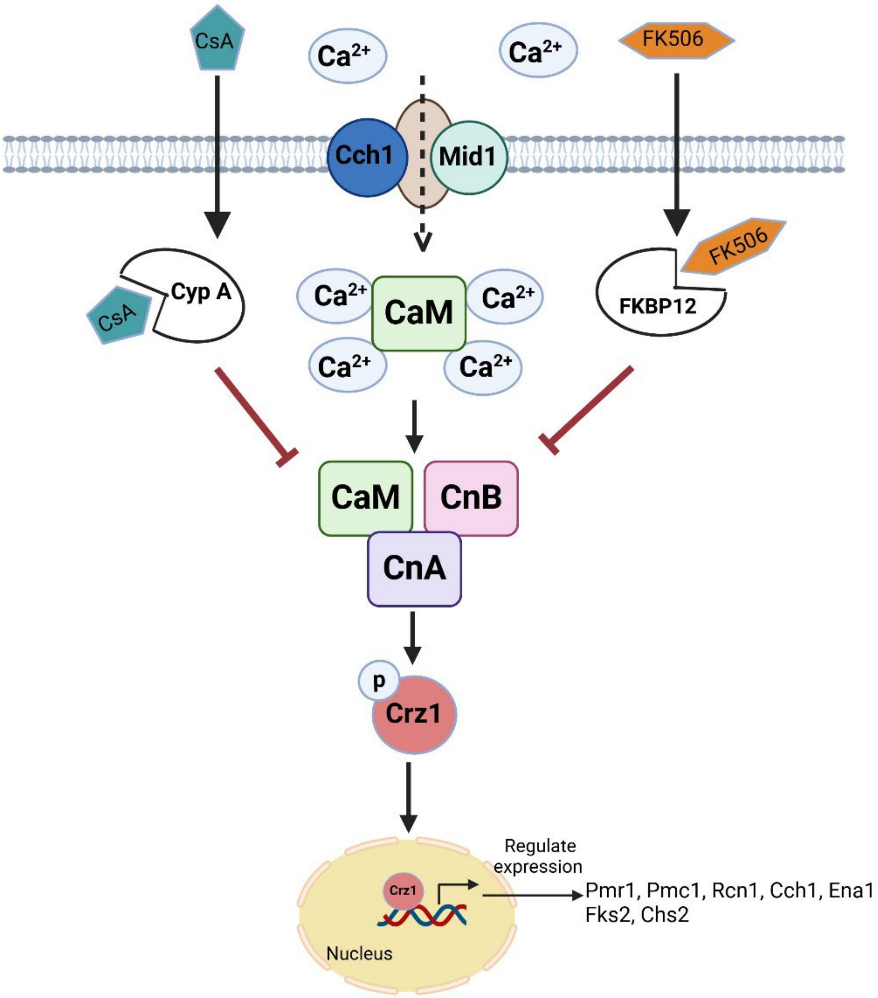

Figure 1.4. Illustration of the calcineurin signaling pathway. External stimuli trigger the entry of Ca^{2+} ions into the cell through the high-affinity channels Cch1 and Mid1. The activated Ca^{2+}-CaM complex then binds to the calcineurin heterodimer (CnA and CnB), enhancing phosphatase activity. Calcineurin activity is inhibited by the binding of FK506-FKBP12 and CsA-CypA, (immunophilin-immunosuppressant) complexes. The activated calcineurin complex dephosphorylates the calcineurin-dependent transcription factor Crz1, enabling its translocation into the nucleus. In the nucleus, Crz1 activates the transcription of genes involved in growth, stress responses, cell wall integrity, and drug resistance. The figure was adapted and redrawn from Juvvadi, Lee et al. 2017 and Ying-Lien Chen et al. 2010.

MOTIVATION AND OBJECTIVES
OF THE PRESENT INVESTIGATIONS

Conventionally, *N. crassa* has been widely recognized as a model organism for investigating fundamental biological processes due to its genetically and biochemically tractable life cycle (Borkovich et al. 2004; Laxmi and Tamuli 2017; Víglaš and Olejníková 2023). However, the cellular role of calcineurin and Golgi calcium ATPase PMR-1 in azole drug susceptibility remains unexplored in *N. crassa*. Therefore, the current thesis explored the roles of calcineurin and PMR-1 in azole susceptibility in *N. crassa*. Calcineurin is an essential gene in *N. crassa*, and the knockout of the *cna-1* gene in *N. crassa* is lethal (Tamuli et al. 2016). Therefore, I used the calcineurin RIP mutants *Cna-1*$^{\mathrm{RIP}}$ 24 a and *Cna-1*$^{\mathrm{RIP}}$ 122 A, which were previously generated in our laboratory, to investigate the role of calcineurin in azole drug susceptibility (Kumar et al. 2020). Additionally, the Δ*pmr-1* a knockout mutant (FGSC 11616) procured from the Fungal Genetics Stock Centre (FGSC; University of Missouri, Kansas City, MO 64110; McCluskey et al. 2010). Moreover, only a limited mechanistic study of calcineurin in complex with FK506-FKBP12 has been reported (Tong et al. 2016). Therefore, understanding the molecular interaction of azoles with calcineurin and PMR-1 could helpful to design potent antifungals to overcome antifungal drug resistance. In addition, the computer-aided drug designing (CADD) approaches, including molecular docking, offer a promising pathway to identify new bioactive compounds with potential antifungal properties. The CADD facilitates the rapid and cost-effective screening of large libraries of compounds, such as those available in the PubChem database, against target proteins of interest (Kitchen et al. 2004). I also performed molecular docking, molecular dynamics (MD) simulations, and CADD to understand the interaction of antifungal drugs with calcineurin and PMR-1. The study of calcineurin and PMR-1 interactions with azole drugs may aid in developing of new antifungals for invasive fungal infections, which currently have exceedingly high mortality rates (Hoy et al. 2022). In addition, I used CADD to identify phytochemical compounds with potential antifungal activity targeting calcineurin and PMR-1. Therefore, this thesis work is structured on the following three broad objectives.

Objectives

Objective 1: To determine the minimum inhibitory concentrations of azole drugs and to study the effects of azoles in the calcium signaling gene calcineurin and *pmr-1*, in *Neurospora crassa*

Objective 2: To study the interaction of the CNA-1, CNB-1, and PMR-1 proteins with azole drugs using the molecular docking and Molecular Dynamics (MD) Simulations Approaches.

Objective 3: To study the phytochemical inhibitors targeting calcineurin and PMR-1 proteins using computer-aided drug design (CADD).

References

ABD EL MOTELIB T, AMEN O (2019) Role of essential oil for control of avian aspergillosis in experimentally infected chickens. Assiut Veterinary Medical Journal 65:152-160

Agarwal R et al. (2022) Evaluation of Simpler Criteria for Diagnosing Allergic Bronchopulmonary Aspergillosis Complicating Asthma. Frontiers in cellular and infection microbiology:353

Akand A, Bulbul K, Hasin D, Parbin S, Hussain J, Sheikh I (2020) Perspective of gapeworm infection in birds. International Journal of Veterinary Sciences and Animal Husbandry 5:68-71

Al-Ewaidat OA, Gogia S, Begiashvili V, Naffaa MM (2024) The multifaceted role of calcium signaling dynamics in neural cell proliferation and gliomagenesis. AIMS Biophysics 11:296-328

Antebi A, Fink GR (1992) The yeast Ca (2+)-ATPase homologue, PMR1, is required for normal Golgi function and localizes in a novel Golgi-like distribution. Molecular biology of the cell 3:633-654

Aramayo R, Selker EU (2013) Neurospora crassa, a model system for epigenetics research. Cold Spring Harbor Perspectives in Biology 5:a017921

Arastehfar A et al. (2021) Aspergillus fumigatus and aspergillosis: From basics to clinics. Studies in mycology 100:100115-100115

Arendrup MC, Patterson TF (2017) Multidrug-resistant Candida: epidemiology, molecular mechanisms, and treatment. The Journal of infectious diseases 216:S445-S451

Arikan-Akdagli S, Ghannoum M, Meis JF (2018) Antifungal resistance: specific focus on multidrug resistance in Candida auris and secondary azole resistance in Aspergillus fumigatus. Journal of Fungi 4:129

Arné P, Risco-Castillo V, Jouvion G, Le Barzic C, Guillot J (2021) Aspergillosis in wild birds. Journal of fungi 7:241

Astvad K et al. (2014) First detection of TR46/Y121F/T289A and TR34/L98H alterations in Aspergillus fumigatus isolates from azole-naive patients in Denmark despite negative findings in the environment. Antimicrobial agents and chemotherapy 58:5096-5101

Bagur R, Hajnóczky G (2017) Intracellular Ca2+ sensing: its role in calcium homeostasis and signaling. Molecular cell 66:780-788

Bajwa J (2017) Canine Malassezia dermatitis. The Canadian Veterinary Journal 58:1119

Baker CL, Loros JJ, Dunlap JC (2012) The circadian clock of Neurospora crassa. FEMS microbiology reviews 36:95-110

Bates S et al. (2005) Candida albicans Pmr1p, a secretory pathway P-type Ca2+/Mn2+-ATPase, is required for glycosylation and virulence. Journal of Biological Chemistry 280:23408-23415

Beadle GW, Tatum EL (1941) Genetic control of biochemical reactions in Neurospora. Proceedings of the National Academy of Sciences 27:499-506

Beernaert LA et al. (2009) Designing a treatment protocol with voriconazole to eliminate Aspergillus fumigatus from experimentally inoculated pigeons. Veterinary Microbiology 139:393-397

Beltaire KA, Cheong SH, Coutinho da Silva M (2012) Retrospective study on equine uterine fungal isolates and antifungal susceptibility patterns (1999–2011). Equine Veterinary Journal 44:84-87

Belton H, Lobb J (2023) Treatment options for dogs diagnosed with sinonasal aspergillosis. Veterinary Evidence 8

Berkow EL, Lockhart SR (2017) Fluconazole resistance in Candida species: a current perspective. Infection and drug resistance:237-245

Berman J, Krysan DJ (2020) Drug resistance and tolerance in fungi. Nature Reviews Microbiology 18:319-331

Berridge MJ, Bootman MD, Roderick HL (2003) Calcium signaling: dynamics, homeostasis and remodelling. Nature reviews Molecular cell biology 4:517-529

Berthelot J-M, Darrieutort-Laffite C, Trang C, Maugars Y, Le Goff B (2021) Contribution of mycobiota to the pathogenesis of spondyloarthritis. Joint Bone Spine 88:105245

Bistis G (1981) Chemotropic interactions between trichogynes and conidia of opposite mating-type in Neurospora crassa. Mycologia 73:959-975

Bistis GN, Perkins DD, Read ND (2003) Different cell types in Neurospora crassa. Fungal Genetics Reports 50:17-19

Borkovich KA et al. (2004) Lessons from the genome sequence of Neurospora crassa: tracing the path from genomic blueprint to multicellular organism. Microbiology and molecular biology reviews 68:1-108

Bosetti D, Neofytos D (2023) Invasive Aspergillosis and the Impact of Azole-resistance. Current Fungal Infection Reports 17:77-86

Bowman BJ, Abreu S, Johl JK, Bowman EJ (2012) The pmr gene, encoding a Ca2+-ATPase, is required for calcium and manganese homeostasis and normal development of hyphae and conidia in Neurospora crassa. Eukaryotic Cell 11:1362-1370

Bowman BJ, Abreu S, Margolles-Clark E, Draskovic M, Bowman EJ (2011) Role of four calcium transport proteins, encoded by nca-1, nca-2, nca-3, and cax, in maintaining intracellular calcium levels in Neurospora crassa. Eukaryotic Cell 10:654-661

Bray RN, Raghu CL, Leuin AS, Barry-Heffernan CA, Pritchard JC (2020) Oral administration of voriconazole with surgical fungal plaque debridement for the treatment of sinonasal aspergillosis with cribriform plate lysis in three dogs. Journal of the American Veterinary Medical Association 256:111-116

Brilhante RSN et al. (2015) Trends in antifungal susceptibility and virulence of Candida spp. from the nasolacrimal duct of horses. Sabouraudia 54:147-154

Brun S et al. (2004) Mechanisms of azole resistance in petite mutants of Candida glabrata. Antimicrobial Agents and Chemotherapy 48:1788-1796

Burks C, Darby A, Gómez Londoño L, Momany M, Brewer MT (2021) Azole-resistant Aspergillus fumigatus in the environment: Identifying key reservoirs and hotspots of antifungal resistance. PLoS Pathogens 17:e1009711

Cai W et al. (2021) Biodegradation of typical azole fungicides in activated sludge under aerobic conditions. journal of environmental sciences 103:288-297

Cambareri EB, Jensen BC, Schabtach E, Selker EU (1989) Repeat-induced GC to AT mutations in Neurospora. Science 244:1571-1575

Campbell CJ et al. (2022) White-Nose Syndrome Pathogen Pseudogymnoascus destructans Detected in Migratory Tree-Roosting Bats. The Journal of Wildlife Diseases 58:652-657

Carrasco L, Bautista M, De Las Mulas J, Jensen H (1993) Application of enzyme-immunohistochemistry for the diagnosis of aspergillosis, candidiasis, and zygomycosis in three lovebirds. Avian diseases:923-927

Casalinuovo I, Di Francesco P, Garaci E (2004) Fluconazole resistance in Candida albicans: a review of mechanisms. EUROPEAN REVIEW FOR MEDICAL AND PHARMACOLOGICAL SCIENCES. 8:69-78

Castaño I, Pan SJ, Zupancic M, Hennequin C, Dujon B, Cormack BP (2005) Telomere length control and transcriptional regulation of subtelomeric adhesins in Candida glabrata. Molecular microbiology 55:1246-1258

Ceballos-Garzon A et al. (2022) CRISPR-Cas9 approach confirms Calcineurin-responsive zinc finger 1 (Crz1) transcription factor as a promising therapeutic target in echinocandin-resistant Candida glabrata. Plos one 17:e0265777

Celia-Sanchez B et al. (2023) Pan-azole-and multi-fungicide-resistant Aspergillus fumigatus is widespread in the United States. bioRxiv:2023.2012. 2014.571763

Chakrabarti A, Bonifaz A, Gutierrez-Galhardo MC, Mochizuki T, Li S (2015) Global epidemiology of sporotrichosis. Medical mycology 53:3-14

Chan HM (2008) Pharmacokinetics of voriconazole in horses and alpacas. Auburn University

Chang C-C et al. (2022) Prevalence and risk factors of zoonotic dermatophyte infection in pet rabbits in northern Taiwan. Journal of Fungi 8:627

Chayakulkeeree M, Perfect JR (2008) Cryptococcosis. Diagnosis and treatment of human mycoses:255-276

Chen X et al. (2016) De-repression of CSP-1 activates adaptive responses to antifungal azoles. Scientific reports 6:1-11

Chen Y-L et al. (2011) Calcineurin controls drug tolerance, hyphal growth, and virulence in Candida dubliniensis. Eukaryotic cell 10:803-819

Chen Y-L, Kozubowski L, Cardenas ME, Heitman J (2010) On the roles of calcineurin in fungal growth and pathogenesis. Current Fungal Infection Reports 4:244-255

Cheng S, Clancy CJ, Nguyen KT, Clapp W, Nguyen MH (2007) A Candida albicans petite mutant strain with uncoupled oxidative phosphorylation overexpresses MDR1 and has diminished susceptibility to fluconazole and voriconazole. Antimicrobial agents and chemotherapy 51:1855-1858

Chermette R, Ferreiro L, Guillot J (2008) Dermatophytoses in animals. Mycopathologia 166:385-405

Chin D, Means AR (2000) Calmodulin: a prototypical calcium sensor. Trends in cell biology 10:322-328

Cogoni C, Macino G (1999) Posttranscriptional gene silencing in Neurospora by a RecQ DNA helicase. Science 286:2342-2344

Colot HV et al. (2006) A high-throughput gene knockout procedure for Neurospora reveals functions for multiple transcription factors. Proceedings of the National Academy of Sciences 103:10352-10357

Cools H, Hawkins N, Fraaije B (2013) Constraints on the evolution of azole resistance in plant pathogenic fungi. Plant Pathology 62:36-42

Cornelius G, Nakashima H (1987) Vacuoles play a decisive role in calcium homeostasis in Neurospora crassa. Journal of general microbiology 133:2341-2347

Corrigan V et al. (2016) Treatment of disseminated aspergillosis with posaconazole in 10 dogs. Journal of Veterinary Internal Medicine 30:167-173

Costa C et al. (2013) Candida glabrata drug: H+ antiporter CgQdr2 confers imidazole drug resistance, being activated by transcription factor CgPdr1. Antimicrobial agents and chemotherapy 57:3159-3167

Cowen LE, Sanglard D, Howard SJ, Rogers PD, Perlin DS (2015a) Mechanisms of antifungal drug resistance. Cold Spring Harbor perspectives in medicine 5

Cowen LE, Sanglard D, Howard SJ, Rogers PD, Perlin DS (2015b) Mechanisms of antifungal drug resistance. Cold Spring Harbor perspectives in medicine 5:a019752

Davis JL, Salmon JH, Papich MG (2006) Pharmacokinetics of voriconazole after oral and intravenous administration to horses. American journal of veterinary research 67:1070-1075

Davis RH, de Serres FJ (1970) [4] Genetic and microbiological research techniques for Neurospora crassa. In: Methods in enzymology. Elsevier, pp 79-143

Davis RH, Perkins DD (2002) Neurospora: a model of model microbes. Nature Reviews Genetics 3:397-403

De Castro PA et al. (2014) The involvement of the Mid1/Cch1/Yvc1 calcium channels in Aspergillus fumigatus virulence. PLoS One 9:e103957

Dean R et al. (2012) The Top 10 fungal pathogens in molecular plant pathology. Molecular plant pathology 13:414-430

Debnath C, Mitra T, Kumar A, Samanta I (2016) Evaluation of healthy farm and companion rabbits as carriers of dermatophytes. Veterinarski arhiv 86:805-813

Deka R, Kumar R, Tamuli R (2011) Neurospora crassa homologue of Neuronal Calcium Sensor-1 has a role in growth, calcium stress tolerance, and ultraviolet survival. Genetica 139:885-894

Di Somma A, Bailey T, Silvanose C, Garcia-Martinez C (2007) The use of voriconazole for the treatment of aspergillosis in falcons (Falco species). Journal of Avian Medicine and Surgery 21:307-316

Dogaris I, Mamma D, Kekos D (2013) Biotechnological production of ethanol from renewable resources by Neurospora crassa: an alternative to conventional yeast fermentations? Applied microbiology and biotechnology 97:1457-1473

Drudge J, Szanto J, Wyant A, Elam G (1962) Critical tests on thia-bendazole (MK-360) against parasites of the horse.

Dunlap VB (2013) The Disordered Regulation of Calcineurin: How Calmodulin-induced Regulatory Domain Structural Changes Lead to the Activation of Calcineurin.

Edlind T, Smith L, Henry K, Katiyar S, Nickels J (2002) Antifungal activity in Saccharomyces cerevisiae is modulated by calcium signaling. Molecular microbiology 46:257-268

Farahyar S et al. (2013) Overexpression of aldo-keto-reductase in azole-resistant clinical isolates of Candida glabrata determined by cDNA-AFLP. DARU Journal of Pharmaceutical Sciences 21:1-7

Fawsitt J, Russell O, Alexander A, Peschard A-L, Wong H, Kortum A (2023) Clinical remission of feline sino-nasal aspergillosis despite evidence of persistent infection. Journal of Feline Medicine and Surgery Open Reports 9:20551169231201605

Fehr M (2015) Zoonotic potential of dermatophytosis in small mammals. Journal of Exotic Pet Medicine 24:308-316

Ferrari S, Sanguinetti M, Torelli R, Posteraro B, Sanglard D (2011) Contribution of CgPDR1-regulated genes in enhanced virulence of azole-resistant Candida glabrata. PloS one 6:e17589

Ferreira AV, An Z, Metzenberg RL, Glass NL (1998) Characterization of mat A-2, mat A-3 and ΔmatA mating-type mutants of Neurospora crassa. Genetics 148:1069-1079

Flowers SA, Colón B, Whaley SG, Schuler MA, Rogers PD (2015) Contribution of clinically derived mutations in ERG11 to azole resistance in Candida albicans. Antimicrobial agents and chemotherapy 59:450-460

Franco-Paredes C et al. (2015) Management of Cryptococcus gattii meningoencephalitis. The Lancet Infectious Diseases 15:348-355

Galagan JE et al. (2003) The genome sequence of the filamentous fungus Neurospora crassa. Nature 422:859-868

Garvey M, Meade E, Rowan NJ (2022) Effectiveness of front line and emerging fungal disease prevention and control interventions and opportunities to address appropriate eco-sustainable solutions. Science of the Total Environment 851:158284

Gnat S, Łagowski D, Nowakiewicz A, Dyląg M (2021) A global view on fungal infections in humans and animals: opportunistic infections and microsporidioses. Journal of Applied Microbiology 131:2095-2113

Gonzalez-Jimenez I et al. (2020) A Cyp51B mutation contributes to azole resistance in Aspergillus fumigatus. Journal of Fungi 6:315

Granatiero V, Patron M, Tosatto A, Merli G, Rizzuto R (2014) Using targeted variants of aequorin to measure Ca2+ levels in intracellular organelles. Cold Spring Harbor Protocols 2014:pdb. prot072843

Gulshan K, Moye-Rowley WS (2007) Multidrug resistance in fungi. Eukaryotic cell 6:1933-1942

Hamilton SL (2005) Ryanodine receptors. Cell calcium 38:253-260

Hausmann R, Hausmann R (2002) One Gene—One Enzyme. To Grasp the Essence of Life: A History of Molecular Biology:44-55

Henry KW, Nickels JT, Edlind TD (2000) Upregulation of ERG genes in Candida species by azoles and other sterol biosynthesis inhibitors. Antimicrobial agents and chemotherapy 44:2693-2700

Hobi S, Bęczkowski PM, Mueller R, Tse M, Barrs VR (2024) Malassezia dermatitis in dogs and cats. The Veterinary Journal:106084

Holliday R (2004) Early studies on recombination and DNA repair in Ustilago maydis. DNA repair 3:671-682

Honda S et al. (2020) Establishment of Neurospora crassa as a model organism for fungal virology. Nature communications 11:5627

Howard SJ et al. (2009) Frequency and evolution of azole resistance in Aspergillus fumigatus associated with treatment failure. Emerging infectious diseases 15:1068

Hoy MJ et al. (2022) Structure-guided synthesis of FK506 and FK520 analogs with increased selectivity exhibit in vivo therapeutic efficacy against Cryptococcus. mBio:e01049-01022

Hsu T-H, Huang P-Y, Fan Y-C, Sun P-L (2022) Azole resistance and cyp51A mutation of aspergillus fumigatus in a tertiary referral hospital in Taiwan. Journal of Fungi 8:908

Hu C et al. (2022) Coordinated Regulation of Membrane Homeostasis and Drug Accumulation by Novel Kinase STK-17 in Response to Antifungal Azole Treatment. Microbiology spectrum 10:e00127-00122

IT WI Avian Aspergillosis—What Every Veterinarian Needs to Know.

Jackson EP (2022) Analysis of dermatophyte prevalence and associated risk factors in rabbits. Universidade de Lisboa (Portugal)

Juvvadi PR et al. (2013) Phosphorylation of calcineurin at a novel serine-proline rich region orchestrates hyphal growth and virulence in Aspergillus fumigatus. PLoS pathogens 9:e1003564

Juvvadi PR, Lamoth F, Steinbach WJ (2014) Calcineurin as a multifunctional regulator: unraveling novel functions in fungal stress responses, hyphal growth, drug resistance, and pathogenesis. Fungal biology reviews 28:56-69

Juvvadi PR, Lee SC, Heitman J, Steinbach WJ (2017) Calcineurin in fungal virulence and drug resistance: Prospects for harnessing targeted inhibition of calcineurin for an antifungal therapeutic approach. Virulence 8:186-197

Kang HA et al. (1998) Cloning and characterization of the Hansenula polymorpha homologue of the Saccharomyces cerevisiae PMR1 gene. Yeast 14:1233-1240

Karkowska-Kuleta J, Rapala-Kozik M, Kozik A (2009) Fungi pathogenic to humans: molecular bases of virulence of Candida albicans, Cryptococcus neoformans and Aspergillus fumigatus. Acta Biochimica Polonica 56:211-224

Kaur N, Bains A, Kaushik R, Dhull SB, Melinda F, Chawla P (2021) A review on antifungal efficiency of plant extracts entrenched polysaccharide-based nanohydrogels. Nutrients 13:2055

Kaur R, Castaño I, Cormack BP (2004) Functional genomic analysis of fluconazole susceptibility in the pathogenic yeast Candida glabrata: roles of calcium signaling and mitochondria. Antimicrobial agents and chemotherapy 48:1600-1613

Keniya MV et al. (2018) Crystal structures of full-length lanosterol 14α-demethylases of prominent fungal pathogens Candida albicans and Candida glabrata provide tools for antifungal discovery. Antimicrobial agents and chemotherapy 62:10.1128/aac. 01134-01118

Kim H, Wright SJ, Park G, Ouyang S, Krystofova S, Borkovich KA (2012) Roles for receptors, pheromones, G proteins, and mating type genes during sexual reproduction in Neurospora crassa. Genetics 190:1389-1404

Kitchen DB, Decornez H, Furr JR, Bajorath J (2004) Docking and scoring in virtual screening for drug discovery: methods and applications. Nature reviews Drug discovery 3:935-949

Kumar A, Roy A, Deshmukh MV, Tamuli R (2020) Dominant mutants of the calcineurin catalytic subunit (CNA-1) showed developmental defects, increased sensitivity to stress conditions, and CNA-1 interacts with CaM and CRZ-1 in Neurospora crassa. Archives of microbiology 202:921-934

Kumari S et al. (2022) Unmasking of CgYor1-dependent azole resistance mediated by target of rapamycin (TOR) and calcineurin signaling in candida glabrata. Mbio 13:e03545-03521

Laxmi V, Tamuli R (2017) The calmodulin gene in Neurospora crassa is required for normal vegetative growth, ultraviolet survival, and sexual development. Archives of microbiology 199:531-542

Lee Y, Puumala E, Robbins N, Cowen LE (2020) Antifungal drug resistance: molecular mechanisms in Candida albicans and beyond. Chemical reviews 121:3390-3411

Leonard KJ, Bushnell WR (2003) Fusarium head blight of wheat and barley. American Phytopathological Society (APS Press)

Li H, Rao A, Hogan PG (2011) Interaction of calcineurin with substrates and targeting proteins. Trends in cell biology 21:91-103

Liatis T et al. (2021) Brainstem phaeohyphomycosis due to Curvularia lunata (Cochliobolus lunatus) in a cat. Australian veterinary journal 99:273-278

Liew N et al. (2017) Chytrid fungus infection in zebrafish demonstrates that the pathogen can parasitize non-amphibian vertebrate hosts. Nature Communications 8:1-10

Linder KA, Kauffman CA (2021) Current and new perspectives in the diagnosis of blastomycosis and histoplasmosis. Journal of Fungi 7:12

Liu F-f et al. (2015) Calcium signaling mediates antifungal activity of triazole drugs in the Aspergilli. Fungal Genetics and Biology 81:182-190

Maertens JA (2004) History of the development of azole derivatives. Clinical Microbiology and Infection 10:1-10

Mayer FL, Wilson D, Hube B (2013) Candida albicans pathogenicity mechanisms. Virulence 4:119-128

McCluskey K (2003) The fungal genetics stock center. from molds to molecules 52:245-262

McCluskey K, Wiest A, Plamann M (2010) The Fungal Genetics Stock Center: a repository for 50 years of fungal genetics research. Journal of biosciences 35:119-126

McKinnell JA, Pappas PG (2009) Blastomycosis: new insights into diagnosis, prevention, and treatment. Clinics in chest medicine 30:227-239

McLellan GJ, Aquino SM, Mason DR, Kinyon JM, Myers RK (2006) Use of posaconazole in the management of invasive orbital aspergillosis in a cat. Journal of the American Animal Hospital Association 42:302-307

Meis JF, Chowdhary A, Rhodes JL, Fisher MC, Verweij PE (2016) Clinical implications of globally emerging azole resistance in Aspergillus fumigatus. Philosophical Transactions of the Royal Society B: Biological Sciences 371:20150460

Michielse CB, Rep M (2009) Pathogen profile update: Fusarium oxysporum. Molecular plant pathology 10:311

Mielniczki-Pereira AA, Hahn ABB, Bonatto D, Riger CJ, Eleutherio ECA, Henriques JAP (2011) New insights into the Ca2+-ATPases that contribute to cadmium tolerance in yeast. Toxicology letters 207:104-111

Mikoshiba K, Hattori M (2000) IP3 receptor-operated calcium entry. Science's STKE 2000:pe1-pe1

Mishra RP, Singh S, Akil M, Singh P, Gautam K (2022) Risk factors analysis and drugs effective against dermatophytosis in rabbits. Pharma Innov, SP 11:798-800

Miyazaki T et al. (2010) Roles of calcineurin and Crz1 in antifungal susceptibility and virulence of Candida glabrata. Antimicrobial agents and chemotherapy 54:1639-1643

Moriello K (2014) Feline dermatophytosis: aspects pertinent to disease management in single and multiple cat situations. Journal of feline medicine and surgery 16:419-431

Moriello K (2019) Dermatophytosis in cats and dogs: a practical guide to diagnosis and treatment. In Practice 41:138-147

Moriello KA, Coyner K, Paterson S, Mignon B (2017) Diagnosis and treatment of dermatophytosis in dogs and cats. Clinical Consensus Guidelines of the World Association for Veterinary Dermatology. Veterinary dermatology 28:266-e268

Morio F, Loge C, Besse B, Hennequin C, Le Pape P (2010) Screening for amino acid substitutions in the Candida albicans Erg11 protein of azole-susceptible and azole-resistant clinical isolates: new substitutions and a review of the literature. Diagnostic microbiology and infectious disease 66:373-384

Mount HOC et al. (2018) Global analysis of genetic circuitry and adaptive mechanisms enabling resistance to the azole antifungal drugs. PLoS genetics 14:e1007319

Muller EM, Mackin NA, Erdman SE, Cunningham KW (2003) Fig1p facilitates Ca2+ influx and cell fusion during mating of Saccharomyces cerevisiae. Journal of Biological Chemistry 278:38461-38469

Natarajan V, Nath AK, Thappa DM, Singh R, Verma SK (2010) Coexistence of onychomycosis in psoriatic nails: a descriptive study. Indian journal of dermatology, venereology and leprology 76:723

Negre A, Bensignor E, Guillot J (2009) Evidence-based veterinary dermatology: a systematic review of interventions for Malassezia dermatitis in dogs. Veterinary dermatology 20:1-12

Nelson MA, Metzenberg RL (1992) Sexual development genes of Neurospora crassa. Genetics 132:149-162

Niimi M et al. (2004) Regulated overexpression of CDR1 in Candida albicans confers multidrug resistance. Journal of Antimicrobial Chemotherapy 54:999-1006

Nishimoto AT (2019) An Investigation into Clinically Relevant Determinants of Azole Resistance in Candida albicans. The University of Tennessee Health Science Center

Nishimoto AT, Sharma C, Rogers PD (2020) Molecular and genetic basis of azole antifungal resistance in the opportunistic pathogenic fungus Candida albicans. Journal of Antimicrobial Chemotherapy 75:257-270

Odds FC, Brown AJ, Gow NA (2003) Antifungal agents: mechanisms of action. Trends in microbiology 11:272-279

Onyewu C, Blankenship JR, Del Poeta M, Heitman J (2003) Ergosterol biosynthesis inhibitors become fungicidal when combined with calcineurin inhibitors against Candida albicans, Candida glabrata, and Candida krusei. Antimicrobial agents and chemotherapy 47:956-964

Orton ES, Deller S, Brown JK (2011) Mycosphaerella graminicola: from genomics to disease control. Molecular plant pathology 12:413-424

Ou S (1980) Pathogen variability and host resistance in rice blast disease. Annual review of phytopathology 18:167-187

Pais P, Costa C, Pires C, Shimizu K, Chibana H, Teixeira MC (2016) Membrane proteome-wide response to the antifungal drug clotrimazole in Candida glabrata: role of the transcription factor CgPdr1 and the drug: H+ antiporters CgTpo1_1 and CgTpo1_2. Molecular & Cellular Proteomics 15:57-72

Park H-S et al. (2016) Calcineurin targets involved in stress survival and fungal virulence. PLoS pathogens 12:e1005873

Park H-S, Lee SC, Cardenas ME, Heitman J (2019) Calcium-calmodulin-calcineurin signaling: a globally conserved virulence cascade in eukaryotic microbial pathogens. Cell host & microbe 26:453-462

Parker JE, Warrilow AG, Price CL, Mullins JG, Kelly DE, Kelly SL (2014) Resistance to antifungals that target CYP51. Journal of Chemical Biology 7:143-161

Partha ADSL, Widodo ADW, Endraswari PD (2022) Evaluation of fluconazole, itraconazole, and voriconazole activity on Candida albicans: A case control study. Annals of Medicine and Surgery 84:104882

Paul S, Schmidt JA, Moye-Rowley WS (2011) Regulation of the CgPdr1 transcription factor from the pathogen Candida glabrata. Eukaryotic Cell 10:187-197

Perkins DD (1992) Neurospora: the organism behind the molecular revolution. Genetics 130:687

Pfaller MA, Diekema DJ (2010) Epidemiology of invasive mycoses in North America. Critical reviews in microbiology 36:1-53

Pincelli T, Enzler M, Davis M, Tande A, Comfere N, Bruce A (2019) Oropharyngeal histoplasmosis: a report of 10 cases. Clinical and experimental dermatology 44:e181-e188

Pinchai N et al. (2010) The Aspergillus fumigatus P-type Golgi apparatus Ca2+/Mn2+ ATPase PmrA is involved in cation homeostasis and cell wall integrity but is not essential for pathogenesis. Eukaryotic Cell 9:472-476

Pittman JK, Cheng NH, Shigaki T, Kunta M, Hirschi KD (2004) Functional dependence on calcineurin by variants of the Saccharomyces cerevisiae vacuolar Ca2+/H+ exchanger Vcx1p. Molecular microbiology 54:1104-1116

Prasad R, Kapoor K (2005) Multidrug resistance in yeast Candida. International review of cytology 242:215-248

Prasad R, Rawal MK (2014) Efflux pump proteins in antifungal resistance. Frontiers in pharmacology 5:107996

Prusky D (1996) Pathogen quiescence in postharvest diseases. Annual review of Phytopathology 34:413-434

Rad KK, Falahati M, Roudbary M, Farahyar S, Nami S (2016) Overexpression of MDR-1 and CDR-2 genes in fluconazole resistance of Candida albicans isolated from patients with vulvovaginal candidiasis. Current medical mycology 2:24

Raju NB (1992) Genetic control of the sexual cycle in Neurospora. Mycological research 96:241-262

Redmann T, Schildger B (1989) Therapeutic use of enilconazole in broiler chicks with aspergillosis. DTW. Deutsche Tierarztliche Wochenschrift 96:15-17

Revie NM, Iyer KR, Robbins N, Cowen LE (2018) Antifungal drug resistance: evolution, mechanisms and impact. Current opinion in microbiology 45:70-76

Riquelme M et al. (2011) Architecture and development of the Neurospora crassa hypha–a model cell for polarized growth. Fungal biology 115:446-474

Roberson JR, Baird A, Pugh D (2011) Diseases of the integumentary system. Sheep & Goat Medicine-E-Book: Sheep & Goat Medicine-E-Book:256

Roche CM, Loros JJ, McCluskey K, Glass NL (2014) Neurospora crassa: looking back and looking forward at a model microbe. American journal of botany 101:2022-2035

Romano N, Macino G (1992) Quelling: transient inactivation of gene expression in Neurospora crassa by transformation with homologous sequences. Molecular microbiology 6:3343-3353

Roy A, Kumar A, Baruah D, Tamuli R (2021) Calcium signaling is involved in diverse cellular processes in fungi. Mycology 12:10-24

Rusnak F, Mertz P (2000) Calcineurin: form and function. Physiological reviews 80:1483-1521

Sanglard D, Coste AT (2016) Activity of isavuconazole and other azoles against Candida clinical isolates and yeast model systems with known azole resistance mechanisms. Antimicrobial agents and chemotherapy 60:229-238

Sanglard D, Ischer Fo, Calabrese D, Majcherczyk PA, Bille J (1999) The ATP binding cassette transporter gene CgCDR1 from Candida glabrata is involved in the resistance of clinical isolates to azole antifungal agents. Antimicrobial agents and chemotherapy 43:2753-2765

Sanglard D, Kuchler K, Ischer F, Pagani J, Monod M, Bille J (1995) Mechanisms of resistance to azole antifungal agents in Candida albicans isolates from AIDS patients involve specific multidrug transporters. Antimicrobial agents and chemotherapy 39:2378-2386

Sanguinetti M, Posteraro B, Fiori B, Ranno S, Torelli R, Fadda G (2005) Mechanisms of azole resistance in clinical isolates of Candida glabrata collected during a hospital survey of antifungal resistance. Antimicrobial agents and chemotherapy 49:668-679

Schmit JC, Brody S (1976) Biochemical genetics of Neurospora crassa conidial germination. Bacteriological reviews 40:1-41

Scott DW, Miller Jr WH, Griffin CE (2001) Dermatoses of pet rodents, rabbits, and ferrets. Muller & Kirk's Small Animal Dermatology:1415

Seyedmousavi S et al. (2018) Fungal infections in animals: a patchwork of different situations. Medical mycology 56:S165-S187

Seyedmousavi S, Mouton JW, Melchers WJ, Brüggemann RJ, Verweij PE (2014) The role of azoles in the management of azole-resistant aspergillosis: from the bench to the bedside. Drug Resistance Updates 17:37-50

Shapiro RS, Robbins N, Cowen LE (2011) Regulatory circuitry governing fungal development, drug resistance, and disease. Microbiology and molecular biology reviews 75:213-267

Sharma B, Kumar P, Joshi SC (2011) Topical treatment of dermatophytic lesion on mice (Mus musculus) model. Indian journal of microbiology 51:217-222

Sharma B, Nonzom S (2022) Talaromyces stipitatus, a novel agent causing superficial mycosis in a diabetic patient from North India. Microbes and Infection 24:104887

Shear CL, Dodge BO (1927) Life histories and heterothallism of the red bread-mold fungi of the Monilia sitophila group. US Government Printing Office Washington, DC

Shiu PK, Raju NB, Zickler D, Metzenberg RL (2001) Meiotic silencing by unpaired DNA. Cell 107:905-916

Silver PM, Oliver BG, White TC (2004) Role of Candida albicans transcription factor Upc2p in drug resistance and sterol metabolism. Eukaryotic Cell 3:1391-1397

Smith LN, Hoffman SB (2010) A case series of unilateral orbital aspergillosis in three cats and treatment with voriconazole. Veterinary Ophthalmology 13:190-203

Sorin A, Rosas G, Rao R (1997) PMR1, a Ca2+-ATPase in yeast Golgi, has properties distinct from sarco/endoplasmic reticulum and plasma membrane calcium pumps. Journal of Biological Chemistry 272:9895-9901

Springer ML (1993) Genetic control of fungal differentiation: the three sporulation pathways of Neurospora crassa. Bioessays 15:365-374

Springer ML, Yanofsky C (1989) A morphological and genetic analysis of conidiophore development in Neurospora crassa. Genes & development 3:559-571

Sun X et al. (2014) Transcription factor CCG-8 as a new regulator in the adaptation to antifungal azole stress. Antimicrobial agents and chemotherapy 58:1434-1442

Sun X et al. (2013) Sterol C-22 desaturase ERG5 mediates the sensitivity to antifungal azoles in Neurospora crassa and Fusarium verticillioides. Frontiers in Microbiology 4:127

Talazadeh F, Ghorbanpoor M, Shahriyari A (2022) Candidiasis in birds (galliformes, anseriformes, psittaciformes, passeriformes, and columbiformes): a focus on antifungal susceptibility pattern of Candida albicans and non-albicans isolates in avian clinical specimens. Topics in Companion Animal Medicine 46:100598

Tamuli R, Deka R, Borkovich KA (2016) Calcineurin subunits A and B interact to regulate growth and asexual and sexual development in Neurospora crassa. PloS one 11:e0151867

Tamura N et al. (2020) Utility of systemic voriconazole in equine keratomycosis based on pharmacokinetic-pharmacodynamic analysis of tear fluid following oral administration. Veterinary Ophthalmology 23:640-647

Taylor A, Talbot J, Bennett P, Martin P, Makara M, Barrs VR (2014) Disseminated Scedosporium prolificans infection in a Labrador retriever with immune mediated haemolytic anaemia. Medical mycology case reports 6:66-69

Thambugala KM, Daranagama DA, Tennakoon DS, Jayatunga DPW, Hongsanan S, Xie N (2024) Humans vs. Fungi: An Overview of Fungal Pathogens against Humans. Pathogens 13:426

Thewes S (2014) Calcineurin-Crz1 signaling in lower eukaryotes. Eukaryotic cell 13:694-705

Tong Y et al. (2016) Beauvericin counteracted multi-drug resistant Candida albicans by blocking ABC transporters. Synthetic and Systems Biotechnology 1:158-168

Trösken ER et al. (2006) Comparison of lanosterol-14α-demethylase (CYP51) of human and Candida albicans for inhibition by different antifungal azoles. Toxicology 228:24-32

Urbanek AK, Łapińska Z, Derkacz D, Krasowska A (2022) The Role of ERG11 Point Mutations in the Resistance of Candida albicans to Fluconazole in the Presence of Lactate. Pathogens 11:1289

Vale-Silva L, Ischer F, Leibundgut-Landmann S, Sanglard D (2013) Gain-of-function mutations in PDR1, a regulator of antifungal drug resistance in Candida glabrata, control adherence to host cells. Infection and immunity 81:1709-1720

Vermeulen E, Lagrou K, Verweij PE (2013) Azole resistance in Aspergillus fumigatus: a growing public health concern. Current opinion in infectious diseases 26:493-500

Víglaš J, Olejníková P (2023) Antifungal azoles trigger a xenobiotic detoxification pathway and chitin synthesis in Neurospora crassa. Research in Microbiology:104055

Wang K et al. (2015) Transcription factor ADS-4 regulates adaptive responses and resistance to antifungal azole stress. Antimicrobial agents and chemotherapy 59:5396-5404

Wang Z, Daniels JB, Lappin M, Aboellail T, Shropshire S (2023) Sino-orbital aspergillosis with obstructive cervical lymphadenopathy in a cat caused by Aspergillus viridinutans complex. Journal of Feline Medicine and Surgery Open Reports 9:20551169231181863

Whaley SG, Berkow EL, Rybak JM, Nishimoto AT, Barker KS, Rogers PD (2017) Azole antifungal resistance in Candida albicans and emerging non-albicans Candida species. Frontiers in microbiology 7:231851

White TC (1997) Increased mRNA levels of ERG16, CDR, and MDR1 correlate with increases in azole resistance in Candida albicans isolates from a patient infected with human immunodeficiency virus. Antimicrobial agents and chemotherapy 41:1482-1487

Williamson B, Tudzynski B, Tudzynski P, Van Kan JA (2007) Botrytis cinerea: the cause of grey mould disease. Molecular plant pathology 8:561-580

Wray JD, Sparkes AH, Johnson EM (2008) Infection of the subcutis of the nose in a cat caused by Mucor species: successful treatment using posaconazole. Journal of feline medicine and surgery 10:523-527

Wyand RA, Brown JK (2003) Genetic and forma specialis diversity in Blumeria graminis of cereals and its implications for host-pathogen co-evolution. Molecular plant pathology 4:187-198

Xiang M-J et al. (2013) Erg11 mutations associated with azole resistance in clinical isolates of Candida albicans. FEMS yeast research 13:386-393

Xiao L, Madison V, Chau AS, Loebenberg D, Palermo RE, McNicholas PM (2004) Three-dimensional models of wild-type and mutated forms of cytochrome P450 14α-sterol demethylases from Aspergillus fumigatus and Candida albicans provide insights into posaconazole binding. Antimicrobial agents and chemotherapy 48:568-574

Xue W et al. (2019) Transcription factor CCG-8 plays a pivotal role in azole adaptive responses of Neurospora crassa by regulating intracellular azole accumulation. Current genetics 65:735-745

Yin Y et al. (2021a) Fungal Zn (II) 2Cys6 transcription factor ADS-1 regulates drug efflux and ergosterol metabolism under antifungal azole stress. Antimicrobial Agents and Chemotherapy 65:10.1128/aac. 01316-01320

Yin Y et al. (2021b) Fungal Zn (II) 2Cys6 Transcription Factor ADS-1 Regulates Drug Efflux and Ergosterol Metabolism under Antifungal Azole Stress. Antimicrobial Agents and Chemotherapy 65:e01316-01320

Yona AH, Frumkin I, Pilpel Y (2015) A relay race on the evolutionary adaptation spectrum. Cell 163:549-559

Zadoks J (1985) Cereal rusts, dogs and stars in antiquity. Cereal Rusts Bulletin 13:1-10

Zelter A, Bencina M, Bowman BJ, Yarden O, Read ND (2004) A comparative genomic analysis of the calcium signaling machinery in Neurospora crassa, Magnaporthe grisea, and Saccharomyces cerevisiae. Fungal Genetics and Biology 41:827-841

Zeng W, Mak D-OD, Li Q, Shin DM, Foskett JK, Muallem S (2003) A new mode of Ca2+ signaling by G protein-coupled receptors: gating of IP3 receptor Ca2+ release channels by Gβγ. Current Biology 13:872-876

Zhang J, Heitman J, Chen Y-L (2012a) Comparative analysis of calcineurin signaling between Candida dubliniensis and Candida albicans. Communicative & Integrative Biology 5:122-126

Zhang J et al. (2012b) Calcineurin is required for pseudohyphal growth, virulence, and drug resistance in Candida lusitaniae.

Zhang Y et al. (2012c) CDR4 is the major contributor to azole resistance among four Pdr5p-like ABC transporters in Neurospora crassa. Fungal biology 116:848-854

Zhou M et al. (2022) Experimental Evolution of Multidrug Resistance in Neurospora crassa under Antifungal Azole Stress. Journal of Fungi 8:198

Chapter 2

Materials and Methods

2.1. Materials

2.1.1. Laboratory chemicals and other materials

All chemicals and reagents used in this study are listed in Table 2.1. The glassware used was primarily from Borosil (Mumbai, India) and Jain Scientific Glassworks (Ambala, India). Plasticwares were primarily obtained from Genaxy (New Delhi, India) and Tarsons (Kolkata, India).

Table 2.1. List of the chemicals and reagents used in this study

Sl. No.	Chemical/ Reagent	Chemical formula	Make	Catalogue No.
1	Absolute ethanol	C_2H_5OH	MERCK	1.00983.0511
2	Agarose	N/A	Invitrogen	16500-500
3	D-Biotin	$C_{10}H_{16}N_2O_3S$	SRL	248120
4	Bromophenol blue	$C_{19}H_{10}Br_4O_5S$	SRL	240168
5	Cetyltrimethyl ammonium bromide (CTAB)	$C_{19}H_{42}BrN$	Amresco	0833-500G
6	Chloroform	$CHCl_3$	SRL	328101
7	Diethyl pyrocarbonate (DEPC)	$C_6H_{10}O_5$	SRL	46791
8	Dimethyl sulfoxide (DMSO)	C_2H_6OS	MERCK	109678

9	Ethidium bromide (EtBr)	$C_{21}H_{20}BrN_3$	SRL	54817
10	EDTA	$C_{10}H_{16}N_2O_8$	SRL	18240
11	Fluconazole	NA	HIMEDIA	SD232-5VL
12	Formaldehyde	CH_2O	SRL	AS017-500ML
13	Glacial acetic acid	CH_3COOH	MERCK	1.93402.0521
14	D-Glucose	$C_6H_{12}O_6$	SRL	42738
15	Glycerol (glycerin) anhydrous	$C_3H_8O_3$	SRL	72929
16	Hydrochloric acid	HCl	HIMEDIA	AS003-500ML
17	Hydrogen peroxide	H_2O_2	MERCK	6.2E+13
18	Hygromycin B	N/A	HIMEDIA	PCT1503-20ML
19	HEPES buffer	$C_8H_{18}N_2O_4S$	SRL	84023
20	Isopropanol	C_3H_7OH	SRL	92956
21	Itraconazole	NA	HIMEDIA	SD221-5VL
22	Ketoconazole	NA	HIMEDIA	SD224-5VL
23	Lithium chloride	LiCl	SRL	124919
24	Methanol	CH_3OH	HIMEDIA	AS058-500ML
25	*β*-Mercaptoethanol	C_2H_6OS	SRL	1324196

26	MOPS buffer	$C_7H_{15}NO_4S$	HIMEDIA	RM660-100G
27	Phenol: Chloroform: Isoamyl alcohol (25:24:1)	N/A	SRL	69031
28	Sodium dodecyl sulfate (SDS)	$NaC_{12}H_{25}SO_4$	SRL	194821
29	SYBR Green Real-Time PCR Mix	N/A	Life Technologies	4472903
30	Taq DNA Polymerase	N/A	NEB	M0273S
31	Tris Base	$C_4H_{11}NO_3$	RANKEM	T0350
32	TRIzol™ reagent	N/A	Invitrogen	1.6E+07
33	High-Capacity cDNA Reverse Transcription Kits	N/A	Thermo Fisher Scientific	4368813

Not Applicable (N/A): Chemical formula is not available.

2.1.2. *N. crassa* strains

The *N. crassa* strains used in this study were procured from the Fungal Genetics Stock Centre (FGSC; University of Missouri, Kansas City, MO 64110; McCluskey et al. 2010). Additional *N. crassa* strains were received from the laboratory of Prof. Katherine A. Borkovich, University of California Riverside, USA, and also generated at our laboratory (Table 2.1). The *erg-3*^{RIP} mutant was gifted by Prof. Durgadas P. Kasbekar, Centre of Cellular and Molecular Biology, Hyderabad.

Table 2.2. The *N. crassa* strains used in this study

Sl. No.	Strain	Strain type or NCU No.	Genotype	Reference
1	74-OR23-IVA	Wild Type	wild type; *mat A*	FGSC 2489
2	ORS-SL6a	Wild Type	wild type; *mat a*	FGSC 4200
3	24 a	Homokaryotic, RIP strain	Δ*cna-1::hph;* Δ*pan-2::Pccg-1::Cna-1*^{RIP}*::5xGly::V5::gfp; mat a*	Our laboratory (Kumar et al., 2020)
4	28 A	Homokaryotic, RIP strain	Δ*cna-1::hph;* Δ*pan-2::Pccg-1::Cna-1*^{RIP}*::5xGly::V5::gfp; mat A*	Our laboratory (Kumar et al., 2020)
5	122 A	Homokaryotic, RIP strain	Δ*pan-2::Pccg-1::Cna-1*^{RIP}*::5xGly::V5::gfp; mat A*	Our laboratory (Kumar et al., 2020)
6	Δ*pmr-1 a*	NCU03292	Δ*pmr-1 a*	FGSC 11616

2.1.3. Reagents, commonly used solutions, and media

1. **0.5 M EDTA (pH 8.0):** To prepare a 0.5 M EDTA solution, 18.61 g of EDTA was dissolved in 50 ml of distilled water. The pH was adjusted to 8.0 using NaOH, then the volume was brought to 100 ml with distilled water. The solution was sterilized by autoclaving and stored at room temperature.
2. **Diethylpyrocarbonate (DEPC):** To prepare a 0.1% DEPC solution, 1 ml of DEPC was added to 999 ml of sterile distilled water and subsequently sterilized by autoclaving.
3. **Ethidium bromide (EtBr):** To prepare a stock solution of EtBr (10 mg/ml), 20 mg EtBr was dissolved in 2 ml of distilled water.

4. **1 M Tris-HCl (pH 7.5)**: To prepare a 1 M Tris-HCl solution (pH 7.5), 12.11 g of Tris base was dissolved in 70 ml of distilled water. The pH was adjusted to 7.5 using HCl, and the volume was brought up to 100 ml with distilled water. The solution was then sterilized by autoclaving.
5. **1 M Tris-HCl (pH 8.0):** To prepare a 1 M Tris-HCl solution (pH 8.0), 12.11 g of Tris base was dissolved in 70 ml of distilled water. The pH was adjusted to 8.0 using HCl, and the volume was brought up to 100 ml with distilled water, and the solution was then sterilized by autoclaving.
6. **5 M NaCl:** To prepare 5 M NaCl, 29.22 g of NaCl was dissolved in 80 ml of distilled water, then the final volume was adjusted to 100 ml, and sterilized by autoclaving.
7. **1 M LiCl:** To prepare 1 M LiCl, 0.4239 g of LiCl was dissolved in 5 ml of sterile distilled water; further, the final volume was adjusted to 10 ml, and sterilized by autoclaving.
8. **8 M LiCl:** To prepare 8 M LiCl, 33.9 g of LiCl was dissolved in 50 ml of DEPC-treated sterile distilled water; further, the final volume was adjusted to 100 ml, and sterilized by autoclaving.
9. **2 N NaOH:** To prepare 2 N NaOH, 8 g of NaOH pellet was dissolved in 50 ml of DEPC-treated water; further, the final volume was adjusted to 100 ml and sterilized by autoclaving.
10. **10 N NaOH:** 10 N NaOH was prepared by slowly dissolving 40 g of NaOH pellet in 80 ml of distilled water; further, the final volume was adjusted to 100 ml with distilled water and stored at room temperature.
11. **10% SDS:** To prepare 10 % SDS, 1 g of SDS was dissolved in 5 ml sterile double-distilled water while stirring and heating at 65°C. The final volume was adjusted to 10 ml and stored at room temperature.
12. **3 M Sodium-acetate (pH 5.2):** To prepare a 3 M sodium acetate solution (pH 5.2), 24.61 g of sodium acetate was dissolved in 70 ml of DEPC-treated water. The pH was adjusted to 5.2 using glacial acetic acid, and the final volume was brought up to 100 ml with DEPC-treated water. The solution was then sterilized by autoclaving.
13. **50X TAE:** To prepare 50X TAE stock solution, 24.2 g of Tris base was dissolved in 50 ml of distilled water, 5.71 ml of glacial acetic acid, and 10 ml of 0.5 M EDTA (pH 8.0) were added; further, the final volume was adjusted to 100 ml. The solution was stored at 4 °C.

15. **1X TE buffer:** To prepare 1000 ml of 1X TE buffer, 10 ml of 100X TE stock solution was added to 990 ml of deionized water, and the solution was mixed thoroughly to ensure uniformity. The final concentrations in the 1X TE buffer are 10 mM Tris-HCl (pH 8.0) and 1 mM EDTA (pH 8.0). The dilution ratio used is 1:100, meaning that 1 part of the 100X stock was diluted into a total of 100 parts to obtain the working solution. The 100X TE buffer was prepared by measuring 10 ml of 1 M Tris-HCl (pH 8.0) and 2 ml of 0.5 M EDTA (pH 8.0). The components were mixed thoroughly, and deionized water was added to bring the total volume to 100 ml. The prepared 100X TE buffer was stored at room temperature or 4°C for long-term use.
16. **6X Gel-loading Buffer (Type III):** To prepare 6X Gel-loading Buffer (Type III), 0.25 g of bromophenol blue (0.25% w/v), 0.25 g of xylene cyanol FF (0.25% w/v), and 30 ml of glycerol (30% v/v) were dissolved in sterile distilled water, and the final volume was adjusted to 100 ml. The buffer was thoroughly mixed and stored in 500 µl aliquots at 4 °C for long-term use.
17. **0.5 M PIPES buffer (pH 6.7):** To prepare a 0.5 M PIPES buffer (pH 6.7), 1.5 g of PIPES was dissolved in 5 ml of sterile distilled water. The pH was adjusted to 6.7 using 10 N NaOH solution, and the final volume was brought up to 10 ml. The solution was sterilized using a 0.45 µm syringe filter (Himedia, SF182E) and stored at −20 °C.
18. **10X MOPS electrophoresis buffer:** To prepare a 10X MOPS stock solution, dissolve 4.18 g of MOPS in 40 ml of DEPC-treated water. The pH was adjusted to 7.0 using 2 N NaOH. Then, 2 ml of 1 M sodium acetate solution (final concentration of 20 mM) and 2 ml of 0.5 M EDTA, pH 8.0 (final concentration of 10 mM), were added. The final volume was adjusted to 100 ml with DEPC-treated water. Subsequently, the solution was filter-sterilized using a 0.45 µm syringe filter (Himedia, SF182E) and stored in the dark at room temperature.
19. **Alkaline lysis Solution I:** The alkaline lysis solution I contains 50 mM glucose, 25 mM Tris-Cl (pH 8.0), and 10 mM EDTA (pH 8.0); the solution was sterilized by autoclaving and stored at 4 ºC.
20. **Alkaline lysis Solution II:** The alkaline lysis Solution II contains 0.2 N NaOH and 1% SDS, and this solution was freshly prepared before use.
21. **Alkaline lysis Solution III:** The alkaline lysis Solution III was prepared by adding 60 ml of 5 M potassium acetate and 11.5 ml of glacial acetic acid, the final volume

was adjusted to 100 ml by adding distilled water. The solution was sterilized by autoclaving and stored at 4°C.

22. **Lysis buffer for RNA isolation from *N. crassa*:** The lysis buffer for the isolation of RNA from *N. crassa* contained 100 mM Tris HCl (pH 8.0), 0.6 M NaCl, 10 mM EDTA (pH 8.0), 4.5 % SDS, and 2 % β-Mercaptoethanol, this solution is freshly prepared before use.
23. **Inoue transformation buffer:** The Inoue transformation buffer (Inoue et al. 1990) contains 55 mM $MnCl_2$, 15 mM $CaCl_2$, 250 mM KCl, and 10 mM PIPES buffer (pH 6.7).

2.1.4. Solutions for growth, maintenance, and crossing of *N. crassa* strains

i. Biotin solution: Biotin solution was prepared by dissolving 5 mg biotin in 100 ml 50% (v/v) ethanol and stored at 4°C.

ii. L-Histidine: From a L-Histidine stock solution of 50 mg/ml in sterile water, 2 ml per 100 ml of medium was added. The stock solution of L-Histidine was autoclaved and stored at 4 °C.

iii. Trace element solution: To prepare the trace element solution, the following chemicals are sequentially dissolved in 80 ml of distilled water while stirring. The final volume was then adjusted to 100 ml. Then, 1 ml of chloroform is added as a preservative, and the solution is stored at 4 °C.

Trace element component	Amount
$C_6H_8O_7.H_2O$	5.00 g
$ZnSO_4.7H_2O$	5.00 g
$Fe(NH_4)_2(SO_4)_2.6H_2O$	1.00 g
$CuSO_4.5H_2O$	0.25 g
$MnSO_4.H_2O$	0.05 g
H_3BO_3	0.05 g
$Na_2MoO_4.2H_20$	0.05 g

iv. Vogel's Medium N (VGN): A 50X stock solution of Vogel's Medium N (Vogel 1964) was prepared by sequentially adding the following chemicals in distilled water while stirring. Further, the final volume was adjusted to 100 ml. Chloroform was added as a preservative and stored at 4 °C.

Chemicals	**100 ml stock (50 X) (To 75 ml of distilled water, the following ingredients were added in order, dissolving each one prior to the addition of the next)**
Na_3citrate.$5H_2O$	12.67g
KH_2PO_4	25g
NH_4NO_3	10g
$MgSO_4.7H_2O$	1g
$CaCl_2.2H_2O$ (pre-dissolved in 20 ml H2O)	0.5 g
Biotin solution	500 µl
Trace element solution	500 µl

VG medium	
Vogel's Medium N	1X
Glucose	1.5% (w/v)

Vogel's glucose agar (VGA) medium	
Vogel's Medium N	1X
Glucose	1.5% (w/v)
Agar	2 % (w/v)

Table 2.3. Azole drugs used in this study

Sl. No.	Azole drug	Chemical structure	
		3D	**2D**
1	Fluconazole	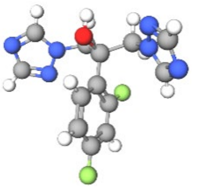	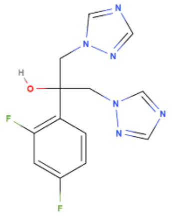
2	Itraconazole	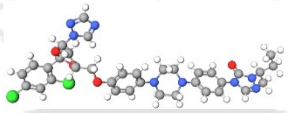	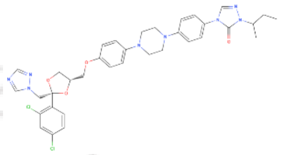
3	Ketoconazole	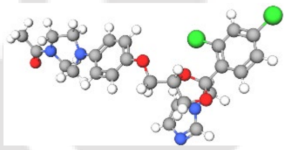	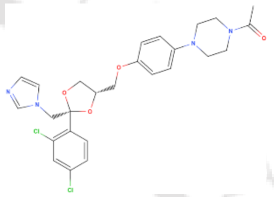

2.1.5. Primers used in this study

The custom oligonucleotide primers used in this study were procured from Bioserve Biotechnologies (India) Pvt. Ltd., Hyderabad, India, and Integrated DNA Technologies (Iowa, USA).

Table 2.4. List of primers used in this study

Sl. No.	Primer name	Sequence (5′→ 3′)
1	Calcineurin forward	CACCTTCAAGCTCGAGTGCA
2	Calcineurin reverse	GATGTCGTCGAGAGTGTGGA
3	*pmr-1* forward	CATGGCAAAGCATAACGCCA
4	*pmr-1* reverse	TCGTCGGTACCGAAAAACCA
5	Tubulin forward	CCCAAGAACATGATGGCTGC
6	Tubulin reverse	TTGTTCTGAACGTTGCGCATC

2.2. Methods

2.2.1. Growth conditions

The growth and maintenance of *N. crassa* strains were carried out essentially as described previously (Davis and de Serres 1970). For vegetative growth, the strains were routinely cultured on 1X Vogel's minimal medium N (Vogel 1956; Vogel 1964). For the growth of the pantothenate auxotrophic strain, the media were supplemented with Calcium-D-pantothenate at a final concentration of 0.01 mg/ml (http://www.fgsc.net/methods/stanford.html).

2.2.2. Determination of minimum inhibitory concentration

The minimum inhibitory concentration (MIC) was determined by performing a series of dilutions of the azoles in a VG liquid culture medium. The antifungals drugs fluconazole, itraconazole, and ketoconazole were procured from the standard source (Himedia, India). The stock concentration of 12 µg/ml was prepared as previously described (Rodriguez-Tudela et al. 2008) . For the inoculum preparation, *N. crassa* strains were pre-cultured on VG medium for three days at 30 °C in the dark and for additional four days at room temperature under light. Then conidia were harvested in sterile distilled water, and then ~1x10^6 conidia were inoculated in the VG medium supplemented with azole drugs and cultured for three days in the dark at 30 °C.

2.2.3. Drug susceptibility assay

A drug susceptibility assay is a laboratory test recommended by the Clinical and Laboratory Standards Institute (CLSI, Pennsylvania, USA) to evaluate the susceptibility of fungal strains to a particular antifungal drug (Berkow et al. 2020). To determine the azole drug susceptibility of *N. crassa* strains, an assay was performed by adding azole drugs to the VG agar medium. The strains were cultured on VG agar medium containing different concentrations of azole for itraconazole, fluconazole, and ketoconazole at half of their MIC. Conidia from the *N. crassa* wild type, *Cna-1*^{RIP} 24 a and 122 A, and Δ*pmr-1* mutant strains were harvested, and ~1 × 10^6 conidia were inoculated at the center of the VG agar plates containing the indicated azole drug. The plates were then incubated at 30 °C for 24 h.

2.2.4. Hyphal morphology assay

To investigate the hyphal morphology of the *N. crassa* strains, VG agar medium was supplemented with fluconazole (0.25 µg/ml), itraconazole (1.5 µg/ml), and ketoconazole (0.5 µg/ml) at half of their respective MIC values. The samples were incubated at 30 °C for 12 to 16 h, then examined under a stereomicroscope (Leica S9i stereomicroscope; Leica Microsystems, Wetzlar, Germany), and images were captured.

2.2.5. Isolation and analysis of ergosterol profile

To isolate ergosterol, *N. crassa* strains were cultured in VG liquid medium, supplemented with the azole drugs fluconazole, itraconazole, and ketoconazole or without the azole supplements (control), and incubated at 30 °C in the dark for 3 days. The mycelial mass was then collected via vacuum filtration, lyophilized, and ground to a powder using a mortar and pestle with 0.2 mm diameter glass beads. Approximately 50 mg of powdered mycelia was mixed with 750 µl each of methanol and chloroform in a 1.5 ml microcentrifuge tube and agitated on a rotary shaker overnight. The mycelial mass was removed by centrifugation at 12,000 rpm for 10 minutes. The chloroform-methanol extract was then washed once with 0.9% NaCl and twice with 2 M KCl. The aqueous and organic layers were separated, and the bottom organic layer was transferred to a new microcentrifuge tube. After air-drying, the sterols in the organic layer were dissolved in ~20 µl of chloroform, diluted to 1:200 in ethanol. The ultraviolet (UV) absorption spectrum (200 to 300 nm) of the isolated ergosterol was recorded using a UV-visible spectrophotometer (Cary 100 Bio UV-visible spectrophotometer, Agilent Technologies, USA).

2.2.6. Determination of ROS level

Intracellular reactive oxygen species (ROS) production in *N. crassa* strains in response to azole drugs (fluconazole, itraconazole, and ketoconazole) was quantified using 2',7'-dichlorodihydrofluorescein diacetate (DCFH-DA), a dye that fluoresces green upon oxidation by ROS (Oiki et al. 2022). Azole-treated conidia from the *N. crassa* strains were incubated with 25 µM of DCFH-DA for 1 h at 37 °C. The fluorescence intensity, indicative of ROS levels, was measured using a fluorescence microplate reader (Infinite 200 Pro, Tecan, Austria).

2.2.7. Gene Expression Analysis

To study the expression of the *cna-1* and *pmr-1* genes, conidial suspensions of ~1 × 10^6 conidia/ml were inoculated in 100 ml conical flasks containing 25 ml of VG liquid medium supplemented with azole drugs. The cultures were incubated in the dark at 30 °C with shaking at 180 rpm for 48 h. Total RNA was isolated from 150 mg of mycelial mass using TRIzol reagent (Cat. No. 15596018, Life Technology, Invitrogen, USA), and then converted into cDNA using the High-Capacity cDNA Reverse Transcription Kit (Cat No. 4368814, Thermo Scientific, USA) following the manufacturer's protocol. The quantitative real-time PCR (qRT-PCR) was performed to analyze the expression profiles of the *cna-1* and *pmr-1* genes using specific primers (Table 2.4). The qRT-PCR was performed using SYBR Green I dye (Rentería-Solís et al. 2020) and an Agilent Real-Time PCR machine (AriaMx, Agilent, USA). The expression levels of *cna-1* and *pmr-1* were analyzed with and without the treatments of fluconazole, itraconazole, and ketoconazole. Relative expression levels, normalized to the untreated control, were used to measure fold changes. The expression of the housekeeping gene *β-tubulin* was used as the endogenous control. Gene expression levels were calculated using the $2^{-\Delta\Delta CT}$ method (Livak and Schmittgen 2001), and relative expression was normalized to the *β-tubulin* expression. Error bars represent the standard deviations of three independent experiments ($n = 3$), statistical significance was assessed using ANOVA, with an asterisk indicating significant results. P-values are provided below the figures, where applicable. The PCR cycling program began with an initial denaturation at 95 °C for 10 minutes, followed by 40 cycles of amplification: 5 seconds at 95 °C for denaturation, 20 seconds at 60 °C for annealing, and 30 seconds at 95 °C for extension, with data acquisition at 60 °C for 1 minute. A final step at 95 °C for 30 seconds concluded each cycle. The fluorescence signal was collected at the end of each 95 °C step, and the cycle threshold (*CT*) value, indicating the point at which the fluorescence signal surpassed a predefined threshold, was automatically determined using the Agilent Real-Time PCR machine (AriaMx, Agilent, USA),

2.2.8. Chlortetracycline Hydrochloride (CTC) Assay

To visualize the intracellular distribution of Ca^{2+} in response to fluconazole treatment in *N. crassa*, strains were cultured on VG agar medium for 12 hours in the dark at 30 °C. The 12-hour-growing hyphae were then supplemented with 200 µM chlortetracycline hydrochloride (CTC) in 0.1% dimethyl sulfoxide (DMSO). The CTC fluorescence was observed using a Nikon ECLIPSE E200 trinocular inverted fluorescence microscope (Nikon, Japan) equipped with DAPI filters and an exposure time of 300−400 ms.

2.2.9. Field Emission Scanning Electron Microscope (FESEM) Analysis

To visualize the conidia and hyphae of *N. crassa* mutant strains using a field emission scanning electron microscope (FESEM), the samples were heat-fixed onto glass coverslips. A thin layer of gold was then sputter-coated onto the samples. The coated samples were loaded into a field emission scanning electron microscope (Gemini 300, Carl Zeiss, Germany). The surface of the samples was scanned by a beam of electrons, and the emitted electrons were collected by a detector to form an image of the surface morphology of the hyphae.

2.2.10. Data Source, Preparation of Ligands, and Target Proteins for Docking

The 3D structure files (sdf format) for the azole drugs fluconazole, ketoconazole, and itraconazole were obtained from the PubChem database (https://pubchem.ncbi.nlm.nih.gov/). These sdf files were then converted to mol2 format using Open Babel (http://openbabel.org/), followed by conversion to pdbqt format using AutoDockTools 1.5.7 (http://autodock.scripps.edu/) and Raccoon (https://autodock.scripps.edu/resources/raccoon/). The protein sequences for the serine/threonine-protein phosphatase 2B catalytic subunit CNA-1 (NCU03804), CNB-1 (NCU03833), and Ca^{2+} transporting ATPase PMR-1 (NCU03292) were retrieved from the FungiDB database (https://fungidb.org/fungidb/app) and are also available in the NCBI database under the accession numbers XP_011394598.1, XP_009848222.1 and XP_964218.1, respectively. The 3D structures of CNA-1, CNB-1, and PMR-1 were generated using the I-TASSER server (https://zhanggroup.org/I-TASSER/). CNA-1 was modeled using the crystal structures of calcineurin proteins from *Homo sapiens* (PDB ID: 1AUI|A), *Rattus norvegicus* (PDB ID: 4IL1|A), and *Cryptococcus neoformans var. grubii* H99 (PDB ID: 6TZ8|A), which share sequence identities of 71%, 66%, and 84% with *N. crassa* CNA-1, respectively. The CNB-1 protein showed 88% and 70% sequence identities, respectively, with the crystal structure of *Coccidioides immitis* calcineurin (RS PDB ID: 5B8I) and crystal structure of *Cryptococcus neoformans* Calcineurin B (PDB ID 6TZ8). The PMR-1 structure was modeled using crystal structures of the sodium-potassium pump from *Sus scrofa* (PDB ID: 3KDP|A), WT transporter state 1 protein from *Homo sapiens* (PDB ID: 7E7S|A), and the gastric proton pump from *Sus scrofa* (PDB ID: 7W4A|A), which show sequence identities of 30%, 33%, and 30%, respectively, with the *N. crassa* PMR-1 protein. The modeled protein structures were validated using Ramachandran plots (Sobolev et al. 2020) generated by the VADAR 1.8 server (http://vadar.wishartlab.com/). Superimposition of the modeled CNA-1, CNB-1, and PMR-1 proteins with their respective protein templates was performed using UCSF Chimera (https://www.cgl.ucsf.edu/chimera/docs/credits.html). Energy minimization of the proteins was conducted using Swiss PDB Viewer software (https://spdbv.unil.ch/) (Guex and Peitsch 1997). The modeled CNA-1, CNB-1, and PMR-1 proteins were further optimized for molecular docking using AutoDock Tools (Morris et al. 1998; Huey and Morris 2008; Umesh et al. 2022). For subsequent analyses, the ligands were optimized and converted from mol2 to pdbqt format (Kundu et al. 2021; Umesh et al. 2022) using the graphical user interface version of Raccoon (https://autodock.scripps.edu/resources/raccoon/), which is integrated into MGLTools-1.5.6, a Python-based AutoDock virtual screening tool (Huey et al. 2012).

2.2.11. Molecular Docking Using Raccoon and AutoDock Tools 1.5.7

Molecular docking studies of azole drug compounds were conducted using AutoDock Tools (ADT) and Raccoon software (Morris et al. 2009). In these studies, the drug ligands were treated as flexible molecules, whereas the protein structures were considered rigid. Key components in the docking process were included in the generation of docking parameter files (.dpf) and grid parameter files (.gpf) through AutoDock4 (Huey and Morris 2008). The grid boxes were configured to target a single active site per docking run, with the grid parameters to identify amino acid residues in the active site of the protein that interacted with the drug ligands. For this study, the grid coordinates (X, Y, Z) were set at 99.997, 79.857, and 97.201 for CNA-1, 54.254, 54.441, and 63.83 for CNB-1, and 95.606, 93.629, and 80.296 for PMR-1. The ligand with the highest binding affinity was identified by its most negative binding energy. The docking sites were visually analyzed using UCSF Chimera and LigPlot (Wallace et al. 1995). The results were validated using ADT (Morris et al. 1998). The LigPlot analysis was further utilized to examine the interactions between the azole inhibitors and the CNA-1 and PMR-1 proteins.

2.2.12. Molecular dynamic simulation studies

Molecular dynamics (MD) simulations were conducted to investigate the interactions between target proteins and an azole drug using GROMACS 2018.1 (Van Der Spoel et al. 2005). The necessary topology files were generated using the CHARMM-GUI server (https://charmm-gui.org/). To maintain system neutrality, appropriate cations (Na^+) or anions (Cl^-) were added to solvate the protein-ligand complex at a salt concentration of 0.15 mol/l. The simulations were conducted under physiological conditions, with the temperature set to 300 K and the pressure to 1 atmospheric unit. A 50-nanosecond (ns) MD simulation was performed, starting with NVT thermal equilibration, followed by NPT equilibration, maintaining the same temperature. The quality and stability of the simulations were evaluated using standard MD parameters. The radius of gyration (Rg) was used to measure protein compactness, while root mean square deviation (RMSD) plots were used to monitor the stability of the ligand within the binding site in the protein. Root-mean-square fluctuation (RMSF) highlighted flexible regions of the protein, and hydrogen bond analysis assessed specific interactions between the ligand and protein. The entire computational workflow was facilitated using the GROMACS software (Pronk et al. 2013), allowing for a comprehensive analysis of simulation dynamics and protein-ligand interactions. The results were meticulously analyzed and visualized using QtGrace version 0.2.6 (https://osf.io/82n73/wiki/QtGrace%20Guide/). Binding affinities and binding energies of the protein-ligand complex were evaluated with a particular focus on hydrogen bond interactions to ensure the stability of the drug-receptor complex. The visualization of intermolecular interactions was performed using Ligplot and UCSF Chimera. After the simulations, hydrogen bonds were analyzed using GROMACS, and trajectory snapshots were stored every picosecond (ps) for structural analysis.

2.2.13. Analyses and Visualization

Docking sites were visually analyzed using UCSF Chimera and Ligplot, with results validated using AutoDock Tools (Morris et al. 1998). The Ligplot analysis (Wallace et al. 1995) was used to scrutinize binding interactions, focusing on the identification of inhibitors and their interactions with the PMR-1, CNA-1, and CNB-1 proteins.

Table 2.5: The structure of the phytochemical compounds obtained from the PubChem database

Sl. No.	Phytochemical compounds	PubChem ID
1	Kaempferol	5280863
2	Isorhamnetin	5281654
3	Myricetin	5281672
4	Dillenetin	5487855
5	Quercetin	5280343
6	Naringenin	439246
7	Betulinaldehyde	99615
8	Betulin	72326
9	Lupeol	259846
10	Betulinic acid	64971
11	Stigmasterol	5280794

2.2.14. Absorption, Distribution, Metabolism, Excretion, and Toxicity (ADMET) Prediction

The ligands exhibiting high binding affinity and docking within the modeled protein were further subjected to ADME profiling using SwissADME tool (Daina et al. 2017). The determination of drug-likeness based on Lipinski's and Veber's rules was also conducted using the Swiss ADME. To design rational drugs, a careful evaluation of the Lipinski's rule of five (Lipinski et al. 2012) is essential, and the SwissAdme server was employed to verify adherence to Lipinski's rules. I used structure data files and simplified molecular data input formats to evaluate how drugs are absorbed, distributed, metabolized, excreted, and their toxicity. These files provided the input for assessing ADMET values in terms of absorption, distribution, metabolism, excretion, and toxicity.

2.3. Databases and software programs used in this study

1. **Autodocktool-1.5.7 (ADT):** AutoDockTools (ADT) version 1.5.7 is a graphical user interface (GUI) that facilitates the docking of ligands to their receptor molecules, proteins (Morris et al. 2009).
2. **Basic Local Alignment Search Tool (BLAST):** The BLAST program (Altschul et al. 1990; Altschul et al. 1997) was used to compare nucleotide or protein sequences to the reference sequence databases. This is available at http://blast.ncbi.nlm.nih.gov/Blast.cgi.
3. **Graph Pad Prism:** It is a software used for data organization, statistical analysis, and scientific graphing.
4. **GROMACS 2018.1**: In bioinformatics studies, particularly for molecular dynamics (MD) simulations, GROMACS 2018.1 is used to investigate the interactions between the target proteins and azole drugs due to its suitability for studying biological macromolecules (Van Der Spoel et al. 2005).
5. **ImageJ/Fiji:** The ImageJ/Fiji is an open-source platform for biological image processing and analysis. This is available online at https://imagej.net/software/fiji/ (Schindelin et al. 2012) .
6. **I-TASSER:** The Iterative Threading ASSEmbly Refinement (I-TASSER) is an online approach to protein structure prediction and structure-based function identification (Yang and Zhang 2015; Zheng et al. 2021). This is available online at https://zhanggroup.org/I-TASSER/.

7. **Jalview:** This is a bioinformatics tool used for multiple sequence alignment analysis, visualization, and editing (https://www.jalview.org/download/).
8. **FungiDB:** The *N. crassa* genome databases, genome resource for *Neurospora* is available at http://fungidb.org.
9. **FGSC:** The web site for Fungal Genetics Stock Center is http://www.fgsc.net/.
10. **Ligplot analysis**: The Ligplot (Wallace et al. 1995) was used to analyze binding interactions, focusing on the identification of inhibitors and their interaction with the proteins PMR-1, CNA-1, and CNB-1 proteins.
11. **MGLTools-1.5.6:** A Python-based AutoDock virtual screening tool (Huey and Morris 2008).
12. **Multiple sequence alignment (MSA):** To align sequences of unknown structure with sequences of known structure was performed by using (https://www.ebi.ac.uk/jdispatcher/msa/clustalo). This alignment is vital in building homology models of proteins.
13. **NCBI/EMBL:** The online servers of the National Center for Biotechnology Information (NCBI) and European Molecular Biology Laboratory (EMBL)) were used to retrieve the primary sequence of proteins or nucleic acid. These are available online, NCBI at http://www.ncbi.nlm.nih.gov/, and EMBL at http://embl.org/.
14. **Open Babel:** Open Babel is an open-source chemical toolbox that standardizes chemical data by converting it to widely accepted formats. It can perform basic molecular mechanics optimization to improve the geometry of molecular structures (https://openbabel.org/docs/GUI/GUI.html). Open Babel helps in preparing input files for further computational docking studies.
15. **Pubchem:** PubChem provides a large repository of chemical information, including structures and properties for numerous compounds. This comprehensive database is essential for retrieving detailed chemical information for new drug discovery (https://pubchem.ncbi.nlm.nih.gov/).
16. **PyMol**: The PyMOL v2.5 software is a versatile tool in bioinformatics and structural biology. It enables visualization of the predicted proteins three dimensional structures. This is available online at https://pymol.org/2.
17. **QtGrace version 0.2.6:** The MD simulations were performed using GROMACS, results were thoroughly analyzed, and graphical representations were made using QtGrace version 0.2.6

(https://sourceforge.net/projects/qtgrace/files/qtgrace_v026_Win7.zip/download) for enhanced visualization and interpretation.

18. **Swiss ADME:** The SwissADME is a web-based tool(https://www.expasy.org/resources/swissdrugdesign) used in bioinformatics and drug discovery to predict the pharmacokinetic properties, drug-likeness, and physicochemical characteristics of small molecules based on Lipinski's and Veber's rules. In this study, this tool was used for designing and selecting phytochemical compounds with the best potential for development into safe and effective drugs (Lipinski et al. 2012; Daina et al. 2017).
19. **UCSF ChimeraX:** The UCSF ChimeraX program is utilized for the interactive visualization and analysis of molecular structures (protein structures) (Pettersen et al. 2004). This is available online at https://www.cgl.ucsf.edu/chimera/.
20. **VADAR 1.8 Server:** The VADAR 1.8 (Volume, Area, Dihedral Angle Reporter) is tool a web-based server used for the detailed structural analysis and validation of protein molecules (http://vadar.wishartlab.com/).
21. **VMD:** The Visual Molecular Dynamics v1.9.4 (VMD) is a molecular visualization program (Humphrey et al. 1996) that enhances the understanding of complex biomolecular systems in molecular modeling and simulation systems using 3D graphics and built-in scripting. This is available online at https://www.ks.uiuc.edu/Research/vmd/.

References:

Altschul SF, Gish W, Miller W, Myers EW, Lipman DJ (1990) Basic local alignment search tool. Journal of molecular biology 215:403-410

Altschul SF et al. (1997) Gapped BLAST and PSI-BLAST: a new generation of protein database search programs. Nucleic acids research 25:3389-3402

Berkow EL, Lockhart SR, Ostrosky-Zeichner L (2020) Antifungal susceptibility testing: current approaches. Clinical Microbiology Reviews 33:10.1128/cmr. 00069-00019

Daina A, Michielin O, Zoete V (2017) SwissADME: a free web tool to evaluate pharmacokinetics, drug-likeness and medicinal chemistry friendliness of small molecules. Scientific reports 7:42717

Davis RH, de Serres FJ (1970) [4] Genetic and microbiological research techniques for Neurospora crassa. In: Methods in enzymology. Elsevier, pp 79-143

Guex N, Peitsch MC (1997) SWISS-MODEL and the Swiss-Pdb Viewer: an environment for comparative protein modeling. electrophoresis 18:2714-2723

Huey R, Morris GM (2008) Using AutoDock 4 with AutoDocktools: a tutorial. The Scripps Research Institute, USA 8:54-56

Huey R, Morris GM, Forli S (2012) Using AutoDock 4 and AutoDock vina with AutoDockTools: a tutorial. The Scripps Research Institute Molecular Graphics Laboratory 10550:1000

Humphrey W, Dalke A, Schulten K (1996) VMD: visual molecular dynamics. Journal of molecular graphics 14:33-38

Inoue H, Nojima H, Okayama H (1990) High efficiency transformation of Escherichia coli with plasmids. Gene 96:23-28

Kundu D, Umesh, Dubey VK (2021) Interaction of selected biomolecules and metabolites with amyloidogenic proteins. Journal of Biomolecular Structure and Dynamics 39:3061-3070

Lipinski CA, Lombardo F, Dominy BW, Feeney PJ (2012) Experimental and computational approaches to estimate solubility and permeability in drug discovery and development settings. Advanced drug delivery reviews 64:4-17

Livak KJ, Schmittgen TD (2001) Analysis of relative gene expression data using real-time quantitative PCR and the 2− ΔΔCT method. methods 25:402-408

Morris GM et al. (1998) Automated docking using a Lamarckian genetic algorithm and an empirical binding free energy function. Journal of computational chemistry 19:1639-1662

Morris GM et al. (2009) AutoDock4 and AutoDockTools4: Automated docking with selective receptor flexibility. Journal of computational chemistry 30:2785-2791

Oiki S, Nasuno R, Urayama S-i, Takagi H, Hagiwara D (2022) Intracellular production of reactive oxygen species and a DAF-FM-related compound in Aspergillus fumigatus in response to antifungal agent exposure. Scientific Reports 12:13516

Pettersen EF et al. (2004) UCSF Chimera—a visualization system for exploratory research and analysis. Journal of computational chemistry 25:1605-1612

Pronk S et al. (2013) GROMACS 4.5: a high-throughput and highly parallel open source molecular simulation toolkit. Bioinformatics 29:845-854

Rentería-Solís Z, Nguyen-Ho-Bao T, Taha S, Daugschies A (2020) A SYBR green I real-time polymerase chain reaction (PCR) assay for detection and quantification of Trichomonas gallinae. Parasitology research 119:3909-3913

Rodriguez-Tudela J et al. (2008) EUCAST Definitive Document EDef 7.1: method for the determination of broth dilution MICs of antifungal agents for fermentative yeasts: Subcommittee on Antifungal Susceptibility Testing (AFST) of the ESCMID European Committee for Antimicrobial Susceptibility Testing (EUCAST)∗. Clinical Microbiology and Infection 14:398-405

Schindelin J et al. (2012) Fiji: an open-source platform for biological-image analysis. Nature methods 9:676-682

Sobolev OV et al. (2020) A global Ramachandran score identifies protein structures with unlikely stereochemistry. Structure 28:1249-1258. e1242

Umesh, Prerna K, Dubey VK (2022) Virtual screening and repurposing of FDA-approved drugs from ZINC database to identify potential autophagy inhibitors exploiting autophagy related 4A cysteine peptidase as a target: potential as novel anti-cancer molecule. Journal of Biomolecular Structure and Dynamics 40:5266-5282

Van Der Spoel D, Lindahl E, Hess B, Groenhof G, Mark AE, Berendsen HJ (2005) GROMACS: fast, flexible, and free. Journal of computational chemistry 26:1701-1718

Vogel HJ (1956) A convenient growth medium for Neurospora (Medium N). Microbial Genet. Bull. 13:42-43

Vogel HJ (1964) Distribution of lysine pathways among fungi: evolutionary implications. The American Naturalist 98:435-446

Wallace AC, Laskowski RA, Thornton JM (1995) LIGPLOT: a program to generate schematic diagrams of protein-ligand interactions. Protein engineering, design and selection 8:127-134

Yang J, Zhang Y (2015) I-TASSER server: new development for protein structure and function predictions. Nucleic acids research 43:W174-W181

Zheng W, Zhang C, Li Y, Pearce R, Bell EW, Zhang Y (2021) Folding non-homologous proteins by coupling deep-learning contact maps with I-TASSER assembly simulations. Cell reports methods 1

Chapter 3

To determine the minimum inhibitory concentrations of azole drugs and to study the effects of azoles in the calcium signaling gene calcineurin and *pmr-1*, in *Neurospora crassa*

3.1. Introduction

The analysis of the *N. crassa* genome sequence revealed 48 calcium (Ca^{2+}) signaling proteins, which is significantly higher compared to those in yeast and other fungi, and Drosophila (Borkovich et al. 2004). The *N. crassa* Ca^{2+} signaling proteins are further classified into various types, such as Ca^{2+} channel proteins, Ca^{2+}/cation ATPases, Ca^{2+}/hydrogen exchangers, and Ca^{2+}sensors, calmodulin (CaM), and Ca^{2+} and/or CaM-binding proteins (Galagan et al. 2003; Borkovich et al. 2004). Thus, the *N. crassa* Ca^{2+} signaling machinery is complex, with diverse types of proteins that enable it to respond to various types of physiological and environmental stress conditions, including abiotic stressors, osmotic pressure, and elevated salt levels (Virdi et al. 2009; Dong et al. 2022). Moreover, azole stress can elevate the cytosolic Ca^{2+} concentration ($[Ca^{2+}]_c$) level, which might play a role in mitochondrial-mediated azole resistance in eukaryotic organisms (Li et al. 2019; Li et al. 2020). A typical eukaryotic cell maintains a resting concentration of free $[Ca^{2+}]c$ at approximately 100 nM, but this concentration can spike to 1 μM in response to external stimuli, triggering a Ca^{2+} signaling cascade essential for cellular processes (Berridge et al. 2000; Chin and Means 2000). However, an excessive $[Ca^{2+}]c$ concentration is detrimental to cellular integrity and may potentially lead to cell death (Cerella et al. 2010). Therefore, Ca^{2+} homeostasis in cellular health and stress responses (Berridge et al. 2000; Chin and Means 2000; Cerella et al. 2010).

Calcineurin, the only serine-threonine phosphatase that requires both Ca^{2+} and CaM for its activation (Klee et al. 1998; Bandyopadhyay et al. 2002). The binding of Ca^{2+}-calmodulin complex activates calcineurin, which dephosphorylates the transcription factor called calcineurin responsive zinc-finger-1 (Crz1) in fungi (Thewes 2014). The CRZ-1 homologue in human is called the nuclear factor of activated T cells (NFAT) that is critical in diverse cell functions, including development, immunity, and genome integrity (Aramburu et al. 2004). Calcineurin is essential for virulence and drug resistance in several pathogenic fungi, including *A. fumigatus, C. albicans,* and *C. neoformans* (Karkowska-Kuleta et al. 2009). The CNA-1 catalytic subunit is characterized by an N-terminal phosphatase domain, a helix for regulatory subunit binding (CnBBH), and a domain that binds calmodulin (CaMBD) (Juvvadi et al. 2014). Interestingly, a unique serine-proline-rich (SPRR) linker domain, found exclusively within the calcineurin catalytic subunit, bridges the CnBBH and CaMBD in the filamentous fungi, including *A. fumigatus* (Juvvadi et al. 2013). This SPRR domain undergoes phosphorylation at four serine clusters, and its mutations affect fungal growth and virulence. Calcineurin has also been emerged as a promising target for antifungal treatment for diverse fungal species, including *C. neoformans*, *C. albicans*, and *A. fumigatus* (Juvvadi et al. 2017).

The disruption of calcineurin signaling causes an increased susceptibility to antifungals, suggesting that calcineurin could be a potential target for overcoming drug resistance (Chen et al. 2011; Park et al. 2016; Juvvadi et al. 2017). Calcineurin is also essential for ergosterol biosynthesis and drug efflux, which are crucial mechanisms for azole resistance in pathogenic fungi, including *A. fumigatus* and *C. albicans* (Li et al. 2011; Cowen et al. 2015). The yeast mutants lacking calcineurin and Crz1 exhibit decreased tolerance to azoles and echinocandins (Sanglard et al. 2003; Chen et al. 2011). Moreover, loss of the retrograde transport protein Pep8 function in *C. albicans* enhances calcineurin activity, thereby contributing to an increased azole resistance (Mount et al. 2018).In the *C. lusitaniaev* calcineurin mutants exhibited a decreased azole resistance (Zhang et al. 2012).

In the nucleus, Crz1 also induces the expression of the *pmr-1* gene that regulates stress response, cell wall integrity, growth, and drug resistance (Sorin et al. 1997; Ferreira et al. 2012; Zhao et al. 2013; Juvvadi et al. 2017). The expression of the *pmr-1* gene is necessary for the transport of Ca^{2+} and Mn^{2+} cations across the Golgi membrane and maintaining the structural integrity of the cell wall in various fungi, including *N. crassa* (Antebi and Fink 1992; Bowman et al. 2012). The *pmr-1* gene plays a crucial role in regulating Ca^{2+} homeostasis, cell wall integrity, and antifungal drug resistance in *A. fumigatus* and *C. albicans* (Bates et al. 2005; Pinchai et al. 2010). In *C. albicans*, Pmr1p, a P-type Ca^{2+}/Mn^{2+}-ATPase in the secretory pathway, is necessary for virulence (Bates et al. 2005). The disruption of PMR1 in *S. cerevisiae* results in protein-sorting abnormalities, which causes an increased secretion of heterologously produced proteins (Kang et al. 1998; Bates et al. 2005) and aberrant processing of the α factor (Sorin et al. 1997). The PMR1 pump plays a role in pathogenicity and drug tolerance in pathogenic fungi, including *A. fumigatus*, *C. neoformans*, and *S. cerevisiae* (Kellermayer 2005; Szigeti et al. 2005; Pinchai et al. 2010; Kmetzsch et al. 2011).

In *N. crassa*, the calcineurin catalytic A (CNA-1) and a regulatory B (CNB-1) subunits are necessary for growth, development, and fertility (Tamuli et al. 2016; Kumar et al. 2020). *N. crassa* has also been studied as a model organism for investigating the molecular basis of azole drug resistance (Víglaš and Olejníková 2023). In *N. crassa*, the

ERG11, MDR1, and ABC transporter proteins have been investigated for survival under azole drugs (Zhou et al. 2022). However, the calcineurin and PMR-1 role in azole resistance is yet to be understood. Therefore, I investigated calcineurin and PMR-1 role in azole susceptibility in *N. crassa*.

I determined the minimum inhibitory concentrations (MICs) of fluconazole, itraconazole, and ketoconazole in the *N. crassa* wild type. I used the calcineurin RIP mutants (*Cna-1*$^{\mathrm{RIP}}$) and Δ*pmr-1* mutants to investigate the calcineurin and PMR-1 role in azole susceptibility. The *Cna-1*$^{\mathrm{RIP}}$ and Δ*pmr-1* mutants showed increased susceptibility to azole drugs, reduced levels of ergosterol, and altered reactive oxygen species level (ROS) under azole treatment. Furthermore, field emission scanning electron microscopy (FESEM) studies revealed defects in hyphal morphology in the *Cna-1*$^{\mathrm{RIP}}$ and Δ*pmr-1* mutants when treated with antifungals. These findings suggest that calcineurin and *pmr-1* might play a crucial role in the survival of *N. crassa* under azole-induced stress conditions.

3.2. Results

3.2.1. Determination of the minimum inhibitory concentration of azole drugs and their effect on growth in *N. crassa*

I determined the MIC values of the azole drugs fluconazole, itraconazole, and ketoconazole against the *N. crassa* wild type (Figure 3.1). The MIC values were 0.5 µg/ml, 3 µg/ml, and 1 µg/ml for fluconazole, itraconazole, and ketoconazole drugs, respectively (Table 3.1). Fluconazole, itraconazole, and ketoconazole inhibited the growth of the *Cna-1*$^{\text{RIP}}$ mutants 24 a and 122 A, and the Δ*pmr-1*, compared to the wild type. The *Cna-1*$^{\text{RIP}}$ 24 a mutant showed the highest growth inhibition in the presence of fluconazole (Table 3.2). Furthermore, the relative growth rate analysis demonstrated that the *Cna-1*$^{\text{RIP}}$ and Δ*pmr-1* mutants showed increased susceptibility to fluconazole (Figure 3.3). The relative growth rate percentages of the wild type, *Cna-1*$^{\text{RIP}}$ mutants 24 a and 122 A, and the Δ*pmr-1* strains on the VG medium supplemented with itraconazole were 49.77 ± 2.06, 35.04 ± 1.37, 48.74 ± 1.35, and 28.99 ± 1.99, respectively (Table 3.2). Ketoconazole exhibited the lowest antifungal efficacy, with relative growth percentages of 73.59 ± 2.92, 53.78 ± 1.06, 60.08 ± 4.09, and 67.94 ± 4.48, respectively, for the wild type, *Cna-1*$^{\text{RIP}}$ mutants 24 a and 122 A, and Δ*pmr-1* strains. Notably, fluconazole was the most effective antifungal drug which exhibited the highest antifungal potency against the *N. crassa* strains at half of its MIC concentration (Figure 3.2). The fluconazole treatment resulted in the lowest radial growth percentages of 47.85 ± 2.59, 18.59 ± 2.07, 36.27 ± 1.88, and 30.84 ± 1.12 in the wild type, *Cna-1*$^{\text{RIP}}$ mutants 24 a and 122 A, and Δ*pmr-1* strain, respectively (Table 3.2).

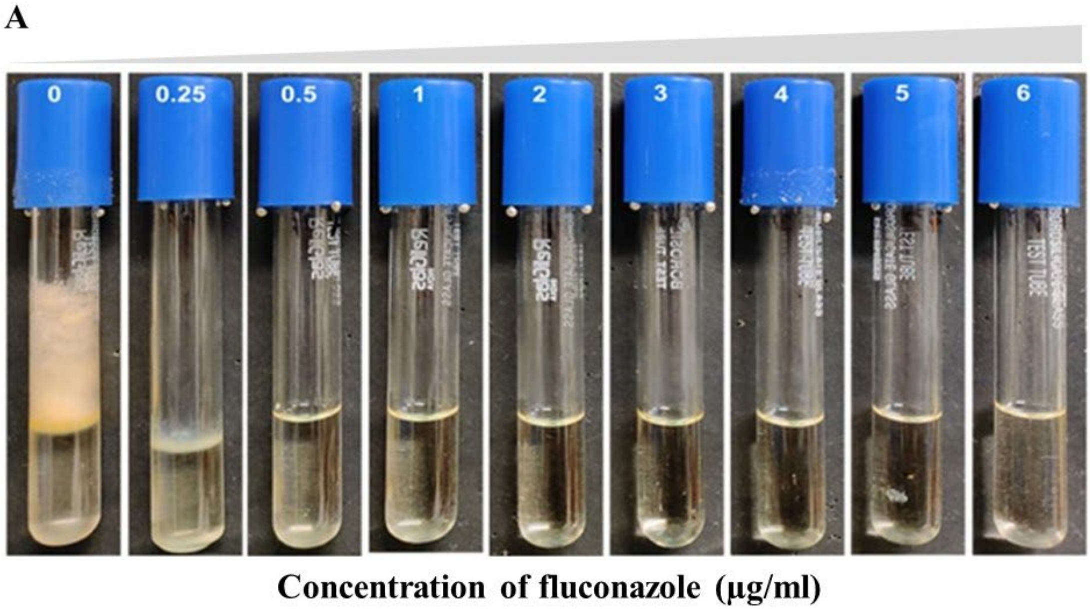
A
0
0.25
0.5
1
2
3
4
5
6
Concentration of fluconazole (µg/ml)

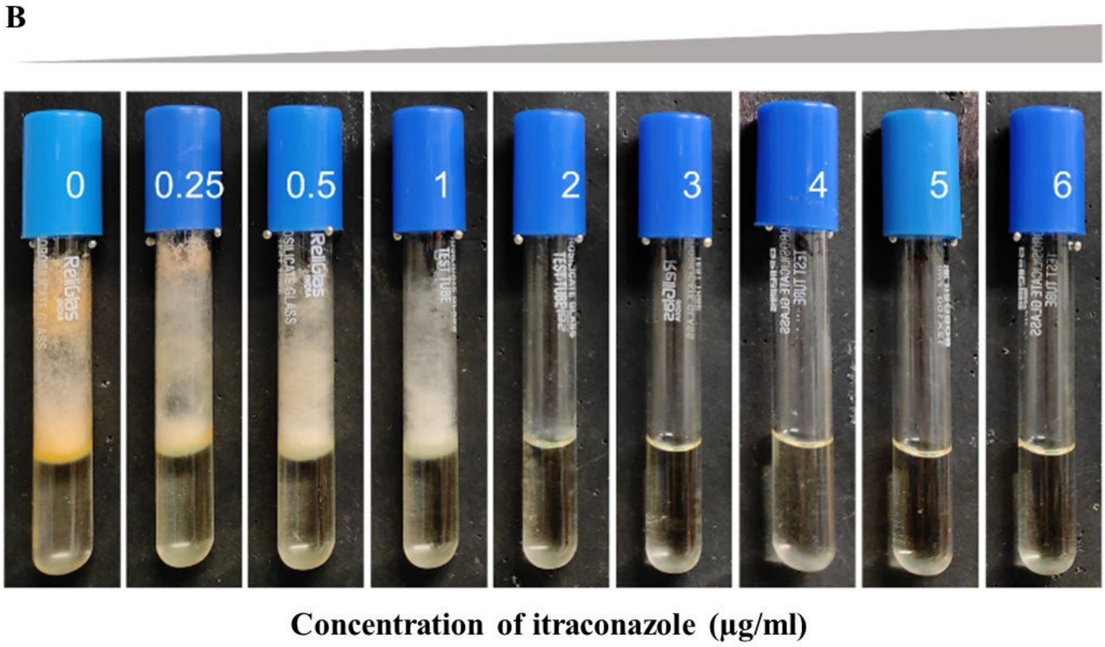
B
0
0.25
0.5
1
2
3
4
5
6
Concentration of itraconazole (µg/ml)

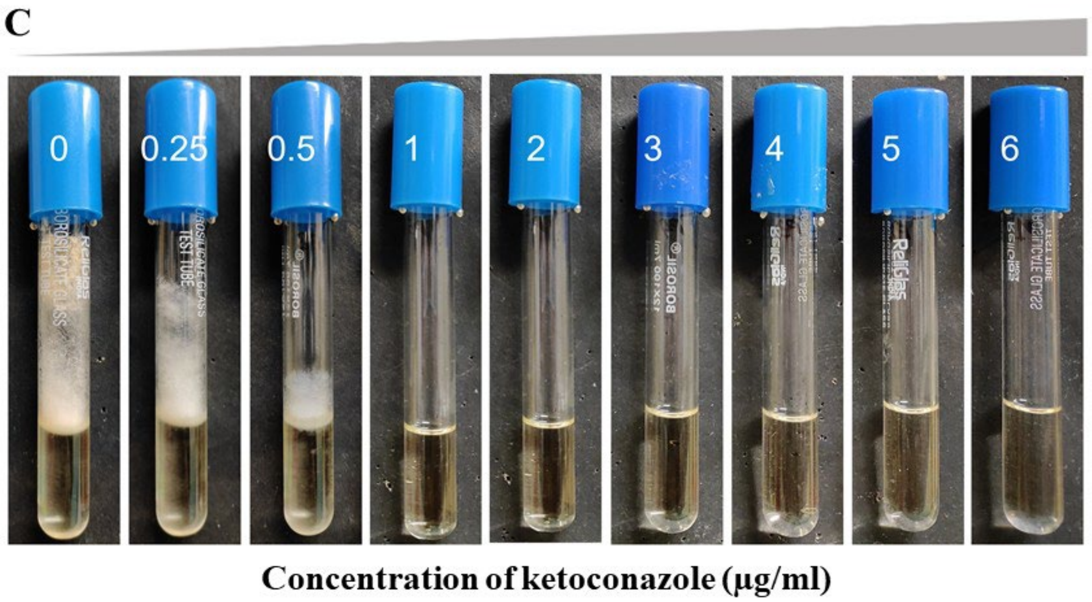

Figure 3.1. Effect of the azole drugs on the growth of aerial hyphae in the *N. crassa* strains. The conidia of the *N. crassa* wild type strain were inoculated at a concentration of 1X 10^6 conidia/ml in the VG liquid medium supplemented with (A) fluconazole, (B) itraconazole, and (C) ketoconazole at various concentrations (labeled with the increasing concentrations from left to right on the tubes). The cultures were incubated at 30°C for three days. Fluconazole showed an MIC at 0.5 µg/ml, whereas itraconazole and ketoconazole showed MIC values of 3 µg/ml and 1 µg/ml, respectively. The experiment was conducted in triplicate (n = 3), and a representative image is shown.

Table 3.1. Minimum inhibitory concentration of azole drugs tested against the *N. crassa* wild type strain.

S. No.	Azole Drug	MIC (µg/ml)
1.	Fluconazole	0.5
2.	Itraconazole	3
3.	Ketoconazole	1

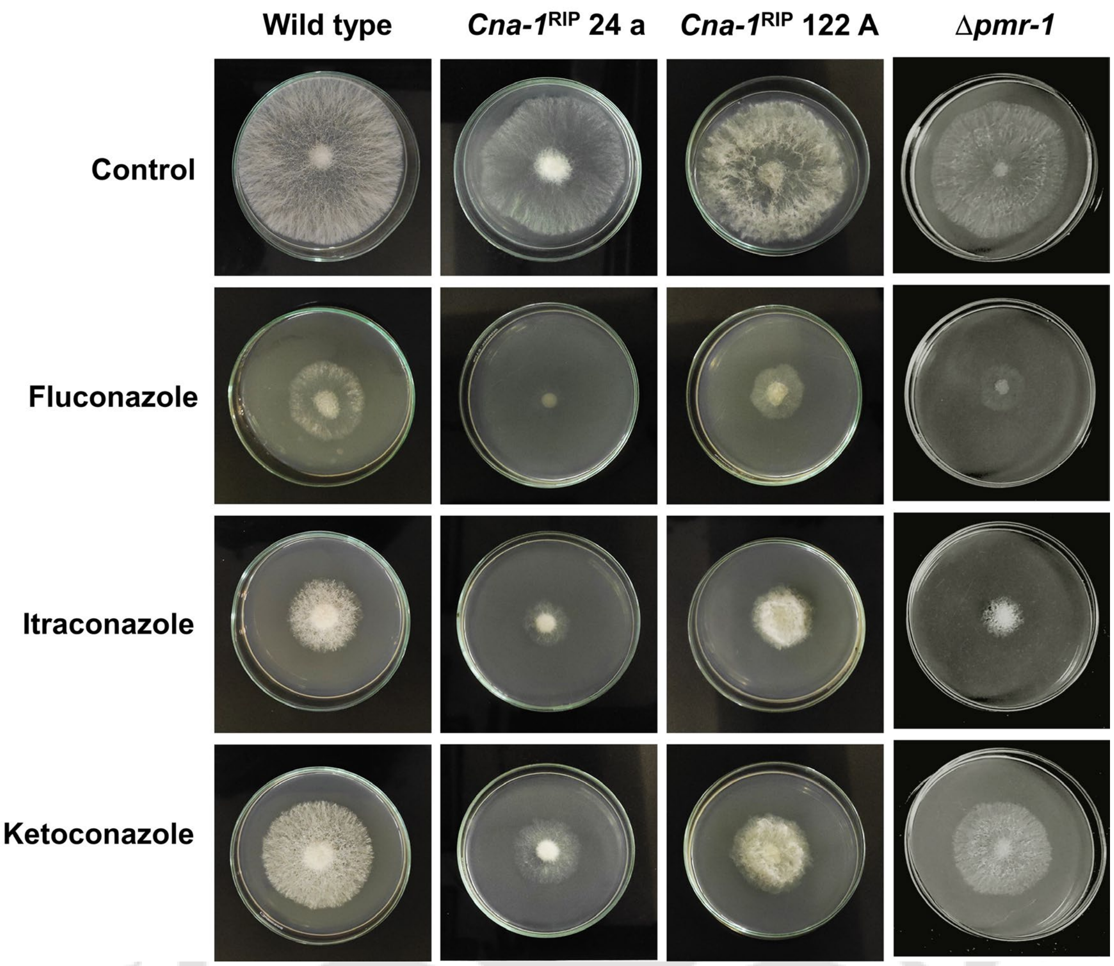

Figure 3.2. Drug susceptibility assay. The drug susceptibility assay was performed in triplicate (n = 3) by inoculating ~1×10^6 conidia/ml in the center of VG agar medium with or without (control) the azole drug treatment. The fluconazole (0.25 µg/ml), itraconazole (1.5 µg/ml), and ketoconazole (0.5 µg/ml) were used at half of their MIC values.

Table 3.2. Radial growth in response to azole drugs

Strains	Relative radial growth (percentage) [a, b]			
	Untreated	**Fluconazole**	**Itraconazole**	**Ketoconazole**
Wild type	100 ± 0	47.85 ± 2.59	49.77 ± 2.06	73.59 ± 2.92
Cna-1$^{\mathrm{RIP}}$ 24 a	100 ± 0	18.59 ± 2.07	35.04 ± 1.37	53.78 ± 1.06
Cna-1$^{\mathrm{RIP}}$ 122 A	100 ± 0	36.27 ± 1.88	48.74 ± 1.35	60.08 ± 4.09
Δ*pmr-1*	100 ± 0	30.84 ± 1.12	28.99 ± 1.99	67.94 ± 4.48

[a] The radial growth of the *N. crassa* strains on VG medium supplemented with fluconazole, itraconazole, and ketoconazole was measured. The untreated condition (control) for each strain was considered as 100% growth, and the relative growth percentages were calculated accordingly.

[b] Data are presented as mean ± standard deviation (SD) of three independent experiments (n = 3).

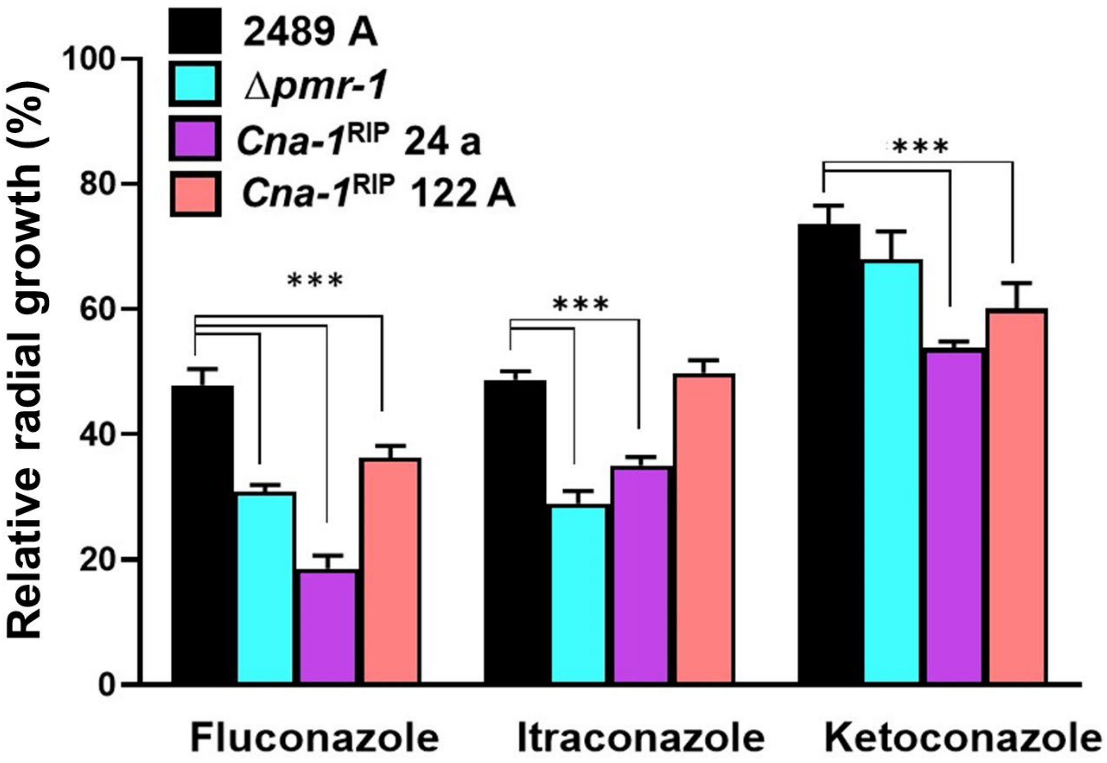

Figure 3.3. The effect of fluconazole, itraconazole, and ketoconazole on the radial growth of the *N. crassa* strains. The growth percentage in the untreated condition (control) for each strain was considered 100%, and the growth percentages under drug-treated conditions were calculated relative to this. An analysis of variance (ANOVA) test was performed in GraphPad Prism software, and significance is indicated as: *** P < 0.0001.

3.2.2. The calcineurin catalytic subunit mutants *Cna-1*^{RIP} 24 a and 122 A, and Δ*pmr-1* showed growth defects in response to azole drugs

3.2.2.1. Azole drugs caused impaired hyphal development in the *Cna-1*^{RIP} and Δ*pmr-1* mutants

The *Cna-1*^{RIP} 24 a, *Cna-1*^{RIP} 122 A, and Δ*pmr-1* mutants were susceptible to the azole drugs and displayed impaired hyphal growth (Figure 3.4). Hyphal growth was severely impaired in the presence of fluconazole, while itraconazole induced bulging structures at hyphal tips, and ketoconazole caused an overall reduction in hyphal extension (Figure 3.4). These results suggested that the calcineurin and *pmr-1* genes play a role in tolerance to azole drugs in *N. crassa*.

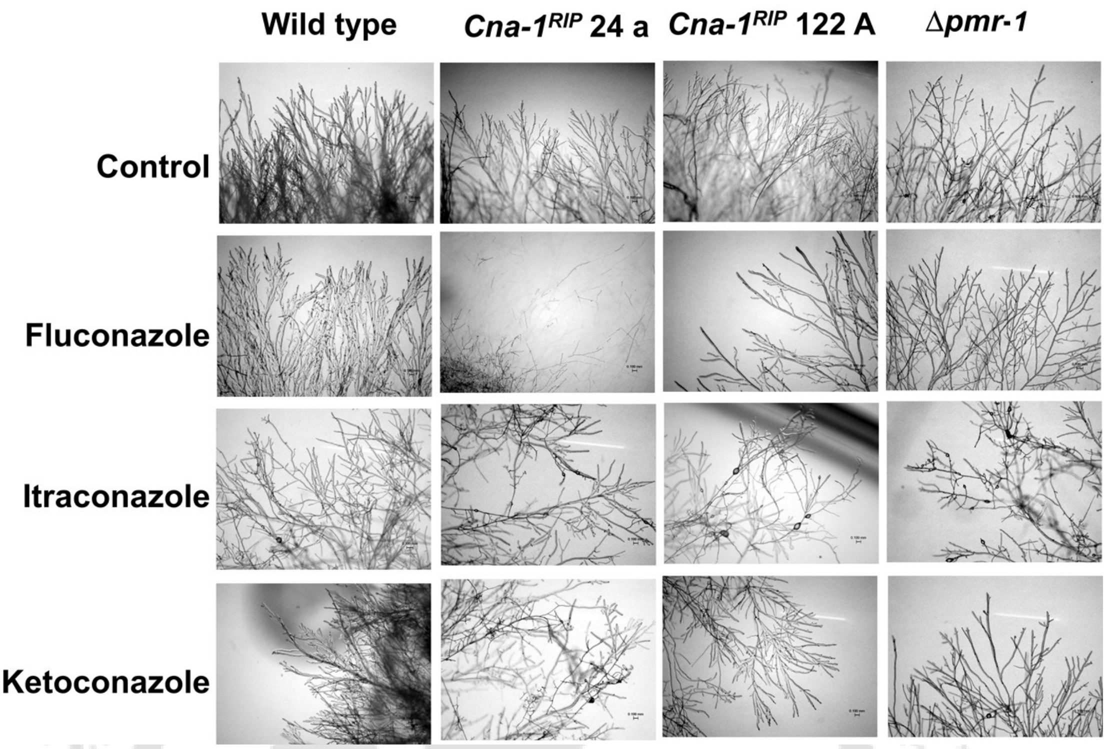

Figure 3.4. Hyphal morphology of *N. crassa* strains in response to the azole drugs. The *N. crassa* wild type, *Cna-1*$^{\mathrm{RIP}}$ mutants 24 a and 122 A, and Δ*pmr-1* strains were inoculated on the surface of Vogel's glucose agar (VGA) medium supplemented with and without (control) azole drugs. The fluconazole (0.25 µg/ml), itraconazole (1.5 µg/ml), and ketoconazole (0.5 µg/ml) were used at half of their MIC values. The samples were incubated at 30°C for 12 to 16 h and examined under a microscope (Leica S9i Stereomicroscope, Leica Microsystems, Wetzlar, Germany). Hyphal morphology was examined, and representative images are shown; the scale bar represents ~200 µm.

3.2.2.2. The calcineurin RIP and Δ*pmr-1* mutants showed reduced ergosterol content in response to the azole treatment

In fungi, reduced hyphal growth and branching are linked to reduced levels of ergosterol, which is necessary for cell membrane integrity (Ha and White 1999). Ergosterol is synthesized from acetyl-CoA via a series of critical intermediates, including squalene, lanosterol, and fecosterol, facilitated by various enzymes (Parks and Casey 1995). Most antifungal compounds target either the formation or the function of ergosterol (Herrick and Hashmi 2019). However, fungi adapt several mechanisms to counteract the effects of inhibitors targeting ergosterol biosynthesis. I studied if the azole drugs inhibit ergosterol biosynthesis in the *Cna-1*$^{\mathrm{RIP}}$ and Δ*pmr-1* mutants. The ergosterol content of these mutants was measured with and without (control) the treatment of fluconazole, itraconazole, and ketoconazole. Ergosterol from the wild type exhibits peak UV absorption at wavelengths of 272 nm, 282 nm, and 293 nm (Naewbanij et al. 1984). The *N. crassa erg-3* mutant showed a peak around 250 nm, indicative of a Δ8,14 sterol composition and a lack of ergosterol (Prakash et al. 1999). Interestingly, the *Cna-1*^{RIP} and Δ*pmr-1* mutants showed a significant reduction in ergosterol production in the presence of fluconazole, itraconazole, and ketoconazole (Figure 3.5).

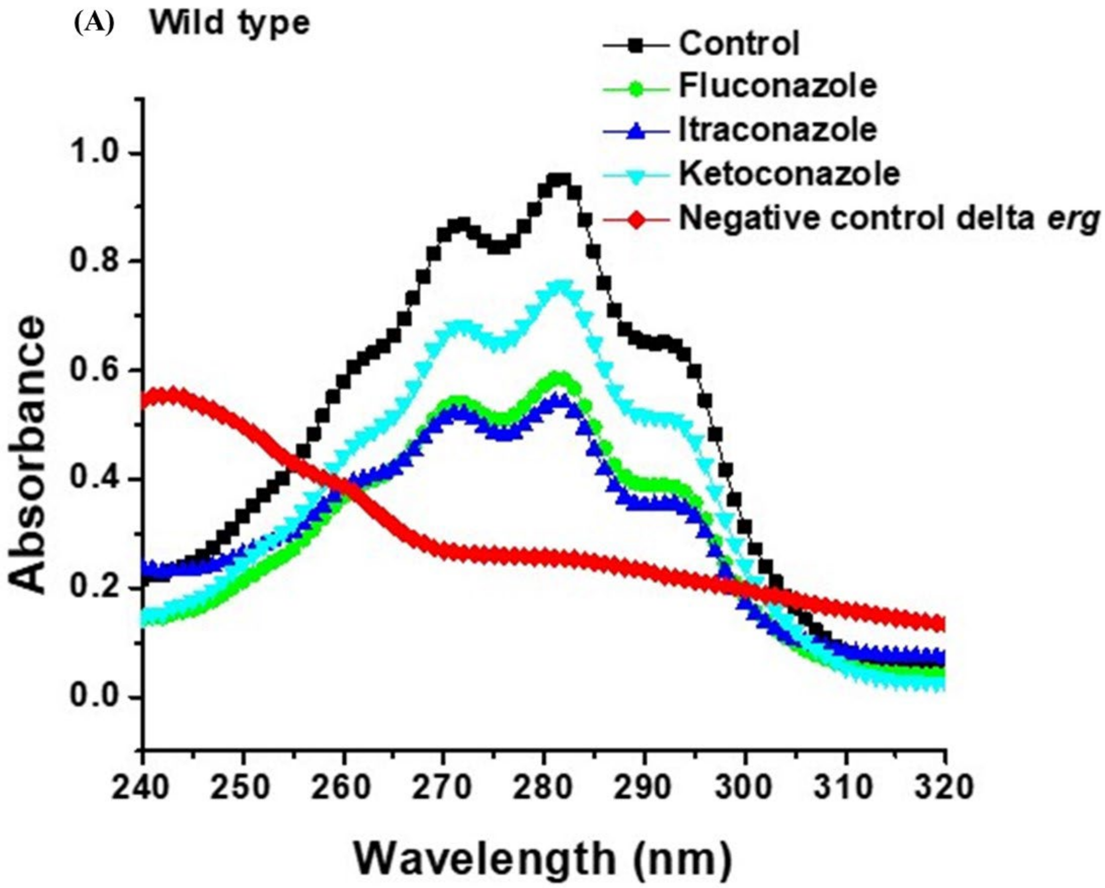

(B) *Cna-1*^{RIP} *24 a*

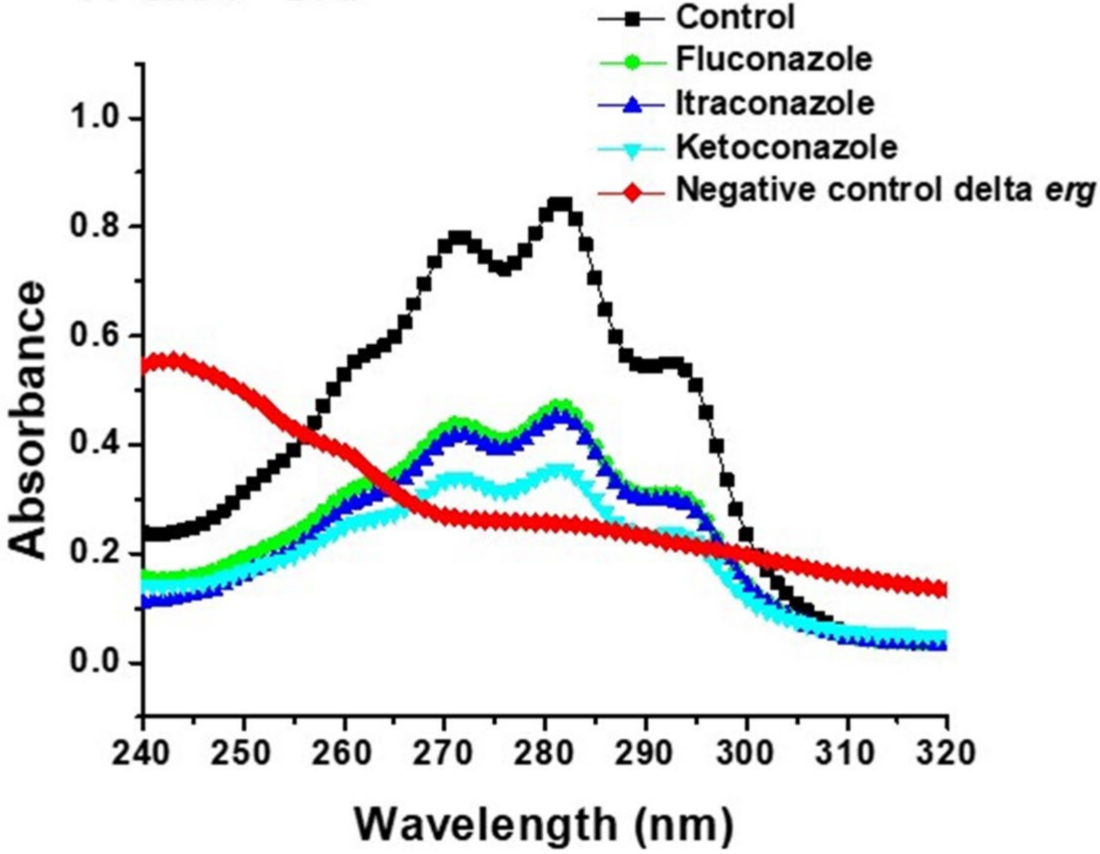

(C) *Cna-1*^{RIP} *122 A*

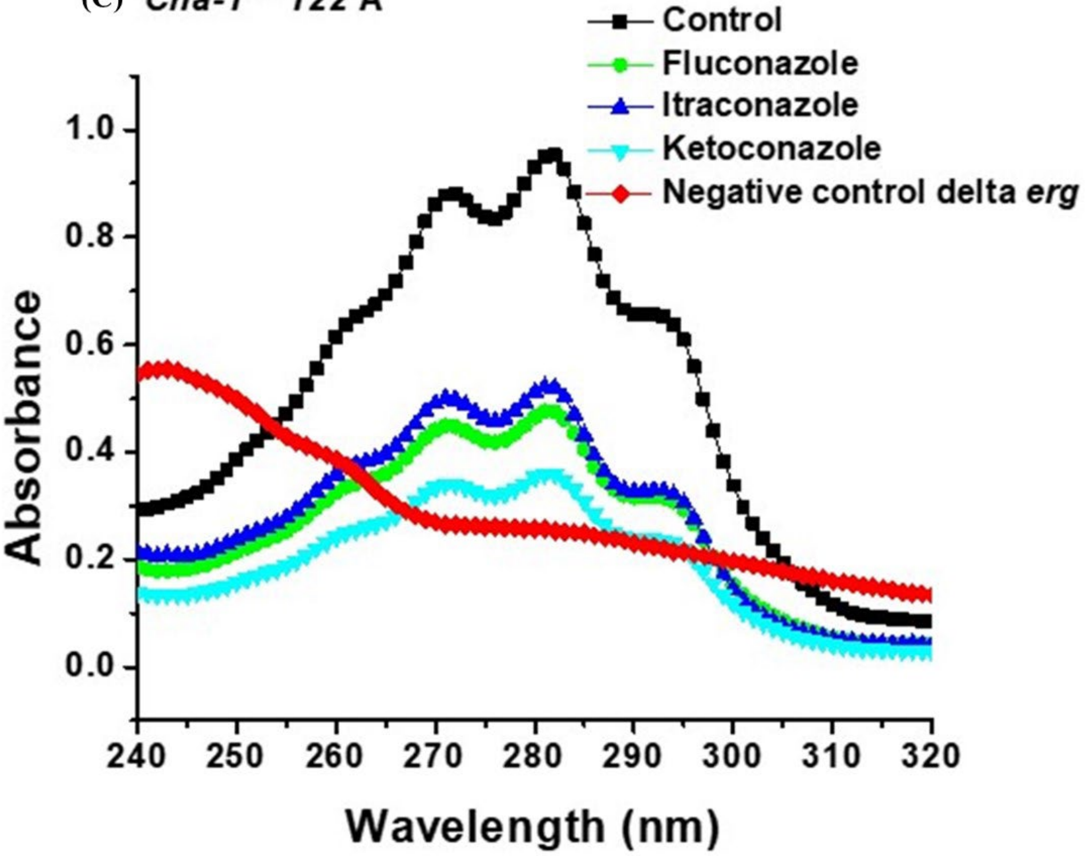

(D) Δ*pmr-1*

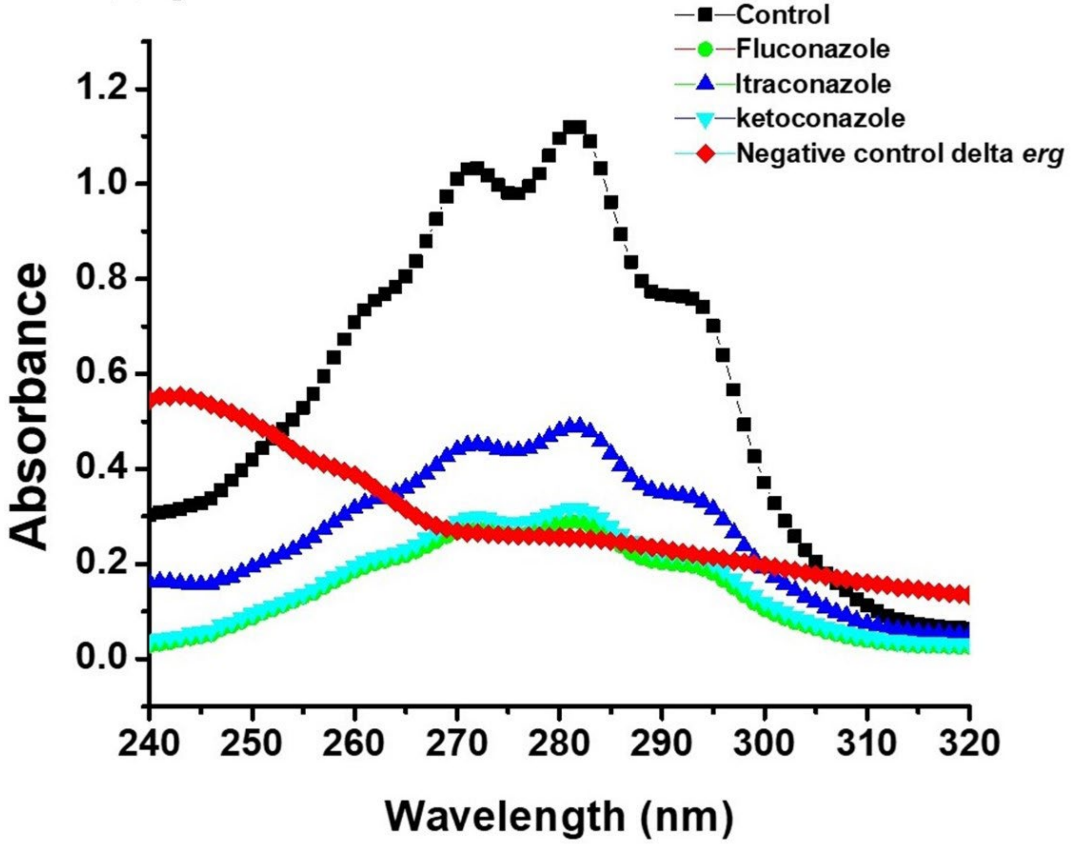
Control
Fluconazole
Itraconazole
ketoconazole
Negative control delta *erg*
Absorbance
1.2
1.0
0.8
0.6
0.4
0.2
0.0
240
250
260
270
280
290
300
310
320
Wavelength (nm)

(E)

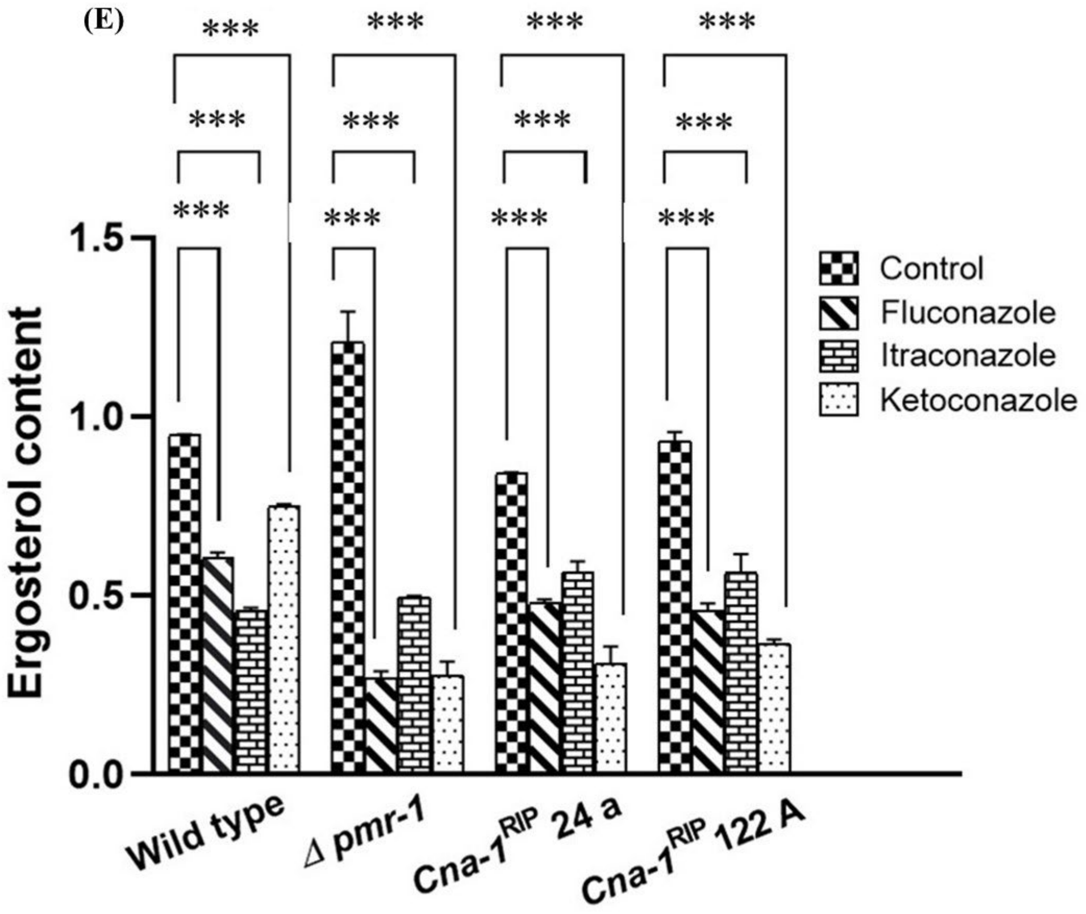
***
***
***
***
***
***
***
***
***
***
***
***
1.5
1.0
0.5
0.0
Ergosterol content
Control
Fluconazole
Itraconazole
Ketoconazole
Wild type
Δ *pmr-1*
*Cna-1*RIP 24 a
*Cna-1*RIP 122 A

Figure 3.5. Ergosterol profile of the *N. crassa* strains with and without (control) the treatment of fluconazole, itraconazole, and ketoconazole. The maximum absorption spectra for ergosterol from the wild type were recorded at 272 nm, 282 nm, and 293 nm in the UV region. However, the sterol from the *erg-3* mutant showed maximum absorption at ~250 nm, characteristic of Δ8,14 sterols, indicating the absence of ergosterol in the *erg-3* mutant (Ellis et al. 1991; Prakash et al. 1999). In comparison to the (A) wild type, the mutant strains (B) *Cna-1*$^{\mathrm{RIP}}$ 24 a, (C) *Cna-1*$^{\mathrm{RIP}}$ 122 A, and (D) Δ*pmr-1* showed reduced levels of the ergosterol under the fluconazole, itraconazole, and ketoconazole treatment. (E) Bar diagram showing the ergosterol content in the *N. crassa* strains under the fluconazole, itraconazole, and ketoconazole treatment. An analysis of variance (ANOVA) test was performed using GraphPad Prism software (https://graphpad-prism.software.informer.com/8.0/) , and statistical significance is indicated as: ***P < 0.0001.

3.2.2.3. The reactive oxygen species (ROS) level was increased in response to the azole treatment

Reactive oxygen species (ROS) are produced as a byproduct of metabolic activities in the cell (Forrester et al. 2018). In fungi, ROS production increases under various stress conditions, such as starvation, light and mechanical damage(Gessler et al. 2007). Azole drugs are commonly used to treat fungal infections, causing the generation of ROS in fungal cells, as disruption of the cell membrane triggers oxidative stress (Shekhova et al. 2017a). I investigated, ROS levels upon exposure to antifungal agents in the *N. crassa* wild type, calcineurin-RIP mutants, and Δ*pmr-1* mutant strains. I used 2′,7′-dichlorofluorescein diacetate (DCFH-DA), a nonfluorescent dye that becomes fluorescent in the presence of ROS, to determine the ROS level with or without (control) the treatment of the azole drugs (de Haan et al. 2022). The intensity levels of the DCFH-derived fluorescence were determined using an Infinite 200 PRO plate reader (INFINITE 200 PRO, Tecan, Austria). In the wild type and *Cna-1*$^{\mathrm{RIP}}$ 122A mutant, treatment with the fluconazole, itraconazole, and ketoconazole resulted in a significant increase of ROS level (Figure 3.6 A, B). The *Cna-1*$^{\mathrm{RIP}}$ 24 a and Δ*pmr-1* mutants exhibited elevated ROS level under the treatment of fluconazole and itraconazole, respectively (Figure 3.6 C, D). These results indicate that although baseline ROS levels vary across strains, the antifungal-induced ROS response remains consistent across wild type and mutant strains.

(A) Wild type

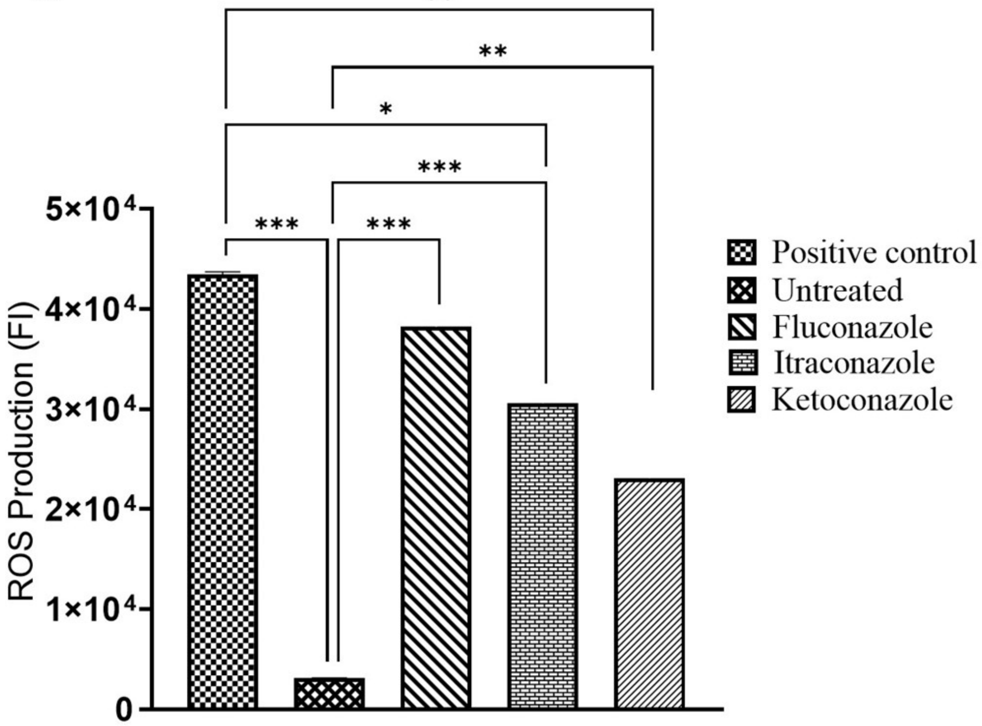

(B) *Cna-1*^{RIP} 122 A

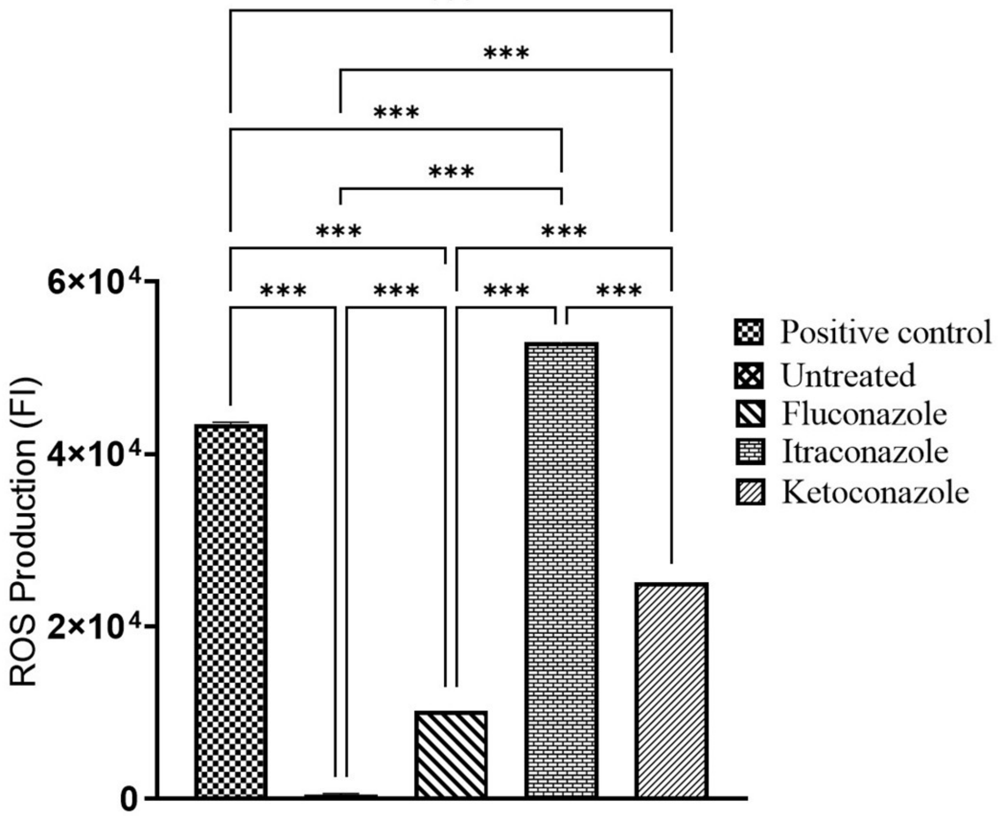

(C) ***Cna-1*^{RIP} 24 a**

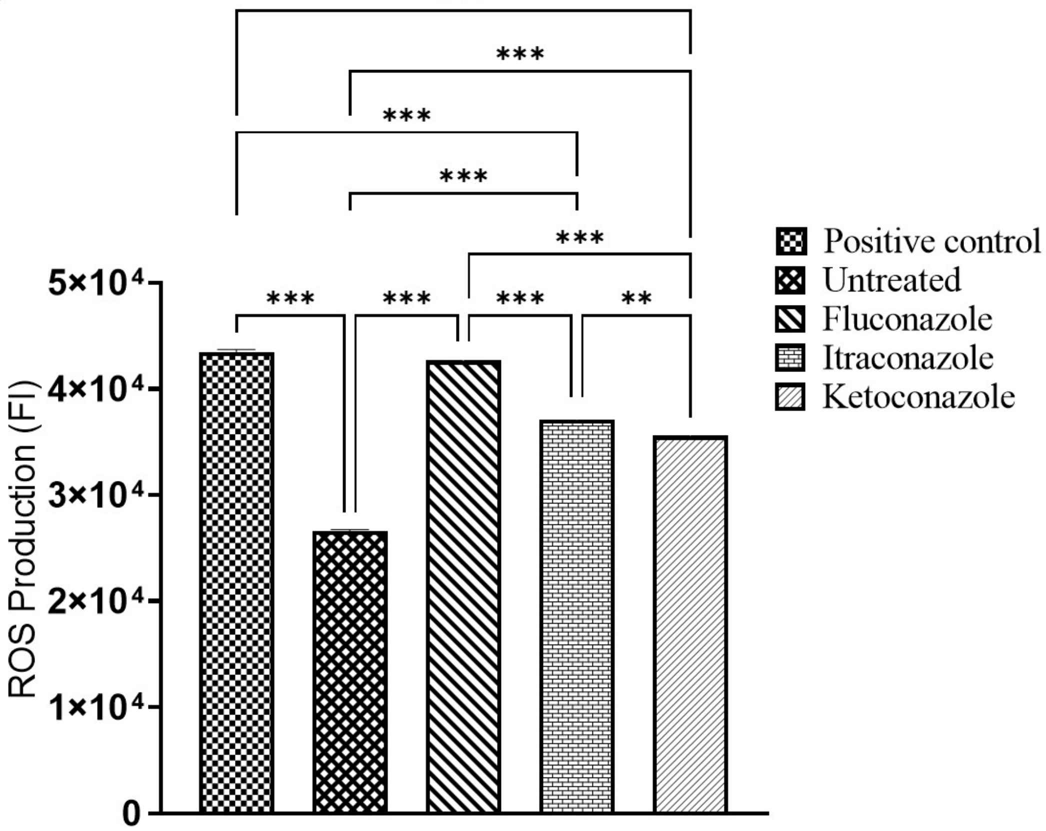

(D) **Δ*pmr-1***

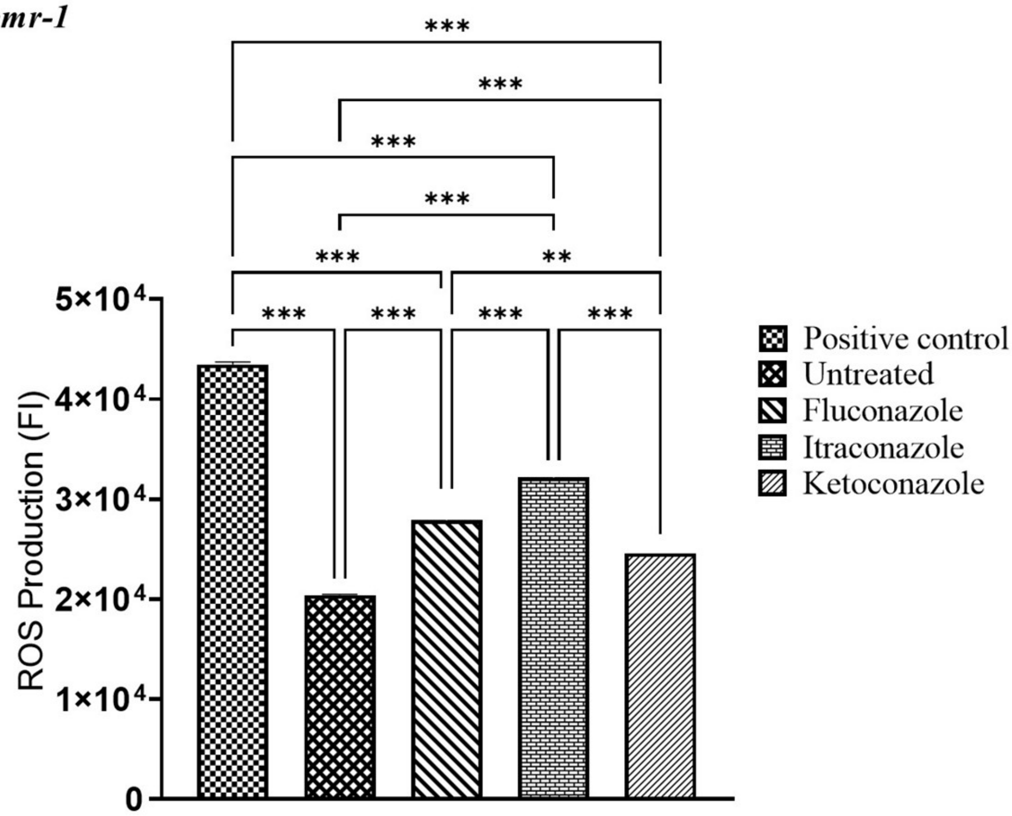

Figure 3.6. Effect of the azole drugs on ROS production. Intracellular ROS levels in the *N. crassa* strains were quantified based on the DCFH-DA fluorescence intensity. Hydrogen peroxide treatment was considered as the positive control for ROS production, and the untreated sample was used as the negative control. The cells were disrupted, and the extracts were used for fluorescence intensity measurement. ROS fluorescence intensity was measured in response to different azole drug treatments in the (A) wild type strain, (B) *Cna-1*$^{\mathrm{RIP}}$ 122 A, (C) *Cna-1*$^{\mathrm{RIP}}$ 24 a, and (D) Δ*pmr-1* mutant. The experiment was performed in three biological replicates ($n = 3$) and presented as mean and the error bars represent ± standard deviation (SD). An ANOVA was performed to assess the statistical significance of differences between the treated and untreated strains, where *** indicates $P < 0.0001$, ** indicates $P < 0.005$, and * indicates $P < 0.05$.

3.2.2.4. Expression of the *cna-1* and *pmr-1* genes under the azole treatment

The calcineurin-crz1 signaling pathway plays a role in antifungal susceptibility (Miyazaki et al. 2010). In *C. glabrata,* calcineurin-induced CDR1 and PDR1 gene expression increases under fluconazole treatment (Vu et al. 2023). Moreover, *PMR1* was upregulated in response to the amiodarone drug treatment *in C. albicans*, suggesting that the amiodarone mechanism of action is likely linked to Ca^{2+} overload, as in the *S. cerevisiae* (Gupta et al. 2003; Zhang and Rao 2007). Therefore, I performed the expression analysis of the calcineurin and *pmr-1* genes to test whether these Ca^{2+} signaling genes play a role in azole antifungal drug susceptibility in *N. crassa*. The expression levels of the *cna-1* and *pmr-1* genes were analyzed with and without (control) the treatment of fluconazole, itraconazole, and ketoconazole. The *cna-1* gene expression was not significantly different and did not show any changes when treated with fluconazole, itraconazole, or ketoconazole, compared to the untreated control group (Figure 3.7 A). However, the *pmr-1* gene was significantly upregulated under the itraconazole treatment ($p \leq 0.0001$), but not under the treatments of fluconazole and ketoconazole treatments ($p > 0.5$) (Figure 3.7 B). The statistical analyses were performed using GraphPad Prism (https://graphpad-prism.software.informer.com/8.0/), and the normality of the ΔCT values was assessed using the Shapiro-Wilk test (Shapiro and Wilk 1965; Goni et al. 2009), which yielded p-values greater than 0.5 for *pmr-1* genes, confirming that the data followed a normal distribution. Homogeneity of variances across the groups was evaluated using the Brown-Forsythe test (Zhang 1998), which provided a p-value of 0.6101 for *cna-1* and a p-value greater than 0.3006 for *pmr-1*, indicating that the assumption of equal variances was satisfied for both *cna-1* and *pmr-1* genes. The one-way ANOVA was performed to compare the mean ΔCT values across the control and treated groups. However, the ANOVA indicated overall significance, therefore, Tukey's multiple comparisons test was used as a post hoc analysis to identify specific group differences, with $p \leq 0.05$ considered as statistically significant (Juarros-Basterretxea et al. 2024). The CT and ΔCT values and fold changes are for Figure 3.7 A and B are provided in the Appendix Chapter in Appendix Table 3.1 and 3.2, respectively.

(A) ***cna-1***

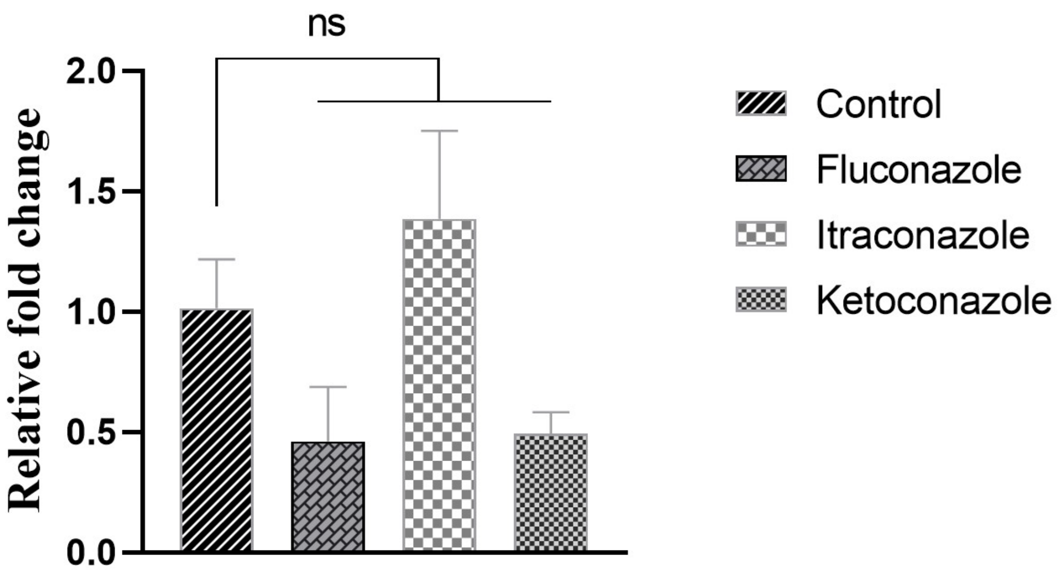

(B) ***pmr-1***

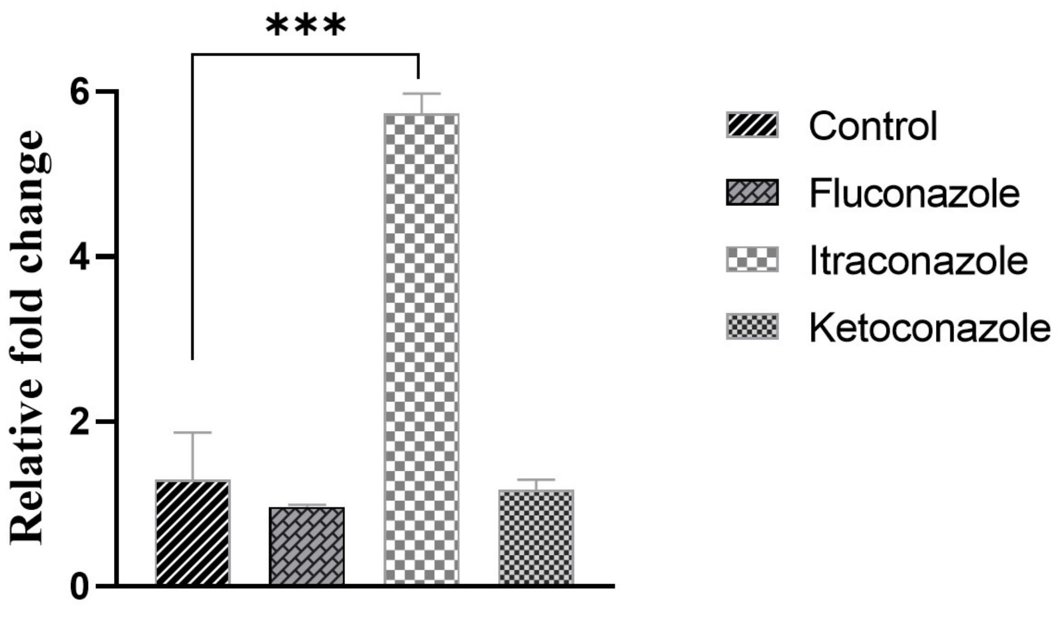

Figure 3.7. Relative fold change of the *cna-1* and *pmr-1* gene expression in response to azole treatments. Bar graphs representing the relative fold change in the expression of the *cna-1* and *pmr-1* genes under different treatment conditions of azoles (fluconazole, itraconazole, and ketoconazole) compared to the control (no drug treatment) in the *N. crassa* wild type. The relative fold change was calculated using the $2^{-\Delta\Delta CT}$ method, where ΔCT values were obtained by normalizing the CT values of the target gene to the CT values of the housekeeping gene for each sample. The control group was used as the reference, with its expression level considered as 1. (A) For the *cna-1* gene, the expression was not significantly different and did not show any changes when treated with fluconazole, itraconazole, or ketoconazole, compared to the untreated control group (Figure 3.7 A). (B) For the *pmr-1* gene, itraconazole treatment resulted in a highly significant upregulation of expression ($p \leq 0.0001$), whereas fluconazole and ketoconazole treatments did not show any significant changes ($p > 0.5$).

3.2.2.5. Azole drug caused Ca^{2+} accumulation in the hyphal tips, and hyphal damage in the *N. crassa* mutant strains

I performed a chlortetracycline hydrochloride (CTC) assay to determine the Ca^{2+} gradient in the hyphal tips in response to fluconazole using a microscope (Trinocular Inverted Fluorescence Microscope, Nikon ECLIPSE E200, Japan). The fluorescence intensity was increased in the *N. crassa Cna-1*^{RIP} and Δ*pmr-1* mutants, suggesting an elevated level of intracellular free Ca^{2+} in these mutants (Figure 3.8). Furthermore, analysis using a field emission scanning electron microscope (FESEM, Zeiss) revealed that fluconazole causes significant hyphal damage in the *Cna-1*^{RIP} 24 a, 122 A, and Δ*pmr-1* mutants compared to the wild type (Figure 3.9). These results suggested that calcineurin and *pmr-1* genes play a role in maintaining hyphal integrity in response to the azole drug fluconazole.

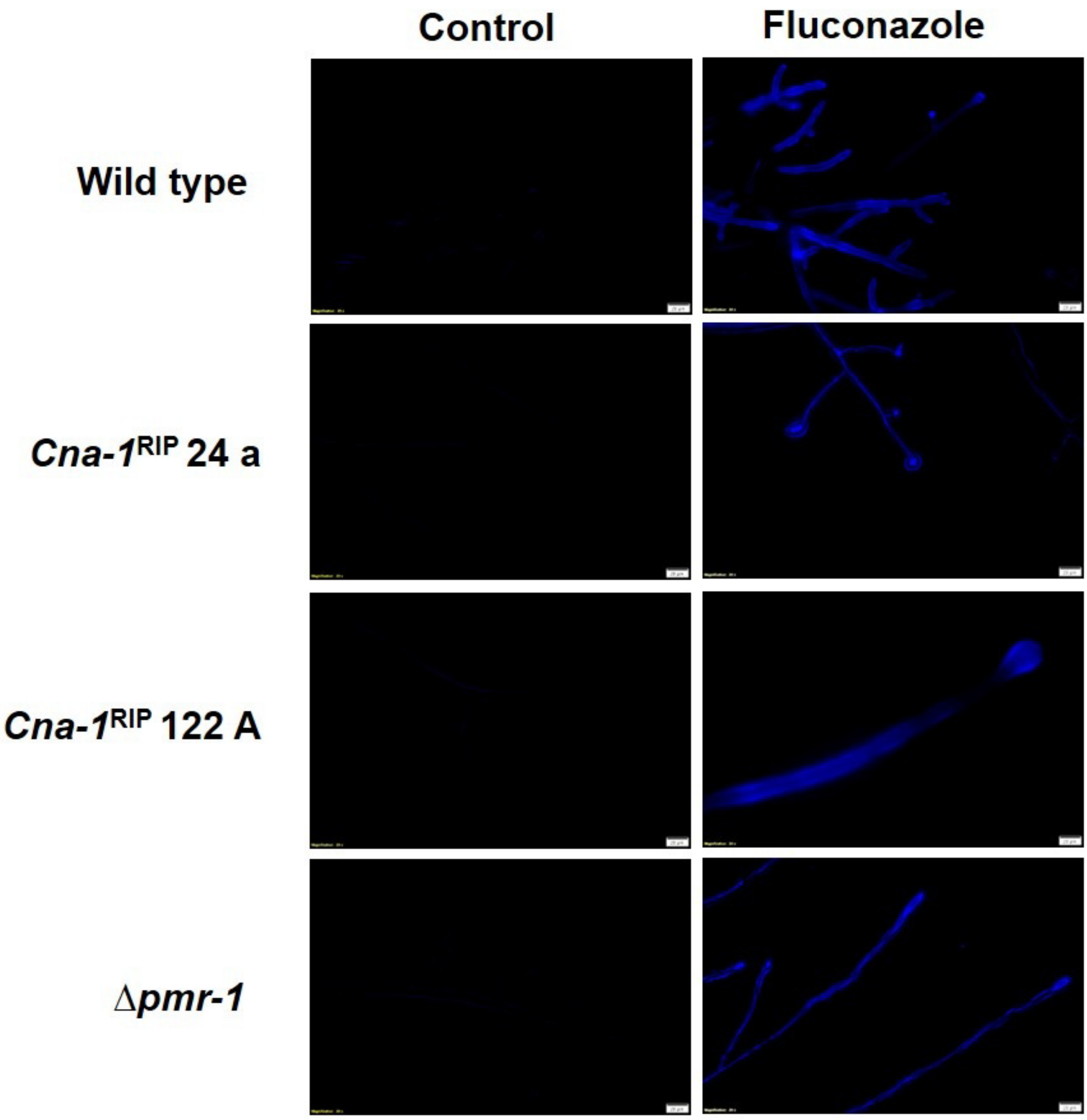

Figure 3.8. Analysis of Ca^{2+} gradient. The Ca^{2+} gradient in the *N. crassa* wild type, calcineurin RIP, and Δ*pmr-1* mutants were obtained with or without (control) the treatment of fluconazole. The CTC fluorescence images of the *N. crassa* strains were captured during the hyphal development stage on VG agar medium after 12 h of incubation at 30 °C in the dark. The hyphae were then treated with 200 µM of CTC prepared in 0.1% DMSO. The fluorescence images were captured using the DAPI filter of a trinocular inverted fluorescence microscope (Nikon ECLIPSE E200, Japan), with an exposure time of 300–400 ms. The images are shown here with consistent magnifications, where the scale bar represents 20 µm. Background and lighting normalization were performed using ImageJ.

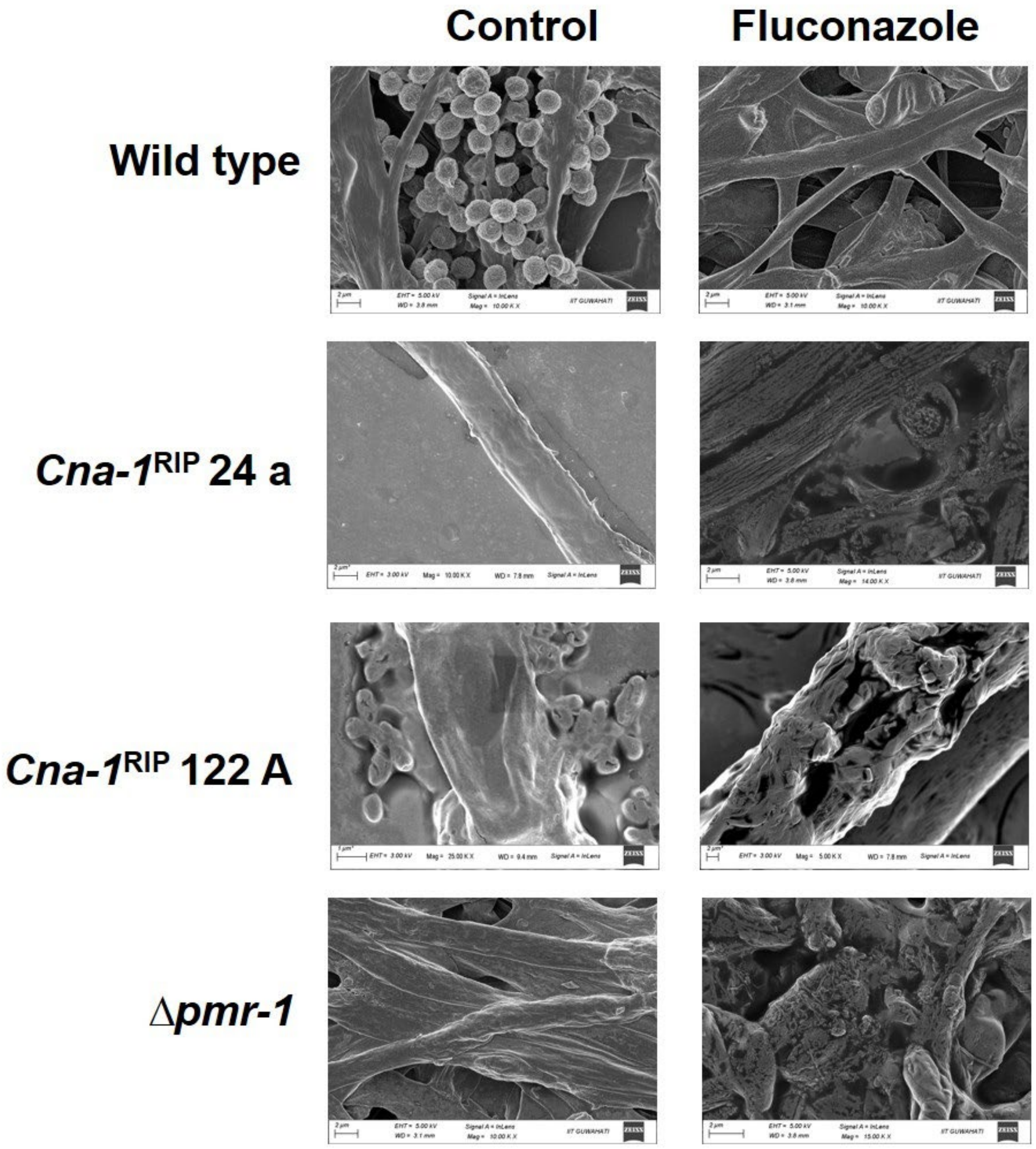

Figure 3.9. Analysis of the effect of fluconazole on cellular surface morphology in the *N. crassa* strains using FESEM. The images were captured using a FESEM microscope (Zeiss, Germany) to evaluate the effect of fluconazole treatment on the hyphal morphology in the *N. crassa* wild type and mutant strains. The strains were treated with fluconazole at half of the MIC (Table 3.1) and compared to untreated controls.

3.3 Discussion

This chapter described the determination of MIC for azole drugs fluconazole, itraconazole, and ketoconazole in the *N. crassa*. In addition, I also investigated the effect fluconazole, itraconazole, and ketoconazole in the *N. crassa cna-1* and *pmr-1* mutants. The *cna-1* and *pmr-1* mutants showed multiple defects in ergosterol biosynthesis, ROS production, hyphal morphology, and calcium accumulation under the azole drugs treatment. I found that fluconazole, itraconazole, and ketoconazole caused a significant reduction in hyphal growth in *N. crassa*. Fluconazole exhibited the most severe effect on hyphal branching, especially in the *Cna-1*$^{\mathrm{RIP}}$ 24 a mutant, while itraconazole induced bulging structures at hyphal tips, and ketoconazole reduced hyphal tip extension. Although azole drugs share a common mechanism of action by targeting 14α-sterol demethylase enzyme (Erg11), structural and bioavailability differences in the azole drugs may account for variations in their antifungal efficacy. Fluconazole has a higher bioavailability compared to itraconazole, which could explain its stronger inhibition of hyphal branching in the calcineurin mutants (Partha et al. 2022). The formation of bulging hyphal tips under itraconazole treatment suggested a structural response to membrane perturbation caused by azole inhibition of ergosterol synthesis (Figure 3.4). Ergosterol is an essential component of fungal membranes (Rodrigues 2018). Previous studies have reported similar swollen hyphal morphology in the soil borne Oomycota *Pythium aphanidermatum* upon exposure to antifungal extracts from the Ascomycota *Talaromyces variabilis* (Halo et al. 2019). In *C. albicans*, reduced ERG11 activity causes impaired hyphal formation (Lees et al. 1990). Antifungal drugs are known to inhibit fungal growth by disrupting ergosterol biosynthesis (Herrick et al. 2024). In the *N. crassa Cna-1*$^{\mathrm{RIP}}$ and Δ*pmr-1* mutants ergosterol content was reduced under the azole treatments (Figure 3.5). The azole-induced reduction of ergosterol was consistent with findings in *C. albicans* and *C. glabrata* where azole treatment caused accumulation of sterol intermediates, resulting in structural defects in the membrane (Ghannoum and Rice 1999; Hosogaya et al. 2013). The expression of the *cna-1* gene remained unchanged in the presence of fluconazole, itraconazole, and ketoconazole (Figure 3.7A). This lack of transcriptional response may be due to alternative or compensatory stress-response pathways that minimize changes in CNA-1 under azole-induced stress. In addition, it is possible that exposure to these antifungal agents triggers post-translational modifications that modify calcineurin activity or influence its interaction with other regulatory proteins, as previously observed in *C. neoformans* under cationic stress (Lev et al. 2012). Although the *cna-1* gene did not show transcriptional changes, other indicators such as increased ROS levels and reduced hyphal growth under azole conditions, demonstrate an active stress response. Interestingly, *pmr-1* expression was significantly upregulated under itraconazole treatment (Figure 3.7 B). In *S. cerevisiae*, deletion of the PMR1 gene potentiates antifungal effects of dodecanol that depend on intracellular Ca^{2+} accumulation (Oyama et al. 2020). Thus, the P-type Ca^{2+} ATPase pump PMR-1 might be involved in drug efflux, a strategy necessary for survival under azole stress. Azole drugs induce oxidative stress and elevate ROS levels in fungal cells (Zhu et al. 2023). I also observed an increase in the ROS levels in the *Cna-1*^{RIP} 24 a and Δ*pmr-1* mutants in response to the fluconazole and itraconazole (Figure 3.6 C, D). Therefore, calcineurin and PMR-1 might be necessary to mitigate oxidative stress during azole treatment. The antifungal activity of azoles has also been linked to mitochondrial ROS production (Shekhova et al. 2017b). The oxidative stress condition is a critical factor in azole-induced cell death (Shekhova et al. 2017b; Gonzalez-Jimenez et al. 2023). In *A. fumigatus* and *C. albicans*, mitochondrial complex I is a major contributor to ROS generation under antifungal stress (Hirst et al. 2008; Gonzalez-Jimenez et al. 2023). Interestingly, rotenone, a mitochondrial complex I inhibitor, has been shown to reduce ROS production and lower azole susceptibility, suggesting that complex I plays a role in the antifungal activity of azoles (Shekhova et al. 2017b).

Calcium signaling is crucial for fungal growth, development, and stress responses (Giuraniuc et al. 2023). The increased Ca^{2+} accumulation in the *Cna-1*^{RIP} and Δ*pmr-1* mutants under fluconazole treatment suggested a disruption of Ca^{2+} homeostasis. In *S. cerevisiae* and *C. albicans*, calcineurin mediates Ca^{2+}-induced stress responses via the Crz1p transcription factor (Gamarra et al. 2010; Liu et al. 2015). In our study, the impaired Ca^{2+} regulation in calcineurin and *pmr-1* mutants may sensitize the *N. crassa* mutants to azole drugs. In summary, these findings suggested that calcineurin and the Ca^{2+} ATPase pump PMR-1 are involved in antifungal drug susceptibility, ergosterol biosynthesis, ROS production, normal cytoplasmic Ca^{2+} level, and hyphal integrity under the azole drug treatments in *N. crassa.* Calcineurin inhibitors, such as cyclosporine A and tacrolimus, have been explored as potential adjuvants to azole therapy in pathogenic fungi (Cho et al. 2023). Similarly, inhibitors targeting *pmr-1* or its homologs could provide a novel strategy for overcoming azole resistance in fungal pathogens. The next chapter focuses on the interactions of these proteins, namely CNA-1, CNB-1, and PMR-

1, with azole drugs fluconazole, itraconazole, and ketoconazole using molecular docking and molecular dynamics simulations.

References:

Antebi A, Fink GR (1992) The yeast Ca (2+)-ATPase homologue, PMR1, is required for normal Golgi function and localizes in a novel Golgi-like distribution. Molecular biology of the cell 3:633-654

Aramburu J, Heitman J, Crabtree GR (2004) Calcineurin: a central controller of signalling in eukaryotes: Workshop on the calcium/calcineurin/nfat pathway: Regulation and function. EMBO reports 5:343-348

Bandyopadhyay J et al. (2002) Calcineurin, a calcium/calmodulin-dependent protein phosphatase, is involved in movement, fertility, egg laying, and growth in Caenorhabditis elegans. Molecular biology of the cell 13:3281-3293

Bates S et al. (2005) Candida albicans Pmr1p, a secretory pathway P-type Ca2+/Mn2+-ATPase, is required for glycosylation and virulence. Journal of Biological Chemistry 280:23408-23415

Berridge MJ, Lipp P, Bootman MD (2000) The versatility and universality of calcium signalling. Nature reviews Molecular cell biology 1:11-21

Borkovich KA et al. (2004) Lessons from the genome sequence of Neurospora crassa: tracing the path from genomic blueprint to multicellular organism. Microbiology and molecular biology reviews 68:1-108

Bowman BJ, Abreu S, Johl JK, Bowman EJ (2012) The pmr gene, encoding a Ca2+-ATPase, is required for calcium and manganese homeostasis and normal development of hyphae and conidia in Neurospora crassa. Eukaryotic Cell 11:1362-1370

Cerella C, Diederich M, Ghibelli L (2010) The dual role of calcium as messenger and stressor in cell damage, death, and survival. International journal of cell biology 2010

Chen Y-L et al. (2011) Calcineurin controls drug tolerance, hyphal growth, and virulence in Candida dubliniensis. Eukaryotic cell 10:803-819

Chin D, Means AR (2000) Calmodulin: a prototypical calcium sensor. Trends in cell biology 10:322-328

Cho O, Takada S, Odaka T, Futamura S, Kurakado S, Sugita T (2023) Tacrolimus (FK506) Exhibits Fungicidal Effects against Candida parapsilosis Sensu Stricto via Inducing Apoptosis. Journal of Fungi 9:778

Cowen LE, Sanglard D, Howard SJ, Rogers PD, Perlin DS (2015) Mechanisms of antifungal drug resistance. Cold Spring Harbor perspectives in medicine 5

de Haan LR et al. (2022) Experimental conditions that influence the utility of 2′ 7′-dichlorodihydrofluorescein diacetate (DCFH2-DA) as a fluorogenic biosensor for mitochondrial redox status. Antioxidants 11:1424

Dong Q, Wallrad L, Almutairi BO, Kudla J (2022) Ca2+ signaling in plant responses to abiotic stresses. Journal of Integrative Plant Biology 64:287-300

Ellis S, Rose M, Grindle M (1991) Identification of a sterol mutant of Neurospora crassa deficient in Δ14, 15-reductase activity. Microbiology 137:2627-2630

Ferreira RT, Silva ARC, Pimentel C, Batista-Nascimento L, Rodrigues-Pousada C, Menezes RA (2012) Arsenic stress elicits cytosolic Ca2+ bursts and Crz1 activation in Saccharomyces cerevisiae. Microbiology 158:2293-2302

Forrester SJ, Kikuchi DS, Hernandes MS, Xu Q, Griendling KK (2018) Reactive oxygen species in metabolic and inflammatory signaling. Circulation research 122:877-902

Galagan JE et al. (2003) The genome sequence of the filamentous fungus Neurospora crassa. Nature 422:859-868

Gamarra S, Rocha EMF, Zhang Y-Q, Park S, Rao R, Perlin DS (2010) Mechanism of the synergistic effect of amiodarone and fluconazole in Candida albicans. Antimicrobial agents and chemotherapy 54:1753-1761

Gessler NN, Aver’yanov AA, Belozerskaya T (2007) Reactive oxygen species in regulation of fungal development. Biochemistry (Moscow) 72:1091-1109

Ghannoum MA, Rice LB (1999) Antifungal agents: mode of action, mechanisms of resistance, and correlation of these mechanisms with bacterial resistance. Clinical microbiology reviews 12:501-517

Giuraniuc C et al. (2023) Dynamic calcium-mediated stress response and recovery signatures in the fungal pathogen, Candida albicans. Mbio 14:e01157-01123

Goni R, García P, Foissac S (2009) The qPCR data statistical analysis. Integromics White Paper 1:1-9

Gonzalez-Jimenez I, Perlin DS, Shor E (2023) Reactive oxidant species induced by antifungal drugs: identity, origins, functions, and connection to stress-induced cell death. Frontiers in Cellular and Infection Microbiology 13:1276406

Gupta SS, Ton V-K, Beaudry V, Rulli S, Cunningham K, Rao R (2003) Antifungal activity of amiodarone is mediated by disruption of calcium homeostasis. Journal of Biological Chemistry 278:28831-28839

Ha KC, White TC (1999) Effects of azole antifungal drugs on the transition from yeast cells to hyphae in susceptible and resistant isolates of the pathogenic yeast Candida albicans. Antimicrobial agents and chemotherapy 43:763-768

Halo BA, Al-Yahyai RA, Maharachchikumbura SS, Al-Sadi AM (2019) Talaromyces variabilis interferes with Pythium aphanidermatum growth and suppresses Pythium-induced damping-off of cucumbers and tomatoes. Scientific reports 9:11255

Herrick EJ, Hashmi MF (2019) Antifungal ergosterol synthesis inhibitors.

Herrick EJ, Patel P, Hashmi MF (2024) Antifungal ergosterol synthesis inhibitors. In: StatPearls [Internet]. StatPearls Publishing

Hirst J, King MS, Pryde KR (2008) The production of reactive oxygen species by complex I. In. Portland Press Ltd.

Hosogaya N et al. (2013) The heme-binding protein Dap1 links iron homeostasis to azole resistance via the P450 protein Erg11 in Candida glabrata. FEMS yeast research 13:411-421

Juarros-Basterretxea J, Aonso-Diego G, Postigo Á, Montes-Álvarez P, Menéndez-Aller Á, García-Cueto E (2024) Post-hoc tests in one-way ANOVA: The case for normal distribution. Methodology 20:84-99

Juvvadi PR et al. (2013) Phosphorylation of calcineurin at a novel serine-proline rich region orchestrates hyphal growth and virulence in Aspergillus fumigatus. PLoS pathogens 9:e1003564

Juvvadi PR, Lamoth F, Steinbach WJ (2014) Calcineurin-mediated regulation of hyphal growth, septation, and virulence in Aspergillus fumigatus. Mycopathologia 178:341-348

Juvvadi PR, Lee SC, Heitman J, Steinbach WJ (2017) Calcineurin in fungal virulence and drug resistance: Prospects for harnessing targeted inhibition of calcineurin for an antifungal therapeutic approach. Virulence 8:186-197

Kang HA et al. (1998) Cloning and characterization of the Hansenula polymorpha homologue of the Saccharomyces cerevisiae PMR1 gene. Yeast 14:1233-1240

Karkowska-Kuleta J, Rapala-Kozik M, Kozik A (2009) Fungi pathogenic to humans: molecular bases of virulence of Candida albicans, Cryptococcus neoformans and Aspergillus fumigatus. Acta Biochimica Polonica 56:211-224

Kellermayer R (2005) Hailey–Hailey disease as an orthodisease of PMR1 deficiency in Saccharomyces cerevisiae. FEBS letters 579:2021-2025

Klee CB, Ren H, Wang X (1998) Regulation of the calmodulin-stimulated protein phosphatase, calcineurin. Journal of Biological Chemistry 273:13367-13370

Kmetzsch L, Staats CC, Rodrigues ML, Schrank A, Vainstein MH (2011) Calcium signaling components in the human pathogen Cryptococcus neoformans: Cryptococcus neoformans. Communicative & integrative biology 4:186-187

Kumar A, Roy A, Deshmukh MV, Tamuli R (2020) Dominant mutants of the calcineurin catalytic subunit (CNA-1) showed developmental defects, increased sensitivity to stress conditions, and CNA-1 interacts with CaM and CRZ-1 in Neurospora crassa. Archives of microbiology 202:921-934

Lees ND, Broughton M, Sanglard D, Bard M (1990) Azole susceptibility and hyphal formation in a cytochrome P-450-deficient mutant of Candida albicans. Antimicrobial agents and chemotherapy 34:831-836

Lev S, Desmarini D, Chayakulkeeree M, Sorrell TC, Djordjevic JT (2012) The Crz1/Sp1 transcription factor of Cryptococcus neoformans is activated by calcineurin and regulates cell wall integrity. PloS one 7:e51403

Li H, Rao A, Hogan PG (2011) Interaction of calcineurin with substrates and targeting proteins. Trends in cell biology 21:91-103

Li Y, Zhang Y, Lu L (2019) Calcium signaling pathway is involved in non-CYP51 azole resistance in Aspergillus fumigatus. Medical mycology 57:S233-S238

Li Y et al. (2020) Mitochondrial dysfunctions trigger the calcium signaling-dependent fungal multidrug resistance. Proceedings of the National Academy of Sciences 117:1711-1721

Liu F-f et al. (2015) Calcium signaling mediates antifungal activity of triazole drugs in the Aspergilli. Fungal Genetics and Biology 81:182-190

Miyazaki T et al. (2010) Roles of calcineurin and Crz1 in antifungal susceptibility and virulence of Candida glabrata. Antimicrobial agents and chemotherapy 54:1639-1643

Mount HOC et al. (2018) Global analysis of genetic circuitry and adaptive mechanisms enabling resistance to the azole antifungal drugs. PLoS genetics 14:e1007319

Naewbanij M, Seib P, Burroughs R, Seitz LM, Chung D (1984) Determination of ergosterol using thin-layer chromatography and ultraviolet spectroscopy. Cereal Chem 61:385-388

Oyama M, Tamaki H, Yamaguchi Y, Ogita A, Tanaka T, Fujita K-i (2020) Deletion of the Golgi Ca2+-ATPase PMR1 gene potentiates antifungal effects of dodecanol that depend on intracellular Ca2+ accumulation in budding yeast. FEMS Yeast Research 20 doi: 10.1093/femsyr/foaa003

Park H-S et al. (2016) Calcineurin targets involved in stress survival and fungal virulence. PLoS pathogens 12:e1005873

Parks LW, Casey WM (1995) Physiological implications of sterol biosynthesis in yeast. Annual review of microbiology 49:95-116

Partha ADSL, Widodo ADW, Endraswari PD (2022) Evaluation of fluconazole, itraconazole, and voriconazole activity onCandida albicans: A case control study. Annals of Medicine and Surgery 84

Pinchai N et al. (2010) The Aspergillus fumigatus P-type Golgi apparatus Ca2+/Mn2+ ATPase PmrA is involved in cation homeostasis and cell wall integrity but is not essential for pathogenesis. Eukaryotic Cell 9:472-476

Prakash A, Sengupta S, Aparna K, Kasbekar DP (1999) The erg-3 (sterol Δ14, 15-reductase) gene of Neurospora crassa: generation of null mutants by repeat-induced point mutation and complementation by proteins chimeric for human lamin B receptor sequences. Microbiology 145:1443-1451

Rodrigues ML (2018) The multifunctional fungal ergosterol. MBio 9:10.1128/mbio. 01755-01718

Sanglard D, Ischer F, Marchetti O, Entenza J, Bille J (2003) Calcineurin A of Candida albicans: involvement in antifungal tolerance, cell morphogenesis and virulence. Molecular microbiology 48:959-976

Shapiro SS, Wilk MB (1965) An analysis of variance test for normality (complete samples). Biometrika 52:591-611

Shekhova E, Kniemeyer O, Brakhage AA (2017a) Induction of mitochondrial reactive oxygen species production by itraconazole, terbinafine, and amphotericin B as a mode of action against Aspergillus fumigatus. Antimicrobial Agents and Chemotherapy 61:10.1128/aac. 00978-00917

Shekhova E, Kniemeyer O, Brakhage AA (2017b) Induction of mitochondrial reactive oxygen species production by itraconazole, terbinafine, and amphotericin B as a mode of action against Aspergillus fumigatus. Antimicrobial Agents and Chemotherapy 61:e00978-00917

Sorin A, Rosas G, Rao R (1997) PMR1, a Ca2+-ATPase in yeast Golgi, has properties distinct from sarco/endoplasmic reticulum and plasma membrane calcium pumps. Journal of Biological Chemistry 272:9895-9901

Szigeti R, Miseta A, Kellermayer R (2005) Calcium and magnesium competitively influence the growth of a PMR1 deficient Saccharomyces cerevisiae strain. FEMS microbiology letters 251:333-339

Tamuli R, Deka R, Borkovich KA (2016) Calcineurin subunits A and B interact to regulate growth and asexual and sexual development in Neurospora crassa. PloS one 11:e0151867

Thewes S (2014) Calcineurin-Crz1 signaling in lower eukaryotes. Eukaryotic cell 13:694-705

Víglaš J, Olejníková P (2023) Antifungal azoles trigger a xenobiotic detoxification pathway and chitin synthesis in Neurospora crassa. Research in Microbiology:104055

Virdi AS, Thakur A, Dutt S, Kumar S, Singh P (2009) A sorghum 85 kDa heat stress-modulated protein shows calmodulin-binding properties and cross-reactivity to anti-Neurospora crassa Hsp 80 antibodies. FEBS letters 583:767-770

Vu BG, Simonicova L, Moye-Rowley WS (2023) Calcineurin is required for Candida glabrata Pdr1 transcriptional activation. Mbio 14:e02416-02423

Zhang J et al. (2012) Calcineurin is required for pseudohyphal growth, virulence, and drug resistance in Candida lusitaniae.

Zhang S (1998) Fourteen Homogeneity of Variance Tests: When and How To Use Them.

Zhang Y-Q, Rao R (2007) Global disruption of cell cycle progression and nutrient response by the antifungal agent amiodarone. Journal of biological chemistry 282:37844-37853

Zhao Y, Du J, Xiong B, Xu H, Jiang L (2013) ESCRT components regulate the expression of the ER/Golgi calcium pump gene PMR1 through the Rim101/Nrg1 pathway in budding yeast. Journal of molecular cell biology 5:336-344

Zhou M et al. (2022) Experimental Evolution of Multidrug Resistance in Neurospora crassa under Antifungal Azole Stress. Journal of Fungi 8:198

Zhu G, Chen S, Zhang Y, Lu L (2023) Mitochondrial membrane-associated protein mba1 confers antifungal resistance by affecting the production of reactive oxygen species in aspergillus fumigatus. Antimicrobial Agents and Chemotherapy 67:e00225-00223

Chapter 4

Studies on the interactions of the CNA-1, CNB-1, and PMR-1 proteins with azole drugs using molecular docking and molecular dynamics simulations

4.1. Introduction

Calcineurin is the only serine-threonine phosphatase that requires both calcium (Ca^{2+})- and calmodulin (CaM) for its activity (Li et al. 2011). Calcineurin consists of a catalytic subunit A (CNA-1) and a regulatory subunit B (CNB-1), and these subunits physically interact (Tamuli et al. 2016). Calcineurin is crucial for virulence and drug resistance in various pathogenic fungi, including *A. fumigatus*, *C. albicans*, and *C. neoformans* (Karkowska-Kuleta et al. 2009). In *A. fumigatus* and *C. albicans*, calcineurin regulates both ergosterol biosynthesis and drug efflux that are crucial mechanisms contributing to azole resistance (Cowen et al. 2015). The *pmr-1* gene also plays a key role in regulating Ca^{2+} and Mn^{2+} ion transport across the Golgi membrane, maintaining cell wall integrity, and conferring antifungal drug resistance in *A. fumigatus* and *C. albicans* (Bates et al. 2005; Pinchai et al. 2010). Furthermore, *pmrA* is essential for the structural integrity of the cell wall in several fungi, including *A. fumigatus* and *N. crassa* (Antebi and Fink 1992; Pinchai et al. 2010; Bowman et al. 2012).

In chapter 3, I described that the *N. crassa* calcineurin RIP mutants and Δ*pmr-1* knockout mutants were more susceptible to azole drugs. In the current chapter, I discuss the interactions of the calcineurin subunits CNA-1 and CNB-1, and the Ca^{2+} ATPase PMR-1 with the azole drugs fluconazole, itraconazole, and ketoconazole. I performed molecular docking and molecular dynamics (MD) simulations to investigate the interactions of the CNA-1, CNB-1, and PMR-1 proteins and azole drugs. Molecular docking and MD simulations studies also revealed the key interacting amino acid residues of CNA-1, CNB-1, and PMR-1 proteins in binding with fluconazole, itraconazole, and ketoconazole drugs. I also determined the binding affinities of CNA-1, CNB-1, and PMR-1 with fluconazole, itraconazole, and ketoconazole. Identification of the key amino acid residues that are critical for the interactions with azole drugs might lead to the development of new, target-specific antifungal drugs in the future. A molecular understanding of drug-protein interactions is vital for the advancement of antifungal drug therapy and for preventing the emergence of drug resistance in fungi.

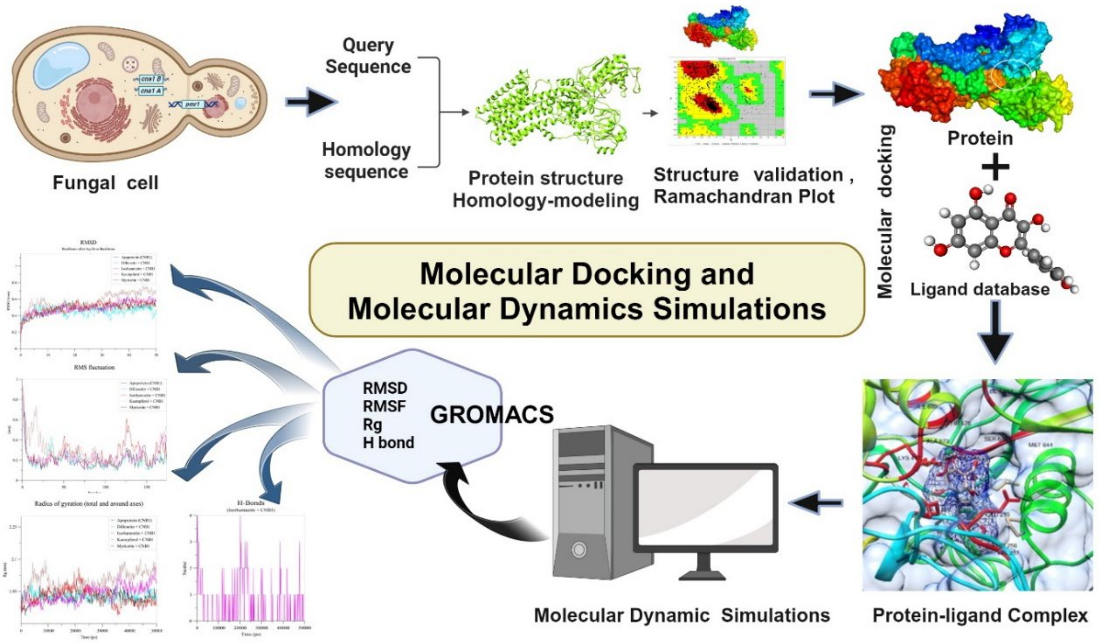

Figure 4.1. Schematics illustrating the molecular docking and MD simulations used to study protein-ligand interactions. The workflow described in this chapter includes the prediction of protein structure followed by structure validation, protein-ligand complex formation, molecular docking, MD simulations, and the analysis of the output.

4.2. Results

4.2.1. Structure prediction of CNA-1, CNB-1, and PMR-1 protein and molecular docking

4.2.1.1. CNA-1, CNB-1, and PMR-1 proteins structure prediction

The protein structure prediction of the CNA-1, CNB-1, and PMR-1 proteins was performed using I-TASSER tool (Figure 4.2 A.i, B.i, C.i). The predicted protein structures were validated using Ramachandran plots (Sobolev et al. 2020). The 3D protein structures of CNA-1, CNB-1, and PMR-1 were superimposed with their respective protein templates using UCSF Chimera (https://www.cgl.ucsf.edu/chimera/download.html). The superimposed structures were represented as ribbon structures (Figure 4.2 A.ii, B.ii, C.iii); and the multiple sequence alignment (MSA) of each protein was also performed (Figure 4.2 A.iii, B.iii, C.iii). The predicted structure of CNA-1 (*N. crassa* OR74A; NCBI Ref. Seq: XP_011394598.1) (yellow color) showed superimposition with the crystal structures of calcineurin from *C. neoformans* var. *grubii*, *Rattus norvegicus*, and *Homo sapiens* (Figure 4.2 A-i). The 3D protein structure of CNB-1 from *N. crassa* was superimposed with the crystal structure of calcineurin A and B in complex with FKBP12 and FK506 from *Coccidioides immitis* RS, as well as with the crystal structure of *C. neoformans* calcineurin A and B, FKBP12, and FK-506 (Figure 4.2 B-i). Similarly, the 3D protein structure of PMR-1 (*N. crassa* OR74A; NCBI Ref. Seq: XP_964218.1) (olive drab color) showed superimposition with the crystal structure of the sodium-potassium pump from *Sus scrofa*, and the gastric proton pump from *S. scrofa*, and the WT transporter state 1 protein from *H. sapiens* (Figure 4.2 C-i).

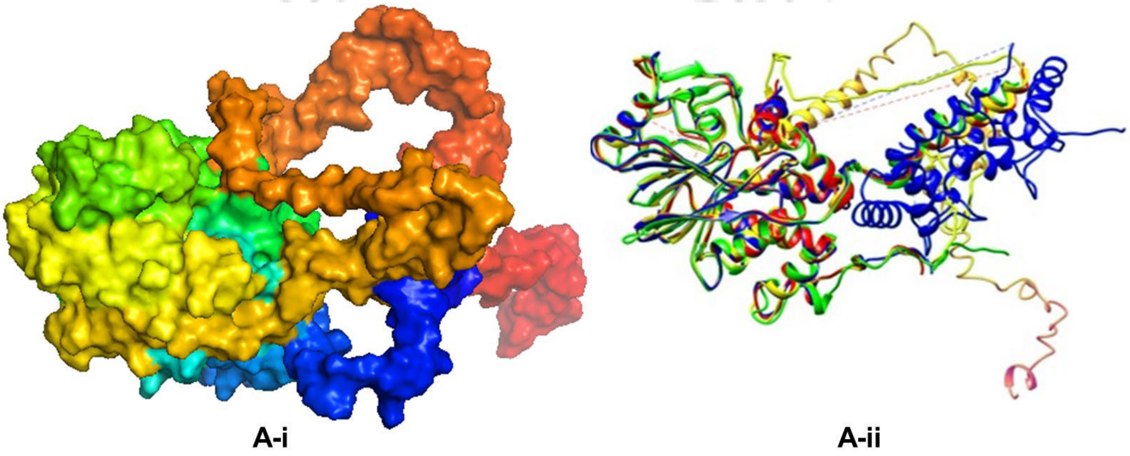

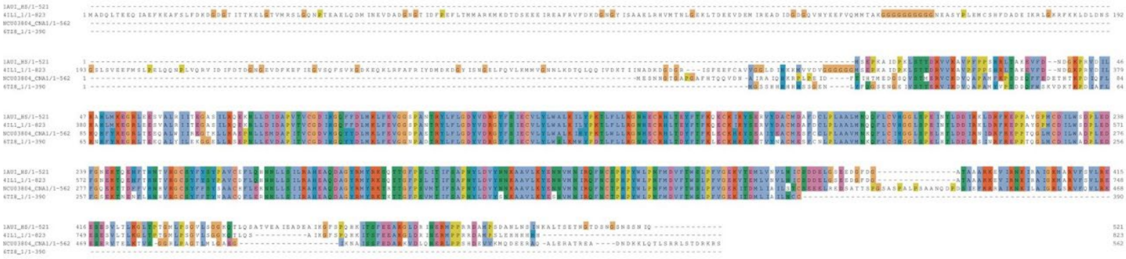

A-iii

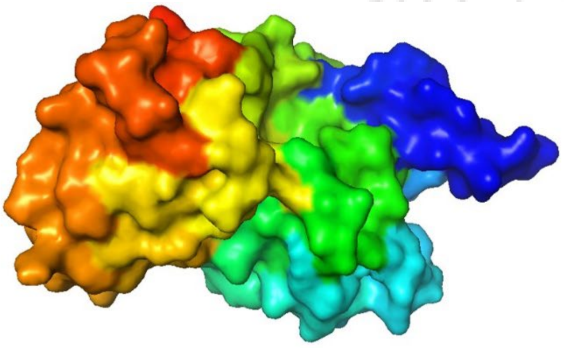

B-i

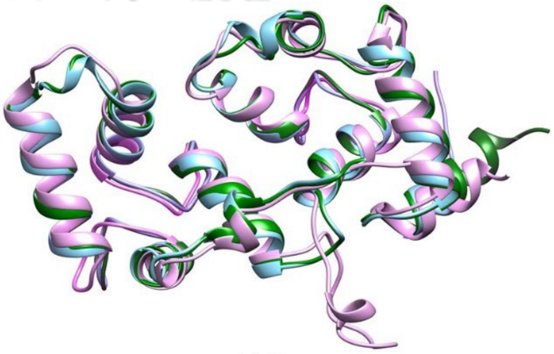

B-ii

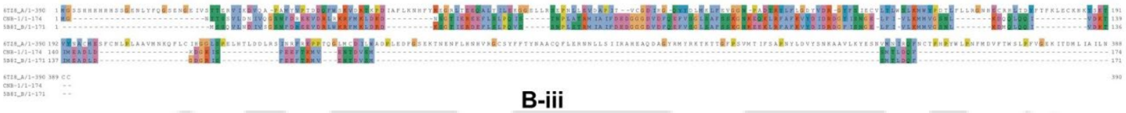

B-iii

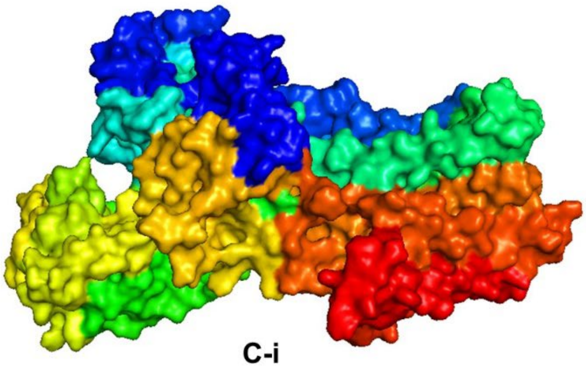

C-i

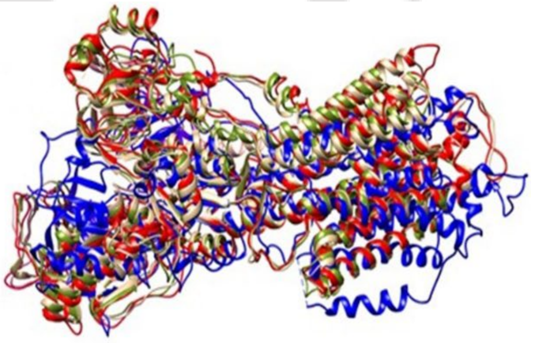

C-ii

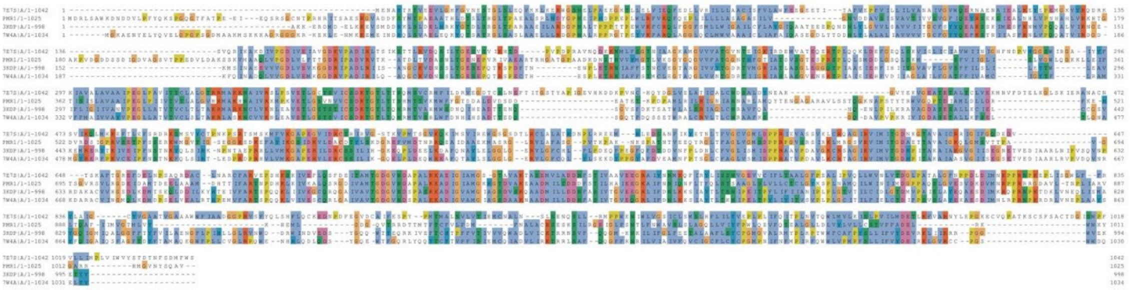

Figure 4.2. Analysis of the CNA-1, CNB-1, and PMR-1 predicted protein structures. (A-i, B-i, and C-i) The predicted structures of CNA-1, CNB-1, and PMR-1, respectively. (A-ii, B-ii, and C-ii) The superimposed structures of CNA-1, CNB-1, and PMR-1 from *N. crassa* with their respective protein template are shown. CNA-1 shows identity with the crystal structures of calcineurin from *H. sapiens* (PDB ID: 1AUI|A; red color), *Rattus norvegicus* (PDB ID: 4IL1|A; Blue color), and *C. neoformans* var *grubii* H99 (PDB ID: 6TZ8|A; Green color). (B-ii) CNB-1 shows identity with the crystal structure of *C. immitis* calcineurin A and B in complex with FKBP12 and FK506 (RS PDB ID: 5B8I; blue color), and with the crystal structure of *C. neoformans* calcineurin A and B, FKBP12 with FK-506 (PDB ID 6TZ8). (C-ii) PMR-1 shows identity with sodium potassium pump from the organism *S. scrofa* (PDB ID: 3KDP|A; red color), gastric proton pump from the *S. scorofa* (PDB ID: 7W4a|A; tan color), and WT transporter state 1 protein from the *H. sapiens* (PDB ID: 7E7s|A;(Blue color). (A-iii, B-iii and C-iii) The multiple sequence alignment (MSA) of CNA-1, CNB-1 and PMR-1 with their respective protein template.

4.2.2. Molecular docking of CNA-1, CNB-1, and PMR-1 with azole antifungals

I performed molecular docking studies to analyze the interactions of CNA-1, CNB-1, and PMR-1 with fluconazole, itraconazole, and ketoconazole. The binding of azole drugs at the active site of the predicted structures of CNA-1, CNB-1, and PMR-1 was analyzed (Figure 4.3 A-i, B-i, C-i), and the ligand binding sites in these proteins were visualized using UCSF Chimera (Figure 4.3 A-ii, B-ii, C-ii). The ketoconazole-CNA-1 complex showed the highest binding affinity of −6.67 kcal/mol. In this complex, hydrogen bonds were formed with the Tyr353 and His189 residues, while hydrophobic interactions occurred with Leu350, Tyr349, Ala321, Glu320, His319, Arg292, Leu194, Trp270, Phe198, and Arg160 residues (Figure 4.4.1). In the fluconazole-CNA-1 complex, the binding affinity was −4.56 kcal/mol (Table 4.1), with hydrogen bonds formed with Tyr349, Ala321, and Arg292 residues, hydrophobic interactions involved His130, Glu320, His319, Asp156, Leu194, His189, Trp270, Asn188, Arg160, Tyr353, and Leu350 residues (Figure 4.4.2). However, the itraconazole-CNA-1 complex showed no significant binding affinity (Table 4.1). The ketoconazole-CNB-1 complex showed the highest binding affinity, with a binding energy of −5.07 kcal/mol. In this complex, hydrogen bonds formed with Arg96, while hydrophobic interactions involved Asp107, Tyr109, Glu154, Phe153, Asp103, Lys100, Arg106, Gly108, and Phe99 residues (Figure 4.4.3). Similar to the itraconazole-CNA-1 complex, itraconazole-CNB-1 complex also showed no significant binding affinity (Table 4.1). Fluconazole-CNB-1 complex showed, the binding energy with −4.2 kcal/mol with the formation of hydrogen bonds with Tyr109, Phe153, Arg96, and hydrophobic interaction with Glu154, Ser152, Phe99, Asp103, Gly108, and Lys100 residues (Figure 4.4.4).The ketoconazole-PMR-1complex exhibited the most efficient binding, with a binding energy of −7.68 kcal/mol, followed by fluconazole-PMR-1 with the binding energy −5.61 kcal/mol, and itraconazole-PMR-1 with the binding energy −3.73 kcal/mol (Table 4.1). In the ketoconazole-PMR-1 complex, hydrogen bonds formed with Asn254, while hydrophobic interactions involved Met426, Asp646, Lys417, Glu255, Ser645, Ser279, Val257, Ile259, Val282, Leu250, Asp277, Asp278, Ala247, Thr251, Glu253, Thr676, Asp672, Gly604, Ile680, and Thr418 residues (Figure 4.4.5). In the itraconazole-PMR-1 complex, only hydrophobic interactions were observed, involving Asn254, Met426, Asp646, His425, Glu255, Asn424, Ser645, Val257, Ile259, Val282, Thr287, Lys276, Asp277, Leu250, Tyr284, Asn278, Ala247, Thr251, Glu253, Thr676, Asp672, and Gly604 residues (Figure 4.4.6). In the fluconazole-PMR-1 complex, hydrogen bonds formed with Asn254, Glu255, and Asp646, while hydrophobic interactions involved Pro506, Met426, His425, Asn424, Ser645, Glu253, Asp672, Gly604, Thr418, and Lys417 residues (Figure 4.4.7).

Table 4.1. Detailed interactions between the amino acid residues in the active site of the CNA-1, CNB-1, and PMR-1 proteins with the azole drugs

Protein	Ligand/Drug	Binding affinity (kcal/mol)	Inhibition constant (Ki)	Active sites amino acid residues^{+}	
				H-bonds	Hydrophobic interactions
CNA-1	Ketoconazole	−6.67	12.95 µM	**Tyr353**, **His189**	**Leu350**, **Tyr349**, **Ala321**, **Glu320**,

					His319, **Arg292**, **Leu194**, **Trp270**, Phe198, **Arg160**
	Itraconazole	NS	NS		--
	Fluconazole	−4.56	481.56 µM	**Tyr349, Ala321, Arg292**	His130, **Glu320**, **His319**, Asp156, **Leu194**, **His189**, **Trp270**, Asn188, **Arg160**, **Tyr353**, **Leu350**
CNB-1	Ketoconazole	−5.07	191.91 µM	**Arg96**	Asp107, **Tyr109, Glu154, Phe153, Asp103**, **Lys100,** Arg106, **Gly108**, **Phe99**
	Itraconazole	NS	NS		--
	Fluconazole	−4.2	839.67 µM	**Tyr109, Phe153, Arg96**	**Glu154**, Ser152, **Phe99**, **Asp103**, **Gly108, Lys100**
PMR-1	Ketoconazole	−7.68	2.35 µM	**Asn254**	**Met426**, **Asp646**, Lys417, **Glu255**, **Ser645**, Ser279, Val257, Ile259, Val282, Leu250, Asp277, Asp278, Ala247, Thr251, **Glu253**, Thr676, **Asp672**, **Gly604**, Ile680, Thr418
	Itraconazole	−3.73	1.85 µM	--	**Asn254**, **Met426**, **Asp646**, His425, **Glu255**, Asn424, **Ser645**, Val257,

				Ile259, Val282, Thr287, Lys276, Asp277, Leu250, Tyr284, Asn278, Ala247, Thr251, **Glu253**, Thr676, **Asp672, Gly604**
Fluconazole	−5.61	77.49 µM	**Asn254**, **Glu255**, **Asp646**	Pro506, **Met426,** His425, Asn424, **Ser645, Glu253,** **Asp672, Gly604**, Thr418, Lys417

[+] The common amino acid residues interacting with the respective azole drug are highlighted in bold.

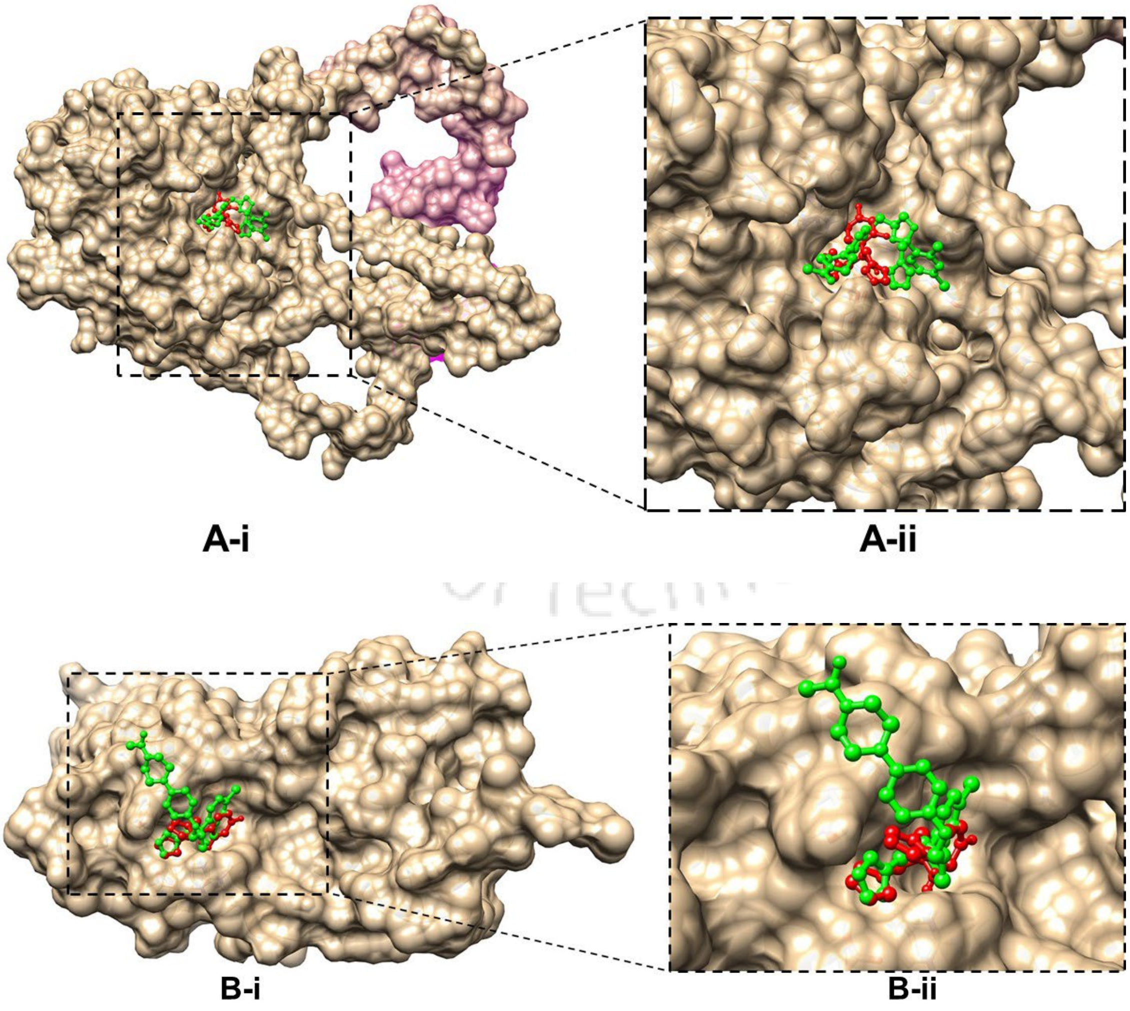

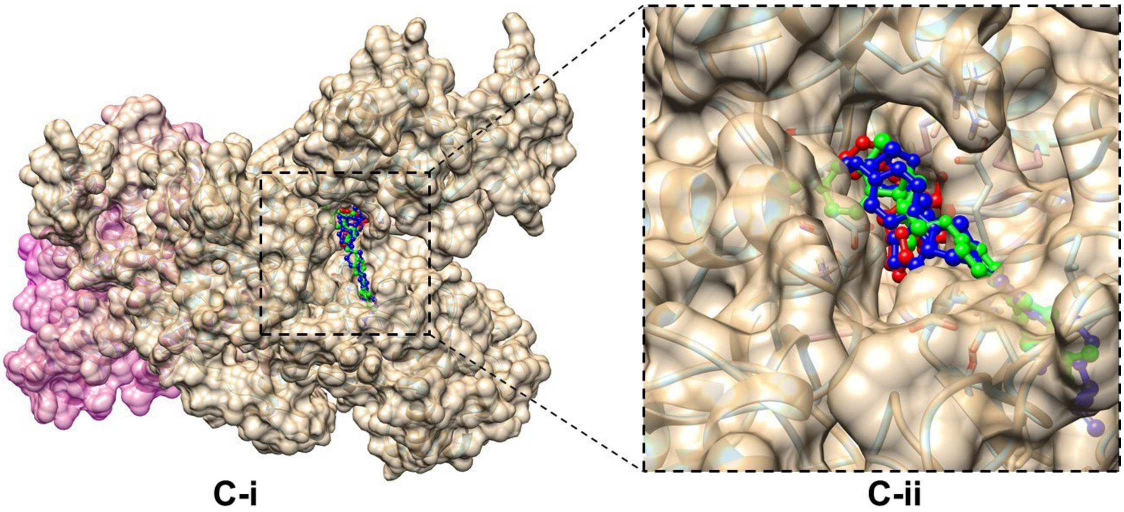

Figure 4.3. Binding of azole drugs at the active sites in the predicted protein structures. (A-i) The CNA-1 protein structure showing the binding of fluconazole (red) and ketoconazole (green) in its active site. (B-i) The CNB-1 protein structure displaying the binding of fluconazole (red) and ketoconazole (green) in its active pocket. (C-i) The PMR-1 protein structure showing the binding of fluconazole (red), itraconazole (blue), and ketoconazole (green) in its active pocket. (A-ii, B-ii, and C-ii) Magnified views of the active pockets in the protein structures with their respective ligands, visualized using UCSF Chimera.

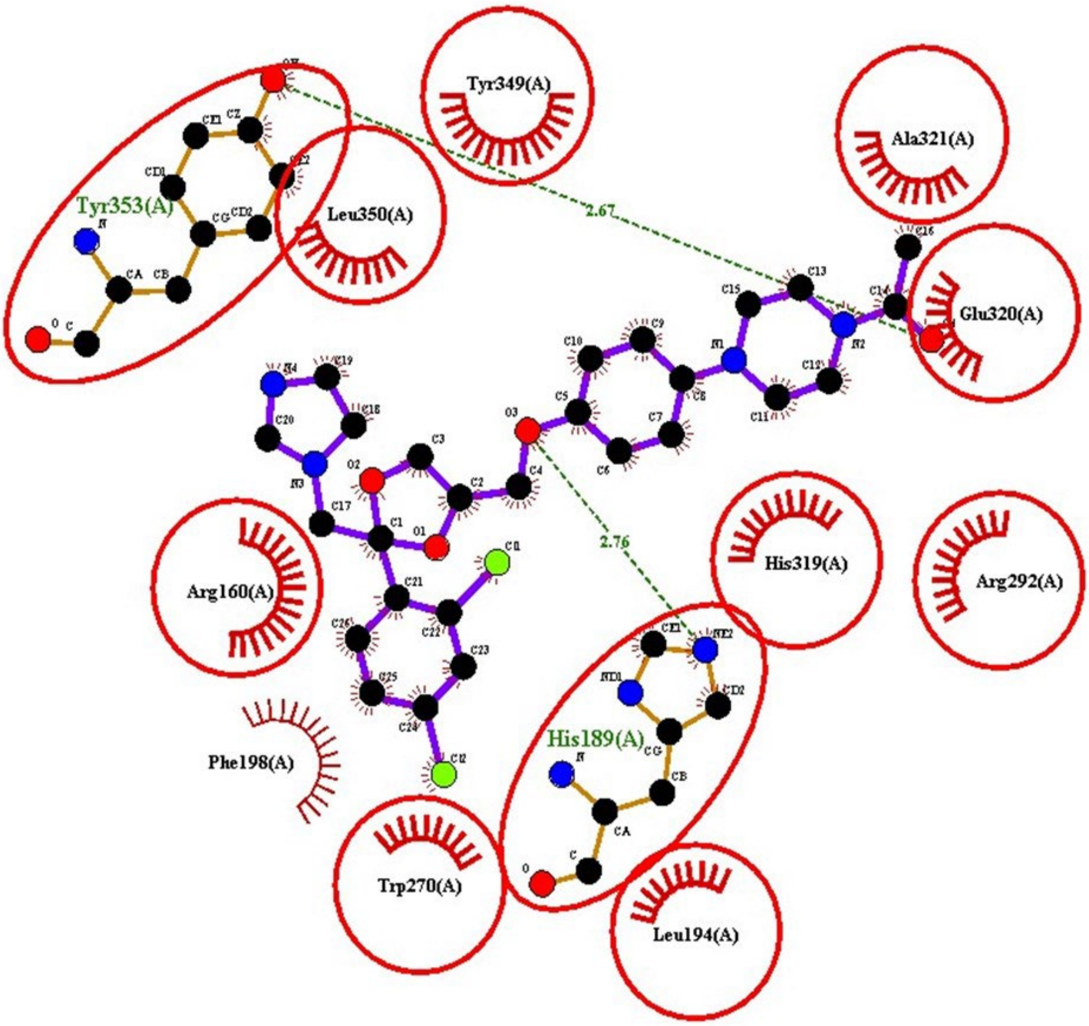

Figure 4.4.1. Molecular docking analysis of ketoconazole with the predicted structure of CNA-1. The amino acid residues interacting with ketoconazole are shown. The amino acid residues are labelled with their respective sequence positions. The Tyr353 and His189 (labelled in green) represent residues involved in hydrogen bond formation, while the dotted lines in green indicate the bond distances of 2.67 Å and 2.76 Å, respectively.

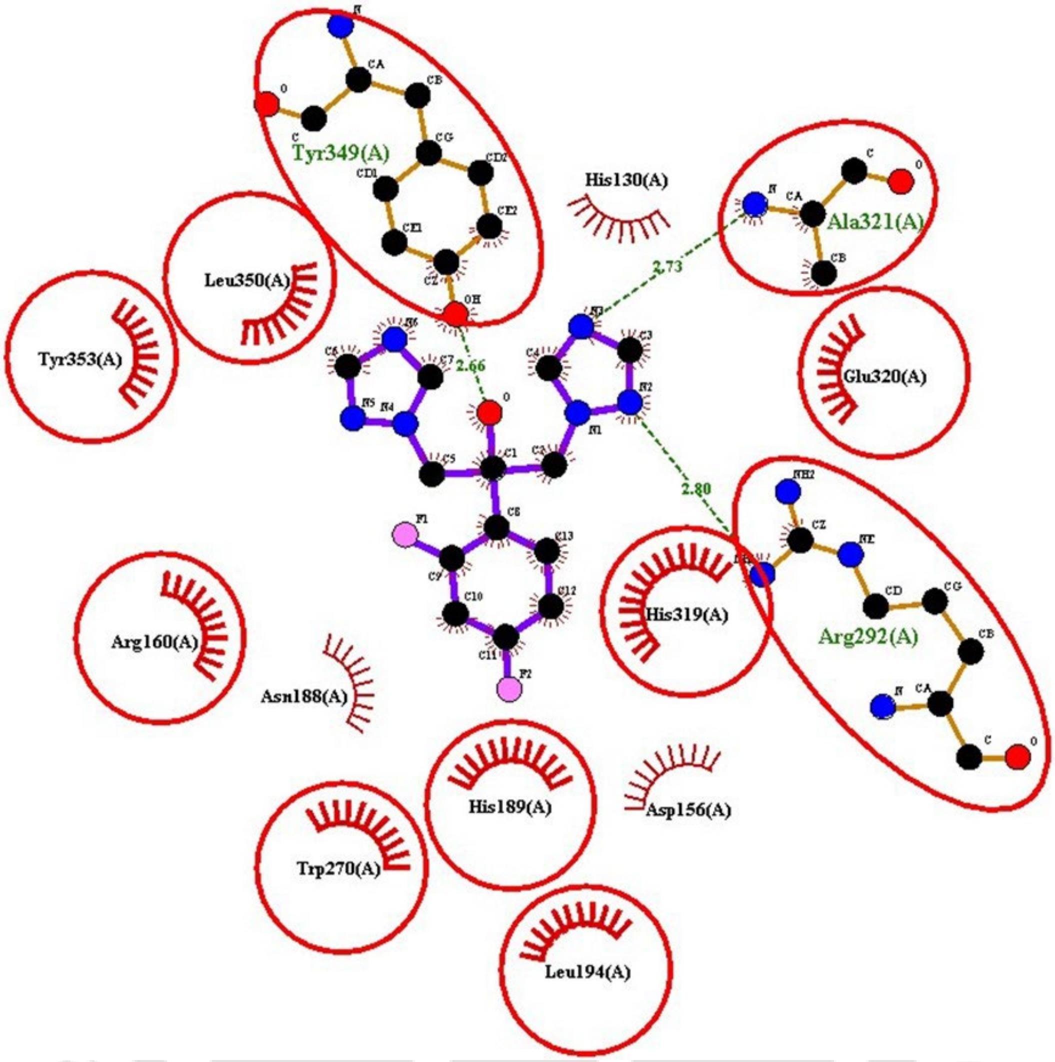

Figure 4.4.2. Molecular docking analysis of fluconazole with the predicted structure of CNA-1. The residues interacting with fluconazole are shown. The amino acid residues are labelled as per their respective sequence positions. The amino acids Tyr349, Ala321, and Arg292 (labelled in green) represent residues involved in hydrogen bond formation, while the dotted lines in green indicate the bond distances of 2.66 Å, 2.73 Å, and 2.80 Å.

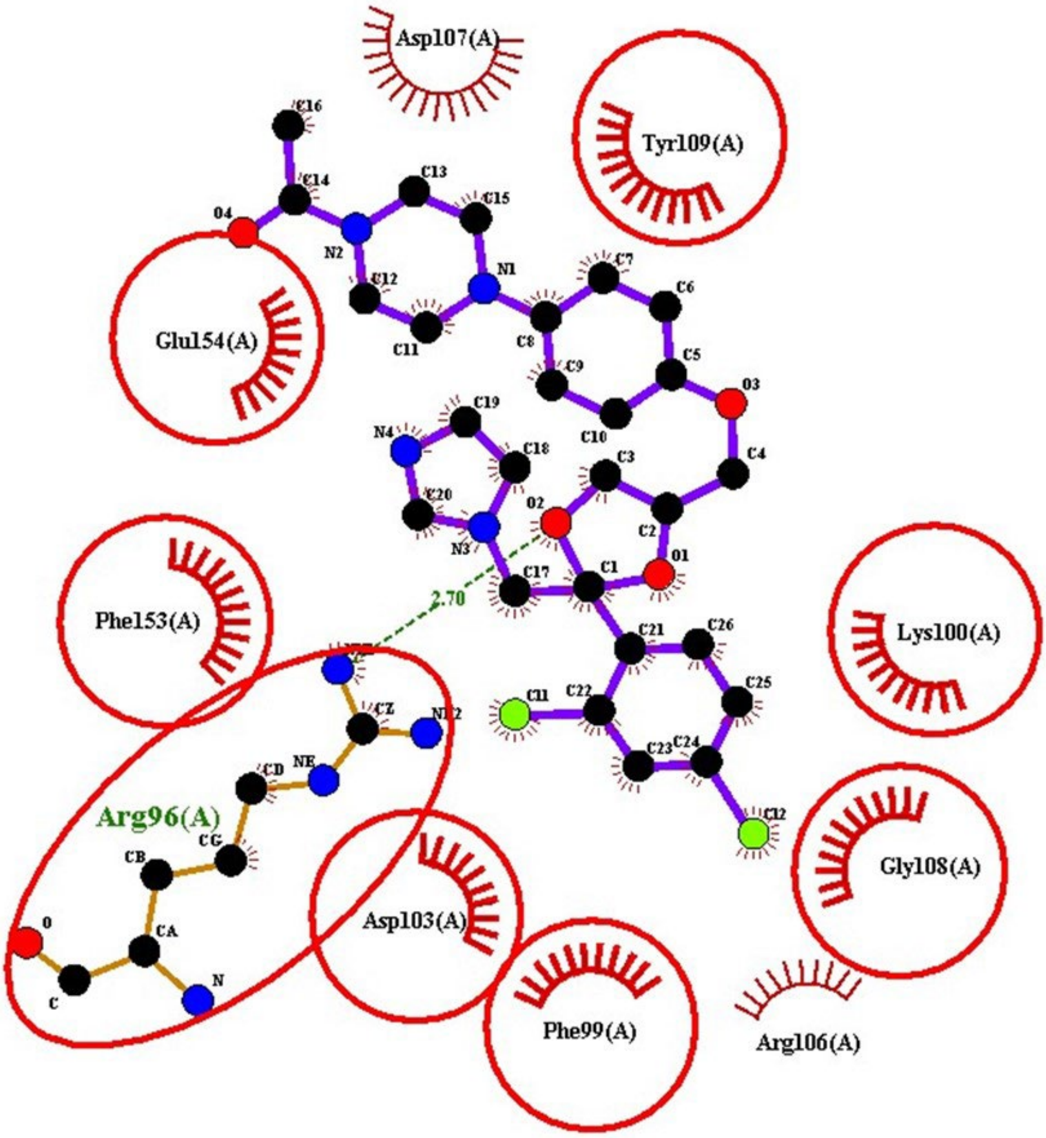

Figure 4.4.3. Molecular docking analysis of ketoconazole with the predicted structure of CNB-1. The interacting amino acid residues in complex with ketoconazole are shown. The amino acid residues are labelled with their respective positions in the protein sequence. The amino acid residue Arg96 (labelled in green) represents its involvement in hydrogen bond formation, while the dotted line in green indicates a bond distance of 2.70 Å.

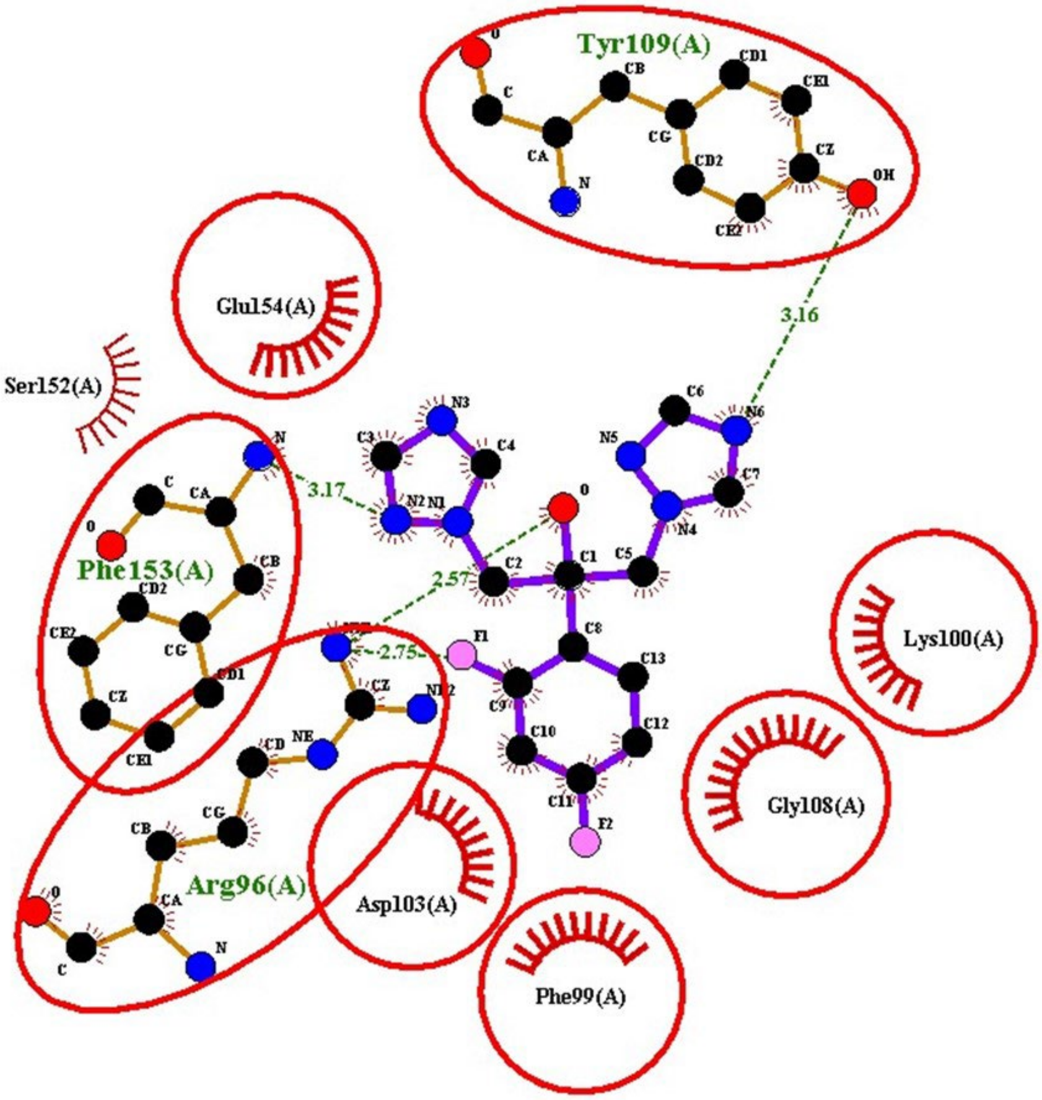

Figure 4.4.4. Molecular docking analysis of fluconazole with the predicted structure of CNB-1. The interacting amino acid residues in the complex with fluconazole are shown. The amino acid residues are labelled with their respective position in the protein sequence. The amino acids Phe153, Arg96, and Tyr109 (labelled in green) represent residues involved in hydrogen bond formation, while the dotted lines in green indicate bond distances of 3.17 Å, 2.75 Å, 2.57 Å, and 3.16 Å.

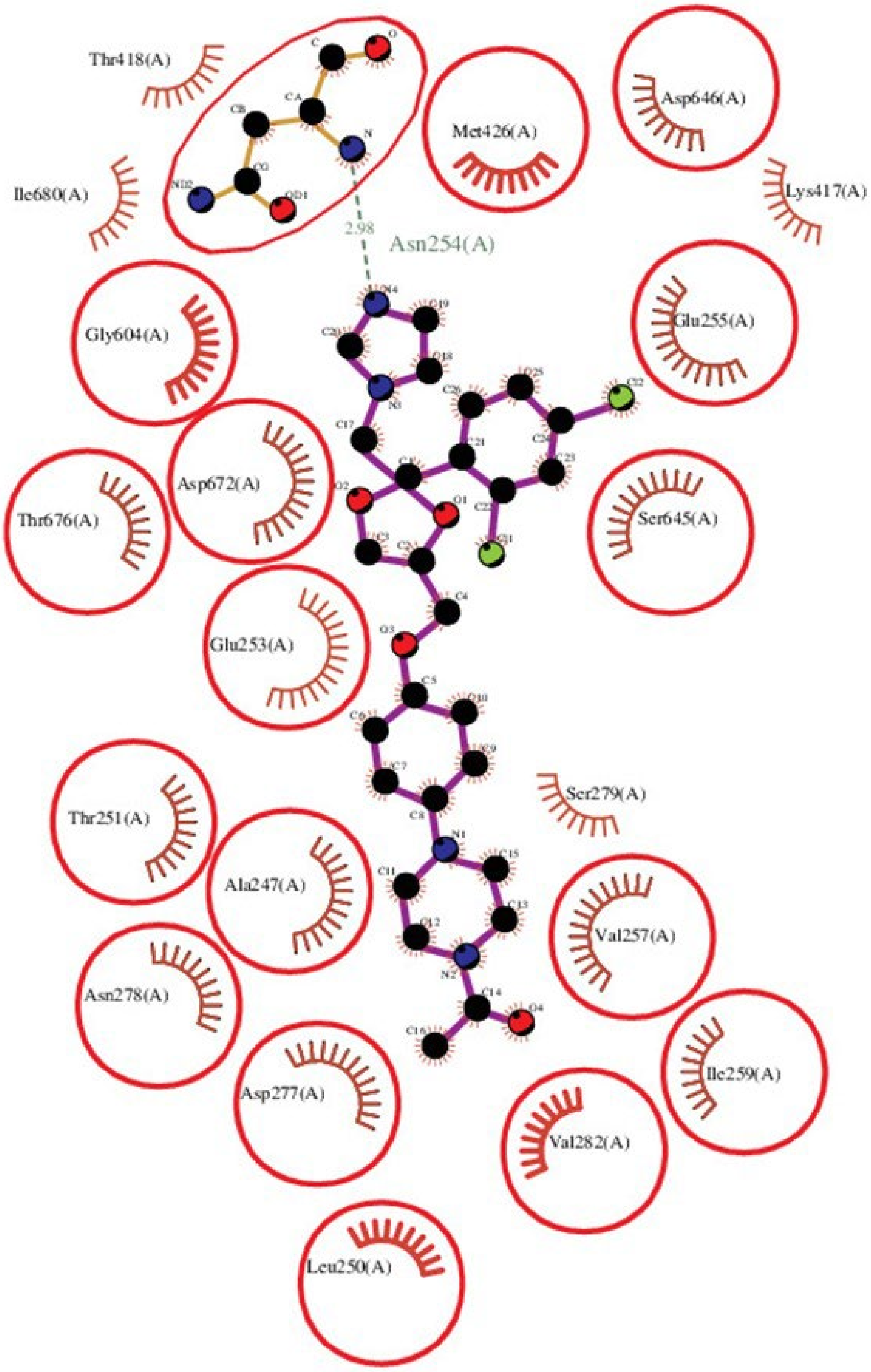

Figure 4.4.5. Molecular docking analysis of ketoconazole with the predicted structure of PMR-1. The interacting amino acid residues in the complex are shown. The amino acid residues are labelled with their respective positions in the protein sequence. The amino acid residue Asn254 (labelled in green) represents its involvement in

hydrogen bond formation, while the dotted line in green indicates a bond distance of 2.98 Å.

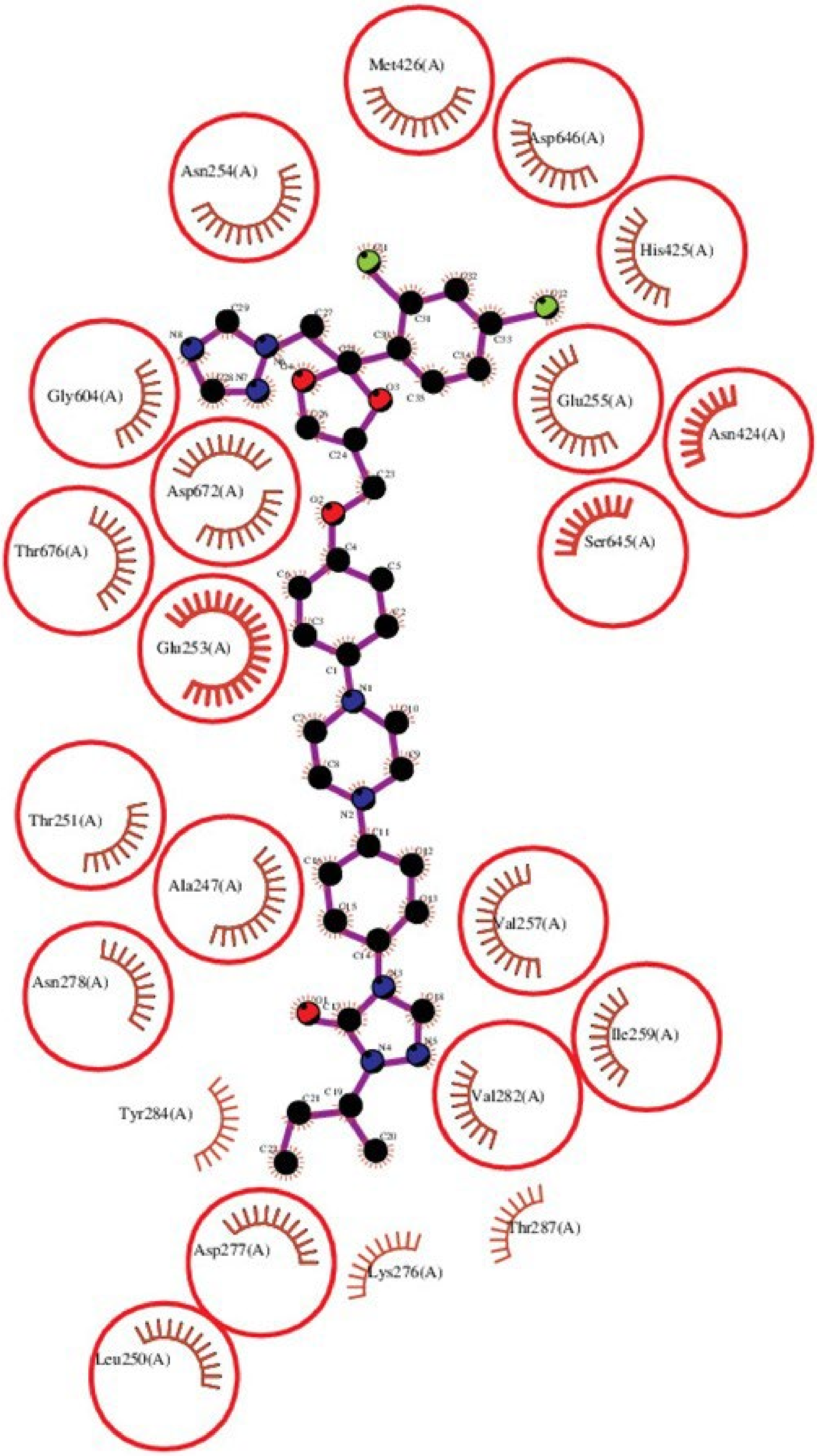
Met426(A)
Asp646(A)
Asn254(A)
His425(A)
Gly604(A)
Glu255(A)
Asn424(A)
Asp672(A)
Ser645(A)
Thr676(A)
Glu253(A)
Thr251(A)
Ala247(A)
Val257(A)
Asn278(A)
Ile259(A)
Val282(A)
Tyr284(A)
Thr287(A)
Asp277(A)
Lys276(A)
Leu250(A)

Figure 4.4.6. Molecular docking analysis of itraconazole with the predicted structure of PMR-1. The interacting amino acid residues in the complex are shown. The amino acid residues are labelled according to their respective position in the protein sequence.

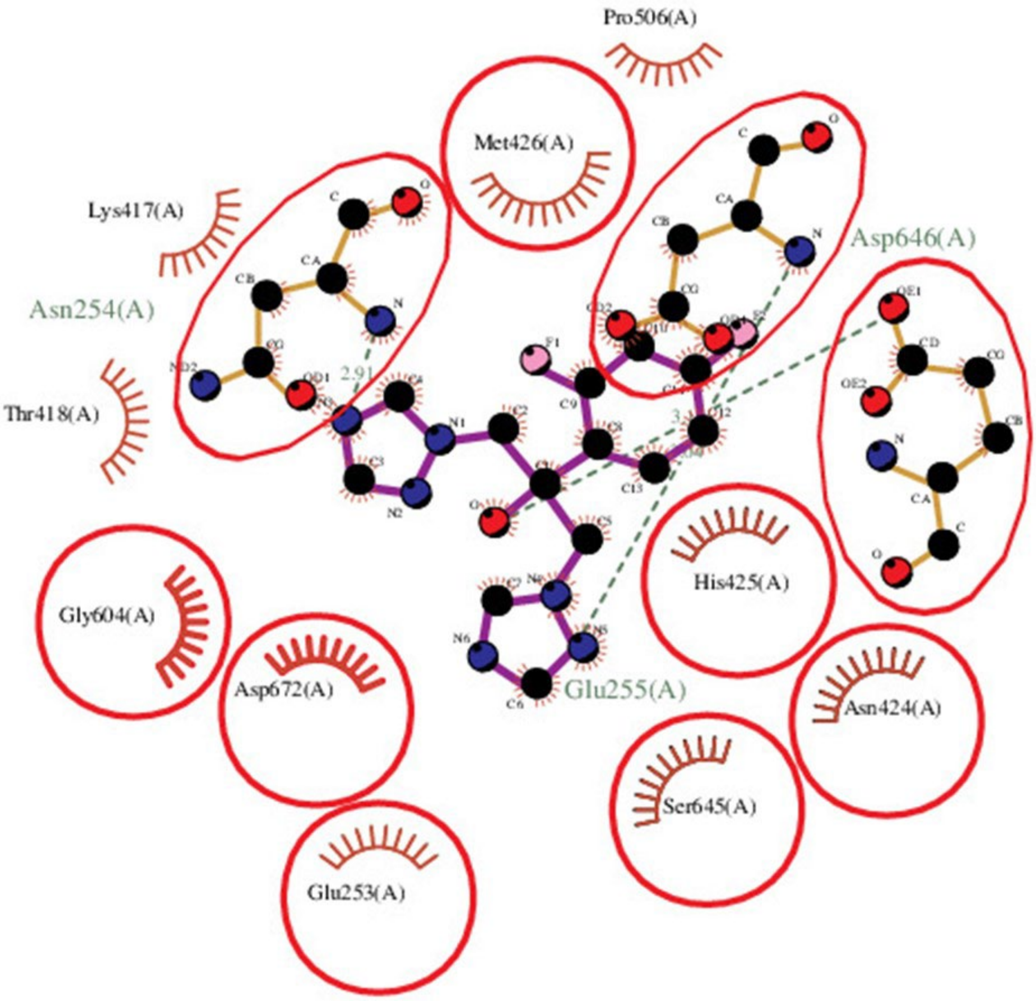

Figure 4.4.7. Molecular docking analysis of fluconazole with the predicted structure of PMR-1. The interacting amino acid residues in the complex are shown. The amino acid residues are labelled according to their respective position in the protein sequence. The amino acids Asn254, Glu255, and Asp646 (labelled in green) represent residues involved in hydrogen bond formation, while the dotted line in green indicates a bond distance of 2.91 Å.

4.2.3. Molecular dynamics simulations

4.2.3.1. Molecular dynamics simulations of the CNA-1 protein with fluconazole and ketoconazole

I performed MD simulations to rigorously assess the binding affinity of fluconazole, itraconazole, and ketoconazole with CNA-1, CNB-1, and PMR-1 (Table 4.1). These simulations were conducted using the predicted 3D structures of the target proteins generated through homology modeling. The MD analysis enables tracking atomic interactions and movements over time, where parameters like root mean square deviation (RMSD), root mean square fluctuation (RMSF), radius of gyration (Rg), and hydrogen bonds provide insights into binding processes (Ghahremanian et al. 2022; Umesh et al. 2022). The RMSD assesses structural stability by quantifying deviations from the initial reference structure, revealing conformational changes essential for understanding system stability (Abd EL Motelib and Amen 2019). The MD simulations incorporating RMSD, RMSF, Rg, and hydrogen bond analysis are crucial for understanding drug-protein binding mechanisms at the atomic level, facilitating the design of improved therapeutic agents (Pinzi and Rastelli 2019; Abdullah et al. 2023). I performed MD simulations to understand the dynamic behavior and stability of both apoprotein (ligand-free protein) and protein-ligand complexes. Moreover, I performed the MD simulations for 50 ns due to the large size of the CNA-1 (526 amino acid residues) and PMR-1 (1026 amino acid residues) proteins. It was previously reported that performing longer MD simulations for large protein requires significant computational resources and time (Gumbart et al. 2009). The RMSD trajectories of the fluconazole-CNA-1 and ketoconazole-CNA-1 complexes revealed highest backbone stability for the ketoconazole-CNA-1 complex that showed the lowest RMSD value with a maximum deviation of ~1.75 nm (Figure 4.5.1). The fluconazole-CNA-1 complex and CNA-1 apoprotein exhibited maximum RMSD values of ~3 nm and ~2 nm, respectively (Figure 4.5.1). The ketoconazole-CNA-1 complex exhibited a maximum RMSD of ~1.75 nm, suggesting that ketoconazole confers greater stability to the CNA-1 protein structure than fluconazole (Figure 4.5.1). The RMSF values for both apoprotein and the protein-ligand complexes were calculated using Groningen Machine for Chemical Simulations (GROMACS) (Ghahremanian et al. 2022) (Figure 4.5.2). The RMSF values for both the apoprotein and the four-ligand complexes were calculated using GROMACS over a 50 ns timescale. The RMSF is the most effective method for analyzing the mobility of protein residues in a protein-ligand complex (Song et al. 2024). The CNA-1 apoprotein and the ketoconazole-CNA-1 complex exhibited maximum RMSF values of ~0.5 nm within the amino acid residues range of 50 to 400 (Figure 4.5.2). The ketoconazole-CNA-1 complex displayed fluctuations similar to the CNA-1 apoprotein, unlike the fluconazole-CNA-1 complex that exhibited higher fluctuations (Figure 4.5.2). In addition, both the CNA-1 apoprotein and its ketoconazole-CNA-1 complex consistently exhibited similar patterns in their Rg values throughout the MD simulations period (Figure 4.5.3). The plot representing the Rg value (nm) versus time (ns), indicated that the CNA-1 apoprotein was rigid and consistent with an average Rg value of ~2.8 nm (Figures 4.5.3, 4.6.3, and 4.7.3). Moreover, the ketoconazole-CNA-1 complex exhibited an Rg value of ~3 nm, which exhibited less deviation (~0.2 nm) than the CNA-1 apoprotein (Figure 4.5.3). The fluconazole-CNA-1 complex showed higher Rg value of ~4.2 nm up to 30 ns, and the lower Rg value of ~3.2 nm after30 ns (Figure 4.5.3). These data consistently suggested that the binding of ketoconazole to CNA-1 was stable with a low Rg profile. I further analyzed hydrogen bond formation in the protein-ligand complexes. Both fluconazole-CNA-1 and ketoconazole-CNA-1 complexes formed a maximum of 2 hydrogen bonds, involving the Tyr353 and His189 residues in the ketoconazole-CNA1 complex (Figures 4.5.4, 4.5.5). The amino acid residues Tyr349, Ala321, and Arg292 were involved in hydrogen bonding in the fluconazole-CNA-1 complex (Table 4.1). These residues played a crucial role in forming intermolecular hydrogen bonds, significantly contributing to the structural stability of the protein-ligand complexes. Moreover, the amino acid residues Tyr353, His189, Leu350, Tyr349, Ala321, Glu320, His319, Arg292, Leu194, Trp270, and Arg160 were common in both the CNA-1 complexes with fluconazole and ketoconazole (Table 4.1, shown in bold letters).

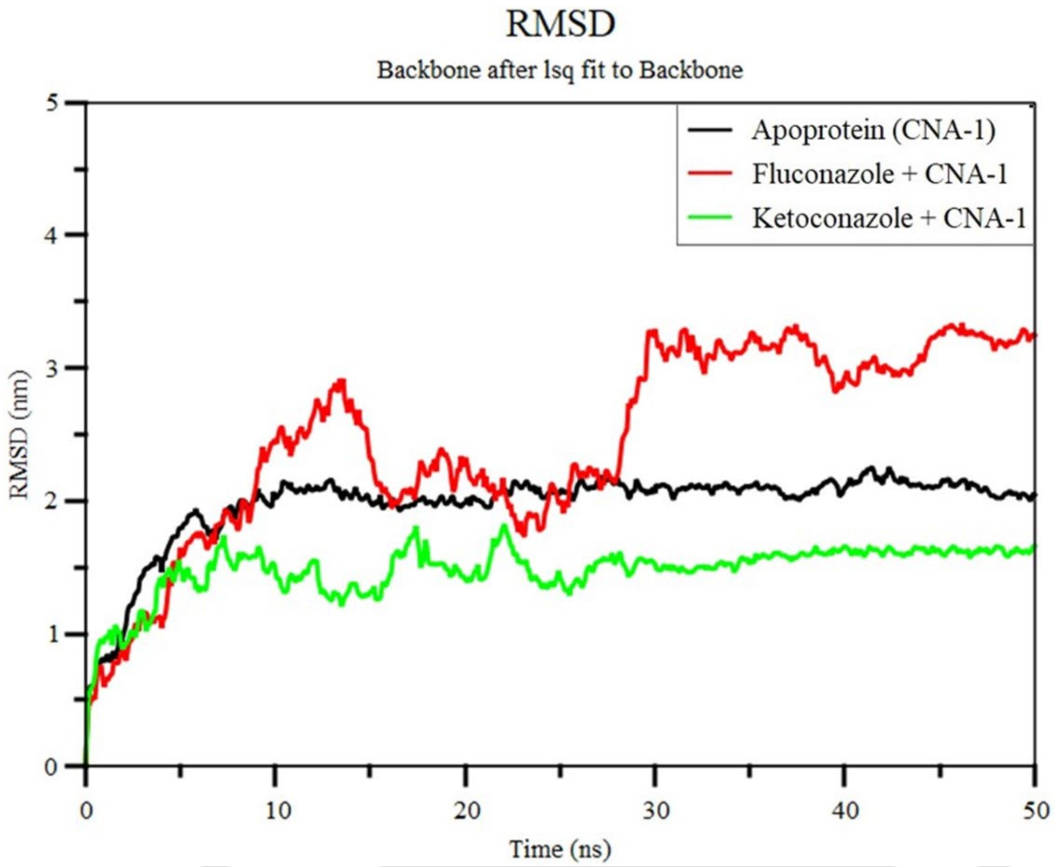

Figure 4.5.1. The MD simulations of the complexes of CNA-1 with azole drugs. The RMSD (nm) values of the predicted CNA-1 apoprotein (black color), fluconazole-CNA-1 complex (red color), and ketoconazole-CNA-1 complex (green color) are plotted against simulation time (ns).

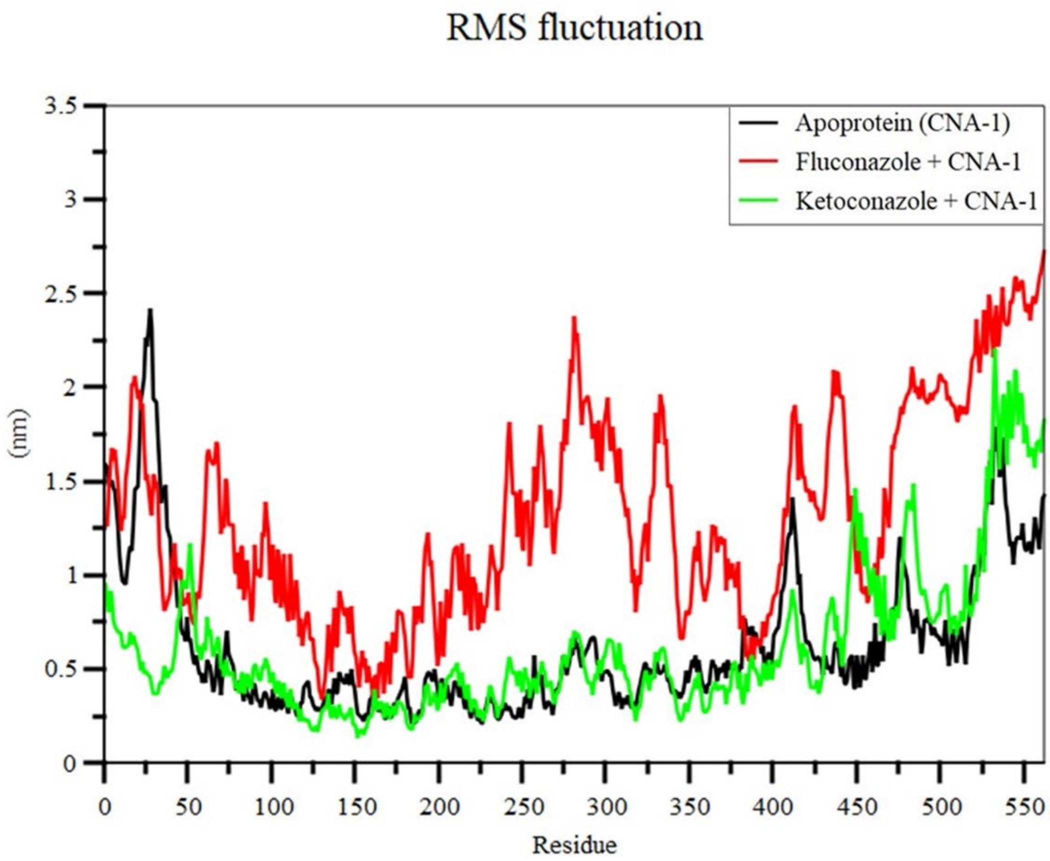

Figure 4.5.2. The RMSF values of the complexes of fluconazole and ketoconazole with CNA-1. The RMSF values for the predicted CNA-1 apoprotein (black color), fluconazole-CNA-1complex (red color), and ketoconazole-CNA-1 complex (green color) are shown for MD simulations over 50 ns time scale.

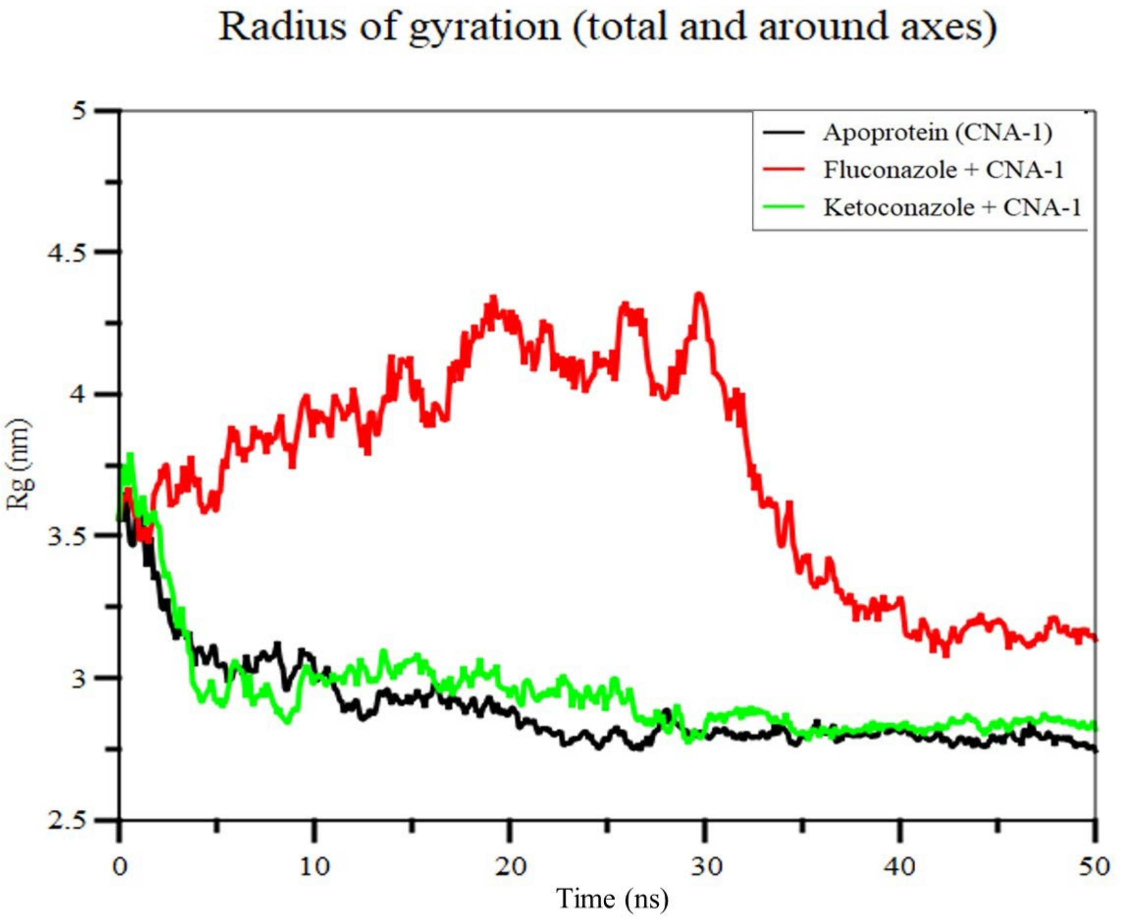

Figure 4.5.3. The Rg value of CNA-1 with and without azole complexes during the MD simulations. The Rg values for the predicted CNA-1 apoprotein (black), fluconazole-CNA-1 complex (red), and ketoconazole-CNA-1 complex (green) in MD simulations for 50 ns are shown.

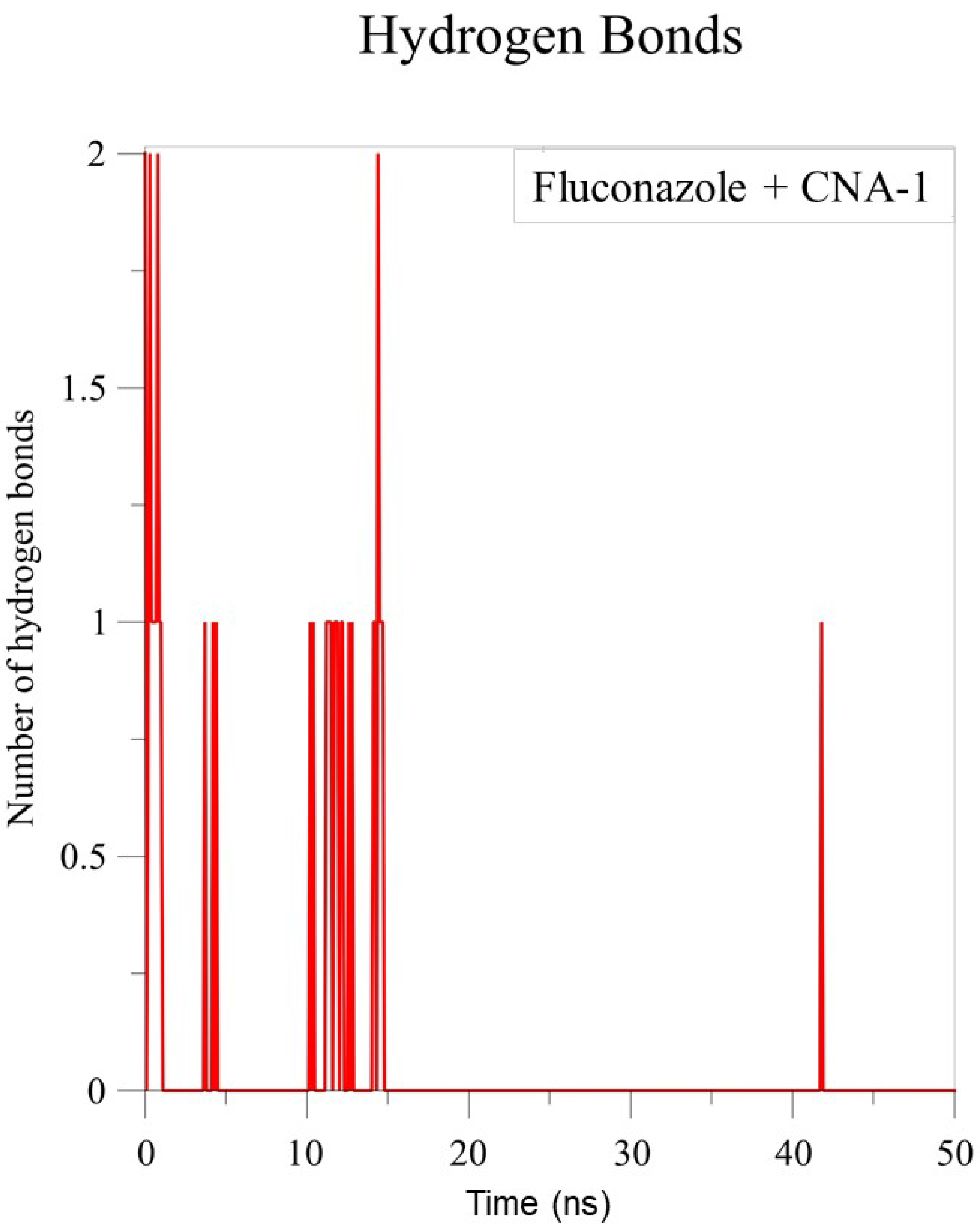

Figure 4.5.4. The interacting hydrogen bonds in the fluconazole-CNA-1 complex. The number of hydrogen bonds against MD simulations for 50 ns is shown for the fluconazole-CNA-1 complex.

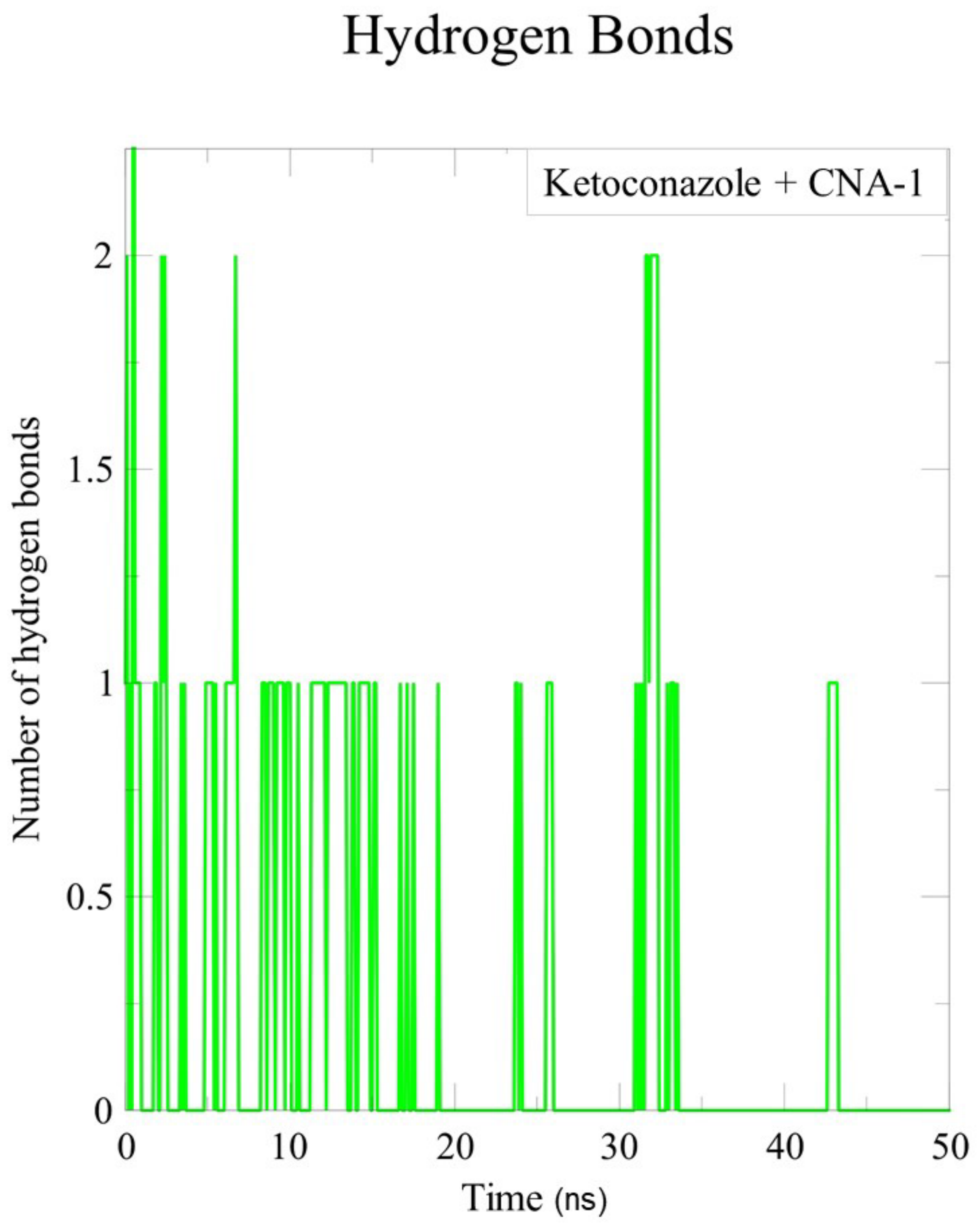

Figure 4.5.5. The interacting hydrogen bonds in the ketoconazole-CNA-1 complex. The number of hydrogen bonds against MD simulations for 50 ns is shown for the ketoconazole-CNA-1 complex.

4.2.3.2. MD simulations of the CNB-1 protein with fluconazole and ketoconazole

The MD simulations and RMSD trajectories of the fluconazole-CNB-1 and ketoconazole-CNB-1 complexes, based on the predicted structure of CNB-1, revealed that ketoconazole-CNB-1, fluconazole-CNB-1 complex, and CNB-1 apoprotein possess RMSD values of ~0.3 nm, ~0.7 nm, and ~4.5 nm, respectively, suggesting that the ketoconazole-CNB-1 complex has the highest backbone stability (Figure 4.6.1). Notably, all 156 amino acid residues in the CNB-1 apoprotein and ketoconazole-CNB-1 complex exhibited the maximum RMSF values at the range of ~0.3 nm (Figure 4.6.3). However, in the fluconazole-CNB-1 complex, amino acid residues ranging from positions 40–60 and 120–135 showed the highest RMSF values of ~0.5 nm and ~0.6 nm, respectively (Figure 4.6.2). The CNB-1 apoprotein and ketoconazole-CNB-1 complex had similar Rg values at an average of ~1.8 nm (Figure 4.6.3). The fluconazole-CNB-1 complex showed marginally high Rg value at ~2.1 nm, which deviates by 0.3 nm, the higher Rg value indicates a less compact flexible protein structure. The lower Rg value of the ketoconazole-CNB-1 complex, similar to CNB-1 apoprotein, indicates the stable and compact protein-ligand complex formation (Figure 4.6.3). Molecular docking studies identified Glu154, Phe153, Arg96, Asp103, Phe99, Gly108, Lys100, and Tyr109 as common amino acid residues in both fluconazole-CNB-1 and ketoconazole-CNB-1 complexes. Additionally, the fluconazole-CNB-1 complex formed hydrogen bonds with the Arg96, Tyr109, and Phe153, whereas the ketoconazole-CNB-1 complex formed a hydrogen bond only with the Arg96 residue.

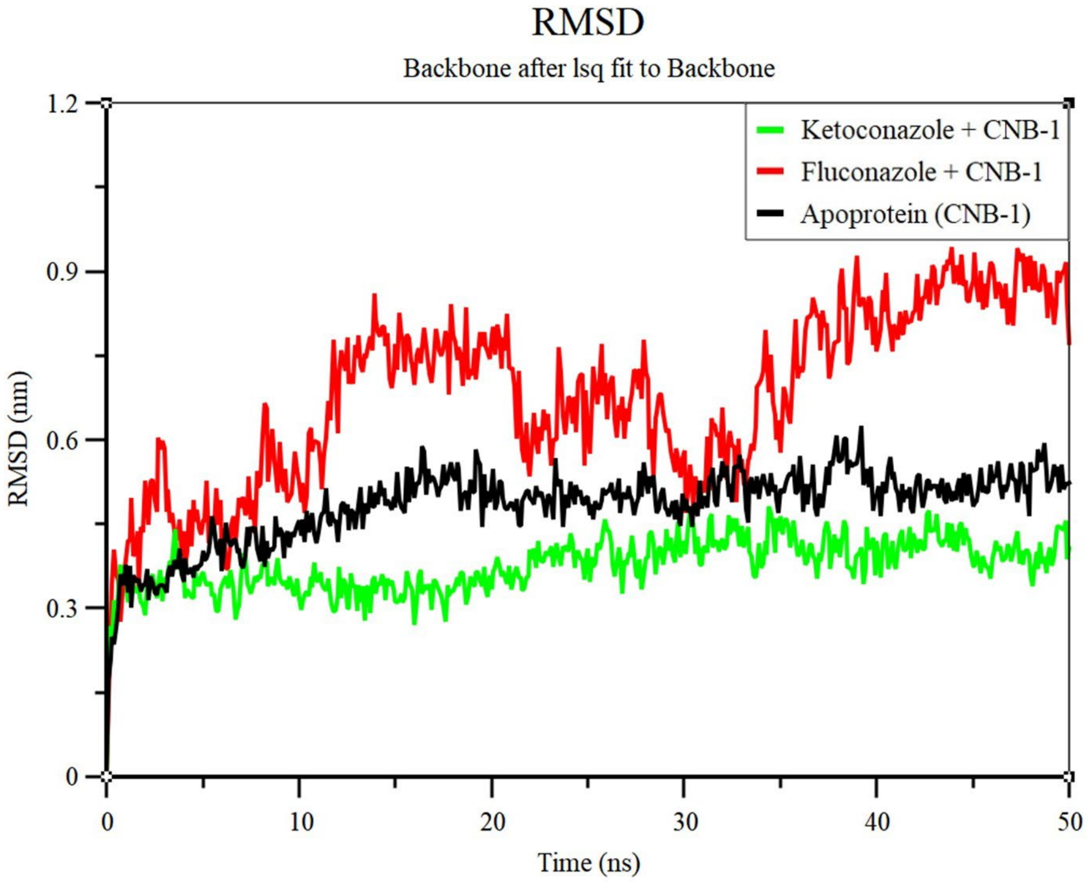

Figure 4.6.1. The MD simulations of the complexes of CNB-1 with azole drugs. The RMSD values for the predicted CNB-1 apoprotein (black color), fluconazole-CNB-1

complex (red color), and ketoconazole-CNB-1 complex (green color) during the MD simulations for 50 ns are shown.

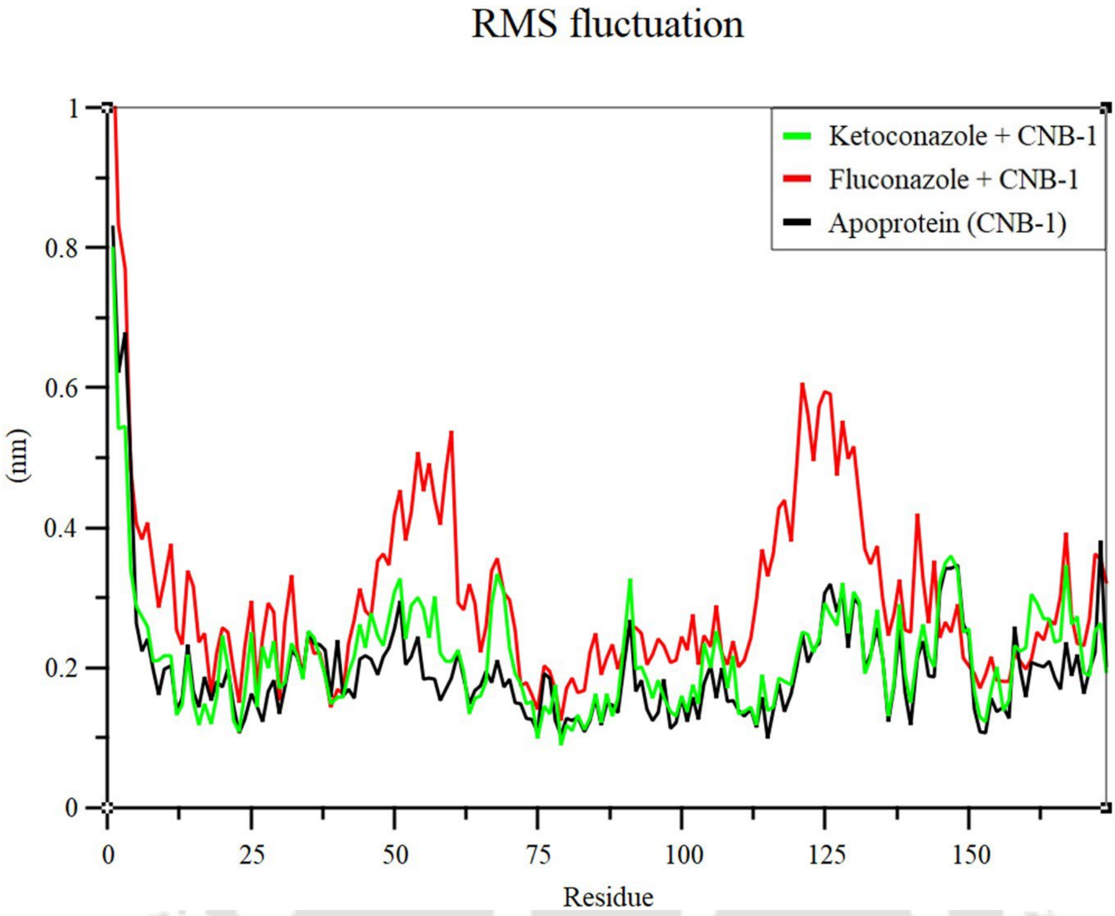

Figure 4.6.2. The RMSF values of the CNB-1 protein and its complexes with azole drugs. The RMSF values for the predicted CNB-1 apoprotein (black color), fluconazole-CNB-1 complex (red color), and ketoconazole-CNB-1 complex (green color) are shown for a period of 50 ns in the MD simulations.

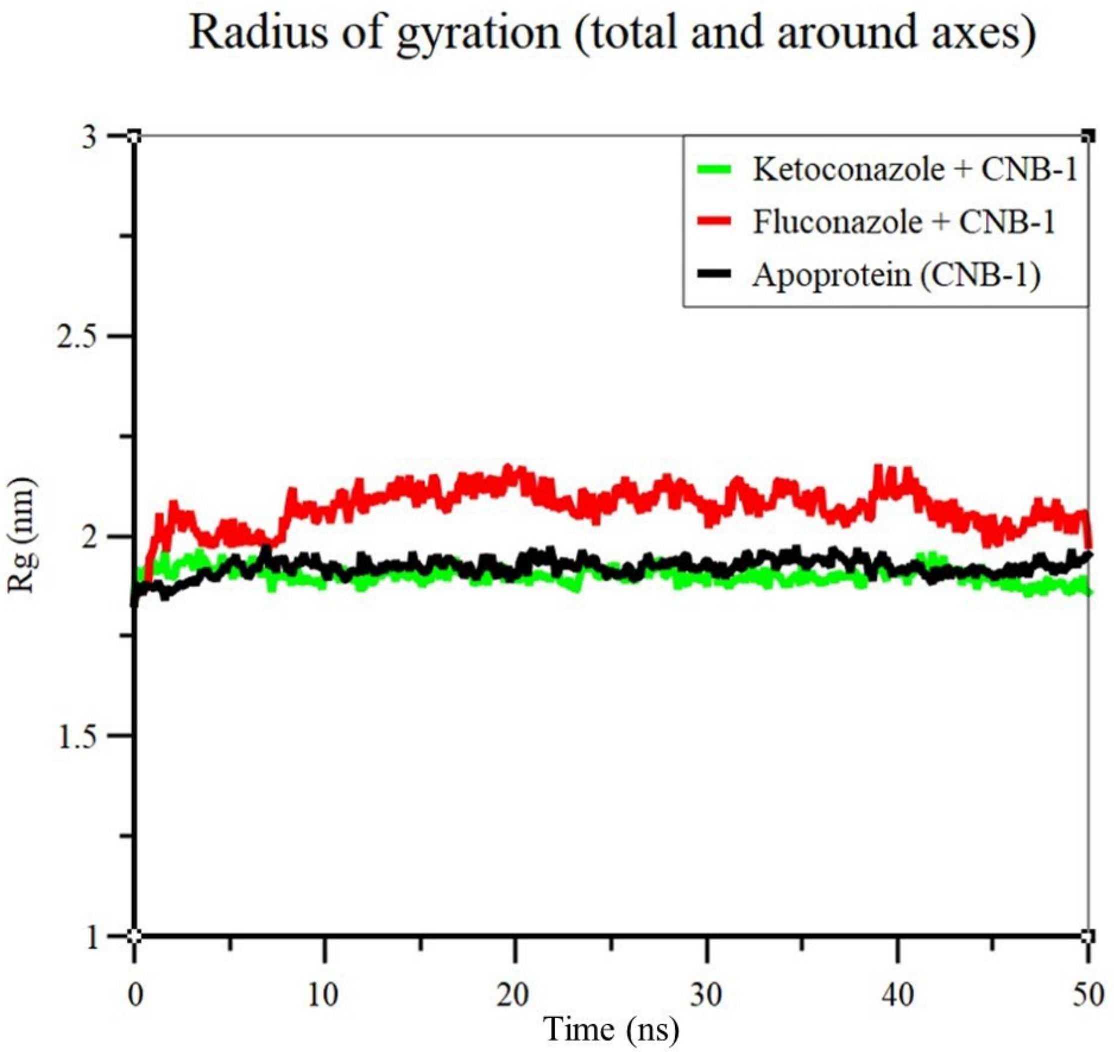

Figure 4.6.3. The Rg of the CNB-1 protein with and without azole complexes. The Rg values for the predicted CNB-1 apoprotein (black), fluconazole-CNB-1 complex (red), and ketoconazole-CNB-1 complex (green) over an MD simulation for a period of 50 ns are shown.

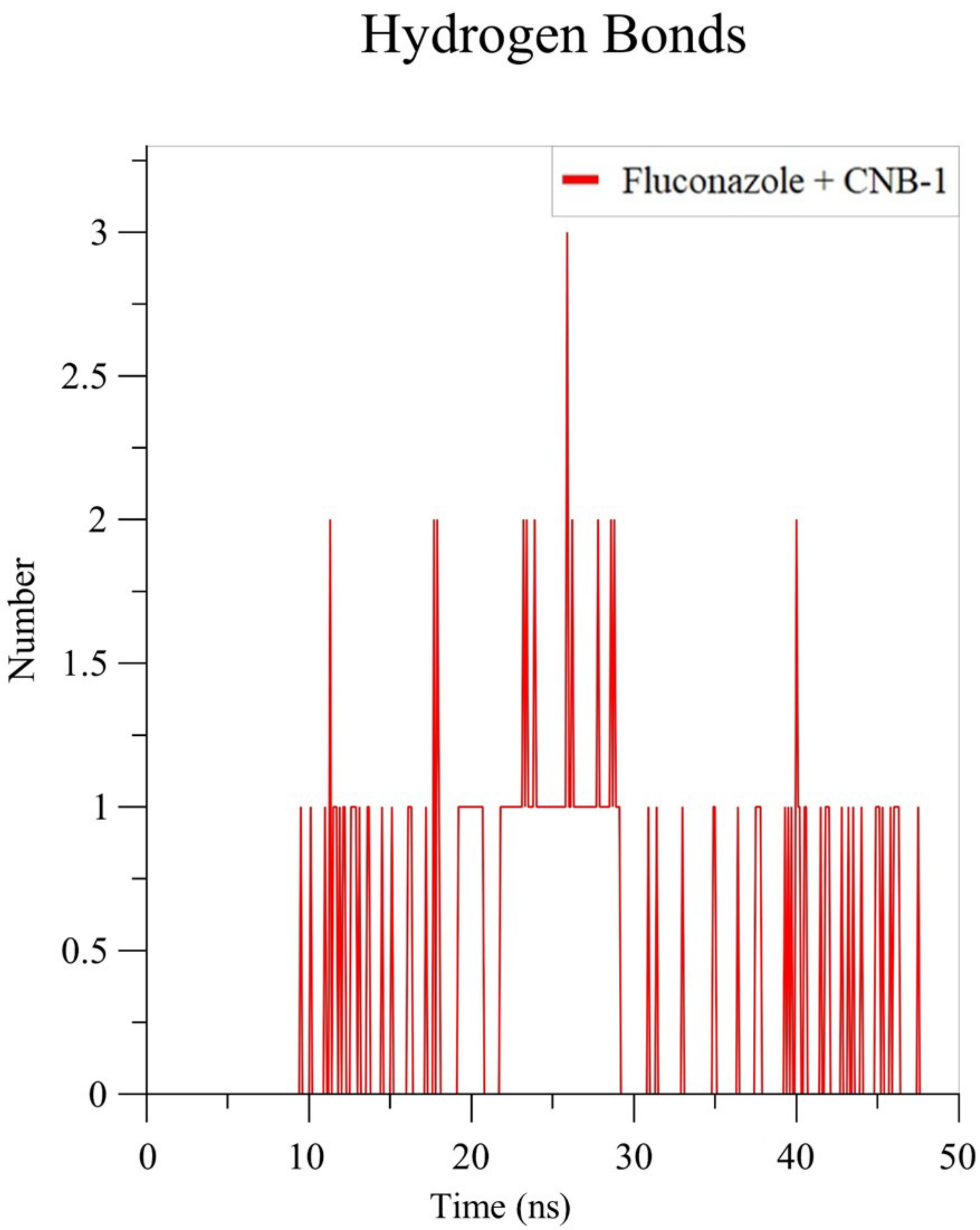

Figure 4.6.4. Hydrogen bonds in the fluconazole-CNB-1 complex. The interacting hydrogen bonds in the fluconazole-CNB-1 complex, based on the predicted CNB-1 structure, over a period of 50 ns time scale in MD simulations, are shown.

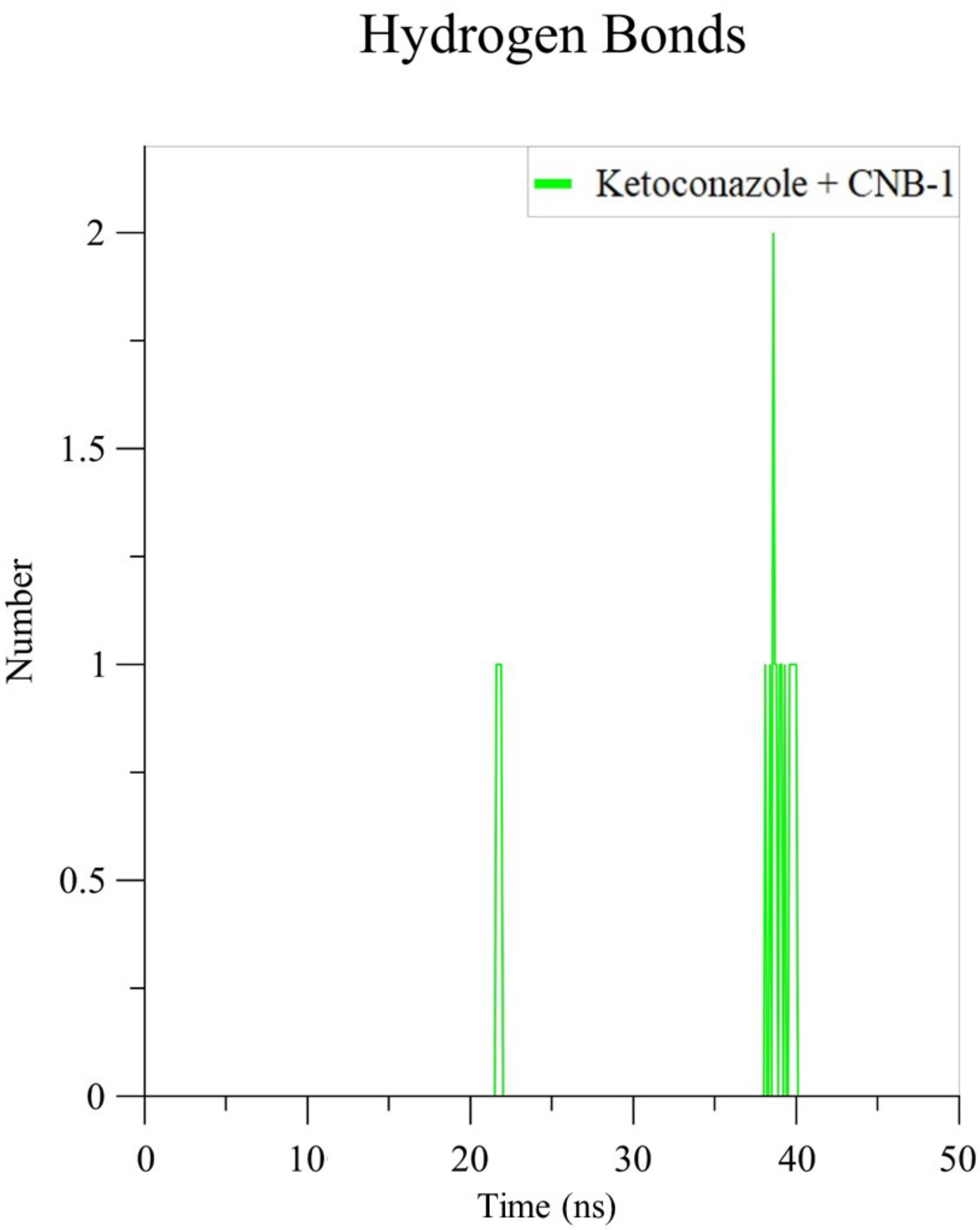

Figure 4.6.5. Hydrogen bonds in the ketoconazole-CNB-1 complex. The interacting hydrogen bonds in the ketoconazole-CNB-1 complex, based on the predicted CNB-1 structure, over a period of 50 ns time scale in MD simulations, are shown.

4.2.3.3. The MD simulations of PMR-1 with fluconazole, itraconazole and ketoconazole

I performed MD simulations using the predicted structure of the PMR-1 protein in its apoprotein state and in complex with the azole drugs fluconazole, itraconazole, and ketoconazole. The RMSD calculations were conducted for the PMR-1 apoprotein and its protein-ligand complexes using GROMACS (Figure 4.7.1). Among the three PMR-1–azole complexes, the itraconazole–PMR-1 complex exhibited the highest backbone stability with a maximum deviation of ~0.6 nm (Figure 4.7.1). The RMSD trajectories for the fluconazole–PMR-1 and ketoconazole–PMR-1 complexes displayed a consistent pattern similar to the PMR-1 apoprotein, ranging from ~0.75 to 0.9 nm after 30 ns. The RMSF values for fluconazole, itraconazole, and ketoconazole complexes with PMR-1, and for the PMR-1 apoprotein were analyzed over a 50 ns trajectory, focusing on active site residues. The RMSF values for both the apoprotein and the three-ligand complexes were computed using GROMACS (Figure 4.7.2). The PMR-1 apoprotein displayed the highest RMSF values up to ~1.75 nm in the amino acids ranging from 180−220 (Figure 4.7.2). The fluconazole-PMR-1 complex displayed maximum fluctuations of ~1.5 nm at positions 450–500 (Figure 4.7.2). The ketoconazole-PMR-1 complex showed a maximum RMSF value of ~ 1.25 nm at positions 610−640. However, the itraconazole-PMR-1 complex exhibited the lowest fluctuation at ~1.15 nm among all complexes during the 50 ns MD simulations trajectory (Figure 4.7.2). To further analyze the binding effects of the azole drugs on PMR-1, a comparative analysis of protein compactness was conducted by determining the Rg value. The ketoconazole-PMR-1 and fluconazole-PMR-1 complexes exhibited average Rg values of ~3.7 nm, which was lower than the PMR-1 apoprotein (Figure 4.7.3). Therefore, ketoconazole-PMR-1 and fluconazole-PMR-1 complexes showed an increased structural compaction necessary for a more stable structure compared to the PMR-1 apoprotein. Among the three azole–PMR-1 complexes, the fluconazole–PMR-1 complex showed the highest stability (Figure 4.7.3). Moreover, critical amino acid residues were strategically positioned within the active site of PMR-1, highlighting their role in stabilizing the protein-drug interactions and maintaining structural integrity. In addition, I evaluated the intermolecular hydrogen bond formation for the PMR-1 protein with fluconazole, ketoconazole, and itraconazole in the entire course of the MD simulations of 50 ns to examine the attachment stability between ligands and proteins. Furthermore, examination of hydrogen bonding interactions between azoles and proteins revealed that the fluconazole-PMR-1 complex formed a maximum of four hydrogen bonds (Figure 4.7.4). The Itraconazole-PMR-1 complex formed a maximum of three hydrogen bonds (Figure 4.7.5). Similarly, the ketoconazole-PMR-1 complex exhibited a maximum of two hydrogen bonds (Figure 4.7.6). I also observed that the residues Glu253, Asn254, Asp646, Met426, Glu255, Asp672, Gly604, and Ser645, were the most common residues found in all the PMR-1 protein-ligand complexes (Table 4.1, shown in bold letters). In the ketoconazole-PMR-1 complex, only the Asn254 residue was involved in hydrogen bonding (Figure 4.4.5). The PMR-1-fluconazole complex showed hydrogen bond interaction with Asn254, Glu255, and Asp646 amino acid residues (Figure 4.4.7). These amino acid residues play a pivotal role in drug binding and structural stabilization, and therefore, identification of these residues might be crucial for antifungal drug design in the future.

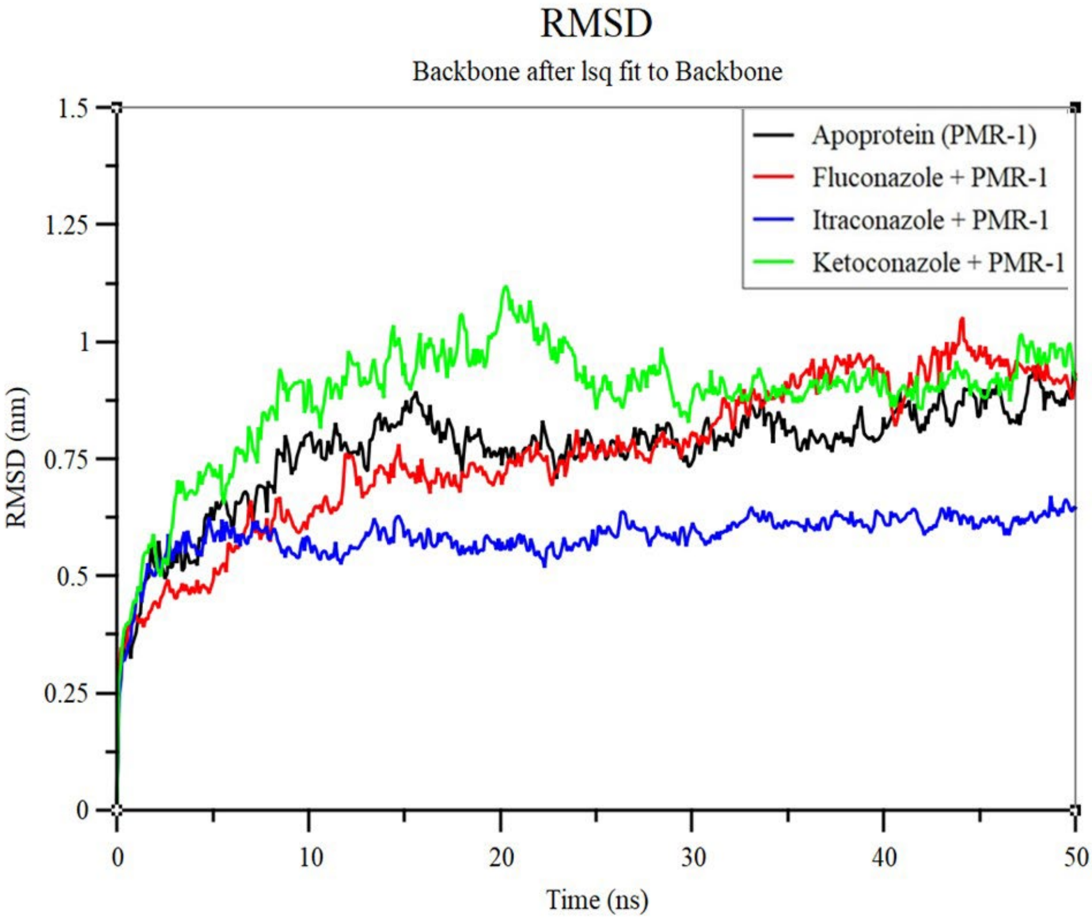

Figure 4.7.1. MD simulations of PMR-1 protein complexes with azole drugs. The RMSD values for the predicted PMR-1 apoprotein (black color), fluconazole-PMR-1 complex (red color), itraconazole-PMR-1 complex (blue color), and ketoconazole-PMR-1 complex (green color) over a 50 ns MD simulation are shown.

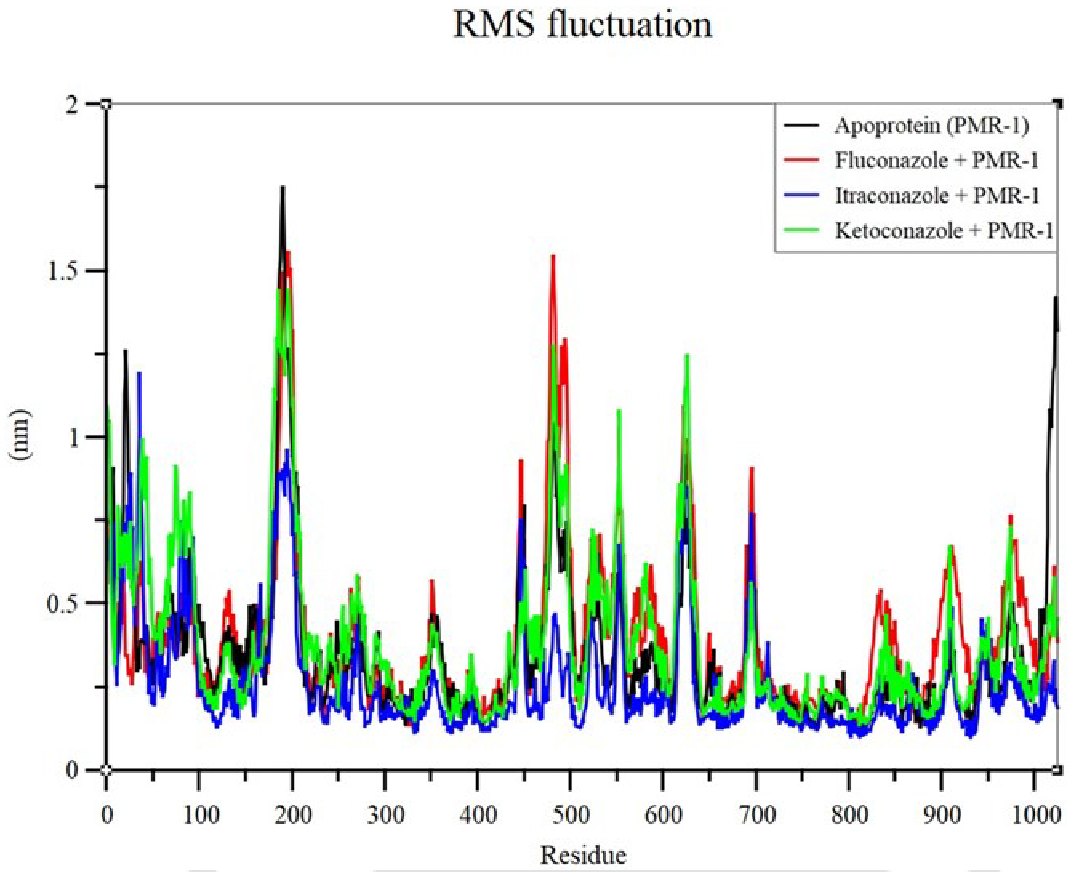

Figure 4.7.2. RMSF values of the PMR-1 protein and its complexes with azole drugs. The RMSF values for the predicted PMR-1 apoprotein (black color), fluconazole-PMR-1 complex (red color), itraconazole-PMR-1 complex (blue color), and ketoconazole-PMR-1 complex (green color) over a 50 ns MD simulation are shown.

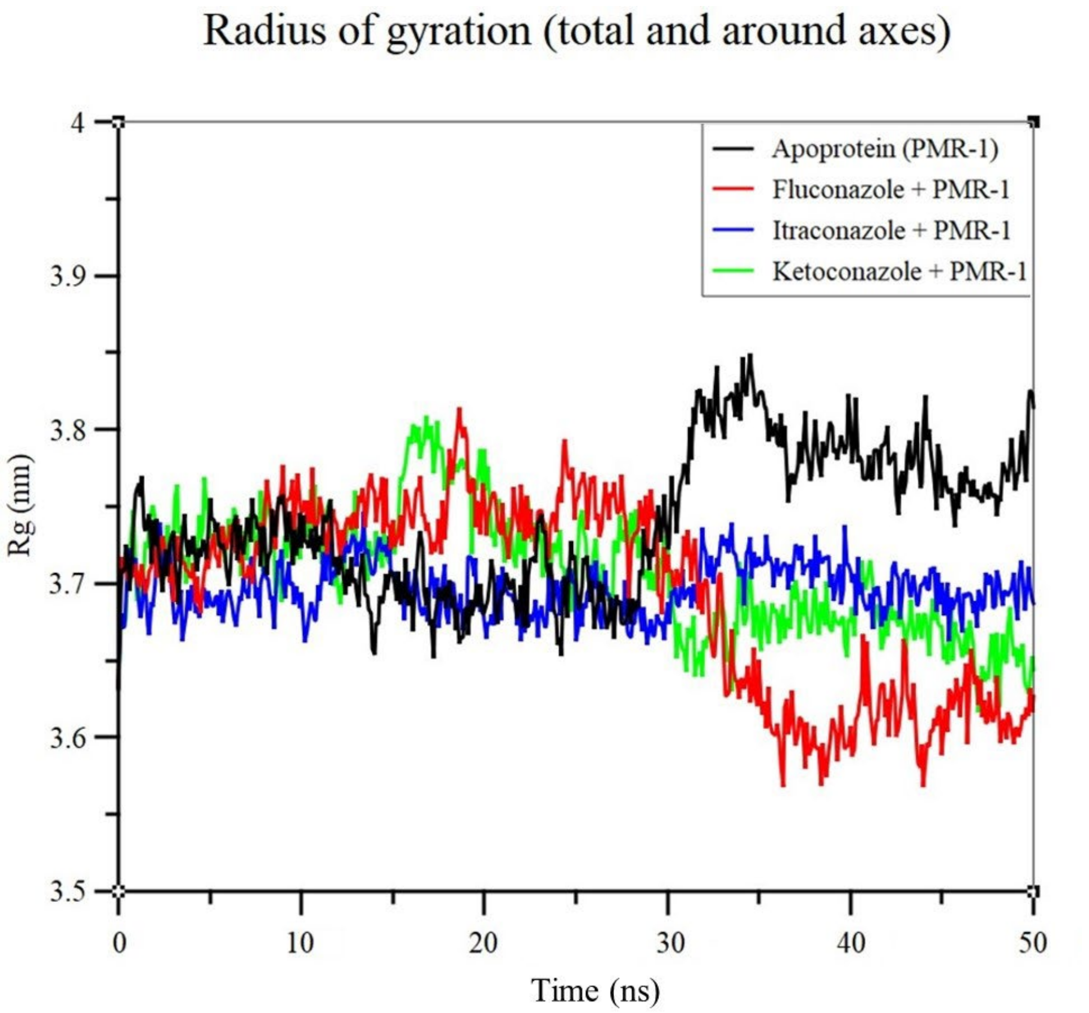

Figure 4.7.3. The analysis of Rg for the PMR-1 protein with and without azole complexes. The Rg values for the predicted PMR-1 apoprotein (black color), fluconazole-PMR-1 complex (red color), itraconazole-PMR-1 complex (blue color), and ketoconazole-PMR-1 complex (green color) over a 50 ns MD simulation are shown.

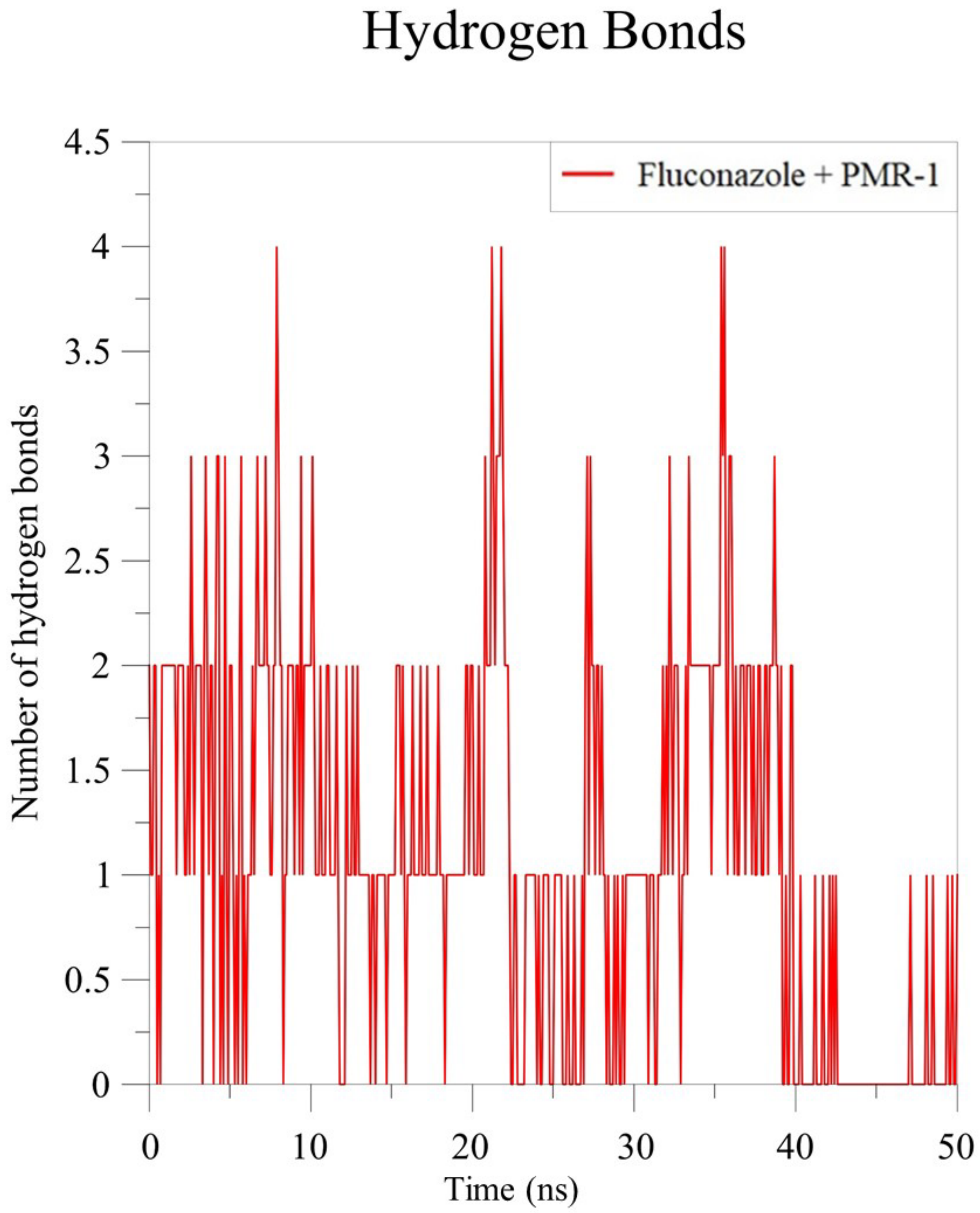

Figure 4.7.4. Hydrogen bonds in the fluconazole-PMR-1 complex. The interacting hydrogen bonds in the fluconazole-PMR-1 complex, based on the predicted PMR-1 structure, over a 50 ns MD simulation are shown.

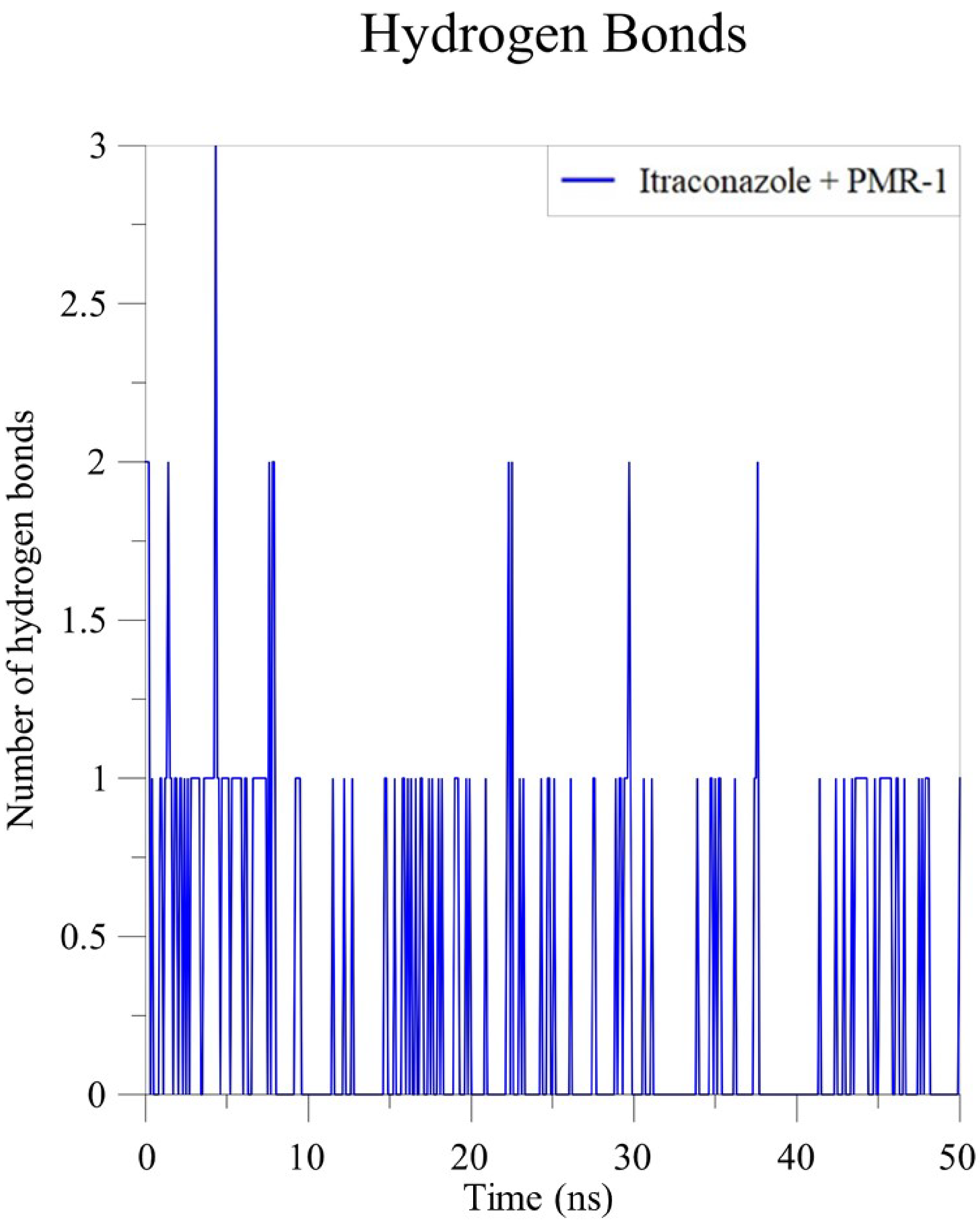

Figure 4.7.5. Hydrogen bonds in the itraconazole-PMR-1 complex. The interacting hydrogen bonds in the itraconazole-PMR-1 complex, based on the predicted PMR-1 structure, over a 50 ns MD simulation, are shown.

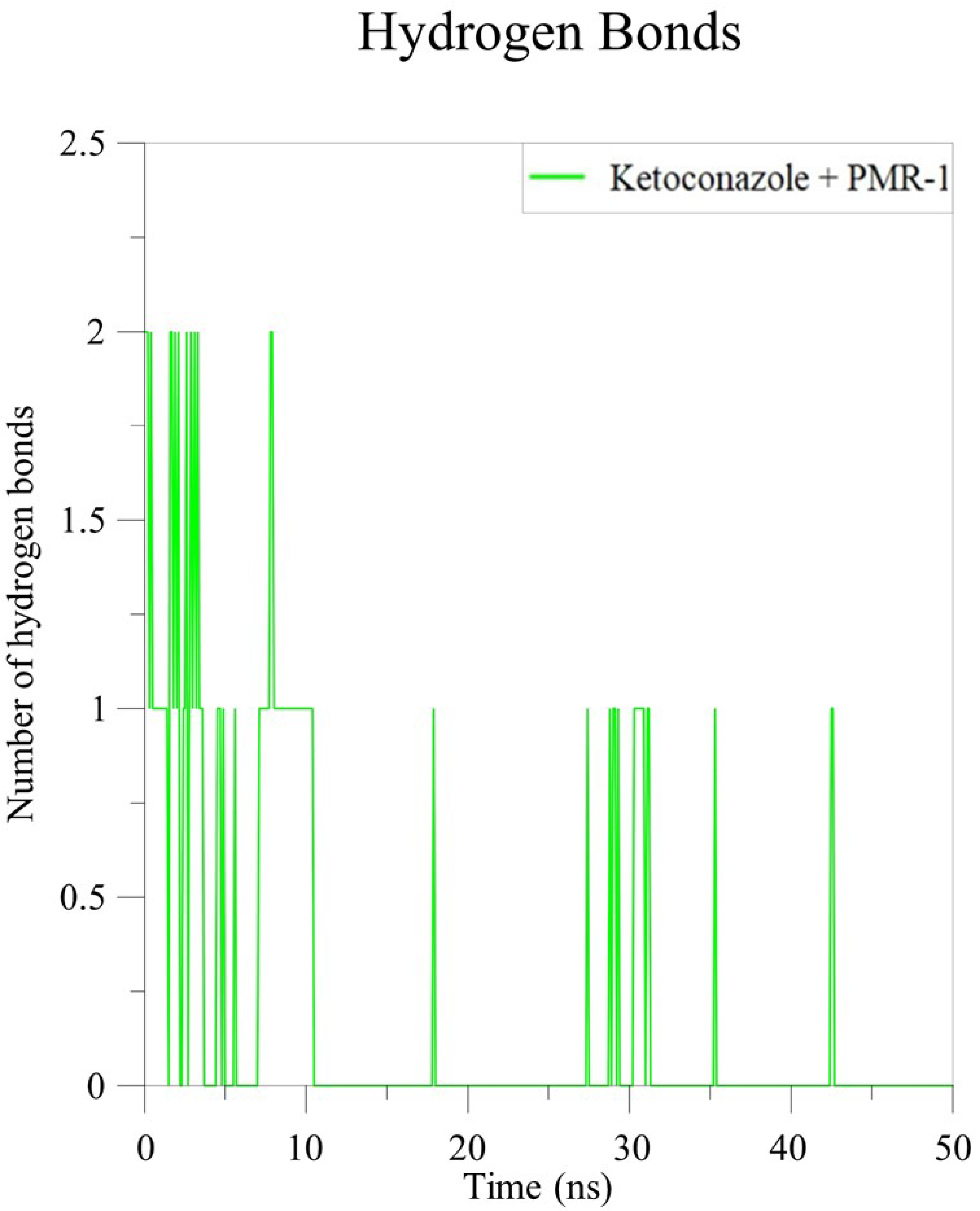

Figure 4.7.6. Hydrogen bonds in the ketoconazole-PMR-1 complex. The interacting hydrogen bonds in the ketoconazole-PMR-1 complex, based on the predicted PMR-1 structure, over a 50 ns MD simulation, are shown.

4.3 Discussion

In this chapter, I studied the interactions of azole drugs fluconazole, itraconazole, and ketoconazole with CNA-1, CNB-1, and PMR-1 using molecular docking and MD simulations. The primary objective was to determine the binding efficacy of azole drugs with CNA-1, CNB-1, and PMR-1. Preliminary computational insights suggest that CNA-1, CNB-1, and PMR-1 proteins exhibited the highest binding affinity to ketoconazole, followed by fluconazole. The CNA-1 and CNB-1 proteins showed no significant binding affinity to itraconazole, while PMR-1 formed a stable complex with itraconazole. In addition, fluconazole and ketoconazole form hydrogen bonds CNA-1, CNB-1, and PMR-1. Moreover, fluconazole, ketoconazole, and itraconazole also exhibited hydrophobic interactions with CNA-1, CNB-1, and PMR-1, which are necessary for stabilization within the active sites. The presence of key hydrogen bonding and hydrophobic interactions indicates potential structural inhibition of these proteins by azole drugs. These interactions and binding observations are derived from preliminary computational insights based on molecular docking and molecular dynamics (MD) simulations, using predicted 3D structures of the target proteins.

The MD simulations are essential for understanding drug-protein interactions at the atomic level, providing crucial insights for designing more effective therapeutic agents. The RMSD, RMSF, Rg, and hydrogen bonding from MD trajectories offer key insights into protein-ligand stability and dynamics. In addition, RMSD analysis is a critical metric derived from MD simulations that provides insights into protein structural conformations and stability when complexed with ligand molecules. Lower RMSD values throughout the simulation indicate higher stability, whereas higher values suggest relative instability (Ghahremanian et al. 2022; Haryadi and Pranowo 2023). Moreover, variations in RMSD to larger values may signify considerable conformational changes within the protein-ligand system during the simulation, and lower RMSD values typically indicate structural stability (Chatterjee et al. 2021).

The CNA-1 and CNB-1 apoproteins attained equilibration at 10 ns, indicating a well performed MD simulations (Figures 4.5.1, 4.6.1, black line). The ketoconazole-CNA-1 complex maintained a lower and more stable RMSD (~1.75 nm) throughout the simulation, whereas the fluconazole-CNA-1 complex exhibited higher deviations at ~3 nm after 30 ns up to 50 ns (Figure 4.5.1, red line). The CNB-1 apoprotein had an RMSD of ~0.4 nm, while the ketoconazole-CNB-1 complex showed lower RMSD (~0.35 nm) and the fluconazole-CNB-1 complex exhibited higher deviation (~0.7 nm). The RMSD value determined for CNB-1 protein in this study is similar to the RMSD value with less than ~0.8 nm for the CnB protein in *A. fumigatus* (Juvvadi et al. 2022). The variable RMSD value observed in the protein-ligand complex may be attributed to a substantial number of rotatable bonds or molecular flexibility (Chatterjee et al. 2021). The PMR-1 apoprotein attained the equilibration at 10 ns over the 50 ns MD simulation period. The MD simulation time was limited to 50 ns, because simulation with large protein for longer periods requires significant computational resources and time (Gumbart et al. 2009). Itraconazole-PMR-1 complex exhibited the lowest RMSD value with a maximum deviation of ~0.6 nm, whereas the maximum deviation for the PMR-1 apoprotein was at ~0.75 nm. The lower RMSD value of the itraconazole-PMR-1 complex suggested more stable conformation (Figure 4.7.1). The ketoconazole-PMR-1 complex exhibited RMSD value with an average of ~1 nm from 15 ns to 20 ns (Figure 4.7.1). The RMSD for ketoconazole-PMR-1 was reduced to ~0.85 nm after 20 ns to 50 ns (Figure 4.7.1). The RMSD value for the fluconazole-PMR-1 complex was ~0.75 nm to 30 ns, and ~0.85 nm after 30 ns to 50 ns, a pattern similar to PMR-1 apoprotein and ketoconazole-PMR-1 complex (Figures 4.7.1). These data suggested that fluconazole-PMR-1 and ketoconazole-PMR-1 complexes exhibit only minor structural variations compared to the PMR-1 apoprotein. The smaller RMSD variations observed in the fluconazole-PMR-1 and ketoconazole-PMR-1 complexes compared to PMR-1 apoprotein indicated that these complexes do not undergo significant structural changes upon binding of these ligands. Moreover, among all the PMR-1-azole complexes, itraconazole-PMR-1 interactions exhibited most stable conformation with the lowest RMSD value at ~0.5 nm (Figure 4.7.1).

The RMSF analysis quantifies the average deviation of each residue over time relative to a reference position and serves as a key dynamic parameter to identify the regions of a protein structure exhibiting either highest or lowest mobility (Song et al. 2024). Higher RMSF values suggest a more flexible protein structure complex (Sala et al. 2018; Sarkar et al. 2021). However, lower RMSF values suggest marginal flexibility of the protein-ligand complex (Rahimi et al. 2023). The ketoconazole-CNA-1 complex showed an RMSF value similar to the CNA-1 apoprotein at an average of ~0.5 nm for the amino acid residues positioned from 50 to 400 (Figure 4.5.2). This suggests that ketoconazole binding does not significantly impact the flexibility of CNA-1 in this region, maintaining its structural integrity and stability. The low RMSF values indicate that ketoconazole may form stable interactions that restrict major conformational shifts.

The C-terminal amino acid residues from positions 400 to 556 in the CNA-1 apoprotein and ketoconazole-CNA-1 complex showed average fluctuations below ~1.5 nm (Figure 4.5.2). In the fluconazole-CNA-1 complex, the average RMSF value was ~0.5 nm for the amino acid residues positioned from 100 to 225, however, RMSF value was ~2 nm for the amino acid residues positioned from ~250 to 556. This increased fluctuation suggests that fluconazole binding induces significant structural flexibility, particularly in the C-terminal region. Such increased flexibility may contribute to altered binding dynamics in CNA-1 upon fluconazole interaction. Hence, the terminal residues exhibited the highest fluctuation in the fluconazole-CNA-1 complex (Figure 4.5.2). Similarly, the CNB-1 apoprotein and ketoconazole-CNB-1 complex showed an average RMSF value below ~0.3 nm (Figure 4.6.2). However, the fluconazole-CNB-1 complex showed higher fluctuations (~0.5 nm) between residues 35–60 and 110–130, indicating structural flexibility in these regions (Figure 4.6.2). Similarly, the fluconazole-PMR-1, itraconazole-PMR-1, and ketoconazole-PMR-1, including the PMR-1 apoprotein, exhibited the lowest RMSF at ~0.5 nm. Higher fluctuations (~1.5 nm) were observed at residue positions 150–200 and 450–700 (Figure 4.7.2), indicating greater flexibility in these regions. This suggests that while the core structure of PMR-1 remains relatively stable upon ligand binding, specific regions experience enhanced flexibility, which could be essential for ligand accommodation and functional adaptation (Lexa and Carlson 2012; Wankowicz et al. 2022). The observed variations in RMSF values across different protein-ligand complexes highlight the differential impact of antifungal agents on protein stability, which could be critical in understanding their mode of action and effectiveness in molecular interactions. The amino acid residues of PMR-1 showing higher RMSF value indicate more flexibility in the protein-ligand complex. The Rg parameter is described as the mass-weighted root mean square distance of a group of atoms from their average center of mass (Lobanov et al. 2008). This parameter provides insights into the overall dimensions of a structure and helps in assessing changes in protein conformation. A steady variation in Rg value indicates that the protein maintained consistent stability throughout the simulation (Bhowmick et al. 2020). The plot representing the Rg value (nm) versus time (ns) frame, indicated that the CNA-1 apoprotein (ligand-free protein) was rigid and consistent with an average Rg value of ~2.8 nm (Figures 4.5.3, 4.6.3, and 4.7.3). Moreover, the ketoconazole-CNA-1 complex exhibited an Rg value of ~3 nm, which deviates little higher (~0.2 nm) than the CNA-1 apoprotein. Therefore, CNA-1 apoprotein and CNA-1 in complex with ketoconazole display a similar pattern for the Rg value (Figure 4.5.3). Fluconazole-CNA-1 showed higher Rg value of ~4.2 nm up to 30 ns, however, the lower Rg value of ~3.2 nm was exhibited after 30 ns (Figure 4.5.3). These data consistently suggested that the ketoconazole-CNA-1 complex is stable. Similarly, CNB-1 apoprotein and ketoconazole-CNB-1 complex had similar Rg values at an average of ~1.8 nm (Figure 4.6.3). The fluconazole-CNB-1 complex showed a slightly higher Rg value at ~2.1 nm, which deviates by 0.3 nm (Figure 4.6.3); the higher Rg value indicates a less compact flexible protein structure. The Rg value of the ketoconazole-CNB-1 complex was similar to the CNB-1 apoprotein, which indicated stable and compact protein-ligand complex formation (Figure 4.6.3). In addition, the Rg graph for the PMR-1 protein suggested that the azole drugs form a more compact structure than the PMR-1 apoprotein (Figure 4.7.3). The PMR-1 apoprotein exhibited a higher Rg value (~3.8 nm), indicating lower structural compactness relative to its ligand-bound complexes (Figure 4.7.3). The fluconazole-PMR-1 complex exhibited the highest compactness with a lower Rg value of ~3.6 nm, deviating by 0.2 nm less than the PMR-1 apoprotein (Figure 4.7.3). These results suggested that fluconazole binding induces a more compact conformation of PMR-1. The ketoconazole-PMR-1 and fluconazole-PMR-1 complexes exhibited average Rg values of ~3.7 nm (Figure 4.7.3), indicating that ligand binding reduces Rg and results in a more stable and compact structure compared to the PMR-1 apoprotein. The MD simulations also provide information about the transient and potentially weaker hydrogen bonds that may not be detectable in static structural studies. In both fluconazole-CNA-1 and ketoconazole-CNA-1 complexes, the ligand-protein interactions involved the formation of two hydrogen bonds (Figures 4.5.4, 4.6.4). The fluconazole-CNB-1 complex formed three hydrogen bonds, whereas the ketoconazole-CNB-1 complex formed two hydrogen bonds (Figures 4.6.4, 4.6.5). Similarly, PMR-1 exhibited the highest number of hydrogen bonds in complex with fluconazole, compared to itraconazole and ketoconazole (Figures 4.7.4, 4.7.5, 4,7,6). The fluconazole-PMR-1 complex formed four hydrogen bonds, while the itraconazole-PMR-1 and ketoconazole-PMR-1 complexes formed three and two hydrogen bonds, respectively (Figure 4.7.4, 4.7.5, 4.7.6).

The results described in this chapter, based on molecular docking and molecular dynamics simulations, may provide preliminary insights into potential drug interactions with the CNA-1, CNB-1, and PMR-1 proteins. Moreover, identifying the key amino acid residues involved in protein-drug interactions in CNA-1, CNB-1, and PMR-1 might facilitate the design of antifungal drugs specifically targeting these proteins, which could be useful for combating drug resistance in fungi. Furthermore, insights from molecular docking and MD simulations will guide target-specific antifungal strategies in future studies, using various experimental tools such as isothermal titration calorimetry (ITC), nuclear magnetic resonance (NMR) spectroscopy, site-directed mutagenesis, X-ray crystallography or Cryo-electron microscope. Therefore, these findings could be useful for developing novel, target-specific antifungal therapeutics aimed at combating drug-resistant fungal infections. In the next chapter, I described phytochemical compounds potentially inhibiting calcineurin and PMR-1 functions.

References

Abd EL Motelib T, Amen O (2019) Role of essential oil for control of avian aspergillosis in experimentally infected chickens. Assiut Veterinary Medical Journal 65:152-160

Abdullah A et al. (2023) Molecular Dynamics simulation and pharmacoinformatic integrated analysis of bioactive phytochemicals from Azadirachta indica (Neem) to treat diabetes mellitus. Journal of Chemistry 2023:1-19

Antebi A, Fink GR (1992) The yeast Ca (2+)-ATPase homologue, PMR1, is required for normal Golgi function and localizes in a novel Golgi-like distribution. Molecular biology of the cell 3:633-654

Bates S et al. (2005) Candida albicans Pmr1p, a secretory pathway P-type Ca2+/Mn2+-ATPase, is required for glycosylation and virulence. Journal of Biological Chemistry 280:23408-23415

Bhowmick S et al. (2020) Screening and analysis of bioactive food compounds for modulating the CDK2 protein for cell cycle arrest: Multi-cheminformatics approaches for anticancer therapeutics. Journal of Molecular Structure 1216:128316

Bowman BJ, Abreu S, Johl JK, Bowman EJ (2012) The pmr gene, encoding a Ca2+-ATPase, is required for calcium and manganese homeostasis and normal development of hyphae and conidia in Neurospora crassa. Eukaryotic Cell 11:1362-1370

Chatterjee S, Maity A, Chowdhury S, Islam MA, Muttinini RK, Sen D (2021) In silico analysis and identification of promising hits against 2019 novel coronavirus 3C-like main protease enzyme. Journal of Biomolecular Structure and Dynamics 39:5290-5303

Cowen LE, Sanglard D, Howard SJ, Rogers PD, Perlin DS (2015) Mechanisms of antifungal drug resistance. Cold Spring Harbor perspectives in medicine 5:a019752

Ghahremanian S, Rashidi MM, Raeisi K, Toghraie D (2022) Molecular dynamics simulation approach for discovering potential inhibitors against SARS-CoV-2: A structural review. Journal of molecular liquids 354:118901

Haryadi W, Pranowo HD (2023) Molecular docking and dynamics analysis of halogenated imidazole chalcone as anticancer compounds. Pharmacia 70:323-329

Juvvadi PR, Bobay BG, Cole DC, Awwa M, Steinbach WJ (2022) Calcineurin Inhibitor CN585 Exhibits Off-Target Effects in the Human Fungal Pathogen Aspergillus fumigatus. Journal of Fungi 8:1281

Karkowska-Kuleta J, Rapala-Kozik M, Kozik A (2009) Fungi pathogenic to humans: molecular bases of virulence of Candida albicans, Cryptococcus neoformans and Aspergillus fumigatus. Acta Biochimica Polonica 56:211-224

Lexa KW, Carlson HA (2012) Protein flexibility in docking and surface mapping. Quarterly reviews of biophysics 45:301-343

Li H, Rao A, Hogan PG (2011) Interaction of calcineurin with substrates and targeting proteins. Trends in cell biology 21:91-103

Lobanov MY, Bogatyreva N, Galzitskaya O (2008) Radius of gyration as an indicator of protein structure compactness. Molecular Biology 42:623-628

Pinchai N et al. (2010) The Aspergillus fumigatus P-type Golgi apparatus Ca2+/Mn2+ ATPase PmrA is involved in cation homeostasis and cell wall integrity but is not essential for pathogenesis. Eukaryotic Cell 9:472-476

Pinzi L, Rastelli G (2019) Molecular docking: shifting paradigms in drug discovery. International journal of molecular sciences 20:4331

Rahimi M, Taghdir M, Abasi Joozdani F (2023) Dynamozones are the most obvious sign of the evolution of conformational dynamics in HIV-1 protease. Scientific Reports 13:14179

Sala D, Giachetti A, Rosato A (2018) Molecular dynamics simulations of metalloproteins: A folding study of rubredoxin from Pyrococcus furiosus. AIMS BIOPHYSICS 5:77-96

Sarkar A, Sen D, Sharma A, Muttineni RK, Debnath S (2021) Structure-based virtual screening and molecular dynamics simulation to identify potential SARS-CoV-2 spike receptor inhibitors from natural compound database. Pharmaceutical Chemistry Journal 55:441-453

Sobolev OV et al. (2020) A global Ramachandran score identifies protein structures with unlikely stereochemistry. Structure 28:1249-1258. e1242

Song X et al. (2024) Accurate prediction of protein structural flexibility by deep learning integrating intricate atomic structures and Cryo-EM density information. Nature Communications 15:5538

Tamuli R, Deka R, Borkovich KA (2016) Calcineurin subunits A and B interact to regulate growth and asexual and sexual development in Neurospora crassa. PloS one 11:e0151867

Umesh, Prerna K, Dubey VK (2022) Virtual screening and repurposing of FDA-approved drugs from ZINC database to identify potential autophagy inhibitors exploiting autophagy related 4A cysteine peptidase as a target: potential as novel anti-cancer molecule. Journal of Biomolecular Structure and Dynamics 40:5266-5282

Wankowicz SA, de Oliveira SH, Hogan DW, van den Bedem H, Fraser JS (2022) Ligand binding remodels protein side-chain conformational heterogeneity. Elife 11:e74114

Chapter 5

Studies on phytochemical inhibitors of calcineurin and PMR-1 proteins using computer-aided drug design (CADD) approach

5.1. Introduction

The extensive use of commercially available antifungals promotes the development of resistance against the antifungal drugs, which poses a serious challenge to the treatment of fungal infections (Maertens 2004; Gulshan and Moye-Rowley 2007; Revie et al. 2018). Additionally, current antifungal medications pose significant challenges due to their toxicity and effectiveness. Moreover, multidrug resistance is becoming a major concern in immunocompromised patients. The development of potent antifungal drugs to overcome multidrug resistance is essential for global health and agricultural sustainability. Phytomedicines have been playing a pivotal role in combating diseases and infections since ancient times (Dias et al. 2012). Therefore, the identification and exploration of novel phytochemicals from medicinal plants could be crucial for discovering novel therapeutic drugs to combat multidrug resistance fungi.

The *Dillenia indica* plant is commonly referred to as elephant apple and belongs to the Dilleniaceae family. The fruit of *D. indica* plant is known to possess a range of medicinal properties, including anticancer, antimicrobial, antioxidant, analgesic, anti-inflammatory, and antidiabetic (Abdille et al. 2005). Additionally, *D. indica* fruit alleviates complications such as hyperlipidemia, diabetic nephropathy, and neuropathy (Deraedt et al. 1980; Grover et al. 2002). Traditionally, the fruit pulp is also applied to the scalp to combat dandruff and hair loss, while the sepals have long been used to treat stomach ailments (Saiful Yazan and Armania 2014). Despite these known benefits, the detailed chemical composition of *D. indica* remains to be fully investigated.

In this chapter, I describe the phytochemicals found in *D. indica*, which possess potent antifungal properties and target the CNA-1, CNB-1, and PMR-1 proteins. I searched the PubChem database (https://pubchem.ncbi.nlm.nih.gov/) to identify phytochemical compounds from *D. indica* with novel antifungal properties. I followed computer-aided drug design approach and used MGLTools-1.5.6 (https://ccsb.scripps.edu/download/554/) and Raccoon (https://autodock.scripps.edu/download/373/) to identify potential antifungals targeting the CNA-1, CNB-1, and PMR-1 proteins.

The application of CADD approaches, including molecular docking, provides a promising pathway to identify predicted bioactive compounds with potential antifungal properties. In addition, CADD enables the rapid and cost-effective screening of extensive compound libraries, including the PubChem database, against specific target proteins of interest (Kitchen et al. 2004). I conducted molecular docking and molecular dynamics (MD) simulations to understand the binding affinity and specificity of phytochemical compounds targeting the predicted structures of CNA-1, CNB-1, and PMR-1 proteins. Preliminary computational insights suggest that isorhamnetin may act as a potential inhibitor of the CNA-1 and PMR-1 proteins, and dillenetin may inhibit the CNB-1 protein.

The Absorption-Distribution-Metabolism-Excretion Toxicity (ADMET) profile assessment further supports the suitability of these compounds as drug candidates that also adhered to the Lipinski's rule of five, which predicts good oral bioavailability (Lipinski et al. 2012). These computational insights suggest that the phytochemicals from *D. indica* could serve as potent antifungal drug molecules in the future.

5.2. Results

5.2.1. Selection of phytochemical compounds

I explored 11 phytochemicals obtained from the PubChem database (https://pubchem.ncbi.nlm.nih.gov) that are predominantly found in *D. indica* (Figure 5.1).

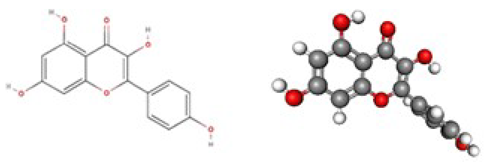
PubChem CID: 5280863 (Kaempferol)

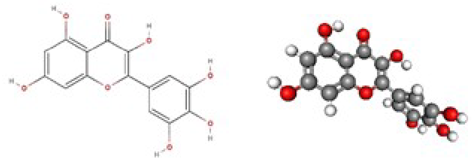
PubChem CID: 5281672 (Myricetin)

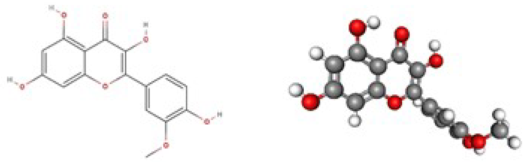
PubChem CID: 5281654 (Isorhamnetin)

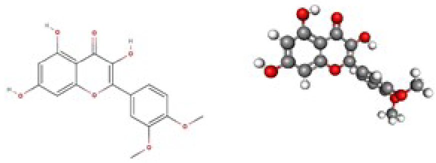
PubChem CID: 5487855 (Dillenetin)

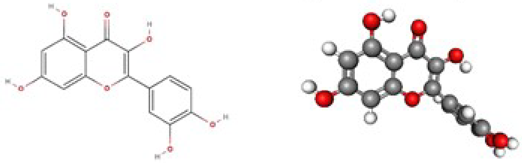
PubChem CID: 5280343 (Quercetin)

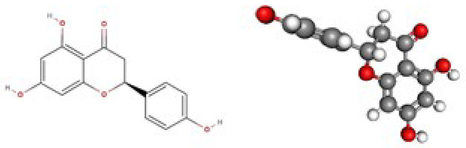
PubChem CID: 439246 (Naringenin)

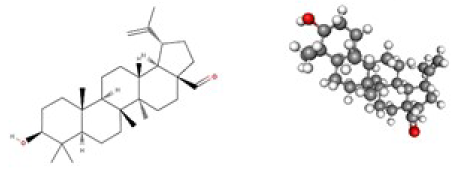
PubChem CID: 99615 (Betulinaldehyde)

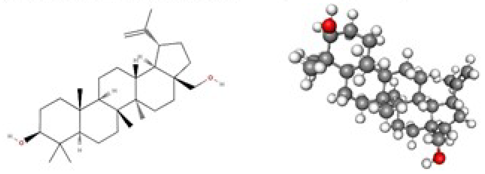
PubChem CID: 72326 (Betulin)

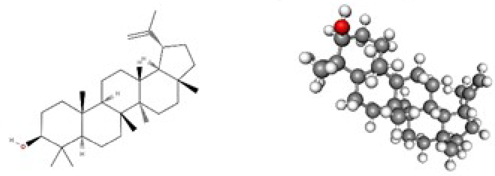
PubChem CID: 259846 (Lupeol)


PubChem CID: 64971 (Betulinic acid)

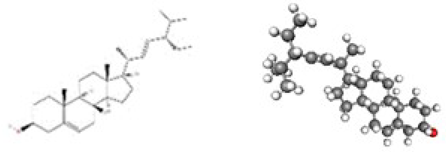
PubChem CID: 5280794 (Stigmasterol)

Figure 5.1. The structures of some selected phytochemicals derived from *D. indica*. The names of the compounds with their 2D and 3D chemical structures, and the respective PubChem IDs (https://molview.org/?cid=5280863) are shown.

5.3. Molecular docking and MD simulations for phytochemical compounds with the CNA-1, CNB-1, and PMR-1 proteins

5.3.1. Molecular docking analysis for the phytochemical compounds binding with CNA-1

The predicted 3D protein structures of CNA-1, CNB-1, and PMR-1 were modeled as described previously in the chapter 4. I performed the molecular docking studies for the phytochemical compounds isorhamnetin, kaempferol, dillenetin, myricetin, naringenin, quercetin, betulinaldehyde, and betulin to evaluate their binding with the CNA-1 protein (Table 5.1). The binding energy for isorhamnetin with the CNA-1 protein was −6.85 kcal/mol, with hydrogen bonds formed with His189, Asp156, and Asp128, along with hydrophobic interactions involving Arg160, Tyr349, Phe344, His319, His130, Arg292, Asn188, Phe198, and Leu350. In the myricetin-CNA-1 complex, which revealed a binding energy of −6.63 kcal/mol, hydrogen bond was formed with His189, His319, Arg292, and Thr199, while hydrophobic interaction was identified for the Arg160, Tyr349, His130, Phe198, Asp159 residues. The kaempferol-CNA-1 complex had a binding energy of −6.4 kcal/mol and showed only hydrophobic interaction with the amino acid residues involving Arg160, Leu350, Tyr349, Tyr353, Phe344, Ala321, Asp156, His319, His130, Asp128, Leu194, His189, Trp270, Asn188, and Arg292. The dillenetin-CNA-1 complex had a binding energy of −6.29 kcal/mol, formed hydrogen bonds with the His189, Asp156, Tyr349, Asp128, His237, Arg292 residues, and showed hydrophobic interactions involving the Arg160, His130, His319, Phe198, Ser426 residues. The naringenin-CNA-1 complex had a binding energy of −6.19 kcal/mol, formed hydrogen bonds with the Ala321, Asp128, Asp156 residues, and hydrophobic interactions involving the Leu350, Arg160, Tyr349, Phe344, His319, Hsi189, Arg292, Asn188, and His130 residues. The betulinaldehyde-CNA-1 complex had a binding energy of −5.83 kcal/mol and formed only hydrophobic interactions with the amino acid residues Asp159, Arg160, His189, Tyr349, Tyr353, Ala321, Glu320, His319, Arg292, Phe198, and Thr199. The quercetin-CNA-1 complex had a binding energy of −5.48 kcal/mol, formed hydrogen bonds with the Asp128, Tyr353 residues, and hydrophobic interactions involving the residues Tyr349, Leu350, Arg160, Arg292, His130, Trp270, His189, Leu194, Asp156, Asn188, His319, Phe344, and Ala321. The betulin-CNA-1 complex had a binding energy −4.92 kcal/mol and showed hydrophobic interactions with amino acid residues Asp159, Arg160, Tyr349, Tyr353, Ala321, Glu320, His319, Arg292, Phe198, and Thr199 (Figure 5.2).

Table 5.1. Specific amino acid residues in the predicted CNA-1 protein structure that interact with ligands, along with the corresponding inhibitor constants and binding energies.

Ligand	**Binding Energy (kcal/mol)**	**Inhibition constant (Ki) (µM)**	**Amino acid residues in the CNA-1 active site**	
			H-bonds	**Hydrophobic interactions**
Isorhamnetin	−6.85	9.59	His189, Asp156, Asp128	Arg160, Tyr349, Phe344, His319, His130, Arg292, Asn188, Phe198, Leu350
Myricetin	−6.63	13.87	His189, His319, Arg292, Thr199	Arg160, Tyr349, His130, Phe198, Asp159
Kaempferol	−6.4	20.46	--	Arg160, Leu350, Tyr349, Tyr353, Phe344, Ala321, Asp156, His319, His130, Asp128, Leu194, His189, Trp270, Asn188, Arg292
Dillenetin	−6.29	34.28	His189, Asp156, Tyr349, Asp128, His237, Arg292	Arg160, His130, His319, Phe198, Ser426
Naringenin	−6.19	20.71	Ala321, Asp128, Asp156	Leu350, Arg160, Tyr349, Phe344, His319, Hsi189, Arg292, Asn188, His130
Betulinaldehyde	−5.83	53.45	--	Asp159, Arg160, His189, Tyr349, Tyr353, Ala321,

				Glu320, His319, Arg292, Phe198, Thr199
Quercetin	−5.48	96.81	Asp128, Tyr353	Tyr349, Leu350, Arg160, Arg292, His130, Trp270, His189, Leu194, Asp156, Asn188, His319, Phe344, Ala321
Betulin	−4.92	247.26	--	Asp159, Arg160, Tyr349, Tyr353, Ala321, Glu320, His319, Arg292, Phe198, Thr199

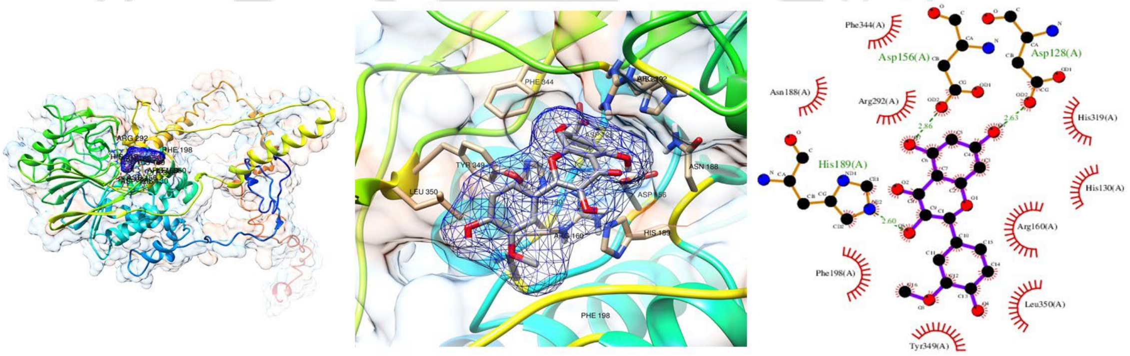

Isorhamnetin + CNA-1

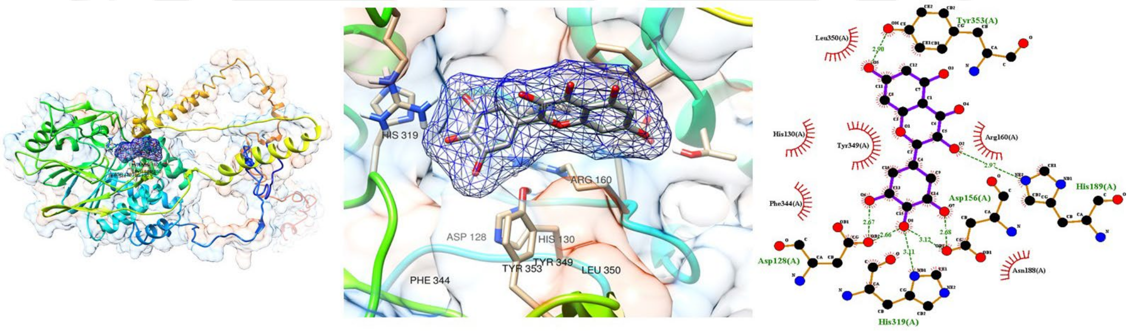

Myricetin + CNA-1

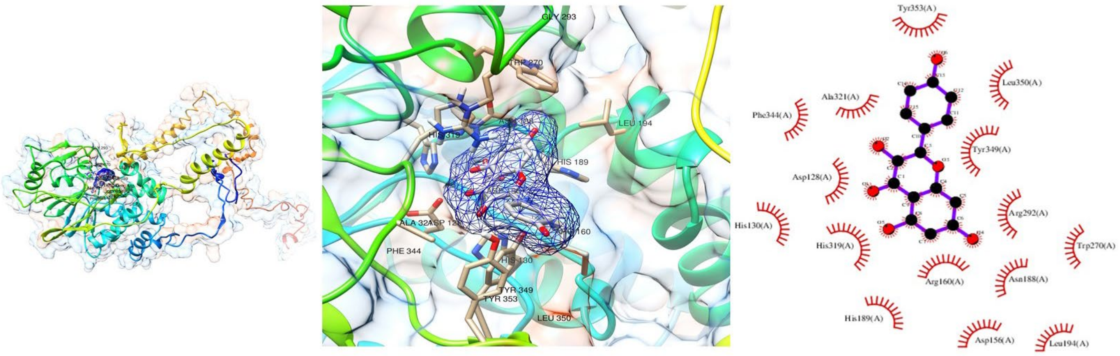

Kaempferol + CNA-1

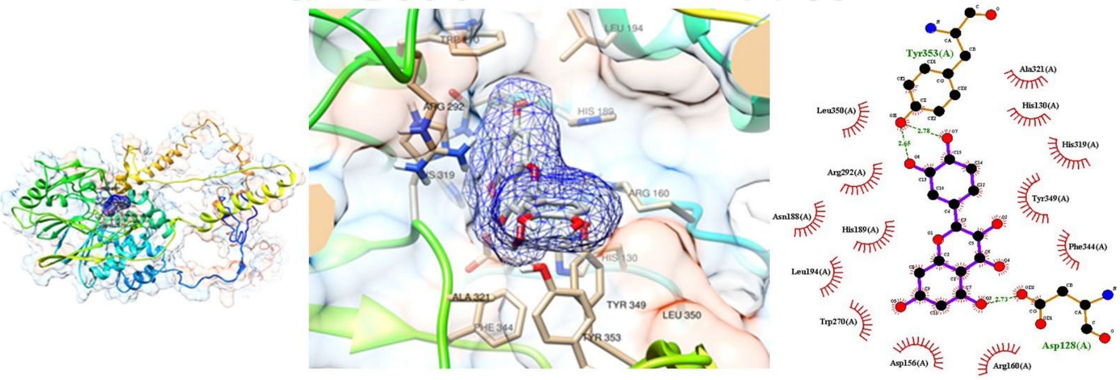

Quercetin + CNA-1

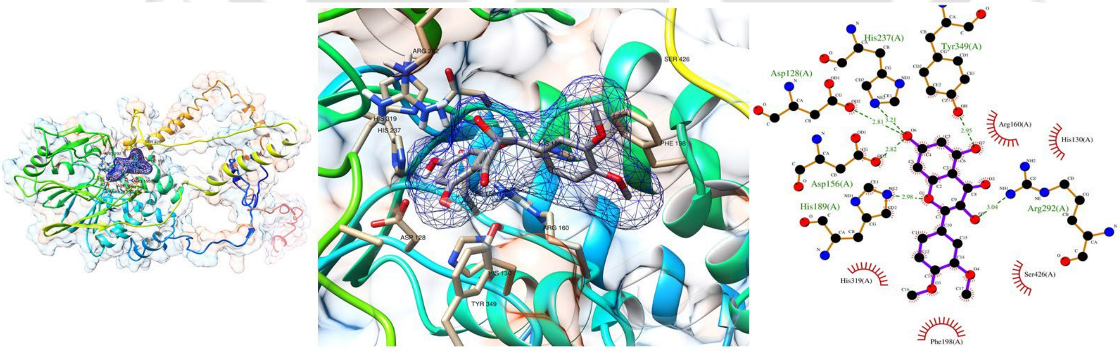

Dillenetin + CNA-1

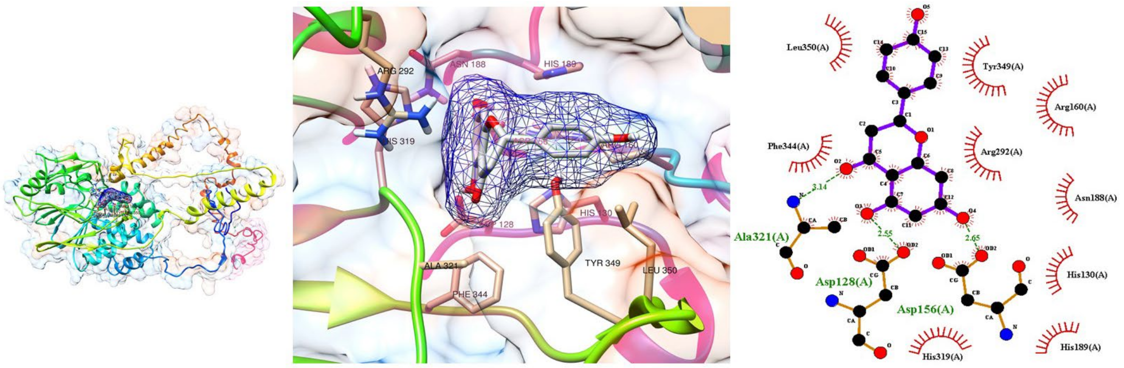

Naringenin + CNA-1

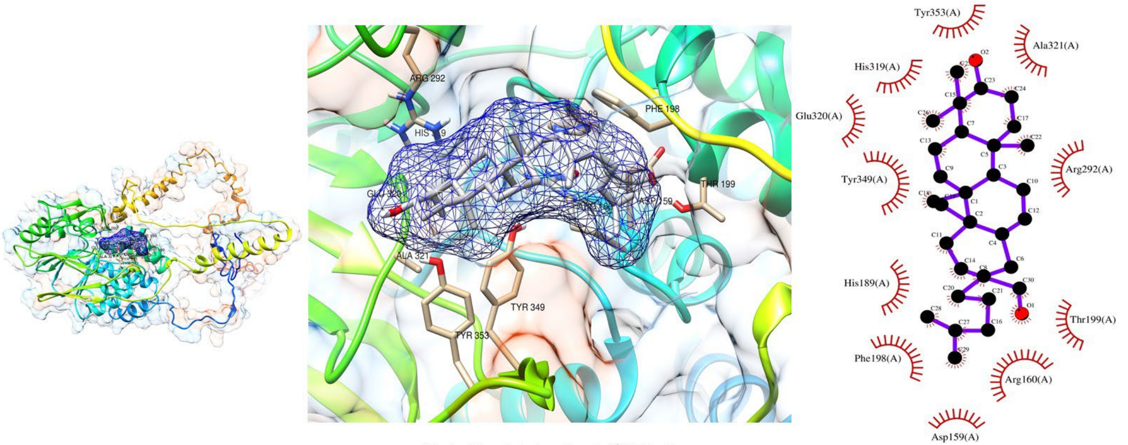

Betulinaldehyde + CNA-1

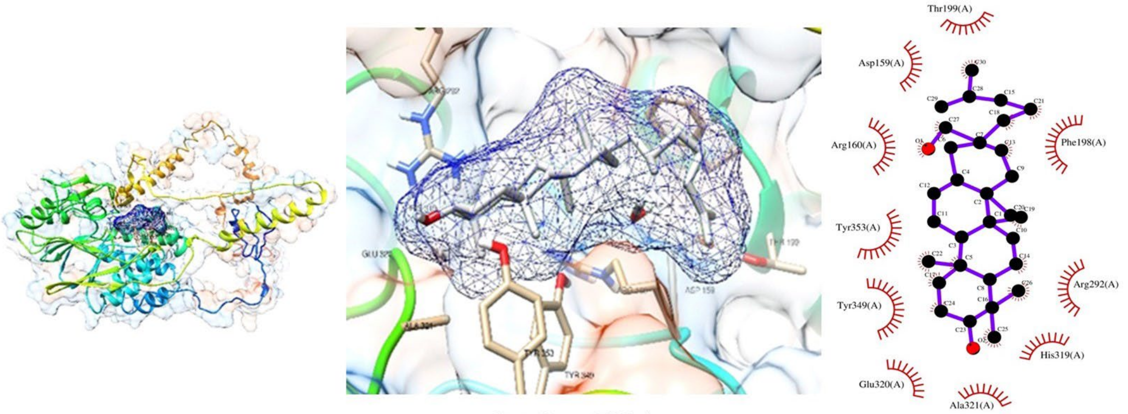

Betulin + CNA-1

Figure 5.2. Molecular docking of the predicted CNA-1 protein structure with phytochemical compounds. The panel on the left shows the ribbon diagram of the predicted CNA-1 protein structure, highlighting the binding site for the respective phytochemical compound within the binding pocket. In the middle panel, a focused view of the binding interactions with phytochemical compounds is shown in the stick representation. The interacting amino acid residues are labelled and shown in the CNA-1 binding pocket. In the right panel 2D interaction map of phytochemical compounds

with the CNA-1 protein is shown. Hydrogen bonds are shown as green dashed lines, and hydrophobic interactions are depicted as red arcs around the interacting residues.

5.3.2. MD simulation analysis of the phytochemical compounds with CNA-1

I performed MD simulation analysis to evaluate the binding affinity between the phytochemical compounds and the predicted structures of the target proteins. The MD simulation allows tracking atomic interactions and movements over time, providing insights into binding processes through parameters such as Root Mean Square Deviation (RMSD), Root Mean Square Fluctuation (RMSF), Radius of Gyration (Rg), and hydrogen bonds (Sneha and Doss 2016; Umesh et al. 2022). To determine stability of the protein-ligand interactions, I calculated three key statistical parameters, RMSD, RMSF, and hydrogen bond (Fatriansyah et al. 2022; Halder et al. 2023). RMSD and RMSF are crucial for understanding the overall structural stability and adaptability of the system during the MD simulations (Fatriansyah et al. 2022). I performed MD simulations for the PMR-1 protein that comprises 1025 amino acid residues, and the CNA-1 protein consisting of 562 residues. Therefore, MD simulations for both the PMR-1 and CNA-1 apoproteins and its ligand complexes were conducted over a 50 ns timescale due to the large size of the proteins. The MD simulations of large proteins for extended periods require significant computational resources and time (Gumbart et al. 2009). The trajectories for the RMSD plot were analyzed to understand the dynamic behavior and stability of the protein-ligand complexes. The RMSD was determined for the apoprotein and its complex with isorhamnetin, kaempferol, dillenetin, myricetin, quercetin, naringenin, and stigmasterol. The complexes of CNA-1 with isorhamnetin and kaempferol exhibited nearly identical and the highest backbone stability, with a maximum deviation of approximately 2.0 nm (Figure 5.3). The complexes of CNA-1 protein with isorhamnetin and kaempferol were more stable than dillenetin and myricetin and showed less deviation compared to the CNA-1 apoprotein (Figure 5.3). The RMSF quantitatively measures the mobility of amino acid residues upon drug binding (Yadav et al. 2024). An increase in RMSF values indicates enhanced flexibility of the atoms (Feng et al. 2009). However, the binding of dillenetin and isorhamnetin lowered the average RMSF value to ~0.3 nm, indicating restricted movement of the CNA-1 active site residues between positions 350 and 400 (Figure 5.4). The lowered RMSF values suggested restricted moment and stable complexes. However, relatively high fluctuations were observed from the amino acid residues 410 to 562 for the CNA-1 phytochemical complexes and CNA-1 apoprotein. Kaempferol showed marginal fluctuations with CNA-1 in the 410 to 562 amino acids residues region, indicating reduced fluctuations and enhanced stability in the complex formation. In addition, Rg is a parameter used to evaluate the structural compactness and globularity of proteins upon interaction with molecules (Lobanov et al. 2008)). Decreased Rg values indicate enhanced stability, corresponding to a more compact protein conformation. On the other hand, higher Rg values reflect a more expanded or disordered protein system (Emmanuel et al. 2019). The complex of isorhamnetin with CNA-1 showed the lowest Rg value compared to all other complexes of phytochemicals with CNA-1. The isorhamnetin-CNA-1 complex exhibited the lowest Rg value, at ~ 2.5 nm, in 25–50 ns MD simulation time (Figure 5.5), suggesting that the isorhamnetin-CNA-1 complex is compact and stable. The dillenetin-CNA-1 and kaempferol-CNA-1 complexes showed highest Rg value at ~3.7 nm and ~3.25 nm, respectively, and myricetin CNA-1 complex forms the plateau at 20‒25 ns at ~3.7 nm. However, myricetin-CNA-1 complex exhibited a similar average Rg value at ~2.75 nm with the CNA-1 apoprotein during 40–50 ns. The Rg plot for CNA-1 and in complex with phytochemical compounds was consistent with its RMSD and RMSF plots, revealing that the binding of isorhamnetin resulted in the formation of a more stable and compact protein-ligand conformation (Figure 5.5). The solvent-accessible surface area (SASA) plot measures the exposure of the protein surface to the solvent environment. Lower SASA values indicate a decreased exposure of hydrophobic amino acid residues to the solvent, which typically enhances system stability by promoting internal hydrophobic interactions (Durham et al. 2009). The average SASA values of the CNA-1 complexes with isorhamnetin, dillenetin, myricetin and kaempferol were 401.1787 nm^2, 403.967 nm^2, 399.7069 nm^2, and 404.4551 nm^2, respectively. The isorhamnetin-CNA-1 and myricetin-CNA-1 complexes had lower SASA values than the CNA-1 apoprotein (401.5965 nm^2), while the dillenetin-CNA-1 and kaempferol-CNA-1 complexes exhibited higher SASA values. These results indicated that the binding of isorhamnetin and myricetin reduced the exposure of hydrophobic amino acid residues and increased the structural stability of the complexes. However, the binding of dillenetin (403.967 nm^2) and kaempferol (404.4551 nm^2) increased the SASA area compared to the CNA-1 apoprotein (401.5965 nm^2) (Figure 5.6). These results suggested that the interactions of dillenetin and kaempferol in complex with CNA-1, results in an increased exposure of hydrophobic residues in CNA-1 to the solvent, and thus reduced the structural stability compared to the isorhamnetin-CNA-1 and myricetin-CNA-1 complexes. In addition, hydrogen bonds contribute to the overall stability of the protein structure. Therefore, I also evaluated the intermolecular hydrogen bond formation for the CNA-1 protein with isorhamnetin, dillenetin, kaempferol and myricetin in the entire course of 50 ns simulation. Hydrogen bond analysis was performed to assess the attachment stability between ligands and proteins. The analysis revealed that the dillenetin-CNA-1 complex formed a maximum of three hydrogen bonds (Figure 5.7 A). The isorhamnetin-CNA-1 complex formed a maximum of four hydrogen bonds (Figure 5.7 B). Similarly, the kaempferol-CNA-1 complex exhibited a maximum of four hydrogen bonds (Figure 5.7 C), while the myricetin-CNA-1 complex exhibited a maximum of five hydrogen bonds (Figure 5.7 D).

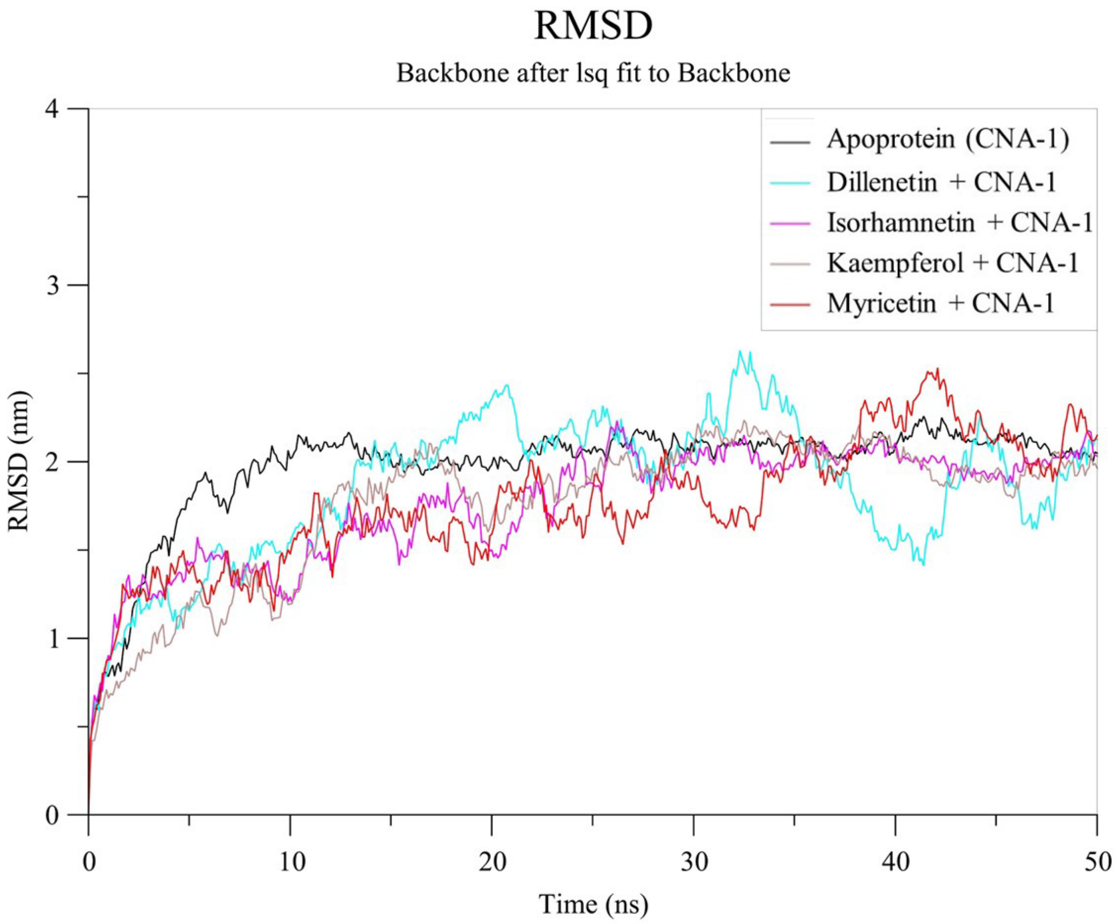

Figure 5.3. The RMSD plot of the predicted CNA-1 apoprotein and its complexes with the ligands. The RMSD plots for the predicted CNA-1 apoprotein and its complexes with the ligands isorhamnetin, myricetin, kaempferol, and dillenetin were derived from MD simulations for 50 ns.

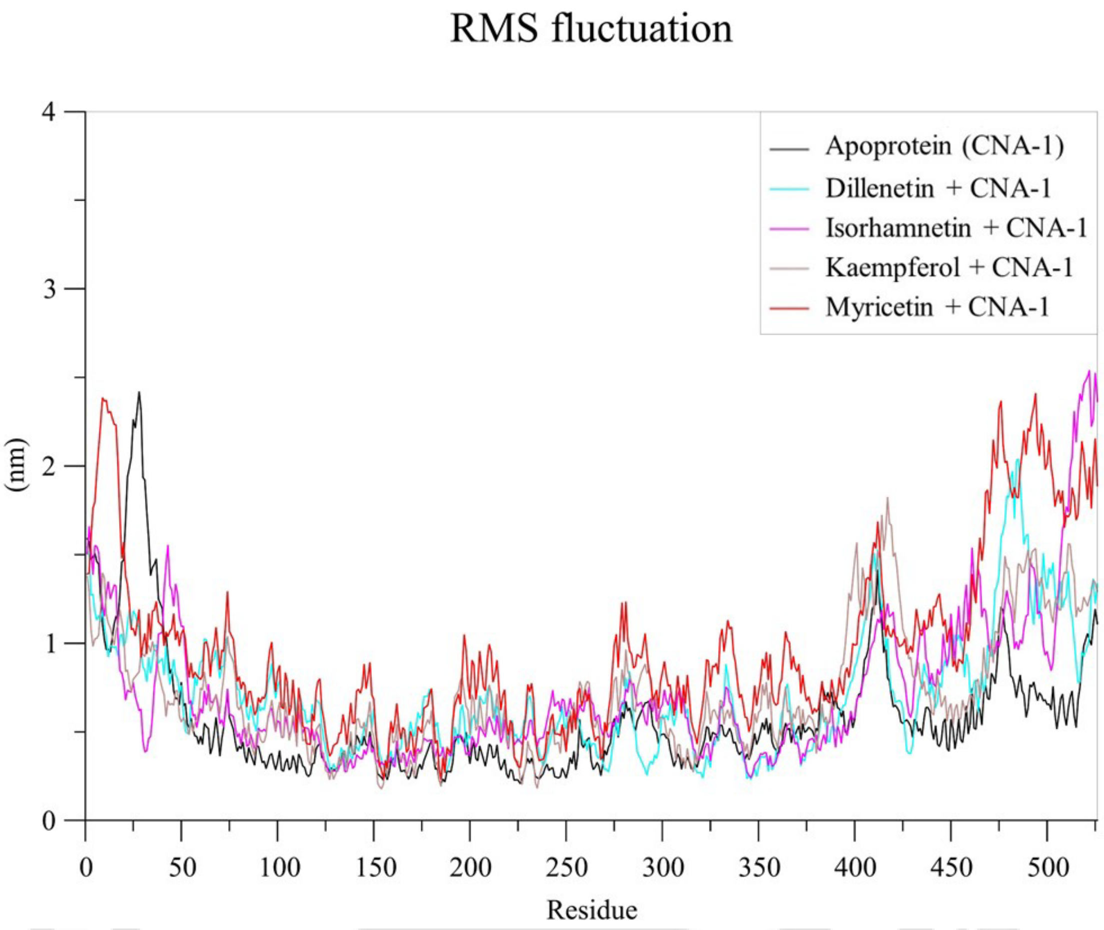

Figure 5.4. The plot shows RMSF fluctuations for the predicted CNA-1 apoprotein and the CNA-1 complexes with phytochemical compounds. The RMSF fluctuation of the isorhamnetin-CNA-1, myricetin-CNA-1, kaempferol-CNA-1, and dillenetin-CNA-1 complexes were derived from MD simulations for 50 ns.

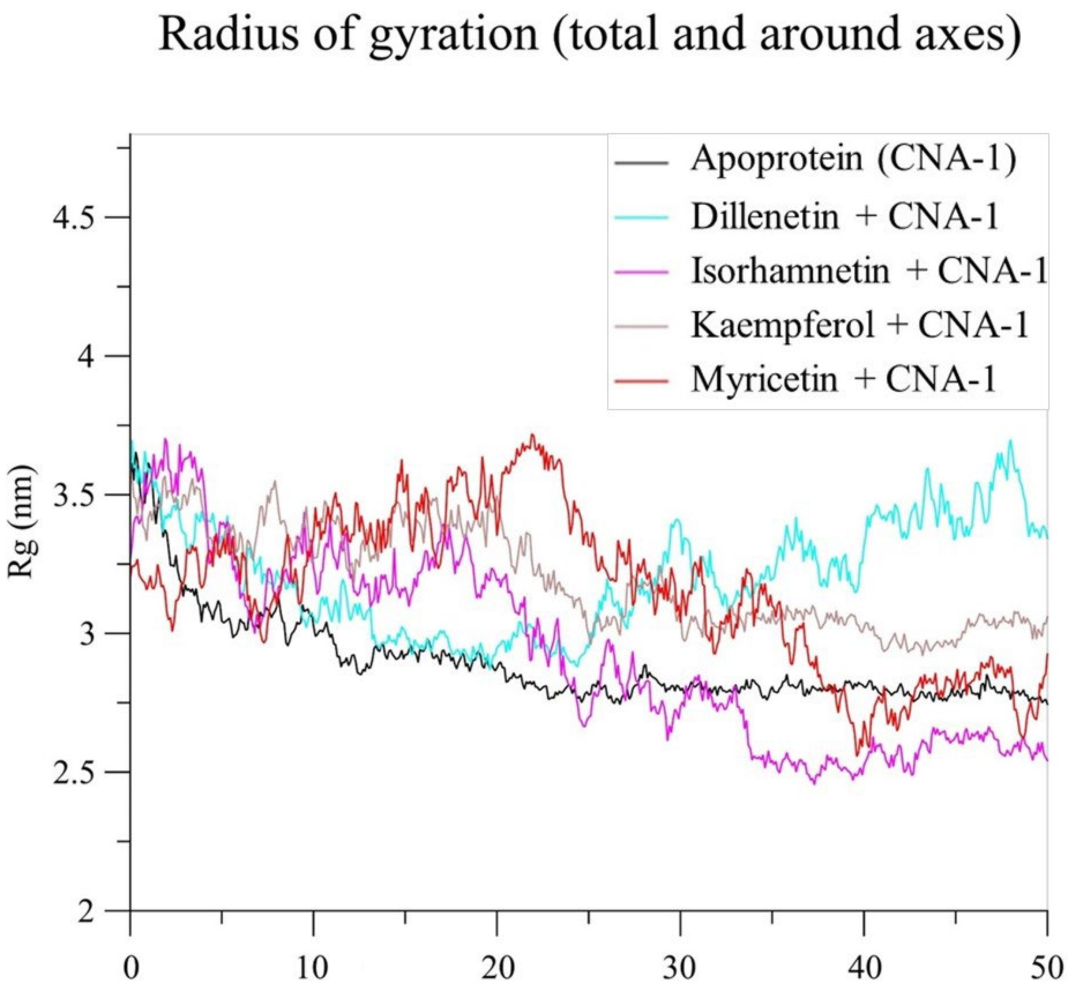

Figure 5.5. The plot of Rg values for the predicted CNA-1 apoprotein and the protein complexes. The plots show Rg values for the predicted CNA-1 apoprotein and its complexes with isorhamnetin, myricetin, kaempferol, and dillenetin derived from MD simulations for 50 ns.

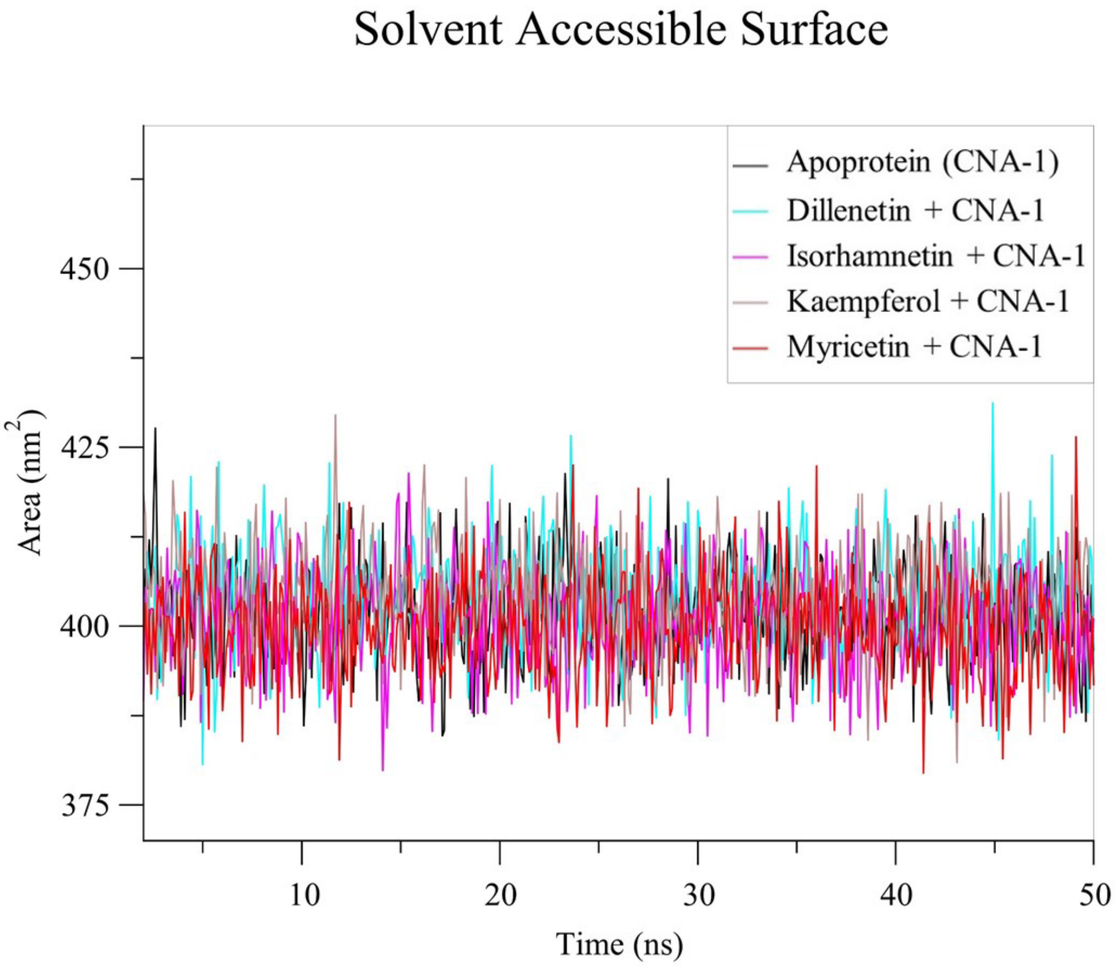

Figure 5.6. The SASA plot for the predicted CNA-1 apoprotein and its complexes. The SASA plots of the predicted CNA-1 apoprotein and its complexes with isorhamnetin, myricetin, kaempferol, and dillenetin were derived from MD simulations for 50 ns.

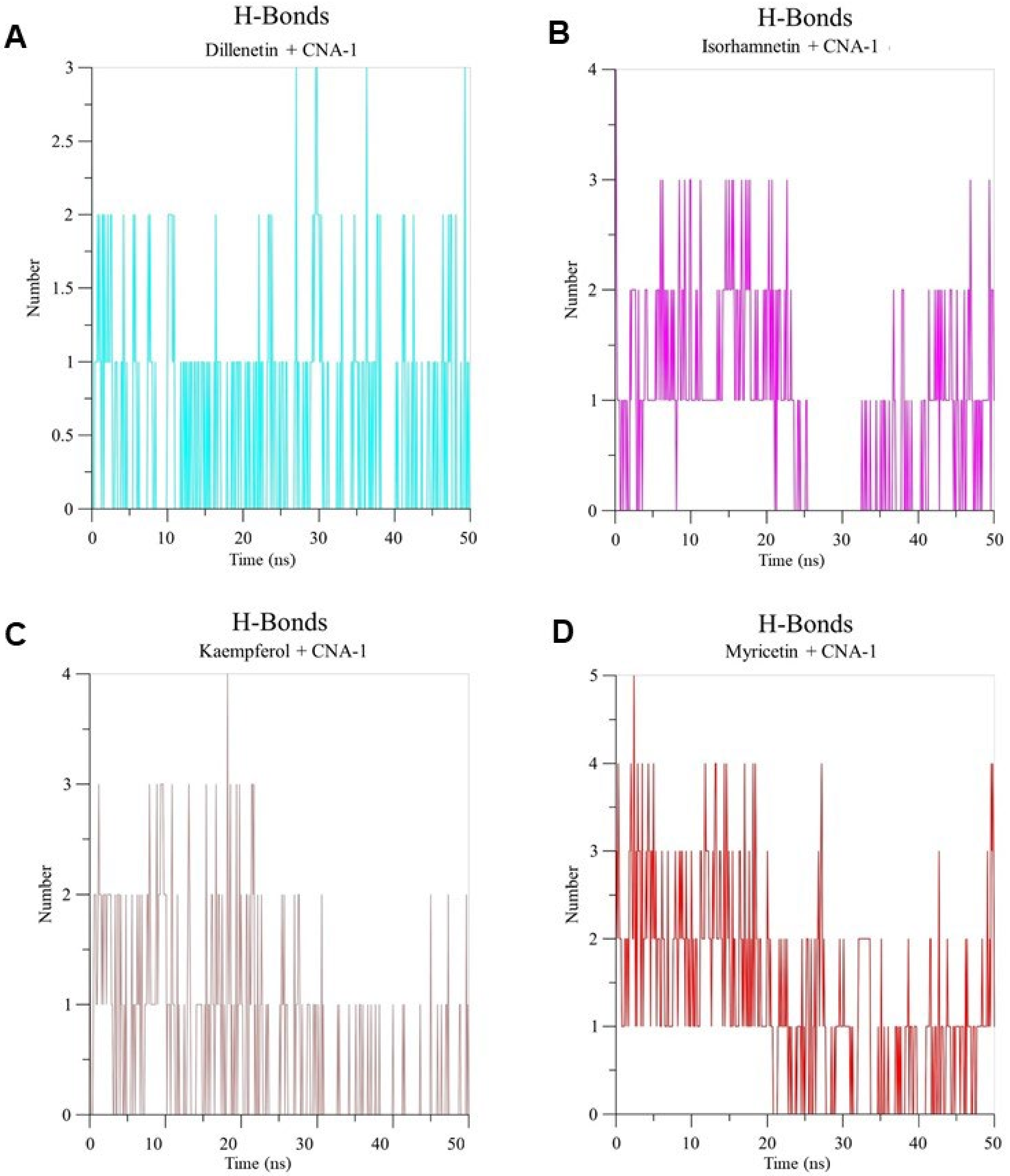

Figure 5.7. The plot of hydrogen bond formation during the MD simulations of the predicted CNA-1 and phytochemical complexes. The plot shows the number of hydrogen (H) bonds with (A) dillenetin, (B) isorhamnetin, (C) kaempferol, and (D) myricetin in MD simulations for 50 ns.

5.3.3. Molecular docking analysis of the complexes of phytochemical compounds with the predicted CNB-1 proteins

I also performed docking analysis for the complexes of the predicted CNB-1 protein with myricetin, isorhamnetin, kaempferol, dillenetin, quercetin, naringenin, betulinaldehyde, betulin, lupeol, and betulinic acid (Table 5.2). In the myricetin-CNB-1 complex, which exhibited a binding energy of −7.41 kcal/mol, Arg96 and Phe153 formed hydrogen bonds, while the amino acid residues Asp103, Phe99, Glu154, Tyr109, Ser152, Gly108, Arg106, and Lys100 were involved in hydrophobic interactions. The binding energy for the isorhamnetin-CNB-1 complex was −6.96 kcal/mol, Asp103, Arg106, Tyr109, and Phe153 residues formed hydrogen bonds, and the Gly108, Ser152, Phe99, Glu154, Lys100, and Arg96 residues were involved in hydrophobic interaction. The kaempferol-CNB-1 complex showed a binding energy of −6.66 kcal/mol, the Arg96 residue formed hydrogen bond, and the Asp103, Arg106, Glu154, Phe153, Gly108, Tyr109, Phe99, Lys100 residues were involved in hydrophobic interaction. The dillenetin-CNB-1 complex had a binding energy of −5.66 kcal/mol, formed hydrogen bonds with the Arg106 and Arg96 residues, and showed hydrophobic interactions with the Asp107, Asp103, Lys100, Phe99, Ser152, Tyr109, Glu154, Gly108, and Phe153 residues. The quercetin-CNB-1 complex showed a binding energy of −5.62 kcal/mol, where hydrogen bonds formed with the Glu154 and Phe153 residues, and hydrophobic interactions involved the amino acid residues Arg106, Asp103, Arg96, Lys100, Phe99, Tyr109, and Ser152. The naringenin-CNB-1 complex had a binding energy of −5.15 kcal/mol, formed hydrogen bonds with the Asp103, Arg96, Lys100, and Arg106 residues, showed hydrophobic interactions with the Tyr109, Phe99, Ser152, Phe153, Glu154, and Gly108 residues. The betulinaldehyde-CNB-1 complex showed a binding energy of −5.56 kcal/mol, formed hydrogen bonds with the Arg96 residue, and showed hydrophobic interactions with the Asp107, Asp103, Lys100, Phe99, Gly108, and Arg106 residues. The binding energy for the betulin-CNB-1 complex was −5.24 kcal/mol, where hydrogen bond formed involving the Asp107 residue, and hydrophobic interactions with Asp103, Arg96, Lys100, Phe99, Gly108, and Arg106 residues were observed. The lupeol-CNB-1 complex had a binding energy of −4.80 kcal/mol, formed hydrogen bond with the Arg106 residue, and hydrophobic interactions with Asp107, Arg96, Ser152, Phe153, Glu154, Gly108, and Tyr109 residues were observed. The betulinic acid-CNB-1 complex exhibited a binding energy of −3.28 kcal/mol, formed hydrogen bonds with the Glu154 residue, and hydrophobic interactions with Phe153, Tyr109, Arg106, Asp107, Glu67, Arg96, and Gly108 residues were observed.

Table 5.2. Specific amino acid residues in the predicted CNB-1 protein structure interacting with the ligands and the corresponding inhibitor constants and binding energies

Ligand	**Binding Energy (Kcal/mol)**	**Inhibition constant (Ki) (µM)**	**Amino acid residues in the CNB-1 active site**	
			H-bonds	**Hydrophobic interactions**
Myricetin	−7.41	3.69	Arg96, Phe153	Asp103, Phe99, Glu154, Tyr109, Ser152, Gly108, Arg106, Lys100
Isorhamnetin	−6.96	7.96	Asp103, Arg106, Tyr109, Phe153	Gly108, Ser152, Phe99, Glu154, Lys100, Arg96
Kaempferol	−6.66	13.19	Arg96	Asp103, Arg106, Glu154, Phe153, Gly108, Tyr109, Phe99, Lys100
Dillenetin	−5.66	118.09	Arg106, Arg96	Asp107, Asp103, Lys100, Phe99, Ser152, Tyr109, Glu154, Gly108, Phe153
Quercetin	−5.62	14.09	Glu154, Phe153	Arg106, Asp103, Arg96, Lys100, Phe99, Tyr109, Ser152
Naringenin	−5.15	31.09	Asp103, Arg96, Lys100, Arg106	Tyr109, Phe99, Ser152, Phe153, Glu154, Gly108
Betulinaldehyde	−5.56	84.34	Arg96	Asp107, Asp103, Lys100, Phe99, Gly108, Arg106
Betulin	−5.24	144.75	Asp107	Asp103, Arg96, Lys100, Phe99, Gly108, Arg106
Lupeol	−4.8	304.06	Arg106	Asp107, Arg96, Ser152, Phe153, Glu154, Gly108, Tyr109
Betulinic acid	−3.28	3.95	Glu154	Phe153, Tyr109, Arg106, Asp107, Glu67, Arg96, Gly108

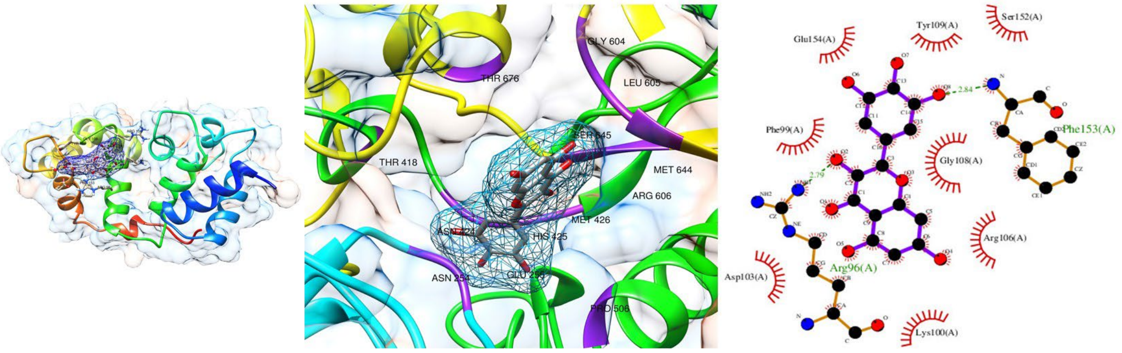

Myricetin + CNB-1

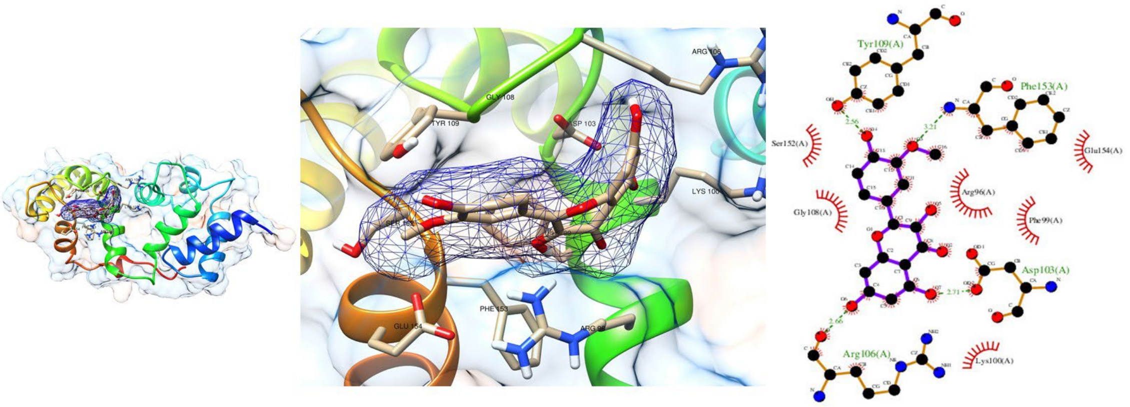

Isorhamnetin + CNB-1

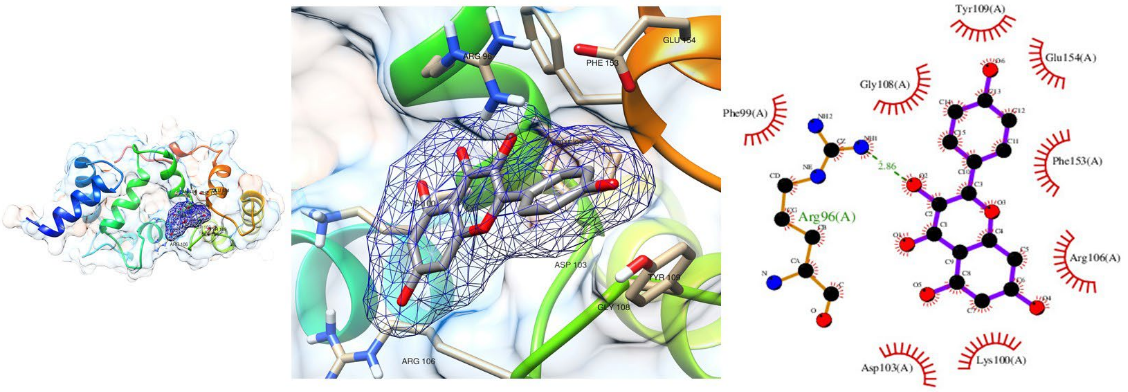

Kaempferol + CNB-1

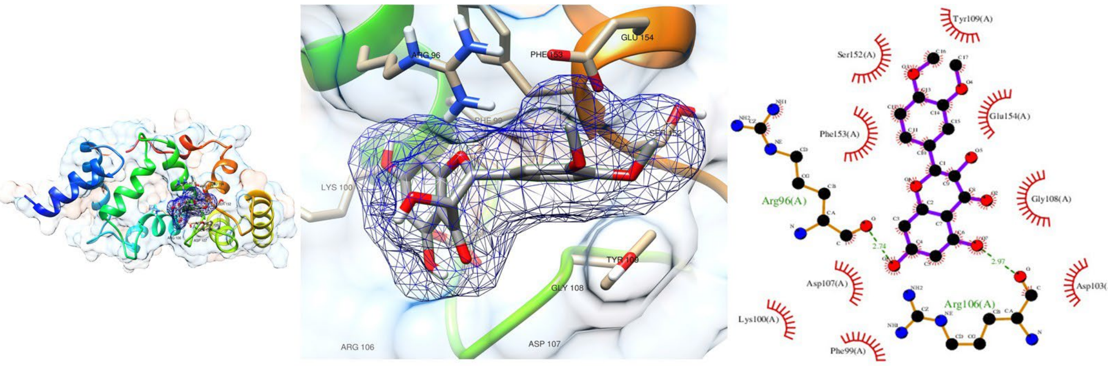

Dillenetin + CNB-1

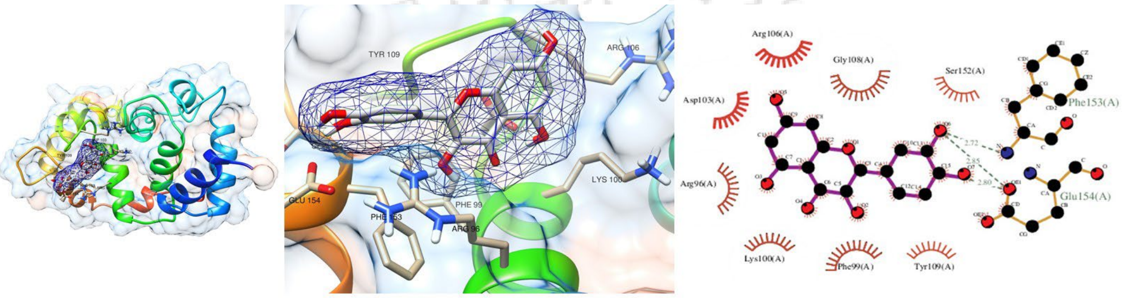

Quercetin + CNB-1

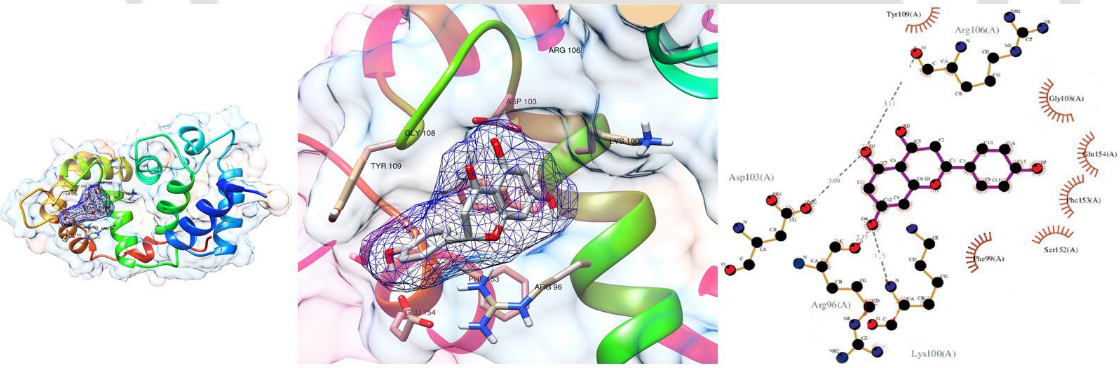

Naringenin + CNB-1

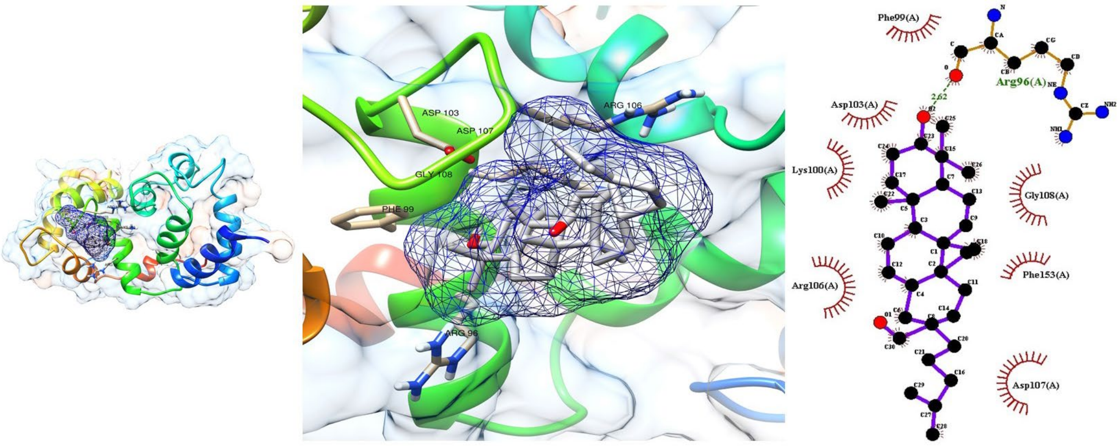

Betulinaldehyde + CNB-1

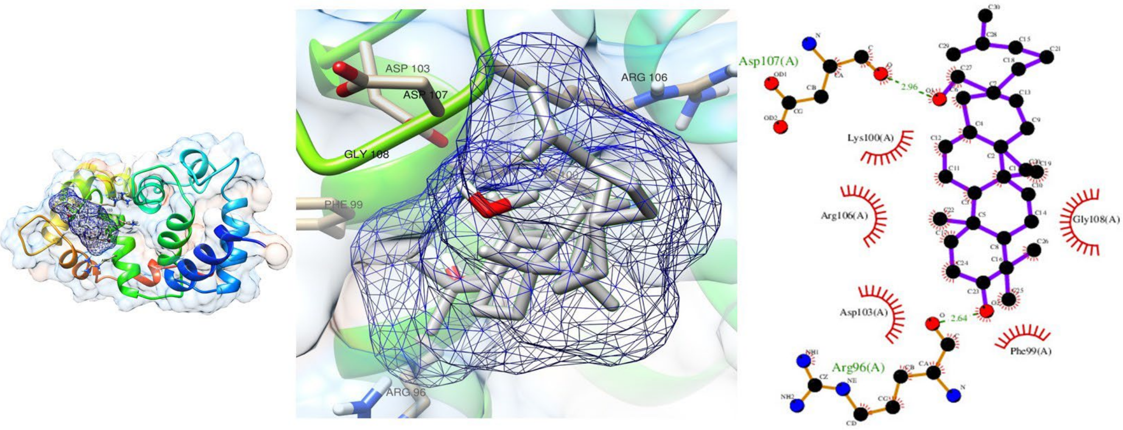

Betulin + CNB-1

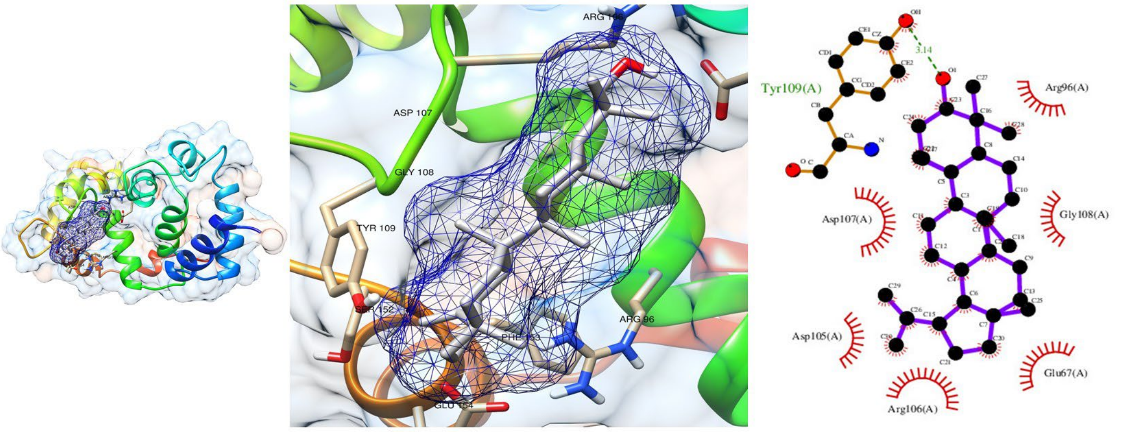

Lupeol + CNB-1

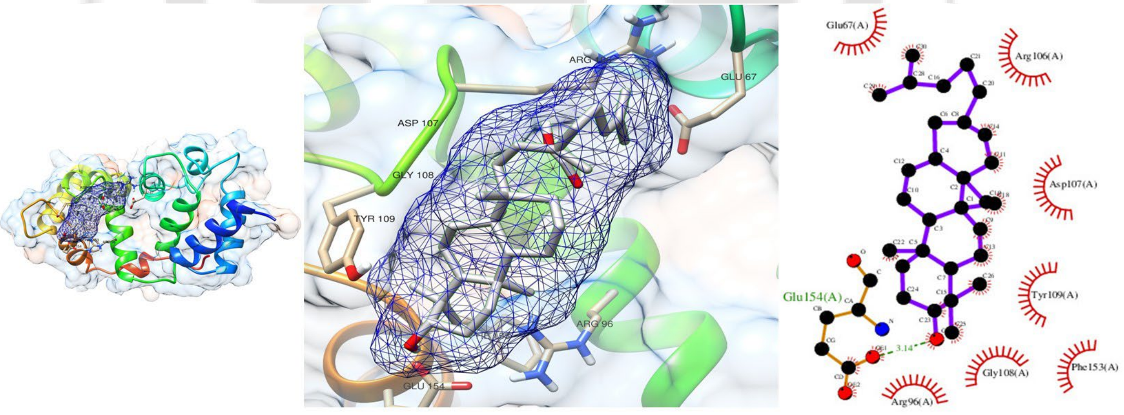

Betulinic + CNB-1

Figure 5.8. Molecular docking of the predicted CNB-1 protein structure with phytochemical compounds. The panel on the left shows the ribbon diagram of the predicted CNB-1 protein structure, highlighting the binding site for the respective phytochemical compound within the binding pocket. In the middle panel, the binding

interactions between phytochemical compounds are focused and shown in a stick representation. The interacting amino acid residues are labelled and displayed in stick form within the CNB-1 binding pocket. In the right panel, the 2D interaction maps of the phytochemical compounds with the CNB-1 protein are shown. Hydrogen bonds are represented as green dashed lines, and hydrophobic interactions are depicted as red arcs around the interacting residues.

5.3.4. MD simulations of the predicted CNB-1 protein with phytochemical compounds

I performed the RMSD analysis for the predicted CNB-1 apoprotein and its complex with the phytochemical compounds dillenetin, isorhamnetin, kaempferol, and myricetin (Figure 5.9). The dillenetin-CNB-1 protein complex exhibited the highest backbone stability among all the four complexes studied, with a maximum deviation of ~0.55 nm. The RMSD trajectories for the isorhamnetin and myricetin complexes with CNB-1 displayed consistent patterns similar to the CNB-1 apoprotein throughout the 50 ns MD simulation. The kaempferol-CNB-1 complex showed the highest RMSD value, with a maximum deviation at ~0.6 nm (Figure 5.9). However, the dillenetin-CNB-1 complex exhibited greater stability than the other four studied phytochemicals, with the lowest RMSD value. The dillenetin-CNB-1 complex showed a lower deviation compared to the CNB-1 apoprotein after 15 ns and throughout the MD simulation. These data suggested that among the CNB-1 complexes with phytochemicals, the dillenetin-CNB-1 complex possesses the greatest protein-ligand stability. I conducted a comparative analysis of RMSF values, specifically focusing on the active site of the CNB-1 protein in the complexes with phytochemical compounds and the CNB-1 apoprotein. The mobility of protein residues in the presence and absence of ligands were studied based on the RMSF changes. The RMSF is one of the most effective methods for analyzing the mobility of protein residues in a protein-ligand complex (Song et al. 2024). The RMSF values for both the apoprotein and the four-ligand complexes were calculated using GROMACS over a 50 ns timescale. The RMSF graph for the CNB-1 protein, encompassing amino acid residues 174 in complexes with phytochemicals in an MD simulation for 50 ns revealed that most amino acid residues exhibited fluctuations between ~ 0.1 nm to 0.3 nm (Figure 5.10). Notably, among all the complexes, dillenetin demonstrated the lowest fluctuations in the amino acid residues from 75 to 174, indicating the stability of the relative secondary conformation and minimal fluctuation of the CNB-1 protein, followed by the isorhamnetin, kaempferol, and myricetin compounds. Amino acid residues in the N-terminal of CNB-1 showed RMSF fluctuations similar to the CNB-1 and phytochemical compounds dillenetin, isorhamnetin, and myricetin complexes, except for the kaempferol-CNB-1 complex (Figure 6.0). The kaempferol-CNB-1 complex showed a higher deviation up to 0.72 nm in the amino acid residue positions 10 to 20, whereas dillenetin CNB-1 complex showed the lowest deviation in this range (Figure 6.0). Moreover, all the complexes and the CNB-1 apoprotein showed the same fluctuation pattern for the amino acid residues in positions 50 to 120. Interestingly, in the C-terminal region from the residues 120–130 of CNB-1, high RMSF, fluctuations were observed for the myricetin-CNB-1 complex, while the dillenetin-CNB-1 complex (cyan color) exhibited the lowest RMSF, suggesting less fluctuations indicating stability in the dillenetin-CNB-1 complex (Figure 5.10). The CNB-1 apoprotein and dillenetin-CNB-1 complex showed the same pattern throughout the MD simulations from 0 to 50 ns at an Rg value ~1.90 nm (Figure 5.11). The myricetin-CNB-1 complex showed a pattern similar to the CNB-1 apoprotein and dillenetin-CNB-1 complex, but showed the minimum Rg value of approximately 0.5 nm after 25 ns. Isorhamnetin-CNB-1 and kaempferol-CNB-1 showed the maximum Rg values at ~2.0 nm and ~2.1 nm, respectively. Therefore, in comparison to the compared to the CNB-1 apoprotein, compactness was maximum for the CNB-1 complexes with dillenetin and myricetin that exhibited lowest Rg values, followed by the CNB-1 complexes with isorhamnetin and kaempferol. Additionally, SASA values were determined for the CNB-1 apoprotein and its associated compounds over the 50 ns simulation period (Figure 5.12). The SASA value for the dillenetin-CNB-1 complex was lower (106.5436 nm^2) compared to the CNB-1 apoprotein (107.1956 nm^2). In contrast, isorhamnetin (107.8618 nm^2) and myricetin (107.7882 nm^2) displayed higher SASA values in complexes with CNB-1 protein compared to that of the CNB-1 apoprotein. The kaempferol-CNB-1 complex showed an SASA value of 107.6089 nm^2. The dillenetin-CNB-1 complex demonstrated the best compactness and stability among all the compounds studied (Figure 5.12). In addition, I evaluated the intermolecular hydrogen bond formation for the CNB-1 protein with isorhamnetin, myricetin, kaempferol, and dillenetin throughout the MD simulations for 50 ns. In addition, the CNB-1 protein in complex with isorhamnetin showed a maximum of four intermolecular hydrogen bonds (Figure 5.13 A). The dillenetin-CNB-1 complex showed a maximum of three intermolecular hydrogen bonds (Figure 5.13 B). The myricetin-CNB-1 complex showed a maximum of seven intermolecular hydrogen bonds (Figure 5.13 C), whereas the kaempferol-CNB-1 complex showed a maximum of two intermolecular hydrogen bonds (Figure 5.13 D).

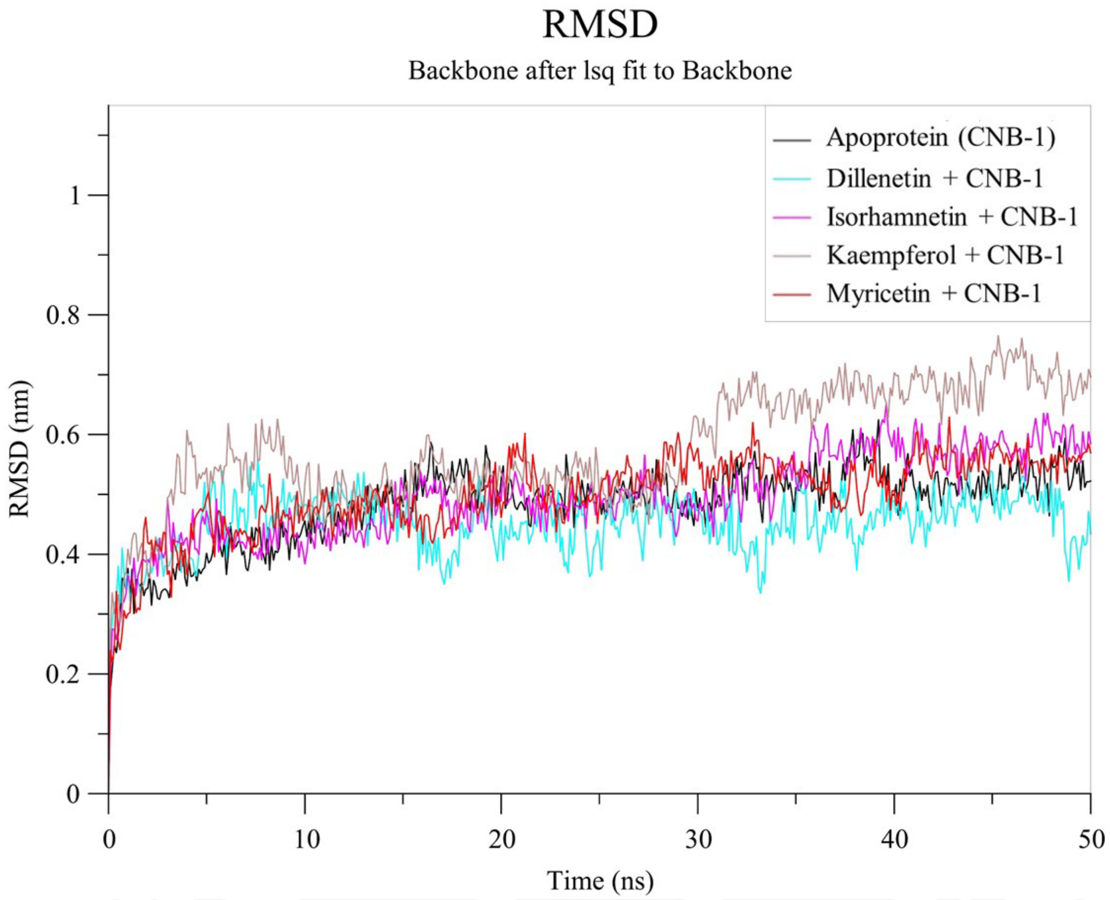

Figure 5.9. The RMSD plot for the predicted CNB-1 apoprotein and its complexes. The RMSD plots for the predicted CNB-1 protein with the isorhamnetin, myricetin, kaempferol, and dillenetin ligands were derived from MD simulations for 50 ns.

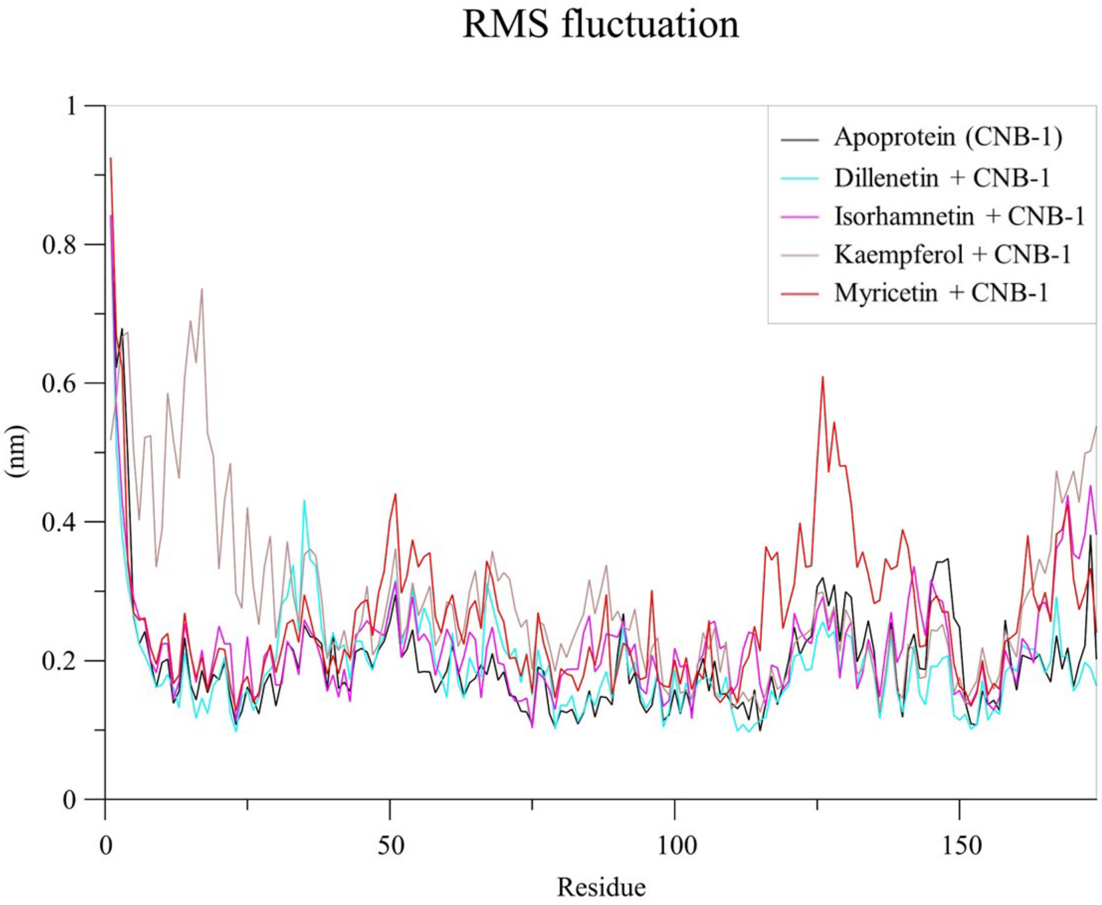

Figure 5.10. The plot shows the RMSF fluctuation of the predicted CNB-1 apoprotein and its complexes with phytochemical compounds. The plots for isorhamnetin-CNB-1, myricetin-CNB-1, kaempferol-CNB-1, and dillenetin-CNB-1 complexes in MD simulations for 50 ns are shown.

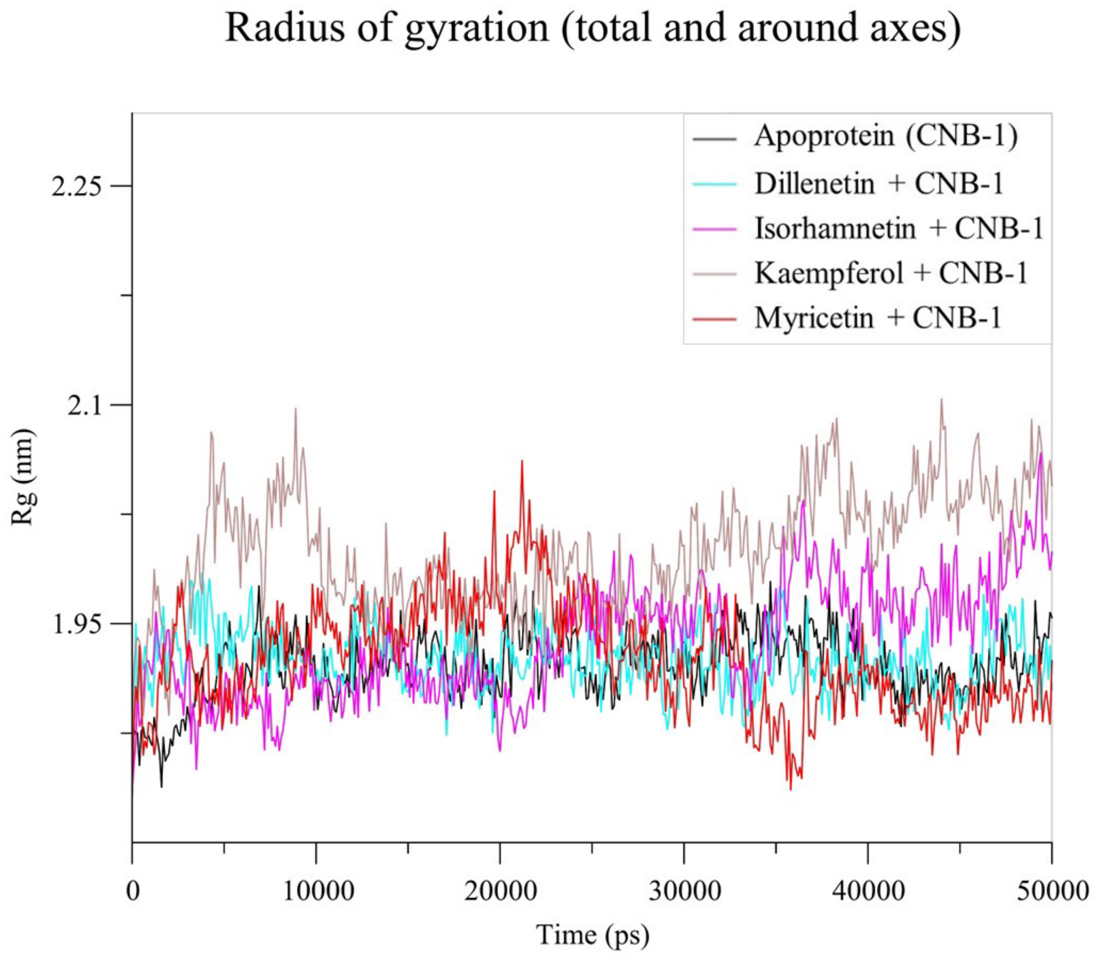

Figure 5.11. The graph plotted for the Rg values of the predicted CNB-1 apoprotein and the CNB-1 protein-ligand complexes. The Rg values for the CNB-1 protein with isorhamnetin, myricetin, kaempferol, and dillenetin were derived from MD simulations for 50 ns.

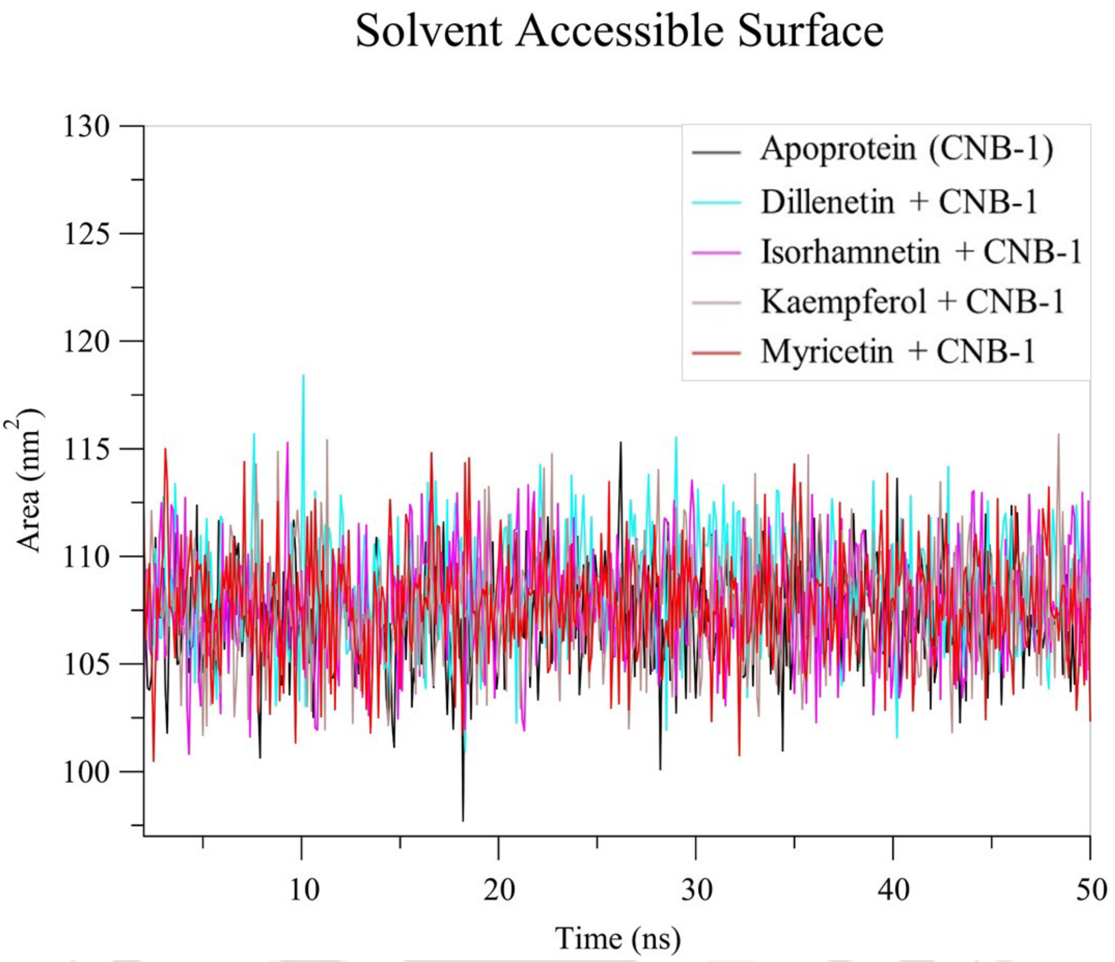

Figure 5.12. The SASA plot for the CNB-1 and its complexes with phytochemical compounds. The graph represents the SASA value for the predicted CNB-1 apoprotein and CNB-1 protein-ligand complexes of isorhamnetin, myricetin, kaempferol, and dillenetin, in MD simulations for 50 ns.

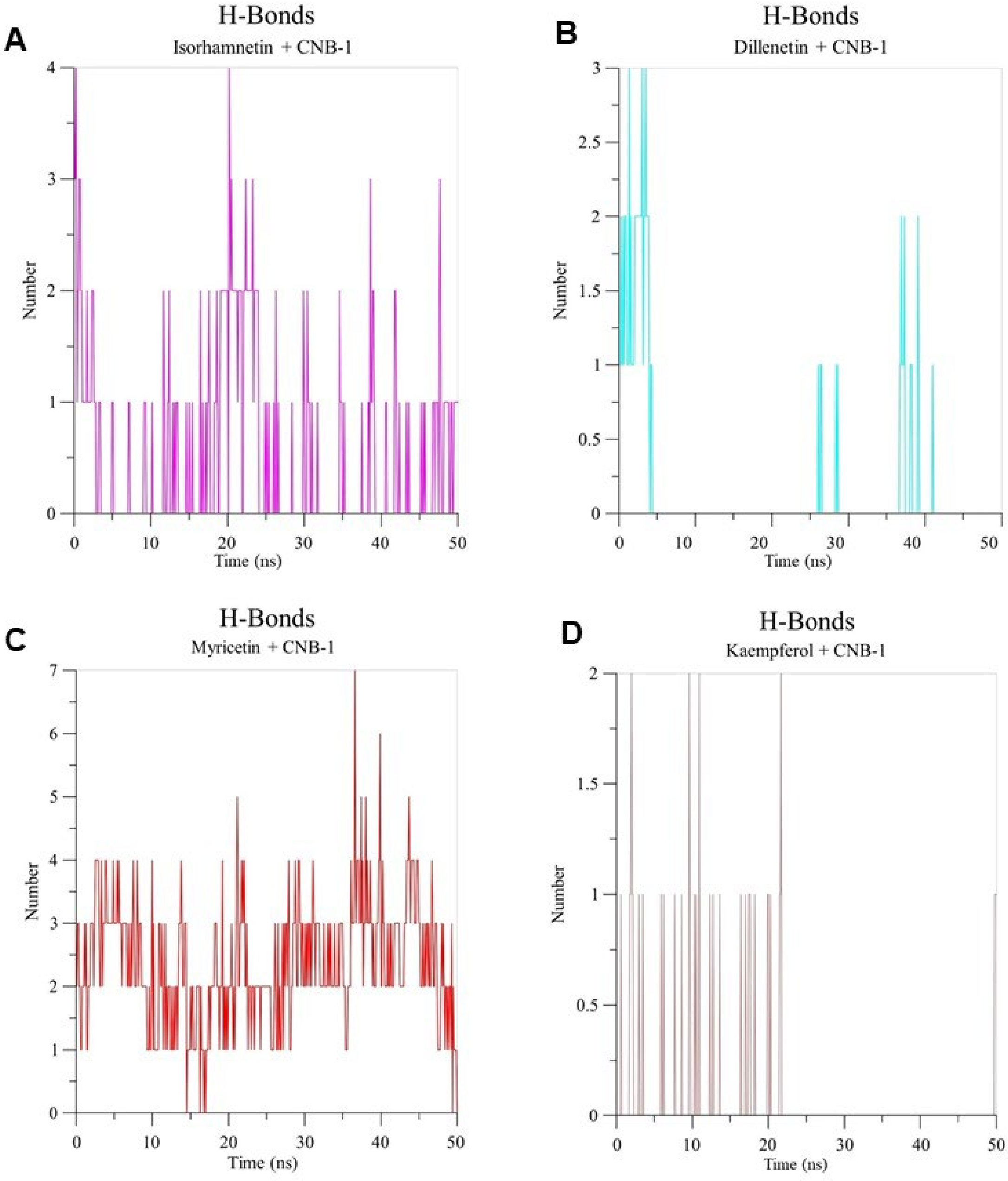

Figure 5.13. Plot of hydrogen bond formation in the predicted CNB-1 protein and phytochemical complexes. The hydrogen bond in the predicted CNB-1 protein with (A) isorhamnetin, (B) dillenetin, (C) myricetin, and (D) kaempferol as revealed in the MD simulations.

5.3.5. Molecular docking analysis for phytochemical compounds with predicted PMR-1 proteins

I performed the docking studies for the predicted PMR-1 protein and the phytochemical compounds isorhamnetin, kaempferol, dillenetin, myricetin, quercetin, naringenin, and stigmasterol (Figure 5.14). The binding energy for the isorhamnetin-PMR-1 protein-ligand complex was −7.82 kcal/mol, with hydrogen bonds formed in the Asp646, Asn424, Asn254, and Asp672 residues, and the hydrophobic interactions involved the Pro506, Met426, Pro256, Ser645, Lys417, Glu253, Glu255, and His425 residues (Table 5.3). The kaempferol-PMR-1 complex had a binding energy of −7.77 kcal/mol and showed hydrogen bonds with the amino acid residues Arg606, Asn254, and Lys417, and hydrophobic interaction with Pro506, Met426, Gly604, Leu605, Ser645, Thr676, Met644, Asp646, Asp672, Thr418, His425, and Asn424 residues. In the myricetin-PMR-1 complex, which had a binding energy of -7.33 kcal/mol, a hydrogen bond was formed with the Asp646 residue, while hydrophobic interactions involved the Pro506, Met426, Gly604, Arg606, Ser645, Thr676, Leu605, Met644, Glu255, Thr418, Asn254, His425, and Asn424 residues. The dillenetin-PMR-1 complex showed a binding energy of −6.96 kcal/mol, forming hydrogen bonds with the Asp672 and Asn254 residues, and hydrophobic interactions with the Thr418, Met426, Asp646, Asn278, Glu253, Ala673, and Glu255 residues. The quercetin-PMR-1 complex exhibited a binding energy−6.90 kcal/mol, formed hydrogen bonds with the Asn424, Gly604, Arg606, Met644, Asp672, and Asn254 residues, and displayed hydrophobic interactions involving the Pro506, Met426, Leu605, Ser645, Asp646, Thr676, and His425 residues. The naringenin-PMR-1 complex had a binding energy of −6.88 kcal/mol, formed a hydrogen bond with the Lys417 residue, and displayed hydrophobic interactions with the Pro506, Asn426, Gly604, Arg606, Ser645, Met644, Asp672, Asp646, Glu255, Asn254, His425, and Asn424 residues. The stigmasterol-PMR-1 complex had a binding energy of −4.39 kcal/mol, formed only hydrophobic interactions with the residues Asn424, Pro506, Met426, Thr418, Thr676, Ala673, Glu253, Asp672, Asn278, Asp646, Lys417, Glu255, Asn254, and His425.

Table 5.3. Interactions of the amino acids in the active site of the predicted PMR-1 protein in complex with phytochemical compounds.

Ligand	**Binding Energy (kcal/mol)**	**Inhibition constant (Ki)**	**Amino acid residues in the active site**$^{+}$	
			H-bonds	**Hydrophobic interactions**
Isorhamnetin	−7.82	1.84 µM	Asp646, Asn424, Asn254, Asp672	Pro506, Met426, Pro256, Ser645, Lys417, Glu253, Glu255, His425
Kaempferol	−7.77	2.02 µM	Arg606, Asn254, Lys417	Pro506, Met426, Gly604, Leu605, Ser645, Thr676, Met644, Asp646, Asp672, Thr418, His425, Asn424
Myricetin	−7.33	5.91 µM	Asp646	Pro506, Met426, Gly604, Arg606, Ser645, Thr676, Leu605, Met644, Glu255, Thr418, Asn254, His425, Asn424
Dillenetin	−6.96	13.09 µM	Asp672, Asn254	Thr418, Met426, Asp646, Asn278, Glu253, Ala673, Glu255
Quercetin	−6.9	8.83 µM	Asn424, Gly604, Arg606, Met644, Asp672, Asn254	Pro506, Met426, Leu605, Ser645, Asp646, Thr676, His425
Naringenin	−6.88	4.52 µM	Lys417	Pro506, Asn426, Gly604, Arg606, Ser645, Met644, Asp672, Asp646, Glu255, Asn254, His425, Asn424

Stigmasterol	−4.39	610.57 µM	--	Asn424, Pro506, Met426, Thr418, Thr676, Ala673, Glu253, Asp672, Asn278, Asp646, Lys417, Glu255, Asn254, His425

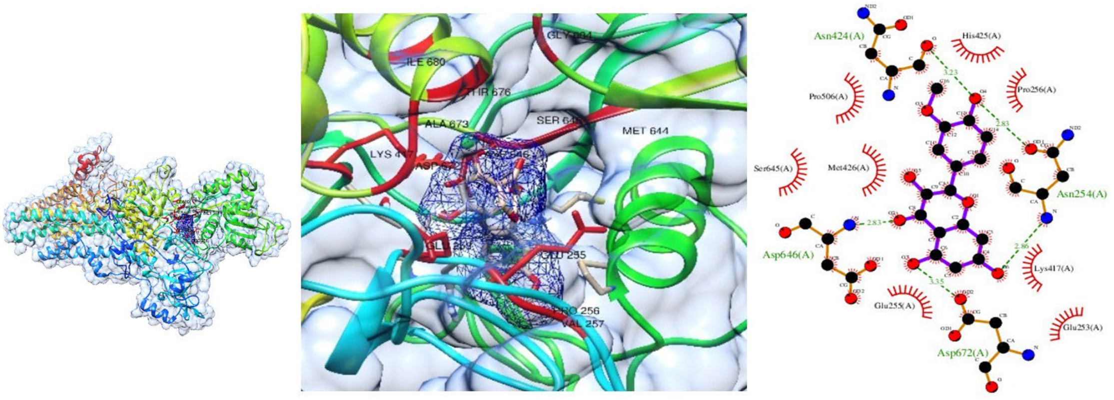

Isorhamnetin + PMR-1

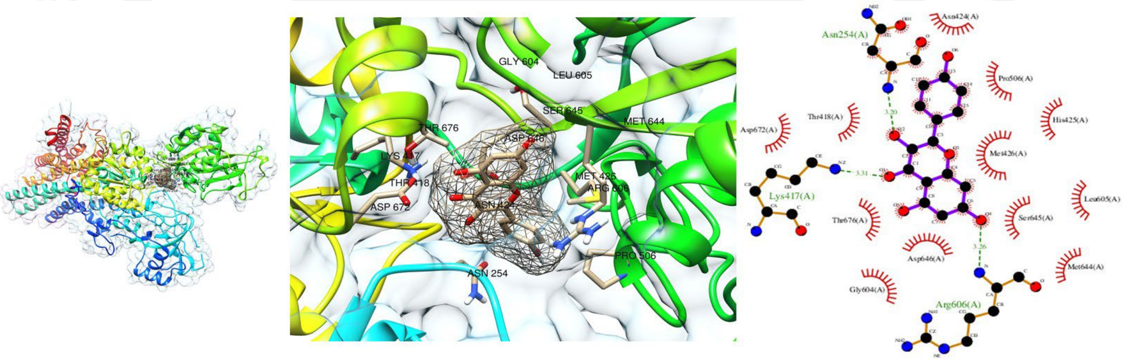

Kaempferol + PMR-1

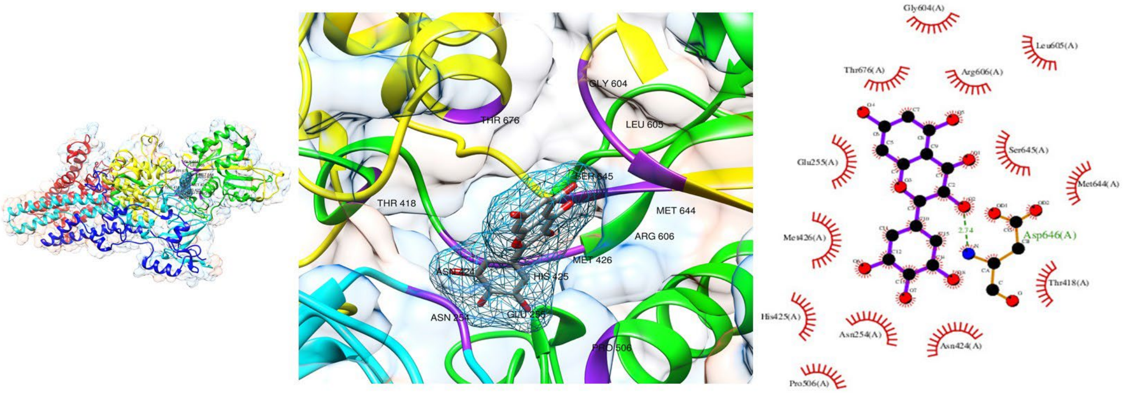

Myricetin + PMR-1

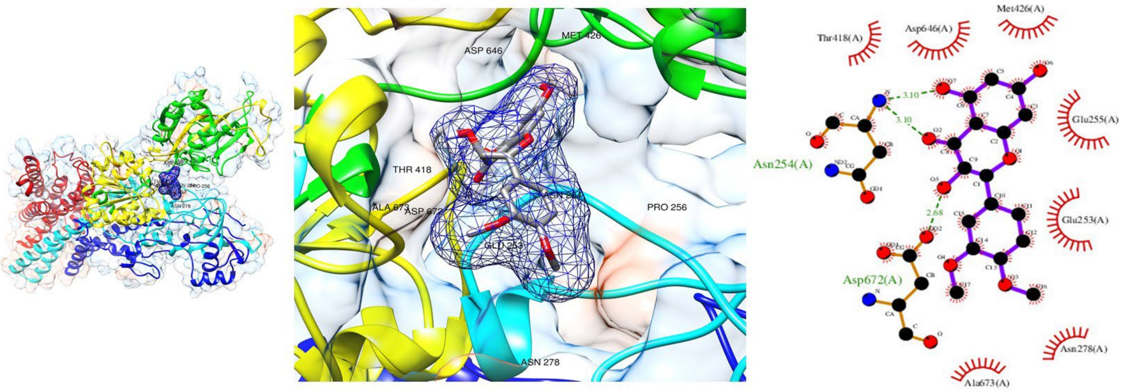

Dillenetin + PMR-1

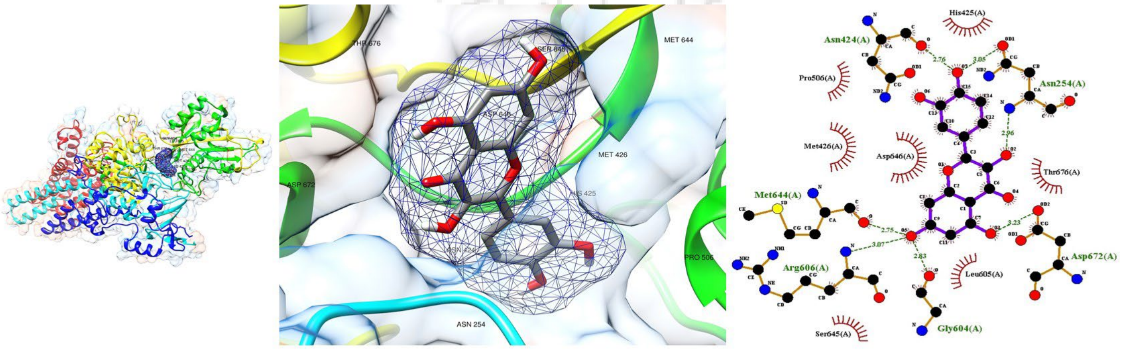

Quercetin + PMR-1

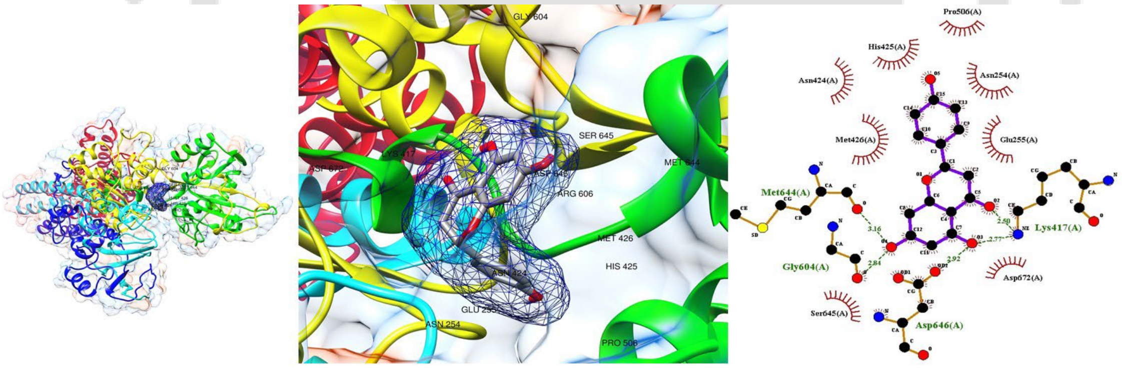

Naringenin + PMR-1

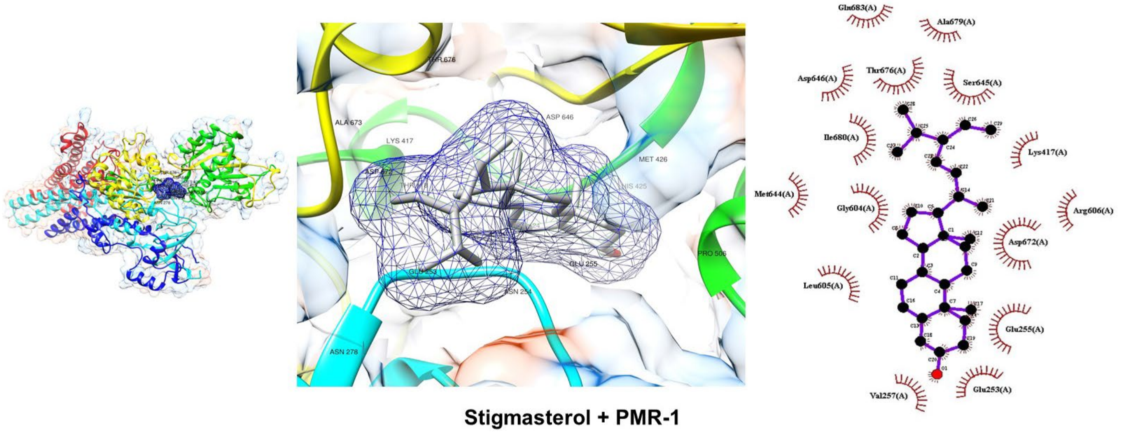

Stigmasterol + PMR-1

Figure 5.14. Molecular docking of the predicted PMR-1 with the phytochemical compounds. The panel on the left shows the ribbon diagram of the predicted PMR-1 protein structure, highlighting the binding site for the respective phytochemical compound within the binding pocket. In the middle panel, a focused view of the binding interactions between phytochemical compounds is shown as the stick representation. The interacting amino acid residues are labelled and displayed in the stick form within PMR-1 binding pocket. The right panel is the 2D interaction map of phytochemical compounds with the PMR-1 protein. Hydrogen bonds are represented as green dashed lines, and hydrophobic interactions are depicted as red arcs around the interacting residues.

5.3.6. MD simulations of the predicted PMR-1 protein complex with phytochemical compounds

The calculation of RMSD for the predicted PMR-1 apoprotein and PMR-1 protein-ligand complexes was performed using the GROMACS (Figure 5.15). The dillenetin (~0.75 nm), isorhamnetin (~0.6 nm), and kaempferol (~0.62 nm) complexes with the predicted PMR-1 protein showed lower RMSD values compared to the PMR-1 apoprotein (~0.8 nm). In addition, the myricetin-PMR-1 complex exhibited RMSD value of ~1 nm (Figure 5.15). Therefore, the complexes of isorhamnetin and kaempferol with the PMR-1 protein exhibited similar RMSD values and the highest backbone stability among the four complexes (Figure 5.15). Moreover, the RMSD trajectories for both the isorhamnetin and kaempferol complexes consistently displayed similar patterns for RMSD values in the MD simulations from 13−50 ns. The lower RMSD values for these complexes suggested stable protein-ligand structures. I also conducted a comparative analysis of the RMSF values and examined fluctuations of residues in the active site in the PMR-1 protein in a complex with phytochemical compounds. The RMSF values for the PMR-1 apoprotein and the four-ligand complexes were calculated using GROMACS over a 50 ns time scale (Figure 5.16). The RMSF values of all the amino acid residues in the PMR-1 apoprotein and its bound complexes ranged from ~0.2 to 1.7 nm over the entire simulation. In the GROMACS simulation, Isorhamnetin, kaempferol, and dillenetin showed a maximum RMSF value of ~1.2 nm, which was lower than that of the PMR-1 apoprotein ~ 1.7 nm over the entire MD simulation period (Figure 5.16). Moreover, correlating with the RMSD result, the RMSF value for the myricetin-PMR-1 complex showed the highest fluctuations at ~1.8 nm (Figure 5.16). A lower RMSF value suggests for a more rigid protein-ligand complex, and therefore indicates greater stability in the structure conformations of the complex. High rigidity in a specific region of protein is crucial for maintaining the structural integrity necessary for the protein function (Huber 1987; Sljoka 2022). Among all the complexes of phytochemical compounds with PMR-1, isorhamnetin-PMR-1 displayed the lowest fluctuation with a minimum RMSF value of ~ 0.1 nm. The compactness and globularity of protein-ligand complexes, as determined by the Rg value, showed an average range between ~3.55 to ~3.75 nm (Figure 5.17). However, the PMR-1 apoprotein showed the Rg value of ~3.85 nm (Figure 5.17). Among all the phytochemicals, the most compact protein-ligand structures with the lowest Rg values were formed by isorhamnetin, kaempferol, dillenetin, and myricetin. These results suggested that the phytochemical compounds form compact complexes with the PMR-1 protein. I also analyzed the structural compaction level in the PMR-1 apoprotein and its complexes with phytochemicals by determining the SASA using GROMACS (Figure 5.18). The SASA values for all the complexes of the phytochemicals with the PMR-1 were lower. The SASA values for the protein-ligand complexes of kaempferol (363.0732 nm^2), myricetin (362.5763 nm^2), and dillenetin (363.2358 nm^2) were lower than the PMR-1 apoprotein (363.6068 nm^2). Interestingly, the isorhamnetin-CNB-1 complex showed the lowest SASA value (361.8257 nm^2) among all the complexes. The Rg and SASA analyses collectively indicated that all the four protein-phytochemical complexes were stable and compact. Notably, among the studied compounds, isorhamnetin-PMR-1 complex demonstrated the best compactness and stability. In addition, I evaluated the intermolecular hydrogen bond formation in the complexes of isorhamnetin, myricetin, kaempferol, and dillenetin with PMR-1 over the entire 50 ns simulation. The PMR-1 protein in complex with isorhamnetin formed a maximum of four intermolecular hydrogen bonds (Figure 5.19 A). Dillenetin-PMR-1 complex showed a maximum of five intermolecular hydrogen bonds (Figure 5.19 B). The myricetin-PMR-1 complex formed a maximum of six intermolecular hydrogen bonds (Figure 5.19 C), and the kaempferol-PMR-1 complex showed a maximum of five intermolecular hydrogen bonds (Figure 5.19 D).

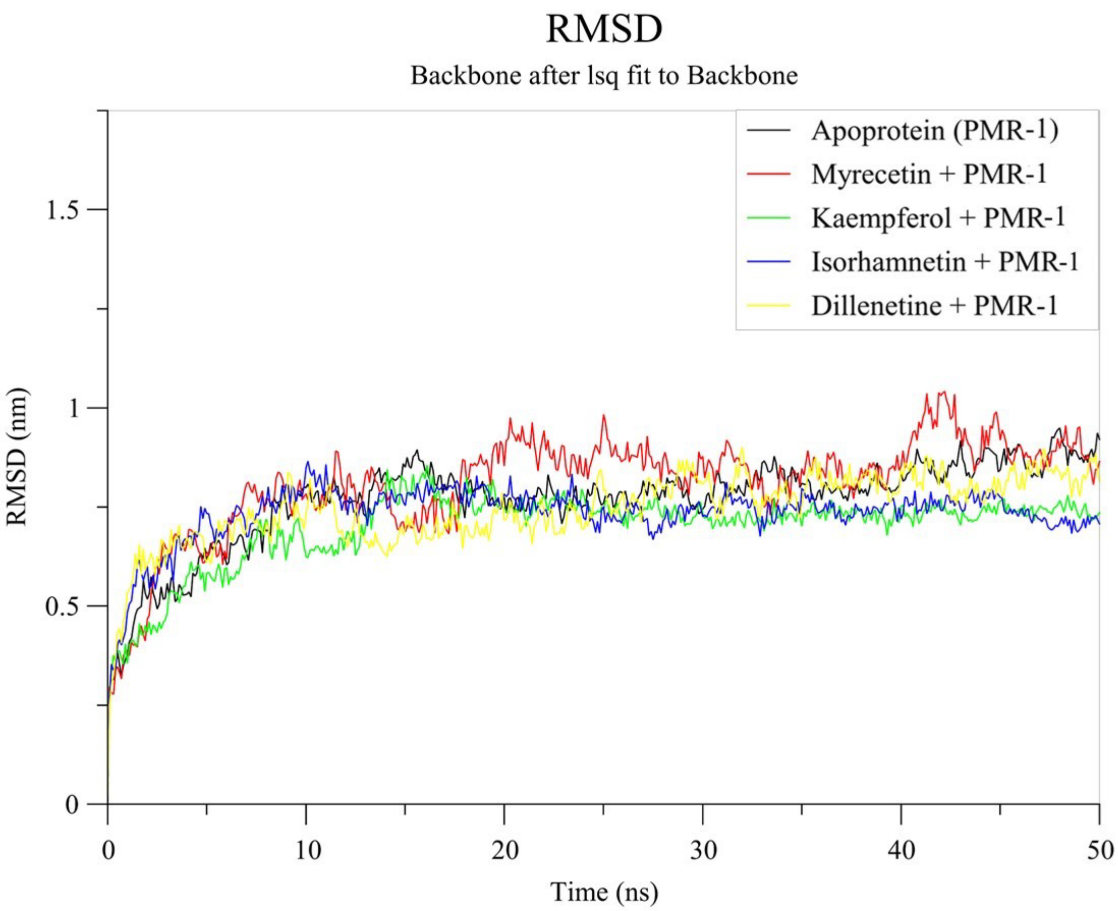

Figure 5.15. The RMSD plot for the predicted PMR-1 apoprotein and its complexes with phytochemicals. The RMSD (nm) values were derived from MD simulations over a 50 ns timescale.

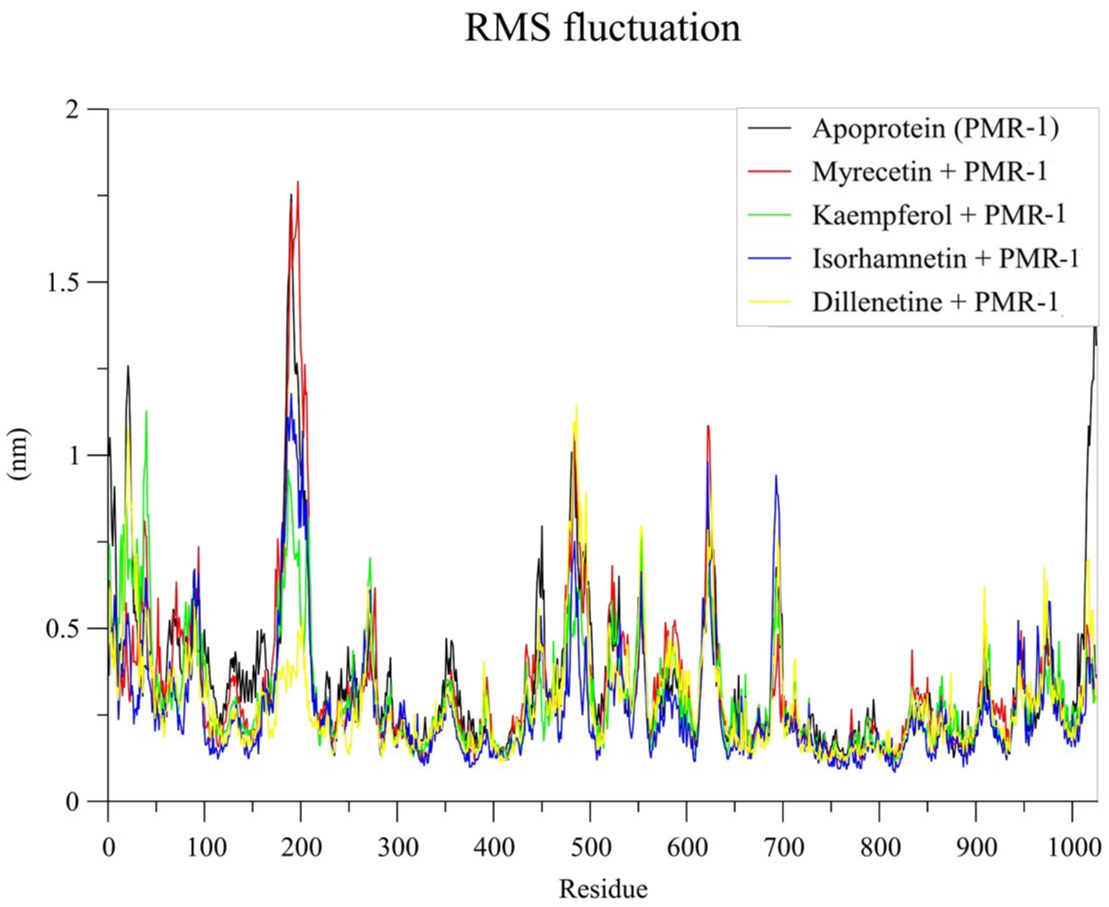

Figure 5.16. The RMSF fluctuations of the predicted PMR-1 apoprotein and the complexes of PMR-1-phytochemical compounds. The RMSF plots for isorhamnetin-PMR-1, myricetin-PMR-1, kaempferol-PMR-1, and dillenetin-PMR-1 were derived from a 50 ns time scale in the MD simulations.

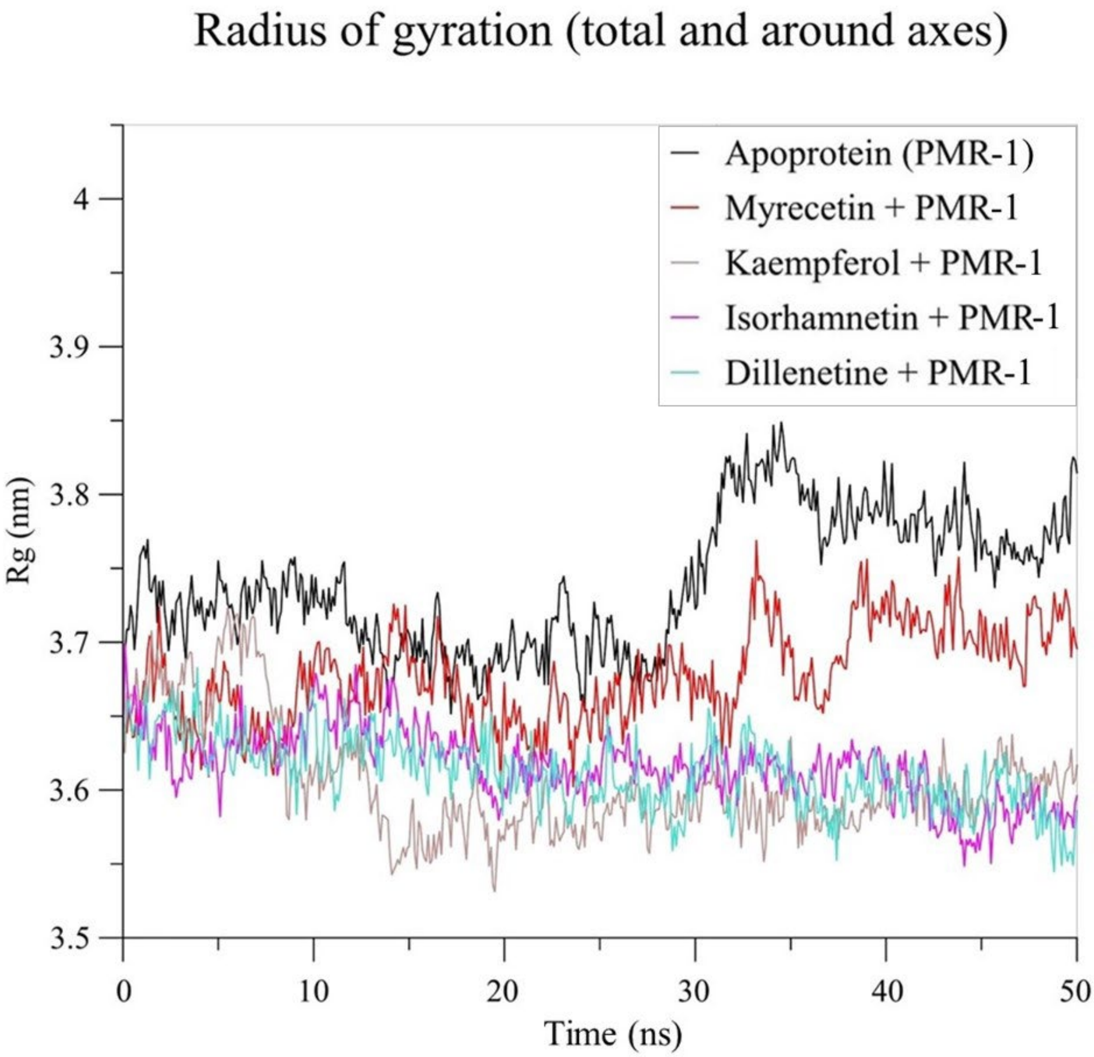

Figure 5.17. The graph shows the Rg plot for the predicted PMR-1 apoprotein and its complexes with the phytochemical compounds. The Rg plots for the complexes of PMR-1 with the isorhamnetin, myricetin, kaempferol, and dillenetin compounds were derived from a 50 ns time scale in the MD simulations.

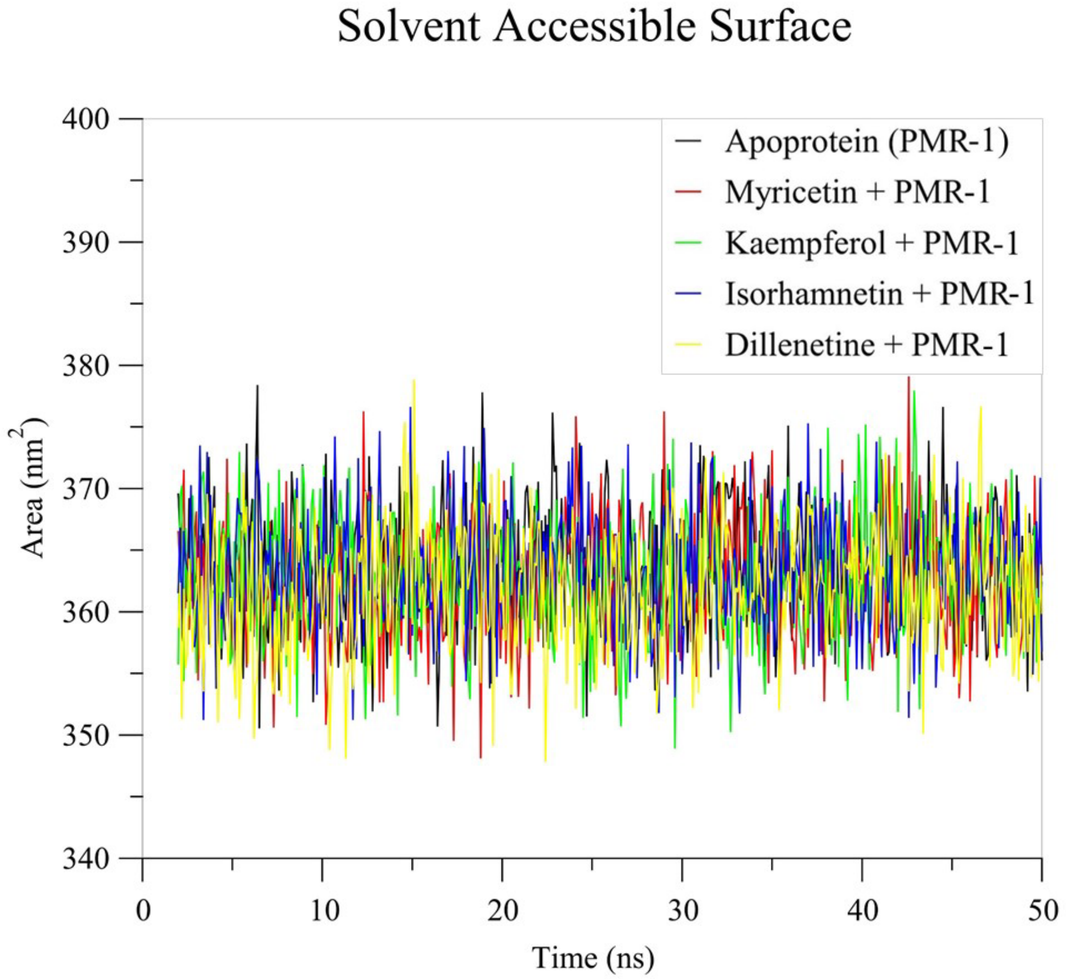

Figure 5.18. The SASA plot for the PMR-1 complexes. The SASA values (nm) for the predicted PMR-1 apoprotein and the complexes of phytochemical compounds with PMR-1 are plotted against MD simulations for a 50 ns time scale.

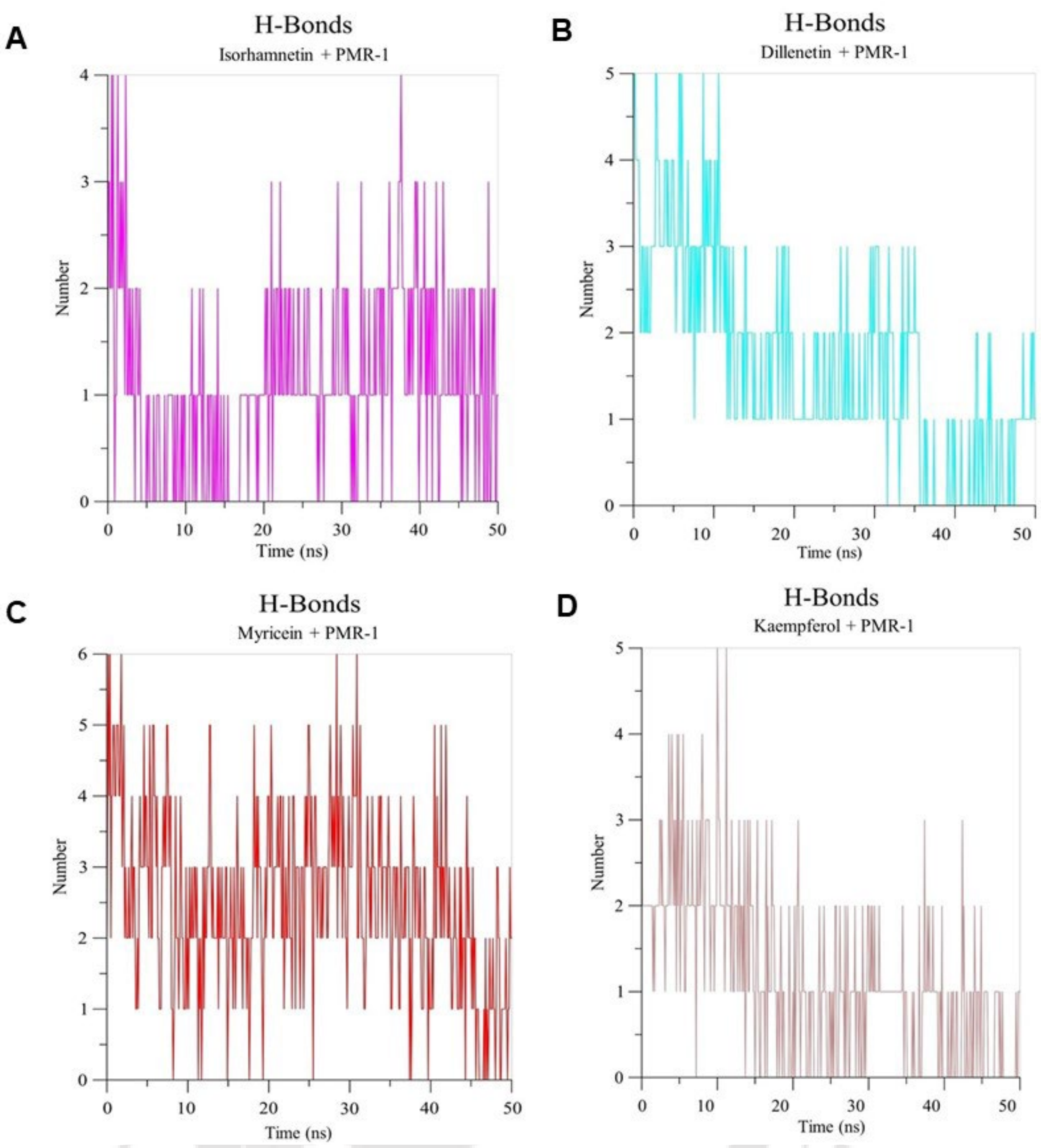

Figure 5.19. Plot of hydrogen bond formation during the MD simulations of the phytochemical complexes with the predicted PMR-1 protein. The complexes of (A) isorhamnetin, (B) dillenetin, (C) myricetin, and (D) kaempferol were analyzed, and the number of hydrogen bonds formed is plotted against a 50 ns time scale in the MD simulations.

5.4. Analysis of the phytochemical compounds for ADME

I studied the physicochemical and pharmacokinetic characteristics of the selected compounds using the SwissADME tool (Daina et al. 2017; Kwofie et al. 2021). I refined the selection of compounds using the Lipinski's and Veber's criterion (Ivanović et al. 2020). Lipinski's rule of five specifies that a drug-like molecule should not exceed 10 hydrogen bond acceptors, have no more than 5 hydrogen bond donors, possess a molecular mass below 500 g/mol, and exhibit an octanol-water partition coefficient (log P) below five (Zhang and Wilkinson 2007; Ivanović et al. 2020). In contrast, Veber's rule specifies that a drug-like molecule should have a topological polar surface area (TPSA) of 140 Å^2 or less and fewer than 11 rotatable bonds (Veber et al. 2002; Kwofie et al. 2021). I studied a total of 11 compounds, isorhamnetin, myricetin, kaempferol, naringenin, dillenetin, betulinaldehyde, quercetin, betulin, betulinic acid, stigmasterol, and lupeol for their suitability as a candidate drug molecule (Figure 5.1). Although myricetin violated two conditions of Lipinski's rule by having 6 hydrogen bond donors (ideally ≤5) and a TPSA of 151.59 Å^2 (ideally <140 Å^2), all other phytochemical compounds strictly adhered to the Lipinski's rule of five for drug-likeness. Despite natural products often deviating from Lipinski's and other absorption–distribution–metabolism–excretion–toxicity (ADMET) rules due to their distinct physicochemical characteristics, previous studies reported that over 50% of natural products display favorable drug-like properties with their predicted pharmacokinetic traits and drug-likeness (Veber et al. 2002). Essentially, most safe natural products adhere to the Veber's rule, although they might not consistently meet Lipinski's criteria for molecular weight and hydrogen bond components, but they predominantly comply with the logP value (Veber et al. 2002; Ganesan 2008). In summary, this study suggested that the phytochemicals from *D. indica* could serve as potent antifungal drugs targeting the calcineurin subunits CNA-1 and CNB-1, and the Golgi Ca^{2+}-ATPase pump PMR-1.

Table 5.4. Summary of the ADME properties and predicted drug-likeness for the phytochemical ligands

Compound	**MLogP**	**TPSA (Å^2)**	**MW (g/mol)**	**H-Donor**	**H-Acceptor**	**Logs**	**Drug likeness (violations)**
Isorhamnetin	-0.31	120.36	316.26	4	7	-3.36	Yes; 0 violation
Myricetin	-1.08	151.59	318.24	6	8	-3.01	Yes; 1 violation: NHorOH>5
Kaempferol	-0.03	111.13	286.24	4	6	-3.31	Yes; 0 violation

Naringenin	0.71	86.99	272.25	3	5	-3.49	Yes; 0 violation
Dillenetin	-0.07	109.36	330.29	3	7	-3.56	Yes; 0 violation
Betulinaldehyde	5.89	37.30	440.70	1	2	-7.57	Yes; 1 violation: MLOGP>4.15
Quercetin	-0.56	131.36	302.24	5	7	-3.16	Yes; 0 violation
Betulin	6.00	40.46	442.72	2	2	-7.67	Yes; 1 violation: MLOGP>4.15
Betulinic acid	5.82	57.53	456.70	2	3	-7.71	Yes; 1 violation: MLOGP>4.15
Stigmasterol	6.62	20.23	412.69	1	1	-7.46	Yes; 1 violation: MLOGP>4.15
Lupeol	6.92	20.23	426.72	1	1	-8.64	Yes; 1 violation: MLOGP>4.15

5.5. Discussion

In this chapter, I studied phytochemical compounds of *D. indica* origin as potential inhibitors of CNA-1, CNB-1, and PMR-1. Natural flavonoids, such as kaempferol and quercetin, are plant-derived compounds with significant health benefits (Jan et al. 2022). These natural compounds are well-documented for their diverse pharmacological activities, including anti-inflammatory, antioxidant, antimicrobial, and anticancer properties (Farag et al. 2013; Tocci et al. 2018a; Tocci et al. 2018b; Tocci et al. 2020). Moreover, these compounds exhibit significant potential in modulating biological pathways and mitigating oxidative stress, making them attractive candidates for therapeutic applications (Jan et al. 2022; Machado et al. 2023; Paul et al. 2024). Kaempferol and quercetin, widely found in plants, demonstrate significant therapeutic potential for human health due to their antimicrobial activity, bioavailability, and bioactivity (Jan et al. 2022). Furthermore, isorhamnetin, found in medicinal plants such as *D. indica*, possesses anti-inflammatory, antioxidant, anti-osteoporosis, anti-hypoxia, anticancer, and anti-hyperuricemia properties (Talukdar et al. 2012; Tian et al. 2021; Tan et al. 2022; Unver 2023). However, the role of isorhamnetin in the treatment of fungal diseases remains underexplored. Therefore, I studied the antifungal potential of isorhamnetin, kaempferol, myricetin, and dillenetin as inhibitors of Ca^{2+} signaling proteins CNA-1, CNB-1, and PMR-1, which are essential for fungal pathogenicity (Bates et al. 2005; Park et al. 2019; Vellanki et al. 2020). Preliminary computational insights suggest that phytochemicals predominantly found in *D. indica* inhibit the activity of CNA-1, CNB-1, and PMR-1 proteins, and thus may possess potential antifungal properties. Previous studies also suggested that isorhamnetin might be useful as a preventive or therapeutic pharmaceutical agent against the *Candida* infections (Unver 2023). The growing resistance to antifungal drugs presents a significant health challenge worldwide, underscoring the need for new natural compounds with potent antifungal properties to combat resistance and provide better treatment options (Jawhara 2020; Jawhara 2022; Camaioni et al. 2023).

I investigated 11 phytochemicals of *D. indica* origin that target the predicted CNA-1, CNB-1, and PMR-1 proteins. The chemical structures of these phytochemicals available in the PubChem database, and used for the molecular docking studies. I selected the top four compounds, isorhamnetin, dillenetin, kaempferol, and myricetin, which showed high binding affinities, in molecular docking studies. Docking analysis revealed that isorhamnetin consistently showed stronger predicted binding affinity and stability with predicted CNA-1 and PMR-1. Previous studies reported that isorhamnetin improves keratitis caused by *A. fumigatus* by inhibiting pattern-recognition receptors and downregulating inflammatory cytokines (Tian et al. 2021). Isorhamnetin improved prognosis in mice by inhibiting fungal growth, reducing neutrophil recruitment, and mitigating inflammatory responses, aligning with its antifungal efficacy demonstrated in this study (Tian et al. 2021). Further, isorhamnetin exhibited potent antifungal activity against *Candida tropicalis*, *C. albicans*, *C. krusei*, and *C. parapsilosis* (Unver 2023). This reinforces broad-spectrum inhibitory potential and ability of isorhamnetin to target essential fungal proteins such as CNA-1 and PMR-1. Dillenetin displayed the highest binding affinity for the CNB-1 protein-ligand complex, indicating that dillenetin could be potential fungal inhibitor. The RMSD and RMSF values are important to understand the overall structural stability and structural adaptability of the system during the course of MD simulations (Ahmad et al. 2020). Based on the RMSD, RMSF, hydrogen bonds, and Rg parameters, I found that isorhamnetin constantly performed better as an inhibitor for the predicted CNA-1 and PMR-1 protein, and dillenetin was a better inhibitor of the predicted CNB-1 protein. A lower RMSF value suggested for a more rigid protein-ligand complex, and therefore, it showed an increased stability in the structure conformations of the complex. High rigidity in specific protein areas can be crucial for maintaining the structural integrity necessary for the protein function. Among the CNB-1 complexes, dillenetin demonstrated the lowest fluctuations, indicating high stability within the CNB-1 structure. Lower RMSF values often suggest that a particular region of a protein is more rigid or stable (Yang and Kar 2024). High rigidity in the protein areas of protein can be crucial for maintaining the structural integrity necessary for function (Yakobi et al. 2024). The Rg is analyzed to assess the structural compactness of proteins upon interaction with molecules (Lobanov et al. 2008). Decreased Rg values suggest enhanced stability, indicating a more compact protein conformation; however, higher Rg values reflect a more expanded or disordered protein system (Mitra et al. 2024). Among the CNA-1 complexes with phytochemicals, isorhamnetin exhibited the lowest Rg value compared to all other phytochemical compounds, suggesting that the isorhamnetin-CNA-1 complex is more compact structure and stable than complexes of other phytochemicals with CNA-1. In complexes with CNB-1, dillenetin and myricetin showed the highest compactness in the protein structure with the lowest Rg values (Figure 5.11). In addition, among the PMR-1 protein-ligand complexes, all the phytochemicals dillenetin, isorhamnetin, kaempferol, and myricetin form compact protein-ligand structures with the lowest Rg value than the PMR-1 apoprotein (Figure 5.17).

A high number of hydrogen bonds significantly enhances the binding affinity of a ligand to its target protein by stabilizing the protein-ligand complex. The hydrogen bonds contribute to the specificity and strength of the binding, ensuring that the ligand remains firmly positioned within the active site (Wu et al. 2012; Chen et al. 2016; Yunta 2017). Moreover, hydrogen bonds play a critical role in optimizing the orientation of the ligand, improving its complementarity to the target, which is essential for effective inhibition or activation characteristics used in a drug design process (Patil et al. 2010). Isorhamnetin forms four hydrogen bonds with the CNA-1 and PMR-1, while dillenetin forms 3 hydrogen bonds with CNB-1 (Figures 5.7, 5.13, 5.19).

In the drug development process, ADMET studies are an integral part and contribute to the understanding of the safety and efficacy profile of drugs (Nisha et al. 2016). The ADMET evaluation in this study revealed favorable pharmacokinetic properties for phytochemical compounds, including isorhamnetin and dillenetin. Moreover, quercetin, a phytochemical flavonol found in *Spondias mombin*, a flowering tree, exhibited a high binding affinity for proteins associated with Parkinson's disease (Olanrewaju et al. 2023). In addition, MD simulations, including RMSD and RMSF data of all four studied compounds, quercetin, catechin, epicatechin, and ellagic acid, suggested that quercetin forms a stable complex with GSK-3β, a key target in Parkinson's disease (Al Aboody and Mickymaray 2020; Olanrewaju et al. 2024). In this study, I found that flavonol ishorhamnetin has the best ligand binding affinity to the CNA-1 and PMR-1 proteins. *In silico* findings suggest that dillenetin shows the best ligand binding affinity and forms a stable complex with the predicted CNB-1 protein. Hence, this study suggested that the isorhamnetin and dillenetin phytochemicals might be potent drug candidates by inhibiting the functions of calcineurin and PMR-1 in fungi. The interaction studies of the phytochemicals with the predicted CNA-1, CNB-1, and PMR-1 proteins could also be useful for overcoming drug resistance and the development of safe antifungals in the future. The molecular docking and MD simulations conducted in this study may offer preliminary insights into binding affinities, interaction stability, and potential mechanisms, which could be useful for identifying candidate phytochemical compounds. These results serve as a foundation for future experimental validation, using in vitro and in vivo studies to confirm the efficacy and mechanisms of action of the identified phytochemicals.

References:

Abdille MH, Singh R, Jayaprakasha G, Jena B (2005) Antioxidant activity of the extracts from Dillenia indica fruits. Food chemistry 90:891-896

Al Aboody MS, Mickymaray S (2020) Anti-fungal efficacy and mechanisms of flavonoids. Antibiotics 9:45

Bates S et al. (2005) Candida albicans Pmr1p, a secretory pathway P-type Ca2+/Mn2+-ATPase, is required for glycosylation and virulence. Journal of Biological Chemistry 280:23408-23415

Camaioni L et al. (2023) Natural Compounds with Antifungal Properties against Candida albicans and Identification of Hinokitiol as a Promising Antifungal Drug. Antibiotics 12:1603

Chen D, Oezguen N, Urvil P, Ferguson C, Dann SM, Savidge TC (2016) Regulation of protein-ligand binding affinity by hydrogen bond pairing. Science advances 2:e1501240

Daina A, Michielin O, Zoete V (2017) SwissADME: a free web tool to evaluate pharmacokinetics, drug-likeness and medicinal chemistry friendliness of small molecules. Scientific reports 7:42717

Deraedt R, Jouquey S, Delevallée F, Flahaut M (1980) Release of prostaglandins E and F in an algogenic reaction and its inhibition. European journal of pharmacology 61:17-24

Dias DA, Urban S, Roessner U (2012) A historical overview of natural products in drug discovery. Metabolites 2:303-336

Durham E, Dorr B, Woetzel N, Staritzbichler R, Meiler J (2009) Solvent accessible surface area approximations for rapid and accurate protein structure prediction. Journal of molecular modeling 15:1093-1108

Emmanuel IA, Olotu F, Agoni C, Soliman ME (2019) Broadening the horizon: Integrative pharmacophore-based and cheminformatics screening of novel chemical modulators of mitochondria ATP synthase towards interventive Alzheimer's disease therapy. Medical Hypotheses 130:109277

Farag MA, Weigend M, Luebert F, Brokamp G, Wessjohann LA (2013) Phytochemical, phylogenetic, and anti-inflammatory evaluation of 43 Urtica accessions (stinging nettle) based on UPLC–Q-TOF-MS metabolomic profiles. Phytochemistry 96:170-183

Fatriansyah JF, Rizqillah RK, Yandi MY, Sahlan M (2022) Molecular docking and dynamics studies on propolis sulabiroin-A as a potential inhibitor of SARS-CoV-2. Journal of King Saud University-Science 34:101707

Feng JA, Kao J, Marshall GR (2009) A second look at mini-protein stability: Analysis of FSD-1 using circular dichroism, differential scanning calorimetry, and simulations. Biophysical journal 97:2803-2810

Ganesan A (2008) The impact of natural products upon modern drug discovery. Current opinion in chemical biology 12:306-317

Grover J, Yadav S, Vats V (2002) Medicinal plants of India with anti-diabetic potential. Journal of ethnopharmacology 81:81-100

Gulshan K, Moye-Rowley WS (2007) Multidrug resistance in fungi. Eukaryotic cell 6:1933-1942

Gumbart J, Trabuco LG, Schreiner E, Villa E, Schulten K (2009) Regulation of the protein-conducting channel by a bound ribosome. Structure 17:1453-1464

Halder SK et al. (2023) In Silico Identification and Analysis of Potentially Bioactive Antiviral Phytochemicals against SARS-CoV-2: A Molecular Docking and Dynamics Simulation Approach. BioMed Research International 2023:5469258

Huber R (1987) Flexibility and rigidity, requirements for the function of proteins and protein pigment complexes. Eleventh Keilin memorial lecture. Biochemical Society Transactions 15:1009-1020

Ivanović V, Rančić M, Arsić B, Pavlović A (2020) Lipinski's rule of five, famous extensions and famous exceptions. Popular Scientific Article 3:171-177

Jan R, Khan M, Asaf S, Lubna, Asif S, Kim K-M (2022) Bioactivity and therapeutic potential of kaempferol and quercetin: new insights for plant and human health. Plants 11:2623

Jawhara S (2020) How fungal glycans modulate platelet activation via toll-like receptors contributing to the escape of Candida albicans from the immune response. Antibiotics 9:385

Jawhara S (2022) How gut bacterial dysbiosis can promote Candida albicans overgrowth during colonic inflammation. Microorganisms 10:1014

Kitchen DB, Decornez H, Furr JR, Bajorath J (2004) Docking and scoring in virtual screening for drug discovery: methods and applications. Nature reviews Drug discovery 3:935-949

Kwofie S et al. (2021) Molecular Docking Simulation Studies Identifies Potential Natural Product Derived-Antiwolbachial Compounds as Filaricides against Onchocerciasis. Biomedicines 2021, 9, 1682. In. s Note: MDPI stays neutral with regard to jurisdictional claims in published …

Lipinski CA, Lombardo F, Dominy BW, Feeney PJ (2012) Experimental and computational approaches to estimate solubility and permeability in drug discovery and development settings. Advanced drug delivery reviews 64:4-17

Lobanov MY, Bogatyreva N, Galzitskaya O (2008) Radius of gyration as an indicator of protein structure compactness. Molecular Biology 42:623-628

Machado IF, Miranda RG, Dorta DJ, Rolo AP, Palmeira CM (2023) Targeting oxidative stress with polyphenols to fight liver diseases. Antioxidants 12:1212

Maertens JA (2004) History of the development of azole derivatives. Clinical Microbiology and Infection 10:1-10

Mitra R et al. (2024) Molecular insights into the interaction between a disordered protein and a folded RNA. Proceedings of the National Academy of Sciences 121:e2409139121

Nisha CM et al. (2016) Molecular Docking and In Silico ADMET Study Reveals Acylguanidine 7a as a Potential Inhibitor of β-Secretase. Advances in bioinformatics 2016:9258578

Olanrewaju JA et al. (2024) Spondias mombin flavonoids showed super-binder ability with downstream molecular targets of Parkinson's disease: A structural study. Informatics in Medicine Unlocked 49:101543

Olanrewaju JA et al. (2023) Spondias mombin flavonoids showed super-binder ability with Downstream Molecular Targets of Parkinson's Disease: Folkloric-therapy assessment as a Scaffold for Structural Studies in Neurodegenerative disease.

Park H-S, Lee SC, Cardenas ME, Heitman J (2019) Calcium-calmodulin-calcineurin signaling: a globally conserved virulence cascade in eukaryotic microbial pathogens. Cell host & microbe 26:453-462

Patil R, Das S, Stanley A, Yadav L, Sudhakar A, Varma AK (2010) Optimized hydrophobic interactions and hydrogen bonding at the target-ligand interface leads the pathways of drug-designing. PloS one 5:e12029

Paul JK, Azmal M, Haque ASNB, Talukder OF, Meem M, Ghosh A (2024) Phytochemical-mediated modulation of signaling pathways: A promising avenue for drug discovery. Advances in Redox Research:100113

Revie NM, Iyer KR, Robbins N, Cowen LE (2018) Antifungal drug resistance: evolution, mechanisms and impact. Current opinion in microbiology 45:70-76

Saiful Yazan L, Armania N (2014) Dillenia species: A review of the traditional uses, active constituents and pharmacological properties from pre-clinical studies. Pharmaceutical biology 52:890-897

Sljoka A (2022) Structural and functional analysis of proteins using rigidity theory. Sublinear Computation Paradigm:337-367

Sneha P, Doss CGP (2016) Molecular dynamics: new frontier in personalized medicine. Advances in protein chemistry and structural biology 102:181-224

Song X et al. (2024) Accurate prediction of protein structural flexibility by deep learning integrating intricate atomic structures and Cryo-EM density information. Nature Communications 15:5538

Talukdar A, Talukdar N, Deka S, Sahariah BJ (2012) Dillenia indica (OUTENGA) as anti-diabetic herb found in Assam: a review. International Journal of pharmaceutical sciences and research 3:2482

Tan LF et al. (2022) Plant as an alternative source of antifungals against Aspergillus infections: A review. Plants 11:3009

Tian X et al. (2021) Isorhamnetin ameliorates Aspergillus fumigatus keratitis by reducing fungal load, inhibiting pattern-recognition receptors and inflammatory cytokines. Investigative Ophthalmology & Visual Science 62:38-38

Tocci N, Perenzoni D, Iamonico D, Fava F, Weil T, Mattivi F (2018a) Extracts from Hypericum hircinum subsp. majus exert antifungal activity against a panel of sensitive and drug-resistant clinical strains. Frontiers in pharmacology 9:382

Tocci N et al. (2020) Potent Antifungal Properties of Dimeric Acylphloroglucinols from Hypericum mexicanum and Mechanism of Action of a Highly Active 3′ Prenyl Uliginosin B. Metabolites 10:459

Tocci N et al. (2018b) Phenolic profile, chemical relationship and antifungal activity of Andean Hypericum species. Industrial Crops and Products 112:32-37

Umesh, Prerna K, Dubey VK (2022) Virtual screening and repurposing of FDA-approved drugs from ZINC database to identify potential autophagy inhibitors exploiting autophagy related 4A cysteine peptidase as a target: potential as novel anti-cancer molecule. Journal of Biomolecular Structure and Dynamics 40:5266-5282

Unver T (2023) Isorhamnetin as a promising natural bioactive flavonoid: in vitro assessment of its antifungal property. International Journal of Agriculture Environment and Food Sciences 8:54-61

Veber DF, Johnson SR, Cheng H-Y, Smith BR, Ward KW, Kopple KD (2002) Molecular properties that influence the oral bioavailability of drug candidates. Journal of medicinal chemistry 45:2615-2623

Vellanki S et al. (2020) A novel resistance pathway for calcineurin inhibitors in the human-pathogenic mucorales mucor circinelloides. MBio 11:10.1128/mbio. 02949-02919

Wu MY, Dai DQ, Yan H (2012) PRL-dock: Protein-ligand docking based on hydrogen bond matching and probabilistic relaxation labeling. Proteins: Structure, Function, and Bioinformatics 80:2137-2153

Yadav S et al. (2024) Investigate the binding of pesticides with the TLR4 receptor protein found in mammals and zebrafish using molecular docking and molecular dynamics simulations. Scientific Reports 14:24504

Yakobi S, Zuma L, Pooe O (2024) Molecular Docking and Structure-Activity Relationship Analysis of Target Compounds against Glyceraldehyde-3-Phosphate Dehydrogenase in Azithromycin-Resistant Neisseria gonorrhoeae. ChemistrySelect 9:e202303341

Yang S, Kar S (2024) Protracted molecular dynamics and secondary structure introspection to identify dual-target inhibitors of Nipah virus exerting approved small molecules repurposing. Scientific Reports 14:3696

Yunta MJ (2017) It is important to compute intramolecular hydrogen bonding in drug design. Am. J. Model. Optim 5:24-57

Zhang M-Q, Wilkinson B (2007) Drug discovery beyond the ‘rule-of-five’. Current opinion in biotechnology 18:478-488

Chapter 6

Conclusion and Future Perspective

6.1. Major conclusions of this study

In this study, I investigated the cellular roles of calcineurin and *pmr-1* under azole-treated conditions in *N. crassa*, using their calcineurin RIP mutants and knockout strains. The mutants of the calcineurin catalytic subunit A (*Cna-1*$^{\mathrm{RIP}}$) and the Δ*pmr-1* strains showed a growth defect in response to the azole drugs. Moreover, the *Cna-1*$^{\mathrm{RIP}}$ mutants 24 a and 122A and Δ*pmr-1* knockout strains showed reduced ergosterol content and an increased ROS level upon azole treatment. The light microscopy reveals altered hyphal morphology under azole drug treatment in the *Cna-1*$^{\mathrm{RIP}}$ mutants and the Δ*pmr-1* knockout strains. Moreover, FESEM studies revealed damaged hyphal structures in response to fluconazole treatment. Therefore, the calcineurin and *pmr-1* genes could be pivotal for maintaining hyphal morphology in *N. crassa* mutant strains under azole treatment. Furthermore, the expression levels of *pmr-1* genes were altered upon the treatment with itraconazole in the *N. crassa* wild type. Interestingly, *pmr-1* gene expression was increased in response to itraconazole treatment in the *N. crassa* wild type, suggesting differential regulation of the *pmr-1* genes under the itraconazole stress condition. The above studies suggest that calcineurin and *pmr-1* genes might play an important role in azole susceptibility in *N. crassa*. Moreover, the molecular docking studies of calcineurin and PMR-1 proteins with azole drugs were performed. Preliminary computational insights suggest that the calcineurin catalytic subunit CNA-1 showed the highest binding energy of −6.67 kcal/mol with ketoconazole than the fluconazole-CNA-1 complex, with a binding energy of −4.56 kcal/mol. The ketoconazole-CNA-1 complex formed hydrogen bonds with Tyr353 and His189. In this complex, the hydrophobic interactions occurred between Leu350, Tyr349, Ala321, Glu320, His319, Arg292, Leu194, Trp270, Phe198, and Arg160. Fluconazole-CNA-1 complex formed hydrogen bonds with Tyr349, Ala321, Arg292, and the hydrophobic interactions were formed between amino acid residues His130, Glu320, His319, Asp156, Leu194, His189, Trp270, Asn188, Arg160, Tyr353, and Leu350. MD analysis, including Root Mean Square Deviation (RMSD), root mean square fluctuation (RMSF), radius of gyration (Rg), and hydrogen bond formation, provided insights into binding processes. The RMSD trajectories of the fluconazole and ketoconazole complexes with CNA-1 indicated that the ketoconazole-calcineurin complex possesses the highest backbone stability compared to the CNA-1 apoprotein and fluconazole-CNA-1 complex. Similarly, the ketoconazole-CNB-1 complex exhibited a binding energy of −5.07 kcal/mol, and fluconazole-CNB-1 exhibited a binding energy of −4.2 kcal/mol. The RMSD trajectories of the ketoconazole and fluconazole complexes with CNB-1 indicated that the ketoconazole-CNB-1 complex contained the highest backbone stability compared to the CNB-1 apoprotein and fluconazole-CNB-1 complex. The amino acid residues Phe153, Arg96, Tyr109, Glu154, Asp103, Lys100, Gly108, and Phe99 were common amino acid residues within the CNB-1 protein-ligand complexes throughout the molecular docking study of CNB-1 protein with fluconazole and ketoconazole. Moreover, the ketoconazole-CNB-1 complex formed the hydrogen bond with Arg96, and fluconazole-CNB-1 formed the hydrogen bond with Phe153, Arg96, and Tyr109.

The ketoconazole-PMR-1 complex also showed the highest binding energy, −7.68 kcal/mol, whereas the itraconazole-PMR-1 and fluconazole-PMR-1 complexes showed the binding energies of −3.73 kcal/mol and −5.61 kcal/mol, respectively. Among the three PMR-1-azole complexes, the itraconazole-PMR-1 complex exhibited the highest backbone stability. In ketoconazole-PMR-1 complex, hydrogen bond was formed with Asn254 and the hydrophobic interactions were formed between Met426, Asp646, Lys417, Glu255, Ser645, Ser279, Val257, Ile259, Val282, Leu250, Asp277, Asp278, Ala247, Thr251, Glu253, Thr676, Asp672, Gly604, Ile680, Thr418. The fluconazole-PMR1 complex exhibited the hydrogen bond formation with the specific amino acid residues Asn254, Glu255, Asp646, and hydrophobic interactions with Pro506, Met426, His425, Asn424, Ser645, Glu253, Asp672, Gly604, Thr418, and Lys417. The itraconazole and PMR-1 complex showed only hydrophobic interaction with the amino acid residues Asn254, Met426, Asp646, His425, Glu255, Asn424, Ser645, Val257, Ile259, Val282, Thr287, Lys276, Asp277, Leu250, Tyr284, Asn278, Ala247, Thr251, Glu253, Thr676, Asp672, Gly604. However, for the PMR-1 protein complexes with fluconazole, itraconazole, and ketoconazole, the Asp646, Glu255, Asn254, Met426, Ser645, Glu253, Asp672, and Gly604 were common amino acid residues involved in hydrogen bond formation and hydrophobic interactions. Hydrogen bond formation and hydrophobic interactions are crucial for drug binding and in stabilizing protein-ligand interactions.

CADD studies and molecular docking reveal that phytochemical compounds isorhamnetin, myricetin, kaempferol, dillenetin, naringenin, betulinaldehyde, quercetin, betulin, betulinic acid, lupeol, and stigmasterol interact with the CNA-1, CNB-1, and PMR-1 proteins. Therefore, the *N. crassa* proteins CNA-1, CNB-1, and PMR-1 might be considered potent targets for new antifungal phytochemical compounds. Based on the molecular docking studies and higher binding affinity, the top four chemical compounds, namely isorhamnetin, dillenetin, kaempferol, and myricetin, were further selected for the MD simulations. The ADMET profiles confirmed that the phytochemicals isorhamnetin and dillenetin possess the required characteristics as per Lipinski's 'Rule of Five' and Veber's criteria. The isorhamnetin-CNA-1 complex formed the hydrogen bonds with the amino acid residues His189, Asp156, Asp128, and hydrophobic interactions with the amino acid residues Arg160, Tyr349, Phe344, His319, His130, Arg292, Asn188, Phe198, and Leu350. Preliminary computational insights suggest that the compound dillenetin is the most potent inhibitor targeting the CNB-1 proteins. It forms a stable complex through hydrogen bonding with key amino acid residues Arg106 and Arg96, and through hydrophobic interaction with amino acids Asp107, Asp103, Lys100, Phe99, Ser152, Tyr109, Glu154, Gly108, and Phe153. Isorhamnetin-PMR-1 complex formed hydrogen bond with the amino acid residues Asp646, Asn424, Asn254, Asp672, and hydrophobic interaction with the amino acid residues Pro506, Met426, Pro256, Ser645, Lys417, Glu253, Glu255, and His425. These results suggested that isorhamnetin and dillenetin could serve as potent antifungal candidates targeting calcineurin and PMR-1, offering a path forward to inhibiting key proteins involved in fungal pathogenicity. These findings could contribute to the development of target specific antifungal drugs in the future, with the potential to overcome resistance mechanisms in fungal pathogens. However, further validation through *in vitro* and *in vivo* experiments is necessary for a comprehensive understanding of their mechanism of action and therapeutic potential. Preliminary CADD and molecular docking studies revealed strong interactions between selected phytochemicals with the calcineurin and PMR-1 proteins. MD simulations and ADMET profiling suggest that isorhamnetin and dillenetin could be promising phytochemical compounds for use as antifungals. In the future, these findings could be further extended to the translational level.

6.2. Future Perspectives

(i) Protein-Protein Interaction Studies: Performing co-immunoprecipitation (Co-IP) and yeast two-hybrid assays can identify interacting partners of calcineurin and PMR-1 under azole-treated conditions. This can provide insights into the mechanism of signaling pathways involved in drug metabolism and resistance.

(ii) Chromatin Immunoprecipitation (ChIP) and Electrophoretic Mobility Shift Assay (EMSA): ChIP-sequencing will identify genomic transcriptional activator binding sites in the promoter sequences of calcineurin and *pmr-1*. In addition, EMSA will identify the specific DNA-binding sequences necessary for transcriptional activator binding in the promoters of calcineurin and *pmr-1* under azole treatment.

(iii) Phosphoproteomics: The phosphorylation of proteins in the *N. crassa* wild type, calcineurin-RIP, and Δ*pmr-1* mutant strains treated with azoles. This can help to identify phosphorylation events regulating calcineurin and PMR-1 and their role in azole susceptibility.

(iv) Cloning and expression of CNA-1, CNB-1, and PMR-1 proteins in *E. coli*. Purification of CNA-1, CNB-1, and PMR-1 proteins by affinity chromatography and isothermal titration calorimetry (ITC), surface plasmon resonance (SPR) will be useful to quantify the binding affinity of isorhamnetin, dillenetin, kaempferol, and myricetin to these target proteins.

(v) Protein Interaction Studies: Co-immunoprecipitation and mass spectrometry to identify interacting partners of calcineurin and PMR-1 in the presence of the selected phytochemicals.

(vi) Enzyme Inhibition Assays: This will be useful to assess the inhibitory effect of the azole compounds and phytochemical compounds on calcineurin and PMR-1 activity using phosphatase assays.

(vii) Molecular docking and MD Simulations: To investigate the effect of point mutations in the calcineurin and PMR-1 proteins upon interactions with the azole drugs and phytochemical compounds. This can provide insights into the development of more effective antifungal therapies.

(viii) Nuclear Magnetic Resonance (NMR) spectroscopy: For identifying ligand binding to calcineurin and PMR-1 protein receptors.

Appendix

Appendix Table 3.1 – Raw *CT* values from real-time PCR analysis of *cna-1* gene expression under azole drug treatment.

Gene	**Sample**	**Replicate**	***CT* (Target Gene)**	***CT* (Housekeeping Gene)**	**Δ*CT* (*CT* Target – *CT* Housekeeping)**	**ΔΔ*CT***	**Fold Change ($2^{-\Delta\Delta CT}$)**
cna-1	Control (No Drug)	Replicate 1	21.21	21.11	0.36	0.323333	0.799221
		Replicate 2	20.83	20.76	-0.02	-0.05667	1.04006
		Replicate 3	20.62	20.68	-0.23	-0.26667	1.203025
	Fluconazole treated	Replicate 1	22.66	21.22	1.585	1.548333	0.341905
		Replicate 2	21.58	20.93	0.505	0.468333	0.722799
		Replicate 3	22.76	21.075	1.685	1.648333	0.319008
	Itraconazole-treated	Replicate 1	23.03	22.41	0.013333	-0.02333	1.016305
		Replicate 2	22.57	22.65	-0.44667	-0.48333	1.39797
		Replicate 3	22.25	23.99	-0.76667	-0.80333	1.745129
	Ketoconazole treated	Replicate 1	23.52	22.05	1.253333	1.216667	0.430276
		Replicate 2	23.45	22.66	1.183333	1.146667	0.451668
		Replicate 3	23.05	22.09	0.783333	0.746667	0.595979

Appendix table 3.2 - Raw *CT* values from real-time PCR analysis of *pmr-1* gene expression under azole drug treatment.

Gene	**Sample**	**Replicate**	***CT* (Target Gene)**	***CT* (Housekeeping Gene)**	**Δ*CT* (*CT* Target – *CT* Housekeeping)**	**ΔΔ*CT***	**Fold Change ($2^{-\Delta\Delta CT}$)**
pmr-1	Control (No Drug)	Replicate 1	23.57	21.11	2.72	0.27	0.82932
		Replicate 2	23.98	20.76	3.13	0.68	1.128452
		Replicate 3	22.35	20.68	1.5	-0.95	1.931873
	Fluconazole treated	Replicate 1	23.54	21.22	2.465	0.015	0.989657
		Replicate 2	23.56	20.93	2.485	0.035	0.976032
		Replicate 3	23.61	21.075	2.535	0.085	0.942785
	Itraconazole -treated	Replicate 1	22.89	22.41	-0.12667	-2.57667	5.965598
		Replicate 2	23.01	22.65	-0.00667	-2.45667	5.489469
		Replicate 3	22.94	23.99	-0.07667	-2.52667	5.762387
	Ketoconazole treated	Replicate 1	24.58	22.05	2.313333	-0.13667	1.099362
		Replicate 2	24.32	22.66	2.053333	-0.39667	1.316463
		Replicate 3	24.56	22.09	2.293333	-0.15667	1.114709

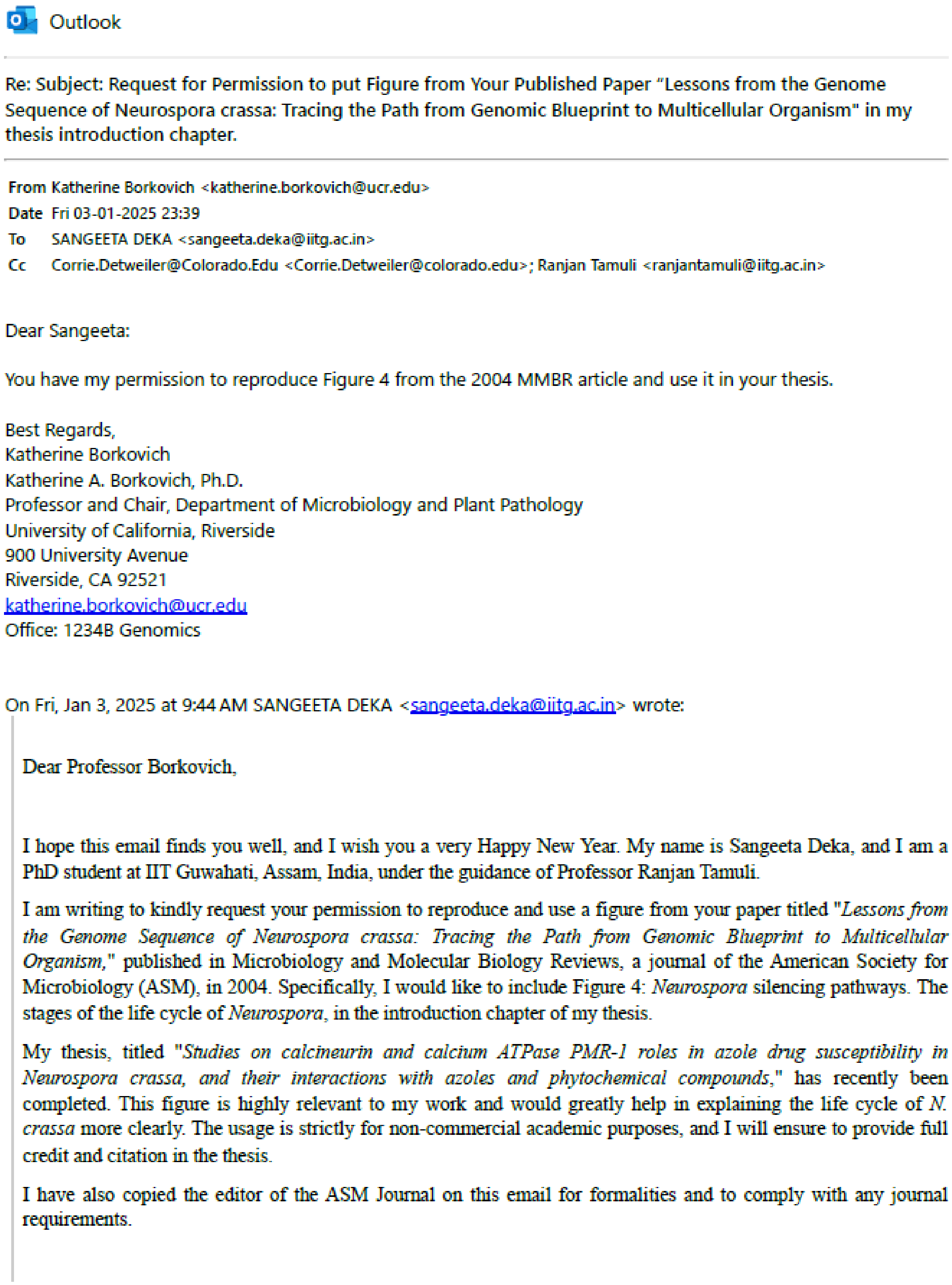

Outlook

Re: Subject: Request for Permission to put Figure from Your Published Paper "Lessons from the Genome Sequence of Neurospora crassa: Tracing the Path from Genomic Blueprint to Multicellular Organism" in my thesis introduction chapter.

From Katherine Borkovich <katherine.borkovich@ucr.edu>
Date Fri 03-01-2025 23:39
To SANGEETA DEKA <sangeeta.deka@iitg.ac.in>
Cc Corrie.Detweiler@Colorado.Edu <Corrie.Detweiler@colorado.edu>; Ranjan Tamuli <ranjantamuli@iitg.ac.in>

Dear Sangeeta:

You have my permission to reproduce Figure 4 from the 2004 MMBR article and use it in your thesis.

Best Regards,
Katherine Borkovich
Katherine A. Borkovich, Ph.D.
Professor and Chair, Department of Microbiology and Plant Pathology
University of California, Riverside
900 University Avenue
Riverside, CA 92521
katherine.borkovich@ucr.edu
Office: 1234B Genomics

On Fri, Jan 3, 2025 at 9:44 AM SANGEETA DEKA <sangeeta.deka@iitg.ac.in> wrote:

> Dear Professor Borkovich,
>
> I hope this email finds you well, and I wish you a very Happy New Year. My name is Sangeeta Deka, and I am a PhD student at IIT Guwahati, Assam, India, under the guidance of Professor Ranjan Tamuli.
>
> I am writing to kindly request your permission to reproduce and use a figure from your paper titled "*Lessons from the Genome Sequence of Neurospora crassa: Tracing the Path from Genomic Blueprint to Multicellular Organism,*" published in Microbiology and Molecular Biology Reviews, a journal of the American Society for Microbiology (ASM), in 2004. Specifically, I would like to include Figure 4: *Neurospora* silencing pathways. The stages of the life cycle of *Neurospora*, in the introduction chapter of my thesis.
>
> My thesis, titled "*Studies on calcineurin and calcium ATPase PMR-1 roles in azole drug susceptibility in Neurospora crassa, and their interactions with azoles and phytochemical compounds,*" has recently been completed. This figure is highly relevant to my work and would greatly help in explaining the life cycle of *N. crassa* more clearly. The usage is strictly for non-commercial academic purposes, and I will ensure to provide full credit and citation in the thesis.
>
> I have also copied the editor of the ASM Journal on this email for formalities and to comply with any journal requirements.

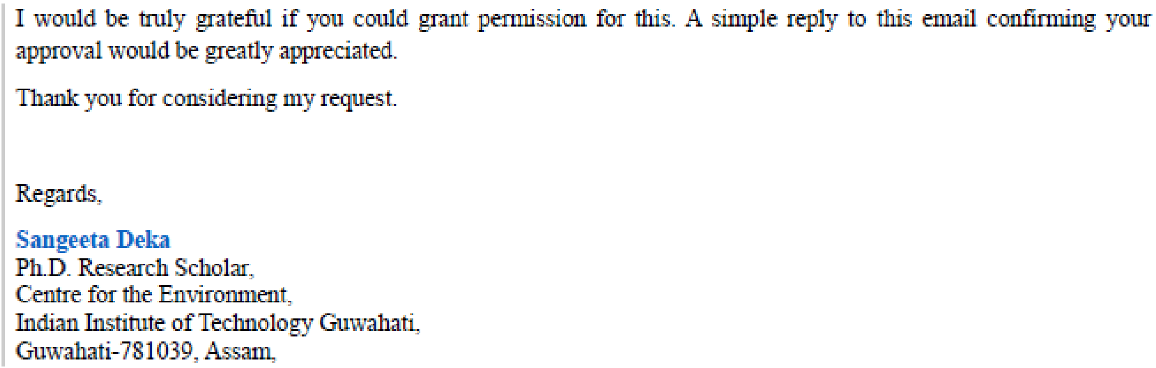

I would be truly grateful if you could grant permission for this. A simple reply to this email confirming your approval would be greatly appreciated.

Thank you for considering my request.

Regards,

Sangeeta Deka
Ph.D. Research Scholar,
Centre for the Environment,
Indian Institute of Technology Guwahati,
Guwahati-781039, Assam,

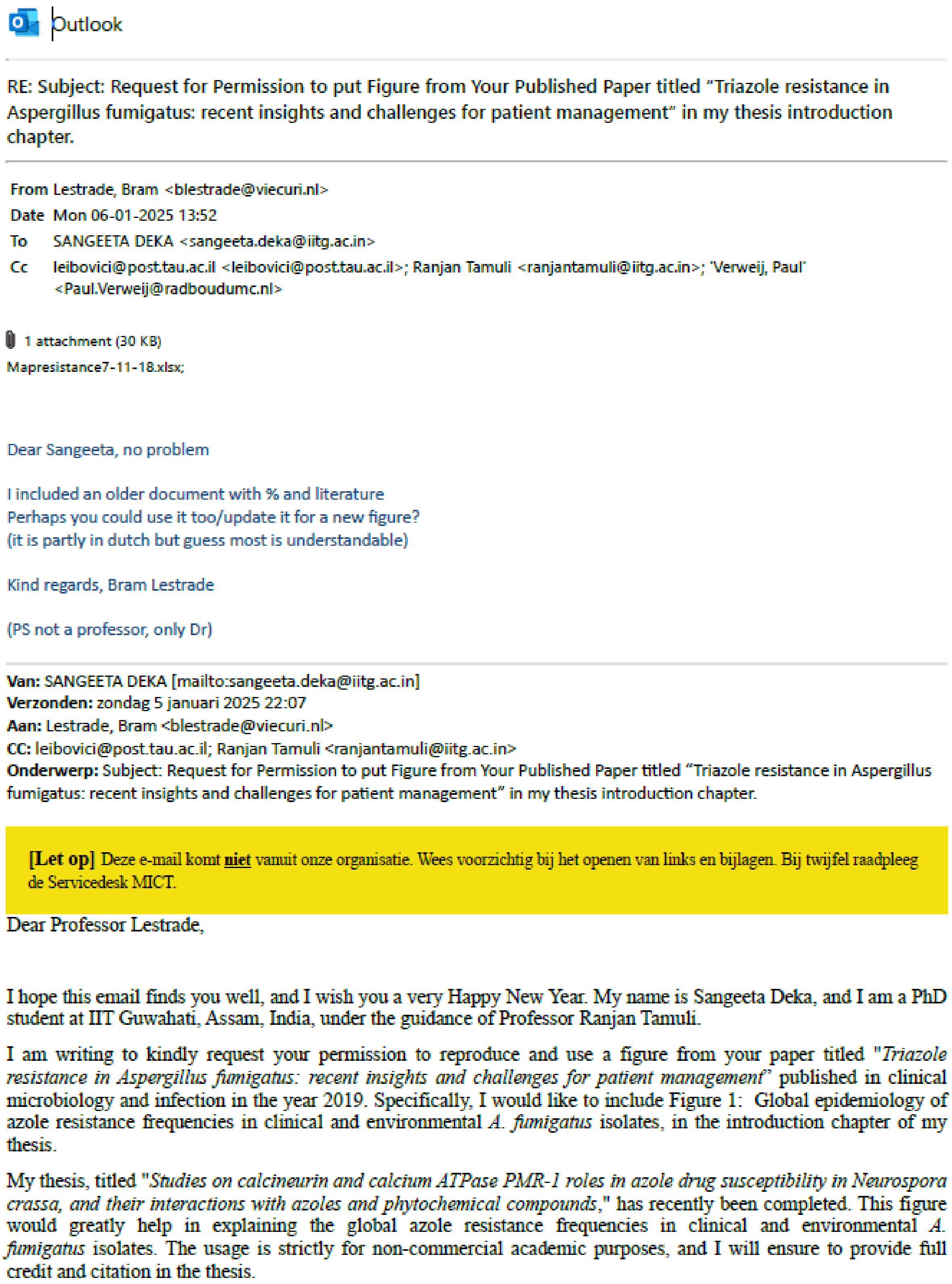

RE: Subject: Request for Permission to put Figure from Your Published Paper titled "Triazole resistance in Aspergillus fumigatus: recent insights and challenges for patient management" in my thesis introduction chapter.

From Lestrade, Bram <blestrade@viecuri.nl>
Date Mon 06-01-2025 13:52
To SANGEETA DEKA <sangeeta.deka@iitg.ac.in>
Cc leibovici@post.tau.ac.il <leibovici@post.tau.ac.il>; Ranjan Tamuli <ranjantamuli@iitg.ac.in>; 'Verweij, Paul' <Paul.Verweij@radboudumc.nl>

1 attachment (30 KB)
Mapresistance7-11-18.xlsx;

Dear Sangeeta, no problem

I included an older document with % and literature
Perhaps you could use it too/update it for a new figure?
(it is partly in dutch but guess most is understandable)

Kind regards, Bram Lestrade

(PS not a professor, only Dr)

Van: SANGEETA DEKA [mailto:sangeeta.deka@iitg.ac.in]
Verzonden: zondag 5 januari 2025 22:07
Aan: Lestrade, Bram <blestrade@viecuri.nl>
CC: leibovici@post.tau.ac.il; Ranjan Tamuli <ranjantamuli@iitg.ac.in>
Onderwerp: Subject: Request for Permission to put Figure from Your Published Paper titled "Triazole resistance in Aspergillus fumigatus: recent insights and challenges for patient management" in my thesis introduction chapter.

[Let op] Deze e-mail komt **niet** vanuit onze organisatie. Wees voorzichtig bij het openen van links en bijlagen. Bij twijfel raadpleeg de Servicedesk MICT.

Dear Professor Lestrade,

I hope this email finds you well, and I wish you a very Happy New Year. My name is Sangeeta Deka, and I am a PhD student at IIT Guwahati, Assam, India, under the guidance of Professor Ranjan Tamuli.

I am writing to kindly request your permission to reproduce and use a figure from your paper titled "*Triazole resistance in Aspergillus fumigatus: recent insights and challenges for patient management*" published in clinical microbiology and infection in the year 2019. Specifically, I would like to include Figure 1: Global epidemiology of azole resistance frequencies in clinical and environmental *A. fumigatus* isolates, in the introduction chapter of my thesis.

My thesis, titled "*Studies on calcineurin and calcium ATPase PMR-1 roles in azole drug susceptibility in Neurospora crassa, and their interactions with azoles and phytochemical compounds*," has recently been completed. This figure would greatly help in explaining the global azole resistance frequencies in clinical and environmental *A. fumigatus* isolates. The usage is strictly for non-commercial academic purposes, and I will ensure to provide full credit and citation in the thesis.

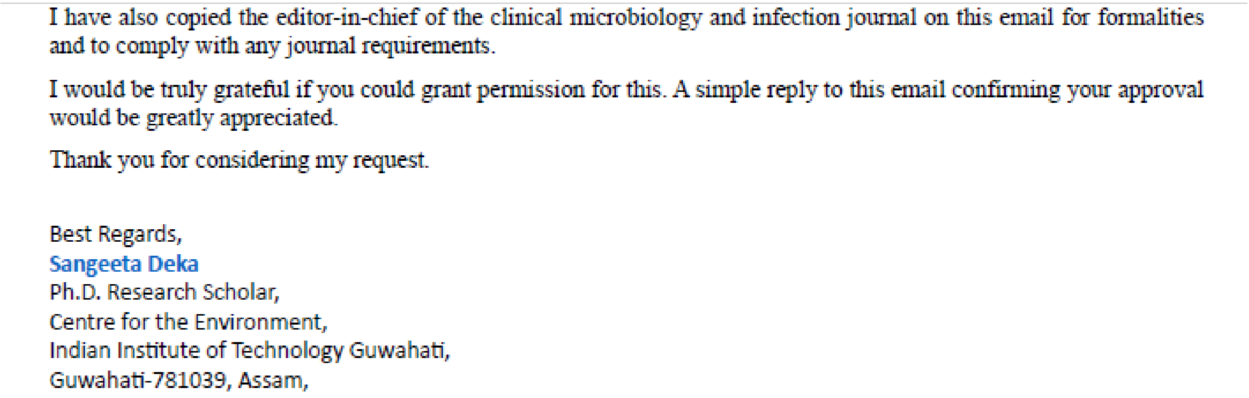

I have also copied the editor-in-chief of the clinical microbiology and infection journal on this email for formalities and to comply with any journal requirements.

I would be truly grateful if you could grant permission for this. A simple reply to this email confirming your approval would be greatly appreciated.

Thank you for considering my request.

Best Regards,
Sangeeta Deka
Ph.D. Research Scholar,
Centre for the Environment,
Indian Institute of Technology Guwahati,
Guwahati-781039, Assam,

LIST OF PUBLICATIONS

Publications from Ph.D. Thesis:

(A) Journal Publications:

1. **Sangeeta Deka** and Prof. Ranjan Tamuli. Cellular roles of the *Neurospora crassa* calcineurin and calcium ATPase PMR-1 in azole susceptibility, and their interactions with azoles determined using molecular dynamics simulation. (Manuscript under revision)

2. **Sangeeta Deka**, Umesh, Ranjan Tamuli. Computational Investigation of Phytochemical inhibitors for Antifungal Drug Exploiting as Calcineurin CNA-1, CNB-1 and PMR-1 as Targets of *Neurospora crassa*. (Manuscript under preparation)

3. **Sangeeta Deka** and Prof. Ranjan Tamuli. Deciphering the Complex Interplay between azole antifungal drug resistance and Heat Shock Proteins in pathogenic fungi. (Manuscript under preparation)

4. Megha Rasaily, Serena Daniel Ngiime, Rahul Kumar Thaosen, Surbhi Gupta, **Sangeeta Deka**, Ranjan Tamuli. Methods for the detection of intracellular calcium in filamentous fungi. MethodX DOI: 10.1016/j.mex.2024.102570.

(B) Conference presentations:

1. **Sangeeta Deka** and Prof. Ranjan Tamuli (2023) Understanding the molecular mechanism of antifungal drug resistance to design antifungal-impregnated medical devices Terasaki Innovation summit 2023 organized by the Terasaki Institute for Biomedical Innovation held at University of California Los Angeles (UCLA). 8th-10th March, 2023.

2. **Sangeeta Deka** and Prof. Ranjan Tamuli (2022) Investigating the Mechanisms of Drug Resistance in *Neurospora Crassa*. North East Research Conclave 2022, organized by IIT Guwahati. 20th-22nd May 2022.

3. **Sangeeta Deka** and Prof. Ranjan Tamuli, Ecological and Molecular Basis of Amphibian chitridiomycosis caused by the amphibian chytrid fungus *Batrachochytrium dendrobatidis.* National Conference on Issues and Challenges in Water Treatment and Allied research for Sustainable Environment (WATER 2020) Organised by Centre for The Environment IIT Guwahati. 23-25 January, 2020.

4. **Sangeeta Deka (2020)** Workshop on Biological Data Analysis and Visualization using R and Molecular Phylogenetics. Organized by DBT Funded NER Bioinformatics Infrastructure Facility, Institute of Advanced Study in Science and Technology, Paschim Boragaon, Garchuk, Guwahati 781035, Assam, India. 5th-6th March 2020.

MethodsX 12 (2024) 102570

Contents lists available at ScienceDirect

MethodsX

journal homepage: www.elsevier.com/locate/methodsx

Methods for the detection of intracellular calcium in filamentous fungi

Megha Rasaily[a,1], Serena Ngiimei D[a,1], Rahul Kumar Thaosen[a,1], Surabhi Gupta[a,1], Sangeeta Deka[b,1], Ranjan Tamuli[a,b,*]

[a] *Department of Biosciences and Bioengineering, Indian Institute of Technology Guwahati, India*
[b] *Centre for the Environment, Indian Institute of Technology Guwahati, India*

ARTICLE INFO

Method name:
Detection of the intracellular calcium in filamentous fungi.

Keywords:
Aequorins
Calcium isotope ^{45}Ca
Chlortetracycline hydrochloride (CTC)
Genetically engineered calcium indicators (GECIs)
Intracellular calcium concentration
Microelectrode
Neurospora crassa
Red fluorescent indicators (R-GECOs)

ABSTRACT

Calcium (Ca^{2+}), a critical secondary messenger, is also known as the molecule of life and death. The cell responds to a minute change in Ca^{2+} concentration and tightly maintains Ca^{2+} homeostasis. Therefore, determining the cell Ca^{2+} level is critical to understand Ca^{2+} distribution in the cell and various cell processes. Many techniques have been developed to measure Ca^{2+} in the cell. We review here different methods used to detect and measure Ca^{2+} in filamentous fungi. Ca^{2+}-sensitive fluorescent chlortetracycline hydrochloride (CTC), Ca^{2+}-selective microelectrode, Ca^{2+} isotopes, aequorins, and RGECOs are commonly used to measure the Ca^{2+} level in filamentous fungi. The use of CTC was one of the earliest methods, developed in 1988, to measure the Ca^{2+} gradient in the filamentous fungus *Neurospora crassa*. Subsequently, Ca^{2+}-specific microelectrodes were developed later in the 1990s to identify Ca^{2+} ion flux variations, and to measure Ca^{2+} concentration. Another method for quantifying Ca^{2+} is by using radio-labeled Ca^{2+} as a tracer. The usage of ^{45}Ca to measure Ca^{2+} in *Saccharomyces cerevisiae* was reported previously and the same methodology was also used to detect Ca^{2+} in *N. crassa* recently. Subsequently, genetically engineered Ca^{2+} indicators (GECIs) like aequorins and RGECOs have been developed as Ca^{2+} indicators to detect and visualize Ca^{2+} inside the cell. In this review, we summarize various methodologies used to detect and measure Ca^{2+} in filamentous fungi with their advantages and limitations.

- Chlortetracycline (CTC) fluorescence assay is used for visualizing Ca^{2+} level, whereas microelectrodes technique is used to determine Ca^{2+} flux in the cell.
- Radioactive ^{45}Ca is useful for quantification of Ca^{2+} in the cellular compartments.
- Genetically modified calcium indicators (GECIs) are used to study Ca^{2+} dynamics in the cell.

---

[*] Corresponding author at: Department of Biosciences and Bioengineering, Indian Institute of Technology Guwahati, Guwahati 781039, Assam, India.

E-mail address: ranjantamuli@iitg.ac.in (R. Tamuli).

[1] These authors contributed equally to this article.

https://doi.org/10.1016/j.mex.2024.102570
Received 19 April 2023; Accepted 11 January 2024

Specifications table

Subject area:	Microbiology
More specific subject area:	Intracellular calcium concentration
Name of the reviewed methodology:	Detection of the intracellular calcium in filamentous fungi
Keywords:	Aequorins; Calcium isotope ^{45}Ca; Chlortetracycline hydrochloride (CTC); Genetically engineered calcium indicators (GECIs); Intracellular calcium concentration; Microelectrode; *Neurospora crassa*; Red fluorescent indicators (R-GECOs)
Resource availability:	Not applicable
Review question:	What are the methods for the detection of intracellular calcium in filamentous fungi?

Method details

Introduction

Calcium (Ca^{2+}), a ubiquitous intracellular messenger, is crucial for regulating almost all cell processes. They are in charge of various cell functions, such as gene transcription, cell proliferation, and differentiation [1]. The cytosolic free Ca^{2+} resting concentration ($[Ca^{2+}]_c$) is ~100 nm, whereas Ca^{2+} concentration in the extracellular fluid is ~10^{-3} M; hence the gradient across the plasma membrane is more than 10,000-fold [2,3]. Numerous Ca^{2+} sensor proteins detect even the minute change in the Ca^{2+} levels, which further triggers downstream signaling processes [3]. Techniques to visualize or determine the intracellular concentration of Ca^{2+} are essential for understanding fungal physiology, adaptation to stress conditions, and virulence. In filamentous fungi, including *N. crassa* and *Aspergillus nidulans*, various techniques have been developed to visualize and measure Ca^{2+}.

Ca^{2+} visualization using chlortetracycline (CTC) is one of the oldest methods described for visualizing changes in intracellular Ca^{2+} levels and morphology in filamentous fungi [4]. CTC, discovered by Benjamin Minge Duggar in 1945, is the first member of the tetracycline class and produced by *Streptomyces aureofaciens* which appears golden in color [5,6]. CTC, produced by a strain of actinomycetes, is a fluorescent Ca^{2+} probe used to measure changes in intracellular Ca^{2+} levels [4,7]. CTC is also used for a variety of other applications, including determining the Ca^{2+} content in the blood by measuring the Ca^{2+}-binding platelet, also used to monitor the intracellular Ca^{2+} binding in cell systems, including sarcoplasmic reticulum [8], red blood cell [9], mitochondria [10], neutrophils [11] and human blood platelets [12–14]. CTC binds to Ca^{2+} and forms a fluorescent complex, making it possible to visualize the distribution pattern of Ca^{2+} [4]. The binding of the complex to membranes increases fluorescence intensity, which subsequently enables the imaging of Ca^{2+} buildup in vesicles and organelles [4,15].

The ion-selective microelectrode is a non-invasive technique to simultaneously measure ionic currents and fluxes in a cell [16]. This method allows us to determine the ion flux from the difference in ion concentration at two locations: one close to and one far from the cell [17]. The external diffusive gradient produced by ion transport across the plasma membrane is collected with the ion-selective microelectrode at two places [17]. The first Ca^{2+} ion-selective electrodes were made based on the Ca^{2+} ligand ETH for detection at the sub-nanomolar range [18] and it was used for Ca^{2+} detection in *N. crassa* [19]. Ca^{2+}-specific microelectrodes have been used for monitoring Ca^{2+} ions in cerebrospinal fluid and cataracts in the lens of rats [20,21]. Likewise, measurement of the effect of gravistimulation on the Ca^{2+} activity in maize roots [22]. In *N. crassa*, Ca^{2+} selective microelectrodes have also been used to measure the cytosolic free Ca^{2+} using mycelial cells.

Radioactive calcium isotopes were also used as a tracer to measure Ca^{2+} levels in the cell. Naturally, calcium is a stable element, comprising six stable isotopes ^{40}Ca, ^{42}Ca, ^{43}Ca, ^{44}Ca, ^{46}Ca, and ^{48}Ca, where ^{40}Ca is the most abundant and constitutes about 97% of all natural calcium. Artificially produced calcium radioactive isotopes ranging from ^{30}Ca to ^{60}Ca, are extensively used as a radioactive tracer. To date, radioactive calcium isotopes have been widely used as Ca^{2+} tracers, for example, to measure Ca^{2+} absorption efficiency in patients,^{48}Ca as the intravenous tracer, ^{47}Ca as an oral trace [23] and ^{41}Ca as a bone tracer [24] have been used. Likewise, the localization of Ca^{2+} in different organelles has been explored widely in *S. cervisiae,* where 95 % of Ca^{2+} was sheltered in vacuoles [25], and the distribution of Ca^{2+} in various organelles using radioactive calcium isotopes has also been reported in *N. crassa* [26].

Genetically modified Ca^{2+} indicators (GECIs) are genetically modified *in vivo* Ca^{2+} sensors that detect Ca^{2+} oscillation in different cellular organelles, such as ER, mitochondria, Golgi, plasma membrane, and other Ca^{2+} stores [27–29]. GECIs are classified into three different classes, including (a) Bioluminescent sensors that are based on aequorin photoproteins, (b) Cameleon type, and (c) Single fluorescent proteins [28]. Aequorin, the first Ca^{2+}-sensitive photoprotein discovered from the jellyfish *Aequorea victoria*, is an excellent Ca^{2+} indicator [30,31]. The circumoral ring of the umbrella of *A. victoria* has specialized cells called photocytes that contain aequorin. On mechanical stimulation, the photocytes luminescent and generate a bluish-green light. Aequorin is associated with the green fluorescent protein (GFP) responsible for the bluish-green light on stimulation [30] and was first used in barnacle muscle cells [32]. Aequorin has been widely used as a Ca^{2+} indicator in a variety of systems, including mammals [33], plants [34–36], yeast [37] and filamentous fungi like *N. crassa* [30,38,39].

Single fluorescent proteins consist of the portion of CaM fused with fluorescent proteins, several members of this class such as camgaroos, pericams, G-CaMPs, case sensors, and grafted EF-hands are used for Ca^{2+} measurement [28]. G-CaMPs, which consist of the circularly permuted green fluorescent proteins (cpGFP), calmodulin (CaM) (Ca^{2+} sensory domain), and Ca^{2+}/CaM-binding M13 peptide (M13pep) [27] are single wavelength intensiometric in nature; therefore, fluorescence intensity is proportional to Ca^{2+} binding [40]. The Ca^{2+} sensory domain is present at the N/C-terminal of the indicator. M13 peptide of the myosin light chain is fused at the other end of the indicators. M13 brings conformational changes in the Ca^{2+} indicator upon Ca^{2+} binding with the CaM fragment [27]. M13 peptide also prevents the interaction of this sensory complex with the other CaM interacting proteins present within the cellular vicinity [27]. GCaMP3 was introduced as a template in the error-prone PCR technique, which resulted in the generation of a large-size mutant library. These mutants were screened on the basis of the change in Ca^{2+}-dependent green fluorescent [41]. Subsequently, they were termed as GECOs for 'genetically encoded Ca^{2+} indicators for optical imaging' [41].

The methods used to monitor intracellular Ca^{2+} are the focus of this review. We describe each methodology with advantages and limitations.

Chlortetracycline hydrochloride (CTC)

CTC is a fluorescent Ca^{2+} probe that measures changes in intracellular Ca^{2+} levels [7]. A unique labeling and Ca^{2+} detection method for studying changes in intracellular Ca^{2+} levels and morphology in *N. crassa* [4]. During the extension process, *N. crassa* maintains a high Ca^{2+} gradient directed toward the hyphal tip, and the Ca^{2+} is stored in the storage vesicles located right beyond the apex [4,42]. Ca^{2+} channels, triggered by IP_3, are responsible for both the production and the maintenance of the high Ca^{2+} gradient at the tip of the cell [43]. However, the membrane density and Mg^{2+} affect the CTC fluorescence [44] yet the membrane-associated Ca^{2+} emits greater fluorescence than Mg^{2+} [45].

Assay for determining the intracellular distribution of Ca^{2+} using CTC

To visualize intracellular Ca^{2+} distribution and quantify the Ca^{2+} in the *N. crassa* hyphal tip, CTC (Sigma-Aldrich C4881-5G), dissolved in 0.1% dimethyl sulfoxide (DMSO), is used at working concentration of 100 µM. The conidia of *N. crassa* strains are inoculated onto a glass slide with Vogel's agar medium containing 100 µM CTC, and incubated at 30°C for 12 h in dark [46]. CTC fluorescence is then observed using an Inverted fluorescence microspore under a bright field and a DAPI filter system with an exposure time of 300−400 ms [47]. CTC fluorescence is affected by membrane density, and therefore, membrane fluorescence is determined using N-phenyl-1-naphthylamine (NPN) is as a control [44].

Advantages. There are several advantages of using CTC as a Ca^{2+}-sensitive fluorescent probe for imaging intracellular Ca^{2+} dynamics in living cells. CTC allows the study of the dynamics of intracellular Ca^{2+} in real-time without affecting the growth of fungi. It has a high sensitivity for detecting intracellular Ca^{2+}, which allows visualizing small changes in Ca^{2+} levels. CTC has a high specificity for Ca^{2+}, and membrane-bound Ca^{2+} gives higher fluorescence than Mg^{2+} [44,45]. It is non-toxic, cost-effective, easy to use, and used in many cell types and organisms, including neurons, cardiomyocytes, and plants, making it versatile for different applications.

Limitations. While CTC has many advantages, yet there are several limitations in its use. It is sensitive to light and can be photobleached over time, limiting the duration of imaging experiments. CTC's fluorescence intensity may be affected by other fluorescent molecules in the cell, and its sensitivity to pH change can lead to interference and inaccurate results. Some tetracycline derivatives may have similar properties to CTC and can interfere with the binding of Ca^{2+} with CTC. Therefore, it may not be the best option for some specific applications, where other indicators have higher sensitivity or better specificity. Hence, it is necessary to consider these limitations and to use appropriate controls and methods to minimize their impact on the accuracy of the imaging results.

Calcium ionic flux measurement by microelectrodes

The Ca^{2+}-selective microelectrodes are complex systems that involve a combination of surface ion exchange and ion diffusion stages. The simple hyphal morphology of *N. crassa* makes it easy to determine the current density of ions with an ion-selective probe [48,49]. The fabrication of Ca^{2+} ion selective probe (Calcium Ionophore I–Cocktail A, catalog number 21048) is done at Bio Currents Facility (Marine Biological Laboratory, Woods Hole, MA, USA) [50]. Ca^{2+} selective probe and a separate reference system must be submerged in the solution to measure the electrode potential, and a millivolt measuring system is connected to both. When the system is in equilibrium, the charge of the reference interface balances out the electrons that the Ca^{2+} selective electrode membrane has added or withdrawn from the solution. As a result, the initial stable reference voltage deviates positively or negatively, which is recorded by the external measuring device (Fig. 1) [16,51,52].

Culture preparation: *N. crassa* strains are grown in Vogel's medium [46] for 2 days in the dark and 1 day under the light for conidiation. The conidia are harvested in Eppendorf tubes using 1 ml of sterile water. Conidia are then transferred onto strips of dialysis tube with Vogel's medium in a Petri dish, and the strain is grown at 28°C overnight. The dialysis tube is cut with a razor blade, attached to the bottom of the plate with double-sided sticky tape, and then covered. The culture is flooded with 3 ml of buffer solution: KCl (10 mM), $CaCl_2$ (1 mM), $MgCl_2$ (1 mM), sucrose (133 mM), and MES (10 mM), and the pH is adjusted to 5.8 with KOH. The mycelia are incubated in the buffer solution, maintaining the pH at 5.5 stable throughout the experiment. Large trunk hyphae *in situ* are used for the study.

Microelectrical measurement of hyphal properties and ion flux: A distance from the first spike site, the hyphae are spiked with a double-barrel micropipette and a single-barrel micropipette, KCl (3 M) is put into both micropipettes [16]. A salt bridge containing KCl (3 M) in 2% agar and an Ag/AgCl electrode is connected to an electrometer and another to the Ca^{2+} -selective probe amplifier completing the circuit. The double-barrel micropipettes are then connected to the electrometer. A data acquisition board is used to control an operational amplifier configured for a voltage clamp. Currents are applied for 160 s and interrupted by 0 current rests (such as -2.5 nA, +2.5 nA, 0 nA, -5.0 nA, +5.0 nA, and 0 nA). The clamped voltage (V_0) is sampled during the last 10 ms of

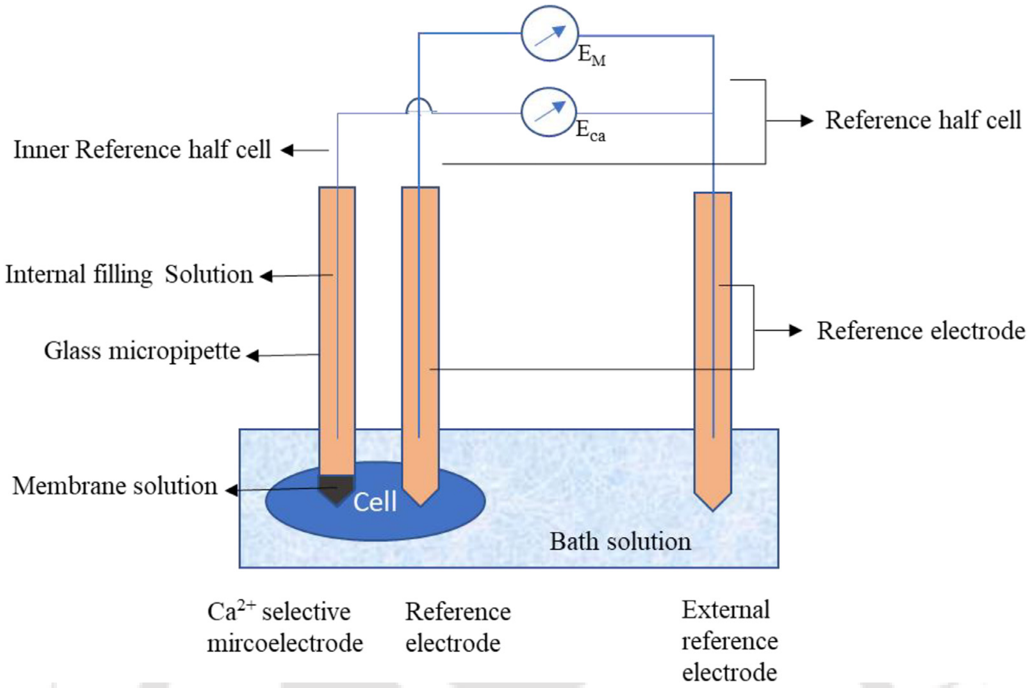

Fig. 1. Schematic representation of a Ca^{2+} membrane microelectrode cell assembly for intracellular Ca^{2+} measurement [52].

voltage clamp and the clamping current. The hyphal voltage (V_d) (measured simultaneously with V_0 at a distance, d, further along the hypha) is then obtained by connecting the single barrel microelectrode to an electrometer. The slope of the relationship between V_d and V_0 was used to compute the fading voltage of the distance d. Ca^{2+} ion fluxes are calculated based on the concentration difference between hyphal cells by considering their cylindrical geometry. The effect of the hyphal voltage on fluxes is measured by the following formula

$$J = \left(\frac{D}{r}\right)\left[\frac{C_2 - C_1}{\ln\left(\frac{r_2}{r_1}\right)}\right]$$

Where J is the net ion (nmol cm^{-2} s^{-1}), D is the diffusion coefficient (value of D for Ca^{2+}, 0.4×10^{-5} cm^2 s^{-1}), r is the hyphal radius, C_1 and C_2 are the concentrations at the two excursion points, and r_2 and r_1 are the distances between the two excursion points at the hyphal centre [16,53].

Advantages. Ca^{2+} selective microelectrodes can measure Ca^{2+} activities of the cytoplasm without disturbing the organelles as their tip size prevents the rupture of organelles. Even though the majority of intracellular Ca^{2+} measurement findings have previously been reported as concentrations, some researchers using Ca^{2+} selective electrodes have opted to convert Ca^{2+} ion concentrations to activities and constantly record the Ca^{2+} changes inside cells as long as the impalement of the cell is adequately maintained. One of the advantages is that there is no upper limit to their sensitivity range, and measurements are still viable at Ca^{2+} concentrations of 10 nM or less even. As many changes occur in intracellular activities quite slowly (on a second-to-minute timescale), the response time is compatible with recording such changes.

Limitations. Many ion-sensitive microelectrodes are not highly selective when measuring only one type of ion. This can lead to interference from other ions, which makes it difficult to ascertain the change in activity regarding the desired ion. Ion-sensitive microelectrodes are sensitive to electrical interference and must be well-shielded to maximize their performance. Ion-sensitive microelectrodes are passive devices that do not alter the cells under test. However, they require the impalement of the cell membrane to function accurately.

Calcium isotope ^{45}Ca

Radioactive isotopes are used as tracers based on the fundamental postulations that it replaces the native element inside the system, and then the added isotopes are absorbed and metabolized in the same proportion [54]. In *N. crassa*, a radioactive ^{45}Ca isotope was successfully used to quantify Ca^{2+} in various cell types and organelles (Fig. 2) [26].

Measurement of cellular calcium uptake (Mycelium mass): Vogel's medium (2% agar) was used to culture *N. crassa* strains [46]. The conidia are collected, diluted to 10^6 conidia/ml, and added to 6 ml of Vogel's medium, which also contains varying amounts of nonradioactive calcium (3 to 3000 μM) and radioactive isotope ^{45}Ca, which has a specific activity of >10 Ci/g (Perkin Elmer Life Sciences). The mixture is then incubated at 30°C for 25 h. 20 mM nonradioactive $CaCl_2$ is then added to the medium before the mycelium mass is promptly harvested using 25 mm acetate Plus filters. Then, ∼6 ml of growing medium containing 20 mM of nonradioactive $CaCl_2$ is used to gently wash the filter paper three times. The mycelium's radioactivity is then calculated using a liquid scintillation counter (Fig. 2(A)) [26].

Measurement of calcium uptake in conidia: In 2 ml of Vogel's medium with 1.6 Ci of ^{45}Ca, wild-type strains are produced. The cultures are incubated at 30°C for 3 days in the dark and then at room temperature for 6 days under the light. Conidia are collected from the liquid's surface in minute quantities, suspended in sterile autoclaved water, and counted using a hemocytometer. A liquid scintillation counter is used to monitor radioactivity and determine the quantity of calcium/conidium (Fig. 2(B)).

Measurement of calcium uptake in cell fractions: The concentration of Ca^{2+} in different cell organelles in *N. crassa* was determined by cell fractionation [55,56] using ^{45}Ca isotope [26]. The strains were cultured in Vogel's medium (1 or 2 L), which contains 50 Ci of ^{45}Ca and 10% conidia/ml of inoculum. The cultures are allowed to grow with vigorous aeration for 15 h at 25°C. The mycelia are harvested by filtering using cheesecloth and adding cold sorbitol (1 M) and Tris buffer (10 mM, pH 7.5). They were vigorously mixed with glass beads in Bead Beater, and unbroken cells were removed by centrifuging the homogenate at 1000 x g for 10 min. The supernatant is centrifuged at 15000 x g for 30 min, resulting in a pellet of dense organelles. A step gradient consisting of 7 ml 50% sucrose, 2 ml 40% sucrose, and 2 ml 30% sucrose, all in Tris buffer (10 mM, pH 7.5), is laid on top of the suspended pellet in sorbitol (1 M) and Tris buffer (10 mM, pH 7.5). After centrifugation at 20000 x g for 1 h, the suspension forms a thick layer of mitochondria on top of the 40% sucrose, with the dense vacuoles remaining in the pellet. A microsomal fraction is produced after centrifuging an aliquot of the supernatant at 250000 x g for 30 min. After the fractions have been well separated, each fraction is suspended in Tris buffer (10 mM, pH 7.5) in separate tubes. The radioactivity of each fraction is then determined using a liquid scintillation counter (Fig. 2(C)) [26].

Advantages. The advantages of measuring Ca^{2+} absorption by this technique are that Ca^{2+} concentration can be estimated with accuracy it has high precision. It can be applied to a wide range of species, including humans to fungi [23,26,57,58]. Additionally, this methodology does not require extensive sample preparation required for the microelectrode-based method.

Limitations. The drawback of this method is the preparation of radioactive isotopes, thus making it expensive. It is also time-consuming as it is not a rapid method to detect Ca^{2+}, and the long half-life of isotopes like ^{45}Ca, which is 162 days, emitting beta rays, this undesirable irradiation can be hazardous.

Genetically modified calcium indicators (GECIs)

Aequorin

Aequorin, a 22 kDa photoprotein that generates a green fluorescent protein, is composed of apoaequorin (the apoprotein), coelenterazine (the luciferin), and bound oxygen [30,59]. It exhibits a strong affinity for free Ca^{2+}, converting aequorin upon binding to Ca^{2+} into apoaequorin, carbon dioxide, and coelenteramide. The reaction's energy is released as blue light (λ_{max} 469 nm) (Fig. 3) [60,61]. It can be employed as a Ca^{2+} reporter because luminescence quantity depends on the amount of free Ca^{2+} present [30]. A chemiluminometer or a photon imaging detector can be used to detect luminescence [62,63]. The native aequorin gene (aeqA and aeqD gene) generates very low luminescence signals for detecting Ca^{2+}. The *aeqS*, a synthetic codon-optimized apoaequorin gene, was created for expression in *N. crassa* to solve codon bias, leading to lower apoaequorin expression [30,38]. This method was further optimized using the codons of the aequorin gene and constructed the recombinant aequorin to accurately determine Ca^{2+} concentration throughout a wide dynamic range in *N. crassa* [30,38].

Strain generation: The *N. crassa* strains *band* mutant strain (*bd A*) (FGSC1858) and 74 A (FGSC262) are routinely grown on Vogel's medium [46]. The *bd A* strain is transformed with pNCAEQ1 plasmid and 74 A is transformed with pNCAEQ3 plasmid, using hygromycin B for selection. Homokaryotic strain 73a is generated for further expression analysis [30,38].

Aequorin expression analysis: For protein extraction, conidia are inoculated in Vogel's medium at 30°C for 18 h, 180 rpm; thereafter the mycelia are harvested, frozen in liquid nitrogen, powdered, and transferred to Eppendorf tubes. Then, 0.2 g of mycelia is suspended in 1 ml extraction buffer (10 mM EGTA, Tris-Cl (50 mM, pH 7.4), 500 mM NaCl, 10 mM β mercaptoethanol, and water). Samples are vortexed for 30 s, then pelleted at 13,000 x g for 5 min, and stored at -70°C. The Bradford protein assay [65] (Bio-Rad Microscience) is used to quantify the total protein concentration in the supernatant, and in vitro protein concentration is then carried out to determine the amount of aequorin present. Then, ∼200 mg aliquot of total soluble protein is mixed with 0.25 mM coelenterazine in methanol to give a final concentration of 2.5 mM, and thereafter it is incubated at 30°C for 4 h in the dark. The in vitro aequorin constitution mixture containing 20 mg of total soluble protein diluted 1:50 in buffer (200 mM Tris-Cl, 0.5 mm EDTA, pH 7.0), which was then integrated for 20 s following the addition of an equal volume of 100 mM $CaCl_2$, and 100 ml of this

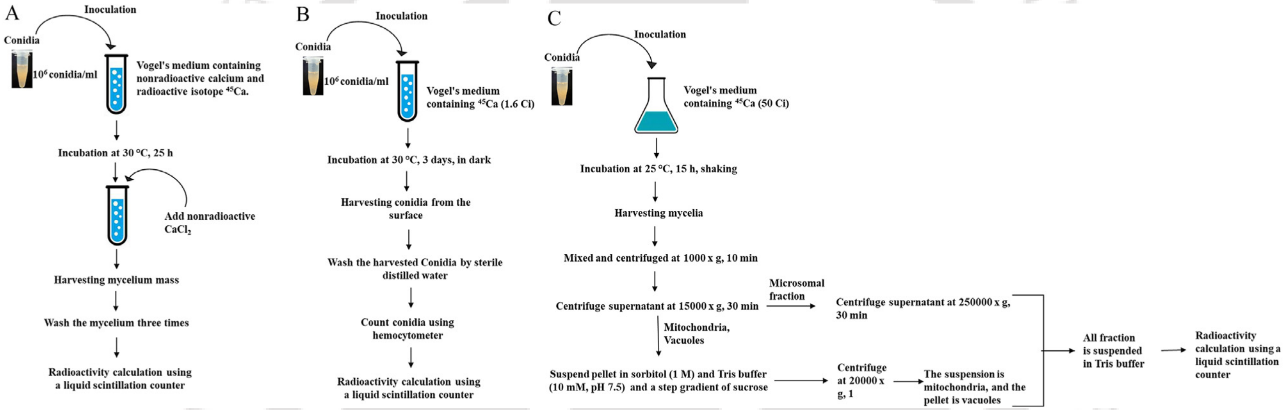

Fig. 2. Schematic detailing the procedures for measuring calcium uptake in *N. crassa* cells using the radioactive isotope ^{45}Ca [26]. (A) Accumulation of calcium in mycelium. (B) Estimation of calcium concentration in conidia. (C) Quantification of calcium concentrations in cellular fractions.

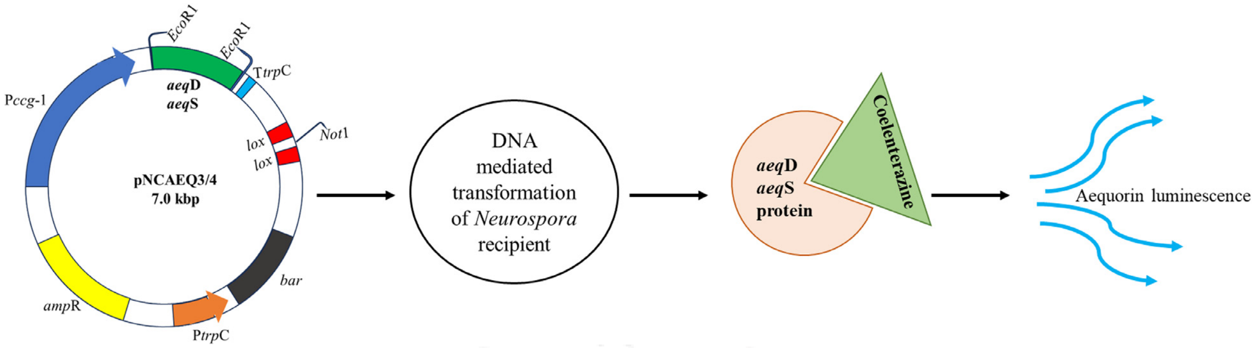

Fig. 3. Schematic representation of Ca^{2+} concentrations detection in *N. crassa* cells by aequorin. The plasmid is transformed in *N. crassa* and the protein radiates blue luminescence, that is measured by a photomultiplier tube [30].

was used to detect aequorin luminescence. Aequorin light emission can be detected using a specially made tube luminometer with a photomultiplier tube (air-cooled type 9829A, Thorn EMI) or a plate luminometer (Berthold MicroLumat LB96P) (Fig. 3) [30,66]. Aequorin concentration is determined using the total luminescence detected by making a standard curve using it, and the values are then converted into µg aequorin g^{-1} total protein.

Calcium levels calibration: The relative light units (RLU) used to measure the light emission are normalized by translating them to Ca^{2+} concentrations using the empirically obtained equation shown below, where k = luminescence (in RLU) s^{-1}/total luminescence (in RLU) [30,67].

$$pCa = 0.332588(-log k) + 5.5593$$

The RLU values are multiplied by 1.24 to account for the 24% quenching of aequorin luminescence caused by ethanol [30].

Advantages. Aequorin has a very strong selectivity for free Ca^{2+}, and measures Ca^{2+} across a dynamic range. It is kept within the cell compartment that it has been intended for, is relatively stable within the cytoplasm, and is non-cytotoxic. In addition, unlike autofluorescence, autoluminescence is not found in most natural systems; hence detecting luminescent light is advantageous [30,63].

Limitations. There are a few limitations of using aequorin for Ca^{2+} detection, including enough light emitted for detection. Other limitations include the free Ca^{2+} level could be very low, the requirement of a very high spatiotemporal resolution, inefficient introduction methods, or the system under study might be too compact. The use of fluorescent dyes in systems other than filamentous fungi could potentially complement the use of aequorin [30,38].

Red fluorescent indicators (R-GECOs)

Members of this class give different chromatic signals according to which the nomenclature has been done [40]. GECOs providing green signal is termed as G-GECOs (green fluorescents genetically encoded Ca^{2+} indicator). G-GECOs have various types based on their dissociation constants like G-GECO1 (750 nM), G-GECO1.1 (620 nM), and G-GECO1.2 (1150 nM). Additionally, they offer nearly two times as much fluorescent light (2300 to 2600%) as standard G-CaMPs, while Ca^{2+} is bound [41]. Red fluorescent indicators (R-GECOs) were generated by replacing the cpGFP (circularly permuted GFP) of GECO1.1 with cp version of mApple (Red fluorescent protein, isolated from Discosoma species) [41,68]. R-GECO construct has been widely used to measure the Ca^{2+} oscillations at different concentrations in *A. nidulans* [64].

Strain generation: Amplify RGECO sequence from pPD60 RGECO.1 plasmid (R-GECO-KpnI-Fw and R-GECO-XbaI-r) and cloned in pJET1.2 plasmid using KpnI and XbaI restriction enzymes. Digest R-GECO ORF clone in the pCMB17apx plasmid with similar restriction enzymes to yield pNT76 plasmid for protein expression. Amplify ORF of *chsB* from genomic DNA using gene-specific primers and clone in the pSH44 plasmid (N-mCherry tagged), to yield pNT77 plasmid. Transform generated plasmids into the *A. nidulans* TH02A3 recipient strain and screen microscopically to confirm fluorescence (Fig. 4) [64].

Visualization and concentration determination: *A. nidulans* strains are generally grown in eight-well glass bottom slides with minimum media and kept overnight at 28°C. Visualize properly grown cells under a fluorescence microscope (Axiophot microscope; Plan-apochromatic 63×1.4 Oil objective lens). Capture images using ZEISS AxioCam MRM CCD camera [64]. The concentration of Ca^{2+} can be calculated by using the given equation, where k_d is the effective dissociation constant, F is Fluorescence intensity, F_{min} is minimum fluorescence intensity, and F_{max} is maximum fluorescence intensity [69].

$$\left[Ca^{2+}\right] = k_d\left(\frac{F - F_{min}}{F\max - F}\right)$$

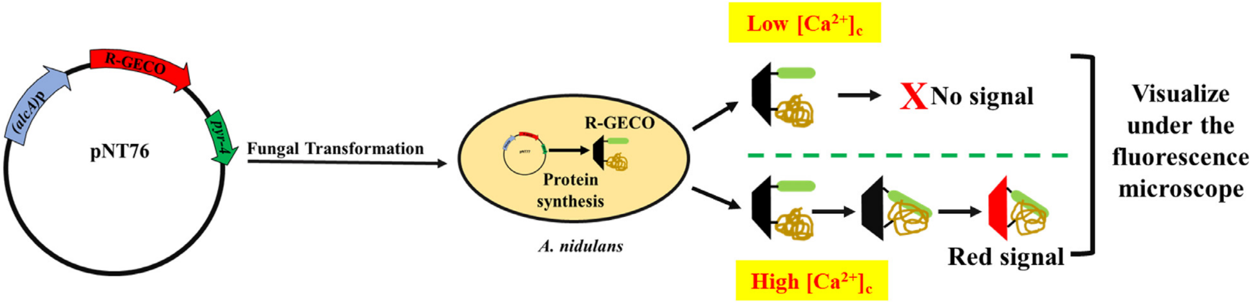

Fig. 4. Schematic representation of the R-GECO containing plasmid (pNT76) followed by transformation into fungi. Activation of R-GECO signaling upon changing the cytosolic calcium concentration $[Ca^{2+}]_c$ [64].

Table 1
Reported range of calcium sensitivity using various methodologies of calcium detection.

Method	Reported range of calcium sensitivity	Reference
Calcium ionic flux measurement by Microelectrodes	10^{-7} to 10^{-8} M	[52]
Cellular calcium uptake (mycelium mass) using radioactive isotope ^{45}Ca	0.0195 µM–0.45 µM	[26]
Calcium uptake in conidia by using radioactive isotope ^{45}Ca	Each conidia contain 0.095 fmol of calcium	[26]
Calcium uptake in cell fraction by using radioactive isotope ^{45}Ca	0.63–9.47 µmol/g protein	[26]
Aequorin	5.2–6.7 pCa ($\log_{10}[Ca^{2+}]$)	[66]
Red fluorescent indicators (R-GECOs)	0 µM to 1 µM	[64]

Advantages. R-GECOs are a valuable tool for the optical imaging of the Ca^{2+} dynamics within cellular compartments having less half-life time [70]. They show specific binding towards Ca^{2+} binding proteins due to the presence of M13 peptide sequence. They can be used to mark various targets simultaneously in deeper cellular regions due to their availability in multiple variants. Most importantly, they are resistant to photobleaching and are easily accessible [71].

Limitations. R-GECOs provide weak intensity and more background noise in red fluorescence [71] and there are high chances of tissue damage while using blue fluorescent excitation. It is difficult to obtain a high spatial resolution with GECOs; hence they are preferable for brain imaging [27,72]. M13 peptide present in the GECOs may interact with other cellular proteins, leading to no specificity and activation of other cellular proteins other than CaM [27].

Conclusion

From prokaryotes to eukaryotes, Ca^{2+} signaling is an evolutionarily conserved process. Ca^{2+} signaling influences various cellular processes in fungi, such as growth, development, fertility, stress tolerance, and virulence [3]. This paper discussed different approaches to visualize and quantify Ca^{2+} in fungal cells. To critically evaluate the function of Ca^{2+} as a signaling molecule in the cells, measuring free cytosolic Ca^{2+} and detecting the changes of Ca^{2+} level is required. However, the range of Ca^{2+} sensitivity varies in various methodologies used (Table 1). Development of a thorough understanding of the stability of Ca^{2+} and by using an indicator that provides the strongest signal possible, we can minimize the possibility of alteration in the cellular functions while using these indicators. CTC has potential applications in the field of cellular and molecular biology for the study of intracellular calcium dynamics. Microscopic analysis showed enhanced fluorescence in the internal Ca^{2+} storing vesicles in the growing hyphae of *N. crassa* [4]. Several reports have provided new insights into the use of CTC as a probe for intracellular Ca^{2+} imaging and highlights the potential of CTC as a valuable tool for the study of Ca^{2+} mediated cellular processes [73][73]. When Ca^{2+} selective microelectrode is properly applied to biological systems, it provides an enormous experimental return. It is a direct effective measurement method for determining how Ca^{2+} transport functions in muscle fibers, plants, and fungal cells in their dynamic living state. In a walled, turgid cell of *N. crassa* hyphae, the voltage dependence of Ca^{2+} fluxes have been quantitatively studied [16]. A recent report describes an in vivo monitoring of Ca^{2+} ions in rat cerebral fluid with the help of improved Ca^{2+} selective microelectrode fabrication [20]. In filamentous fungi, *N. crassa*, the major fraction of Ca^{2+} is deposited in vacuoles [26]. Given the numerous roles that Ca^{2+} plays, Ca^{2+} signaling can serve as a target for developing novel antifungal medications. The radioactive tracers were first used to trace the pathway of Ca^{2+} metabolism in the human body. Radioisotopes are used to study tumor localization and have also helped to trace early tumors. The recent development of recombinant aequorin has made it easy for high-throughput screening of filamentous fungi with compromised calcium signaling. The recombinant aequorin can be used to identify drug targets in filamentous fungi [30]. The study of Ca^{2+} dynamics has become easier after the construction of GECOs. It is now possible to simultaneously image many Ca^{2+} markers in the same cell. The GECO construct has only been used in a limited number of filamentous fungi to date, but it can be made accessible for other filamentous fungi and higher eukaryotes because of its improved sensitivity and specificity [41,64]. Considering the methodology's requirement, resource availability, and cost-effectiveness, a suitable method to visualize and determine the concentration of intracellular Ca^{2+} may be chosen. We described five different techniques for quantifying and visualizing intracellular Ca^{2+}

in filamentous fungi. Each method has different ranges of selectivity and sensitivity, prompt response, the accuracy of quantification, and different cell types. It is necessary to exercise caution while selecting a particular method for a given application. In the future, more accurate methods for measuring Ca^{2+} in filamentous fungi will emerge, which will be immensely helpful for understanding fungal physiology and adaptation to different environmental conditions.

Ethics statements

The authors have complied with MethodsX's ethical standards; no human participants, animal research, or data from social media were used in this study.

Funding

SND, RKT, SG were supported by Research Fellowships from the Ministry of Human Resource Development, Government of India. MR was supported by Research Fellowships from the Department of Biotechnology (DBT), Ministry of Science and Technology, Government of India. We would also like to thank IIT Guwahati for partial financial support.

Declaration of competing interest

The authors declare that they have no known competing financial interests or personal relationships that could have appeared to influence the work reported in this paper.

CRediT authorship contribution statement

Megha Rasaily: Conceptualization, Methodology, Writing – original draft, Writing – review & editing. **Serena Ngiimei D:** Conceptualization, Methodology, Writing – original draft, Writing – review & editing. **Rahul Kumar Thaosen:** Conceptualization, Methodology, Writing – original draft. **Surabhi Gupta:** Conceptualization, Methodology, Writing – original draft. **Sangeeta Deka:** Conceptualization, Methodology, Writing – original draft. **Ranjan Tamuli:** Conceptualization, Methodology, Writing – original draft, Visualization, Supervision, Writing – review & editing.

Data availability

No data was used for the research described in the article.

Acknowledgmnts

We are grateful to all the researchers in the relevant areas whose work made it possible to write this review. We thank Dr. Ayfer Calis, Commissioning Editor, for kindly inviting to write this review. We also thank the Fungal Genetics Stock Center (FGSC), University of Missouri, Kansas City, MO 64110 for *N. crassa* strains.

References

[1] M.J. Berridge, M.D. Bootman, P. Lipp, Calcium - a life and death signal, Nature (1998) 645–648 1998 395:6703. 395, doi:10.1038/27094.
[2] D. Chin, A.R. Means, Calmodulin: a prototypical calcium sensor, Trends Cell Biol. 10 (2000) 322–328, doi:10.1016/s0962-8924(00)01800-6.
[3] A. Roy, A. Kumar, D. Baruah, R. Tamuli, Calcium signaling is involved in diverse cellular processes in fungi, Mycology 12 (2020) 1–15, doi:10.1080/21501203.2020.1785962.
[4] J. Schmid, F.M. Harold, Dual roles for calcium ions in apical growth of *Neurospora crassa*, J. Gen. Microbiol. 134 (1988) 2623–2631, doi:10.1099/00221287-134-9-2623.
[5] M.L. Nelson, S.B. Levy, The history of the tetracyclines, Ann. N. Y. Acad. Sci. 1241 (2011) 17–32, doi:10.1111/J.1749-6632.2011.06354.
[6] T.H. Jukes, Some historical notes on chlortetracycline, Rev. Infect. Dis. 7 (1985) 702–707, doi:10.1093/clinids/7.5.702.
[7] M.H. Farkas, E.R.E. Mojica, M. Patel, D.S. Aga, J.O. Berry, Development of a rapid biolistic assay to determine changes in relative levels of intracellular calcium in leaves following tetracycline uptake by pinto bean plants, Analyst 134 (2009) 1594–1600, doi:10.1039/B902147G.
[8] A.H. Caswell, S. Warren, Observation of calcium uptake by isolated sarcoplasmic reticulum employing a fluorescent chelate probe, Biochem. Biophys. Res. Commun. 46 (1972) 1757–1763, doi:10.1016/0006-291X(72)90047-2.
[9] N.E. Owen, G.C. le Breton, Ca^{2+} mobilization in blood platelets as visualized by chlortetracycline fluorescence, Am. J. Physiol. Heart Circ. Physiol. 241 (1981) 613–619, doi:10.1152/ajpheart.1981.241.4.H613.
[10] R. Luthra, M.S. Olson, Studies of mitochondrial calcium movements using chlorotetracycline, Biochim. Biophys. Acta Bioenerg. 440 (1976) 744–758, doi:10.1016/0005-2728(76)90056-6.
[11] P.H. Naccache, M. Volpi, H.J. Showell, E.L. Becker, R.I. Sha'afi, Chemotactic factor-induced release of membrane calcium in rabbit neutrophils, Science 203 (1979) 461–463, doi:10.1126/SCIENCE.760200.
[12] G.C. le Breton, R.J. Dinerstein, L.J. Roth, H. Feinberg, Direct evidence for intracellular divalent cation redistribution associated with platelet shape change, Biochem. Biophys. Res. Commun. 71 (1976) 362–370, doi:10.1016/0006-291X(76)90291-6.
[13] G.C. le Breton, R.J. Dinerstein, Effect of the calcium antagonist TMB-6 on intracellular calcium redistribution associated with platelet shape change, Thromb. Res. 10 (1977) 521–523, doi:10.1016/0049-3848(77)90161-X.
[14] M.B. Feinstein, Release of intracellular membrane-bound calcium precedes the onset of stimulus-induced exocytosis in platelets, Biochem. Biophys. Res. Commun. 93 (1980) 593–600, doi:10.1016/0006-291X(80)91119-5.
[15] E.J. Bowman, R. Kendle, B.J. Bowman, Disruption of vma-1, the gene encoding the catalytic subunit of the vacuolar H^+-ATPase, causes severe morphological changes in *Neurospora crassa*, J. Biol. Chem. 275 (2000) 167–176, doi:10.1074/jbc.275.1.167.
[16] R.R. Lew, Ionic currents and ion fluxes in *Neurospora crassa* hyphae, J. Exp. Bot. 58 (2007) 3475–3481, doi:10.1093/jxb/erm204.

[17] P.J.S. Smith, K. Hammar, D. Marshall, R.H. Sanger, J.R. Trimarchi, Self-referencing, non-invasive, ion selective electrode for single cell detection of trans-plasma membrane calcium flux, Microsc. Res. Tech. 46 (1999) 398–417. doi:10.1002/(SICI)1097-0029(19990915)46:6<398::AID-JEMT8>3.0.CO;2-H

[18] U. Schefer, D. Ammann, E. Pretsch, U. Oesch, W. Simon, Neutral carrier based calcium (2+)-selective electrode with detection limit in the sub-nanomolar range, Anal. Chem. 52 (1986) 2282–2285, doi:10.1021/ac00124a036.

[19] A.J. Miller, G. Vogg, D. Sanderst, Cytosolic calcium homeostasis in fungi: Roles of plasma membrane transport and intracellular sequestration of calcium, Proc. Natl. Acad. Sci. 87 (1990) 9348–9352, doi:10.1073/pnas.87.23.9348.

[20] J. Zhai, Y. Zhang, D. Zhao, L. Kou, G. Zhao, The data of an all-solid-state acupuncture needle based potentiometric microelectrode for in vivo monitoring of calcium ions in rat cerebrospinal fluid, Data Brief 41 (2022) 107949, doi:10.1016/j.dib.2022.107949.

[21] G. Duncan, T.J.C. Jacob, Calcium and the physiology of cataract, Ciba Found. Symp. 106 (1984) 132–152, doi:10.1002/9780470720875.

[22] T. Björkman, R.E. Cleland, The role of extracellular free-calcium gradients in gravitropic signalling in maize roots, Planta 185 (1991) 379–384.

[23] R. Neer, G. Tully, P. Schatz, D.J. Hnatowich, Use of stable 48Ca in the clinical measurement of intestinal calcium absorption, Calcif. Tissue Res. 26 (1978) 5–11, doi:10.1007/BF02013226.

[24] E. Denk, D. Hillegonds, J. Vogel, A. Synal, C. Geppert, K. Wendt, K. Fattinger, C. Hennessy, M. Berglund, R.F. Hurrell, T. Walczyk, Labeling the human skeleton with 41Ca to assess changes in bone calcium metabolism, Anal. Bioanal. Chem. 386 (2006) 1587–1602, doi:10.1007/S00216-006-0795-5.

[25] D. Halachmi, Y. Eilam, Elevated cytosolic free Ca^{2+} concentrations and massive Ca^{2+} accumulation within vacuoles, in yeast mutant lacking PMR1, a homolog of Ca^{2+}-ATPase, FEBS Lett. 392 (1996) 194–200, doi:10.1016/0014-5793(96)00799-5.

[26] B.J. Bowman, S. Abreu, E. Margolles-Clark, M. Draskovic, E.J. Bowman, Role of four calcium transport proteins, encoded by *nca-1*, *nca-2*, *nca-3*, and *cax*, in maintaining intracellular calcium levels in *Neurospora crassa*, Eukaryot. Cell 10 (2011) 654–661, doi:10.1128/EC.00239-10.

[27] M. Mank, O. Griesbeck, Genetically encoded calcium indicators, Chem. Rev. 108 (2008) 1550–1564, doi:10.1021/cr078213v.

[28] J.E. McCombs, A.E. Palmer, Measuring calcium dynamics in living cells with genetically encodable calcium indicators, Methods 46 (2008) 152–159, doi:10.1016/j.ymeth.2008.09.015.

[29] N.V. Barykina, O.M. Subach, K.D. Piatkevich, E.E. Jung, A.Y. Malyshev, I.V. Smirnov, A.O. Bogorodskiy, V.I. Borshchevskiy, A.M. Varizhuk, G.E. Pozmogova, E.S. Boyden, K.V. Anokhin, G.N. Enikolopov, F.V. Subach, Green fluorescent genetically encoded calcium indicator based on calmodulin/M13-peptide from fungi, PLoS One 12 (2017) e0183757, doi:10.1371/journal.pone.0183757.

[30] G. Nelson, O. Kozlova-Zwinderman, A.J. Collis, M.R. Knight, J.R.S. Fincham, C.P. Stanger, A. Renwick, J.G.M. Hessing, P.J. Punt, C.A.M.J.J. van den Hondel, N.D. Read, Calcium measurements in living filamentous fungi expressing codon-optimized aequorin, Mol. Microbiol. 52 (2004) 1437–1450, doi:10.1111/j.1365-2958.2004.04066.x.

[31] O. Shimomura, F.H. Johnson, Y. Saiga, Extraction, purification and properties of aequorin, a bioluminescent protein from the luminous hydromedusan, Aequorea, J. Cell. Comp. Physiol. 59 (1962) 223–239, doi:10.1002/JCP.1030590302.

[32] E.B. Ridgway, C.C. Ashley, Calcium transients in single muscle fibers, Biochem. Biophys. Res. Commun. 29 (1967) 229–234, doi:10.1016/0006-291X(67)90592-X.

[33] D. Button, M. Brownstein, Aequorin-expressing mammalian cell lines used to report Ca^{2+} mobilization, Cell Calcium 14 (1993) 663–671, doi:10.1016/0143-4160(93)90091-J.

[34] R.E. Williamson, C.C. Ashley, Free Ca^{2+} and cytoplasmic streaming in the alga *Chara*, Nature 296 (1982) 647–651, doi:10.1038/296647a0.

[35] M.R. Knight, A.K. Campbell, S.M. Smith, A.J. Trewavas, Transgenic plant aequorin reports the effects of touch and cold-shock and elicitors on cytoplasmic calcium, Nature 352 (1991) 524–526, doi:10.1038/352524a0.

[36] M.R. Knight, A.K. Campbell, S.M. Smith, A.J. Trewavas, Recombinant aequorin as a probe for cytosolic free Ca^{2+} in *Escherichia coli*, FEBS Lett. 282 (1991) 405–408, doi:10.1016/0014-5793(91)80524-7.

[37] J. Nakajima-Shimada, H. Iida, F.I. Tsuji, Y. Anraku, Monitoring of intracellular calcium in *Saccharomyces cerevisiae* with an apoaequorin cDNA expression system, Proc. Natl. Acad. Sci. 88 (1991) 6878–6882, doi:10.1073/PNAS.88.15.6878.

[38] A.J. Collis, The Development of Transgenic Aequorin as an Indicator for Cytosolic Free Calcium in *Neurospora crassa*, 1996.

[39] A. Muñoz, M. Chu, P.I. Marris, U.S. Sagaram, J. Kaur, D.M. Shah, N.D. Read, Specific domains of plant defensins differentially disrupt colony initiation, cell fusion and calcium homeostasis in *Neurospora crassa*, Mol. Microbiol. 92 (2014) 1357–1374, doi:10.1111/MMI.12634.

[40] S.A. Vella, A. Calixto, B. Asady, Z.H. Li, S.N.J. Moreno, Genetic Indicators for Calcium Signaling Studies in Toxoplasma gondii, in: Methods in Molecular Biology, Humana Press Inc, 2020, pp. 187–207, doi:10.1007/978-1-4939-9857-9_11.

[41] Y. Zhao, S. Araki, J. Wu, T. Teramoto, Y.F. Chang, M. Nakano, A.S. Abdelfattah, M. Fujiwara, T. Ishihara, T. Nagai, R.E. Campbell, An expanded palette of genetically encoded Ca^{2+} indicators, Science 333 (2011) 1888–1891, doi:10.1126/science.1208592.

[42] L.B. Silverman-Gavrila, R.R. Lew, Calcium and tip growth in *Neurospora crassa*, Protoplasma 213 (2000) 203–217, doi:10.1007/BF01282158.

[43] L.B. Silverman-Gavrila, R.R. Lew, An IP3-activated Ca^{2+} channel regulates fungal tip growth, J. Cell Sci. 115 (2002) 5013–5025, doi:10.1242/JCS.00180.

[44] R. Tamuli, A. Kumar, D.A. Srivastava, R. Deka, Calcium Signaling Neurospora, in: Genomics and Molecular Biology, Caister Academic Press, 2013, pp. 35–37.

[45] M. Hallett, A.S. Schneider, E. Carbone, Tetracycline fluorescence as calcium-probe for nerve membrane with some model studies using erythrocyte ghosts, J. Membr. Biol. 10 (1972) 31–44, doi:10.1007/BF01867846.

[46] R.H. Davis, F.J. de Serres, Genetic and microbiological research techniques for *Neurospora crassa*, Meth. Enzymol. 17 (1970) 79–143, doi:10.1016/0076-6879(71)17168-6.

[47] A. Barman, R. Tamuli, Multiple cellular roles of *Neurospora crassa plc-1*, *splA2*, and *cpe-1* in regulation of cytosolic free calcium, carotenoid accumulation, stress responses, and acquisition of thermotolerance, J. Microbiol. 53 (2015) 226–235, doi:10.1007/S12275-015-4465-1.

[48] R.R. Lew, Comparative analysis of Ca^{2+} and H^+ flux magnitude and location along growing hyphae of *Saprolegnia ferax* and *Neurospora crassa*, Eur. J. Cell Biol. 78 (1999) 892–902, doi:10.1016/S0171-9335(99)80091-0.

[49] W. Rall, Core Conductor Theory and Cable Properties of Neurons, Compr. Physiol. (1977) 39–97, doi:10.1002/CPHY.CP010103.

[50] M.A. Messerli, K.R. Robinson, P.J.S. Smith, Electrochemical Sensor applications to the study of molecular physiology and analyte flux in plants, in: Plant Electrophysiology: Theory and Methods, 2006, pp. 73–107, doi:10.1007/978-3-540-37843-3_4.

[51] J. Voipio, M. Pasternack, K. Macleod, in: Ion-sensitive microelectrodes, Microelectrode Techniques: The Plymouth Workshop Handbook, A3 Book chapter, 1994, pp. 275–316.

[52] D. Ammann, Ca^{2+}-selective microelectrodes, Cell Calcium 6 (1985) 39–55, doi:10.1016/0143-4160(85)90033-8.

[53] G.H. Henriksen, D.R. Raman, L.P. Walker, R.M. Spanswick, Measurement of Net Fluxes of Ammonium and Nitrate at the Surface of Barley Roots Using Ion-Selective Microelectrodes1, Plant Physiol. 99 (1992) 734–747, doi:10.1104/pp.99.2.734.

[54] A.B. Beck, S. Bügel, S. Stürup, M. Jensen, C. Mølgaard, M. Hansen, O.W. Krogsgaard, B. Sandström, A novel dual radio- and stable-isotope method for measuring calcium absorption in humans: comparison with the whole-body radioisotope retention method, Am. J. Clin. Nutr. 77 (2003) 399–405, doi:10.1093/AJCN/77.2.399.

[55] C.L. Cramer, J.L. Ristow, T.J. Paulus, R.H. Davis, Methods for mycelial breakage and isolation of mitochondria and vacuoles of *Neurospora*, Anal. Biochem. 128 (1983) 384–392, doi:10.1016/0003-2697(83)90390-1.

[56] E.J. Bowman, B.J. Bowman, [42]Purification of vacuolar membranes, mitochondria, and plasma membrane from *Neurospora crassa* and modes of discriminating among the different H^+-ATPases, Meth. Enzymol. 157 (1988) 562–573, doi:10.1016/0076-6879(88)57104-5.

[57] R. Tisi, E. Martegani, R.L. Brandão, Measurement of calcium uptake in yeast using 45Ca, Cold Spring Harb. Protoc. 2015 (2015) 217–218, doi:10.1101/pdb.prot076877.

[58] A. Winkler, M. Knoche, Penetration of sweet cherry skin by 45Ca-salts: pathways and factors, Sci. Rep. 11 (2021) 11142, doi:10.1038/s41598-021-90727-0.

[59] J.M. Kendall, M.N. Badminton, Aequorea victoria bioluminescence moves into an exciting new era, Trends Biotechnol. 16 (1998) 216–224, doi:10.1016/S0167-7799(98)01184-6.

[60] O. Shimomura, F.H. Johnson, Chemical nature of the light emitter in bioluminescence of aequorin, Tetrahedron Lett. 14 (1973) 2963–2966, doi:10.1016/S0040-4039(01)96293-8.

[61] O. Shimomura, F.H. Johnson, Properties of the bioluminescent protein aequorin, Biochemistry 8 (1969) 3991–3997, doi:10.1021/bi00838a015.

[62] A.K. Campbell, Chemiluminescence. Principles and applications in biology and medicine, FEBS Lett. 247 (1988) 608.

[63] A.L. Miller, E. Karplus, L.F. Jaffe, Imaging [Ca2+] i with aequorin using a photon imaging detector, Methods Cell Biol. (1994) 305–338, doi:10.1016/s0091-679x(08)61120-6.

[64] N. Takeshita, M. Evangelinos, L. Zhou, T. Serizawa, R.A. Somera-Fajardo, L. Lu, N. Takaya, G.U. Nienhaus, R. Fischer, Pulses of Ca^{2+} coordinate actin assembly and exocytosis for stepwise cell extension, Proc. Natl. Acad. Sci. 114 (2017) 5701–5706, doi:10.1073/pnas.1700204114.

[65] M.M. Bradford, A rapid and sensitive method for the quantitation of microgram quantities of protein utilizing the principle of protein-dye binding, Anal. Biochem. 72 (1976) 248–254, doi:10.1016/0003-2697(76)90527-3.

[66] O. Shimomura, Preparation and handling of aequorin solutions for the measurement of cellular Ca^{2+}, Cell Calcium. 12 (1991) 635–643, doi:10.1016/0143-4160(91)90060-R.

[67] M.D. Fricker, C. Plieth, H. Knight, E. Blancoflor, M.R. Knight, N.S. White, S. Gilroy, Fluorescence and luminescence techniques to probe ion activities in plant cells, in: W.T. Mason (Ed.), Fluorescent and Luminescence Probes for Biological Activity, 2nd Ed., Academic Press, New York, 1999, pp. 569–596, doi:10.1016/B978-012447836-7/50044-0.

[68] N.C. Shaner, M.Z. Lin, M.R. McKeown, P.A. Steinbach, K.L. Hazelwood, M.W. Davidson, R.Y. Tsien, Improving the photostability of bright monomeric orange and red fluorescent proteins, Nat. Methods 5 (2008) 545–551, doi:10.1038/nmeth.1209.

[69] G. Grynkiewicz, M. Poenie, R.Y. Tsienb, A New Generation of Ca^{2+} Indicators with Greatly Improved Fluorescence Properties, J. Biol. Chem. 260 (1985) 3440–3450, doi:10.1016/S0021-9258(19)83641-4.

[70] H. Dana, B. Mohar, Y. Sun, S. Narayan, A. Gordus, J.P. Hasseman, G. Tsegaye, G.T. Holt, A. Hu, D. Walpita, R. Patel, J.J. Macklin, C.I. Bargmann, M.B. Ahrens, E.R. Schreiter, V. Jayaraman, L.L. Looger, K. Svoboda, D.S. Kim, Sensitive red protein calcium indicators for imaging neural activity, elife 5 (2016) e12727, doi:10.7554/ELIFE.12727.

[71] J. Oh, C. Lee, B.K. Kaang, Imaging and analysis of genetically encoded calcium indicators linking neural circuits and behaviors, Korean J. Physiol. Pharmacol. 23 (2019) 237–249, doi:10.4196/kjpp.2019.23.4.237.

[72] S. Waldchen, J. Lehmann, T. Klein, S. van de Linde, M. Sauer, Light-induced cell damage in live-cell super-resolution microscopy, Sci. Rep. 5 (2015) 15348, doi:10.1038/srep15348.

[73] L.G. Li, Q.T. Hui, S.D. Russell, Calcium function and distribution during fertilization in angiosperms, Am. J. Bot. 94 (2007) 1046–1060, doi:10.3732/AJB.94.6.1046.